

Micro Mechanism of Fatigue Cracking in Asphalt Concrete

Anqi Chen

Thesis submitted to the University of Nottingham for the degree of Doctor of Philosophy

July 2021

Abstract

Asphalt pavements are the main types of pavement structure in the world. With the increase of the service life, distress occurs gradually on asphalt pavements. One of the main distresses that obviously shorten the service life is fatigue cracking. Study of fatigue cracking is important to predict and extend the service life of asphalt pavements. However, the micro mechanism of fatigue cracking in asphalt concrete is still not very clear, which makes it difficult to understand the development law of fatigue cracking and find an efficient way to improve the fatigue resistance of asphalt concrete.

This thesis aims to investigate the micro mechanism of the figure cracking in asphalt concretes from three different scales, namely mechanical parameter, micro CT-scanning and numerical simulation. First, various laboratory fatigue tests were conducted to reveal mechanism of fatigue cracking in asphalt concrete from the perspective of mechanical parameter (stiffness). Second, fatigue cracking in asphalt concrete was characterised based on the high-resolution X-ray CT, aiming to investigate the fatigue damage evolution of asphalt concretes at the micro-level. The air voids content and surface area before and after loading were also calculated and analysed. Third, crack initiation and propagation of asphalt concrete is simulated by the numerical analysis methods. The realistic aggregate morphology is well reconstructed based on clearly visible CT images, the model embedded zero-thickness cohesive elements (CEs) both in asphalt mastic and interfaces between mastic and aggregates.

A stiffness change tendency method (SCTM) is developed to model the stiffness development of different asphalt mixtures and different test methods. It can be used to link the stiffness development to cracks development, and determine the number of cycles where cracks initiate and propagate. Different fatigue damage stages of asphalt

concrete can be characterised with the three transition points (P1, P2 & P3) obtained from SCTM. The P1 and P2 are proved to be related to the crack initiation and propagation, respectively. Three different evolution stages of microcracks are visualised based on CT images. At the first stage, a few microcracks occur at the aggregate–mastic interfaces; at the second stage, microcracks grow continuously, and some microcracks connect; at the third stage, microcracks develop swiftly. Microcracks are discovered to form constantly during the fatigue damage process. A numerical model is established to simulate the whole cracking process in asphalt concrete. The results show that factors such as aggregate size, distance between aggregates are able to affect the crack initiation. At high temperature, microcracks are found to tend to initiate and propagate in mastic, which delayed the macrocracks formation and growth. Crack development phenomena at micro level are similar to macro level, and the reduction in asphalt concrete performance is the combined effect of macrocracks and microcracks. In future study, the SCTM can be useful in a simulation of pavement deterioration by prediction of remaining fatigue life of asphalt concrete. The combined effect of microcracks and macrocracks on the stiffness deterioration of the specimen can be analysed quantitatively. Parameters of the numerical simulation can be changed, including the aggregate type, the binder type, the aggregate gradation, the load conditions, the temperature conditions, etc., to further study the micro-cracking mechanism.

Acknowledgements

This research was partly conducted during Covid-19 period, and it was more difficult than I thought. The research would not be finished without a lot of support, guidance, encouragement and understanding.

I would like to express my great thankful to Prof. Gordon Airey and Dr. Nick Thom who are my supervisors during my study in the University of Nottingham. They are very helpful to teach me professional knowledge and give precious guidance to my research. Many thanks for all your support, which enables me to finish my research in a very relaxed and comfortable environment.

Great thanks to all technicians, Jonathan Watson, Richard Blakemore, Lawrence Pont and Martyn Barrett in NTEC and Brian Atkinson in Biosciences, who patiently guided me through every step in the test, which enables me to successfully complete all laboratory work.

I am grateful to my colleagues who accompanied me during my PhD life, and let me have great time in Nottingham, especially Rufus Adjetey Nii-Adjei and Liyao Wan who donates valuable time and data to this project. The time with my colleagues will be my precious memories in my life.

Finally, I would like to thank my family. They gave me a lot of love and encouragement, so that I can devote all my efforts to study fearlessly. Without your great sacrifice and support, I cannot complete my research.

Declaration

The research reported in this thesis was conducted at the University of Nottingham, Department of Civil Engineering, Nottingham Transportation Engineering Centre (NTEC) between Oct 2018 and July 2021. I declare that the work is my own and has not been submitted for a degree at another university. The results obtained in this thesis were written as three papers. The Chapter 4 was written as Paper 1: Modelling the stiffness development of asphalt concrete to obtain fatigue failure criteria. The paper is published in the journal: Construction and Building Materials. The Chapter 5 was written as Paper 2: Characterisation of fatigue damage in asphalt mixtures using X-ray computed tomography (CT). The paper was submitted to the journal: Road Materials and Pavement Design. The Chapter 6 was written as Paper 3: Simulation of micro-crack initiation and propagation under repeated load in asphalt concrete using zero-thickness cohesive elements, which has just been completed and has not been submitted to any journals before thesis submission.

Contents

1 Introduction 1

1.1 Fatigue Cracking Behaviour and its Influence on Asphalt Pavement 1

1.2 Field and Laboratory Fatigue Tests 3

1.3 Research on Fatigue Behaviour at Micro Level 4

1.4 Objectives of Research 7

1.5 Scope of Research 9

2 Literature Review 11

2.1 Approaches to Study Fatigue Behaviour in Asphalt Concrete 11

2.1.1 Phenomenological Approach 11

2.1.2 Fracture Mechanics 13

2.1.3 Dissipated Energy Approach 15

2.1.4 Microstructural Approach 19

2.2 Characterisation of Fatigue Behaviour in Different Designs 26

2.2.1 Transport and Road Research Laboratory (TRRL, U.K.) Fatigue Model 27

2.2.2 The University of Nottingham (UoN, U.K.) Model 28

2.2.3 Superior Performing Asphalt Pavements (SUPERPAVE, U.S.) Fatigue Model 28

2.2.4 Asphalt Institute (AI, U.S.) Fatigue Model 29

2.2.5 SHELL Pavement Design Model 30

2.2.6 WesTrack (U.S.) Fatigue Model 30

2.2.7 Specifications for Design of Highway Asphalt Pavement (CHN.) Model 31

2.3 The Logistic Model and its Application 32

2.4 X-ray Computed Tomography (CT) and Digital Image Processing (DIP) 34
2.4.1 X-ray CT 34
2.4.2 DIP 36
2.5 Approaches for Reconstruction in Numerical Simulation 43
2.5.1 The Computer-generated Approach 43
2.5.2 The Image-based Approach 48
2.6 Fracture Processing Behaviour and the Cohesive Zone Model (CZM) Theory 50
2.6.1 Fracture Process Zone 51
2.6.2 Cohesive Zone Model (CZM) 52
2.6.3 CZ Traction-separation Relationships 54
2.6.4 Methods to Embed Cohesive Elements 57
2.6.5 CZM Application in Viscoelastic Materials 59
2.7 Summary 64
3 Materials and Experimental Programme 66
3.1 Introduction 66
3.2 Raw Materials and Mixture Design 66
3.3 Mixing and Compaction 68
3.4 Dynamic Shear Rheometer (DSR) Test 70
3.5 Thermal Oxidative Ageing Test 71
3.6 Moisture Damage Test 72
3.7 Two Point Bending (2PB) Test 73
3.8 Wheel Tracking Fatigue Test (WTT) 76
3.9 Four Point Bending (4PB) Test 78
3.10 Indirect Tensile Fatigue Test (ITFT) 79
3.11 X-ray Computed Tomography (CT) 81
3.12 Bespoke Tensile Strength Test 82

3.13 Summary 83

4 Modelling the stiffness Development and Links to Crack Development 84

4.1 Introduction 84

4.2 Programme 86

4.3 Determination of Fatigue Failure Criteria by Energy-based Approaches 88

4.3.1 Dissipated Energy Approach 88

4.3.2 Energy Ratio (ER) Approach 89

4.3.3 Ratio of Dissipated Energy Change (RDEC) Approach 91

4.4 Development of the stiffness Change Tendency Method (SCTM) 93

4.4.1 The SCTM Definition 93

4.4.2 The SCTM Analysis 96

4.5 Validation of the SCTM 105

4.5.1 Dissipated Energy Approach 105

4.5.2 ER Approach 107

4.5.3 RDEC Approach 109

4.5.4 Comparison between Fatigue Failure Criteria obtained from the SCTM and the Energy-based methods 111

4.6 Factors Affecting the Fatigue Failure Criteria obtained by the SCTM 113

4.6.1 Strain Level 113

4.6.2 Temperature 115

4.6.3 Ageing and Moisture 118

4.6.4 Relating the Stiffness Development to Crack Development 120

4.7 Conclusions 124

5 Characterisation of Fatigue Damage in Asphalt Concrete in Micro Level 127

5.1 Introduction 127

5.2 Programme 129

5.3 Image Analysis Methods 130

5.3.1 Digital Image Processing (DIP) 130
5.3.2 The Coordinate Axis and the Image Area for Calculation 131
5.3.3 Calculation Equations for Volume and Surface Area Parameters 132
5.4 Fatigue Damage Evolution 133
5.5 Air Voids Content Distribution 137
5.6 Air Voids Surface Area Distribution 146
5.7 Volume and Surface Area Parameters 148
5.8 Conclusions 149
6 Numerical Modelling of Fatigue Cracking in Asphalt Concrete Using Cohesive Elements 151
6.1 Introduction 151
6.2 Programme 153
6.3 Background 154
6.3.1 Viscoelastic Model 154
6.3.2 Bilinear Cohesive Zone Model (CZM) 156
6.3.3 Generate Zero-thickness Cohesive Interface Elements 158
6.4 Microstructures Reconstruction Based on X-Ray CT Images 160
6.4.1 Microstructure Acquisition using DIP 160
6.4.2 Numerical Model Generation 161
6.4.3 Cohesive Element Embedment 162
6.5 Parameters for Numerical Modelling of Fatigue Cracking in Asphalt Concrete 163
6.5.1 Viscoelastic Model Parameters 163
6.5.2 Cohesive Element (CE) Properties 165
6.5.3 Aggregates Properties and Load Parameters 166
6.6 Crack Initiation and Propagation 167
6.7 Comparison between the Numerical Simulation and Experimental Results . 170

6.8 Influence of Temperature on Fatigue Cracking Behaviours 173
6.9 Conclusions 175
7 Conclusions and Recommendations 177
7.1 Conclusions 177
7.2 Recommendations and Future work 179
References 181
Appendix A- SCTM Fitting Results under Different Temperatures, Strains, Conditions 206
Appendix B- Air Voids Distribution 212
Appendix C- Increase in Air Voids Content 218

List of Figures

Figure 1.1: Vehicle miles forecasts for England & Wales (Historic & Forecast). 2

Figure 1.2: Load distribution and the bridging and the process zones. 3

Figure 2.1: Three development stages of cracks and the da/dN versus ΔK curve.....15

Figure 2.2: Hysteresis loop of asphalt concrete [27]. 16

Figure 2.3: Lattice model: (a) random nodes inside base mesh; (b) lattice network formed by delaunay triangulation; and (c) lattice mesh [39]. 20

Figure 2.4: Bilinear cohesive zone fracture model [41] [42]. 20

Figure 2.5: Damage state of asphalt mixture [43]. 21

Figure 2.6: Damage ratio (DR) versus fractal dimension [43].....22

Figure 2.7: FESEM micrographs of NA at magnification of (a) 500× and (b) 5,000× [44]. 23

Figure 2.8: FESEM micrographs of CKD3%+CWA3% at magnification of (a) 10,000× and (b) 50,000× [44]. 24

Figure 2.9: AFM phase images (a) asphalt binder A and (b) asphalt binder B (50 × 50 $\mu m2$) after 5% strain. 25

Figure 2.10: Tensile strain contours for FE simulations (a) asphalt binder A and (b) asphalt binder B (50 × 50 $\mu m2$). 25

Figure 2.11: Water replacement at asphalt binder/aggregate interface [46].....26

Figure 2.12: Tension loading process [47]. 26

Figure 2.13: Difference between the linear regression and logistic regression [56]....33

Figure 2.14: Schematic of industrial X-ray CT system.....35

Figure 2.15: Schematic of X-ray radiation absorption. 36

Figure 2.16: (a) X-ray CT 2D image of a mixture sample; (b) Reconstruction of the 3D CT model from 2D image slices. 36

Figure 2.17: Transformation of a scanned digital image into a voxel matrix [79]. 38

Figure 2.18: Image brightness histogram [81]. 38

Figure 2.19: (a) Original X-ray CT image; (b) Contrast enhancement image; (c) Median filtered image of a mixture sample. 39
Figure 2.20: Image profile of a mixture sample.....40
Figure 2.21: Histogram of a mixture sample. 41
Figure 2.22: A mixture sample adjusting the threshold values (a) Aggregate; (b) Mastic and (c) Air voids.....42
Figure 2.23: Image after pseudo colour transformation of a mixture sample.....42
Figure 2.24: (a) Aggregate binary image; (b) After filter and holes filling; (c) After erosion with open and dilation with close.....43
Figure 2.25: Idealised form of user-defined aggregate particles applied in FEM [83] 45
Figure 2.26: Angular form (polyhedral) of aggregate particles applied for 3D FEM in cement concrete [55].....46
Figure 2.27: (a) Automated sphere growth technique, (b) sphere clump after the first growth, and (c) after the second growth [96].....46
Figure 2.28: 3D model reconstructed from digital scanning (left) and from the spherical harmonic mathematical analysis (right) [98]. 47
Figure 2.29: The particle overlapping detection method (left) and visualisation (right) [100].....48
Figure 2.30: Image processing to identify three phases in 2D FEM [104].....49
Figure 2.31: (a) Original image of asphalt concrete, (b) binary image, and (c) DEM simulation [109].....50
Figure 2.32: Reconstruct 3D DEM from 2D DEM [107].....50
Figure 2.33: Concept of fracture process zone [115].....52
Figure 2.34: Concept of the CZM [119]. 53
Figure 2.35: Mechanics of the CZM [120]. 54
Figure 2.36: Traction-separation relationships: (a) cubic polynomial[130], (b)

trapezoidal[131], (c) smoothed trapezoidal[132], (d) exponential[133], (e) linear softening [134-136] and (f) bilinear softening [134-136]. 56
Figure 2.37: (a) Typical atomistic potential ($\boldsymbol{\Psi}$) and (b) its derivative ($\boldsymbol{\Psi'}$) [126]. 57
Figure 2.38: Intrinsic CZM. 58
Figure 2.39: Extrinsic CZM. 59
Figure 2.40: FEM using intrinsic CZM [150]. 60
Figure 2.42: Bilinear CZM and 2D microstructures [151]. 62
Figure 2.43: 3D FEM with mesh and boundary conditions and aggregates with different angularities: (a) 3DTS = 0.395, (b) 0.410, (c) 0.425 and (d) 0.440 [152]. 63
Figure 2.44: Concrete beam divided into homogeneous, and heterogeneous parts with two different 3-phase regions [153]. 63
Figure 3.1: Gradations of (a) DBM-14, (b) DBM-10 and (c) SMA-10 of Hot Mix Asphalt (HMA). 68
Figure 3.2: Mixing procedure (BS EN 12697-35: 2016). 69
Figure 3.3: Compaction of asphalt concrete (BS EN 12697-33: 2003). 69
Figure 3.4 : Testing compaction temperature. 70
Figure 3.5 : DSR test set-up. 71
Figure 3.6: Oven setting and the materials after the (a) Short-term ageing and (b) Long-term ageing. 72
Figure 3.7: Water bath for moisture conditioning of specimens. 73
Figure 3.8: Sample preparation and setting of 2PB: (a) Schematic diagram of preparation of trapezoidal specimens; (b) Gluing of samples and (c) Setting procedure of samples. 74
Figure 3.9: Stress in the 2PB samples. 75
Figure 3.10: Loading mode of 2PB tests. 76
Figure 3.11: (a) Arrangement of the WTT; (b) WTT set-up; (c) Fracture in the middle of the beam sample and (d) Diagram of the mould. 78

Figure 3.12: Set-up of the 4PB test. 79
Figure 3.13: (a) Cutting procedure; (b) Prepared samples. 80
Figure 3.14: (a) Indirect tensile fatigue test set-up; (b) Schematic diagram of the load during the ITFT. 81
Figure 3.15: X-ray CT equipment set-up. 82
Figure 3.16: Asphalt mastic tensile strength test (a) the specially designed mould; (b) the UTM machine set-up; (c) the dog bone-shaped specimen dimensions; and (d) Fracture location. 83
Figure 4.1: Scheme for testing programme. 88
Figure 4.2: lgE versus lgN (10 ℃, 150 με). 89
Figure 4.3 Dissipated energy versus number of load cycles (10 ℃, 150 με). 91
Figure 4.4: ER versus number of load cycles (10 ℃, 150 με). 91
Figure 4.5: RDEC versus number of load cycles (10 ℃, 150 με). 93
Figure 4.6: Four regions of a stiffness reduction curve, based on three transition points 95
Figure 4.7: Typical curves of the logistic regression. 95
Figure 4.8: Fitting logistic equation and it's the second derivative. 96
Figure 4.9: Fitting results under different temperatures, strains and conditions of 2PB tests: (a) 0 ℃ and 200 με; (b) 20 ℃ and 200 με; (c) 10 ℃ and 200 με aged; (d) 10 ℃ and 200 με moisture damaged. 101
Figure 4.10: Fitting results of different asphalt mixtures at 10 ℃ under 270 με of 4PB tests (a) DBM-14+Pen40/60; (b) DBM-10+ CRMB; (c) SMA-10+Pen40/60 103
Figure 4.11: Number of cycles per unit stiffness loss, **Ω**, at P1, P2 and P3. 105
Figure 4.12: Stress-strain hysteresis loops change (10 ℃, 150 με) for controlled strain 2PB test: (a) first stage; (b) second stage and (c) third stage. 107
Figure 4.13: Energy ratio versus number of load cycles for controlled strain 2PB test:

(a) at different temperatures; (b) under different strains; (c) under different conditions; and for 4PB test: (d) of different mixtures. 109

Figure 4.14: ΔA versus number of cycles for controlled strain 2PB test: (a) At different temperatures, (b) Under different strains; (c) Under different conditions and for 4PB test: (d) of different mixtures. 111

Figure 4.15: Comparison of fatigue failure criteria gained from different methods: (a) N_{p1} and N_1; and (b) N_{p1} and N_{fm}. 112

Figure 4.16: Results of (a) Np1, (b) Np2 and (c) Np3 of unaged, aged and aged + moisture damaged specimens at different strain levels. 115

Figure 4.17: The results of (a) Np1, (b) Np2 and (c) Np3 of unaged, aged and aged + moisture damaged specimens at different temperatures. 117

Figure 4.18: Initial stiffness of unaged, aged and aged + moisture damaged specimen at different temperatures. 118

Figure 4.19: The change of Np1, Np2 and Np3 of unaged, aged and moisture damaged specimens (a) at different strain levels and (b) at different temperatures. 120

Figure 4.20: Ageing and moisture modified indexes. 120

Figure 4.21: Fatigue crack development of (a) the beams; (b) at different stages of beam 3#. 123

Figure 4.22: Relation between stiffness development and fatigue crack development of the (a) beam1#; (b) beam2# and (c) beam3#. 124

Figure 5.1 Scheme for testing programme. 130

Figure 5.2: CT X-ray image processing; (a) The geometry and dimensions of samples; (b) Central CT slice image; (c) AOI extracted by gray value; (d) After pseudo colour transformation; the phase (e) Aggregates; (f) Mastic and (g) Air voids after adjusting the threshold values; (h) 3D reconstruction from 2D slices... 131

Figure 5.3: The coordinate axis and the image area for calculation. 132

Figure 5.4: (a) Vertical deformation vs. number of cycles showing three different fatigue

damage stages; (b) Strain vs. time curve and (c) Vertical deformation vs. time curve. 135
Figure 5.5: Air voids of unloaded samples and microcracks of loaded samples under different vertical deformation: (a) 0.4 mm; (b) 0.6 mm; (c) 0.8 mm; (d) 0.9 mm; (e) 1.1 mm and (f) 1.4 mm. 137
Figure 5.6: Air voids distribution in Y direction at (a) 0.4 mm; (b) 0.9 mm; (c) 1.4 mm vertical deformation. 139
Figure 5.7: Increase in air voids content at (a) 0.4 mm and (b) 0.6 mm vertical deformation and the images of slices at the position of the max and min increase in air voids content in Y direction. 140
Figure 5.8: The images at the position of the min increase in air voids content at (a) 0.8 mm, (b) 0.9 mm, (c) 1.1 mm and (d) 1.4 mm in Y direction. 141
Figure 5.9: Images at the position of the max increase in air voids content at (a) 0.8 mm, (b) 0.9 mm, (c) 1.1 mm and (d) 1.4 mm in Y direction. 141
Figure 5.10: Increase in air voids content at (a) 0.4 mm and (b) 0.6 mm vertical deformation and the images at the position of the max and min increase in air voids content in X direction. 142
Figure 5.11: The images at the position of the max increase in air voids content at (a) 0.8 mm, (b) 0.9 mm, (c) 1.1 mm and (d) 1.4 mm in X direction. 144
Figure 5.12: Illustration of morphological characteristic of aggregates: (a) angular and non-angular aggregate; (b) aggregate with many fractured faces; (c) shape characterization [215]. 144
Figure 5.13: Air voids surface area distribution of the whole sample (at 0.4mm vertical deformation). 147
Figure 5.14: Increase rate of the air voids surface area at three ranges. 147
Figure 6.1: Scheme for testing/modelling programme. 154
Figure 6.2: Schematic of the generalized Maxwell model. 156

Figure 6.3: A typical bilinear traction-separation law (normal component). 158
Figure 6.4: Schematic depiction of a 4-noded cohesive element. 160
Figure 6.5: Method to choose images for numerical model generation. 161
Figure 6.6: (a) Original CT image; (b) Two-phase (aggregate and mastic) binary image and (c) Geometry image; (d) FE mesh image. 162
Figure 6.7: Embedding 2D cohesive zone elements (a) In interfaces between aggregates and mastic and (b) Within mastic. 163
Figure 6.8: The master curves with 5 ℃ and 25 ℃ as the reference temperature. 164
Figure 6.9: Force versus displacement curves of the tensile strength test at 5 ℃ and 25 ℃. 166
Figure 6.10: (a) ITFT set-up; (b) Load conditions applied in ITFTs and Load conditions applied in the numerical modelling (c) and (d). 167
Figure 6.11: Transverse tensile stress of (a) Sample 1# and (b) Sample 2# at 100 cycles at 5 ℃, and examples of the crack tip of (c) Sample 1# and (d) Sample 2#. 169
Figure 6.12: Crack initiation of (a) Sample 1# and (c) Sample 2# and propagation of (b) Sample 1# and (b) Sample 2# at 5 ℃. 170
Figure 6.13: Comparison of the vertical deformation versus number of cycles of (a) Sample 1#, and (b) Sample 2# between experimental and numerical results at 5 ℃. 172
Figure 6.14: Comparison of crack paths of (a) (b) Sample 1#, and (c) (d) Sample 2# between experimental and numerical results. 173
Figure 6.15: Microcrack initiation of (a) Sample 1# and (c) Sample 2# and propagation of (b) Sample 1# and (b) Sample 2# at 25 ℃. 175

List of Tables

Table 3.1 Properties of asphalt binder. 67

Table 3.2: The asphalt mastic design. 68

Table 3.3: Dimensions of the 2PB specimens: BS EN 12697-24: 2004. 75

Table 4.1: Testing samples and conditions. 87

Table 4.2 Fitting results for the Logistic model. 98

Table 4.3 Results of second derivative function and the corresponding stiffness ratio (SR). 99

Table 5.1 Results of the trial samples. 129

Table 5.2: Volume and area parameters of samples. 149

Table 6.1: Prony series coefficients of asphalt mastic at 5 ℃ and 25 ℃. 164

Table 6.2: Parameters input in FE modelling at 5 ℃ and 25 ℃. 166

1 Introduction

1.1 Fatigue Cracking Behaviour and its Influence on Asphalt Pavement

Asphalt pavements are widely applied in road engineering due to their advantages such as fast opening to traffic, comfortable driving, easy maintenance, and recyclability. However, various distresses like cracking, rutting and potholes etc. often happen on asphalt pavements, resulting in asphalt pavements being damaged without reaching their designed service life. At the same time, the number of vehicles on the roads is continuously increasing, as shown in Figure 1.1, which presents forecasts in England and Wales up to the year 2050 using the Department for Transport's National Transport Model (NTM) [1]. The increase of vehicles necessitates higher requirements for the quality of asphalt pavements. Improving the fatigue resistance performance of asphalt materials has always been a focus of research, for the reason that fatigue cracking is one of the main forms of asphalt pavement distress.

Under the action of repeated traffic loads, the pavement is under horizontal tensile stress and vertical compressive stress [2], leading to the strength of asphalt pavement gradually decreasing. When the repeated loads exceed a certain number, the strength of the pavement will not be enough to resist the tensile or shear stress generated, normally in the asphalt layer, resulting in fatigue cracks. To investigate these critical stresses and strains and relate them to crack growth, the bridging and the process zone are investigated (Figure 1.2). The so called bridging zone assumes that the surface is smooth and no energy consuming interaction between the already broken parts occurs, therefore, crack growth requires additional energy for either disconnecting the two

layers or breaking the aggregate and pulling the asphalt binder filaments out [3]. Despite these theoretical foundations, it is still difficult to understand fatigue cracking behaviour, and it is even impossible to observe the location of a crack tip using the traditional fatigue tests. In order to ensure good usability and durability of asphalt pavements, it is very important to study the fatigue behaviour of asphalt pavements under specific load and environmental conditions, as well as observe cracking behaviour at micro level.

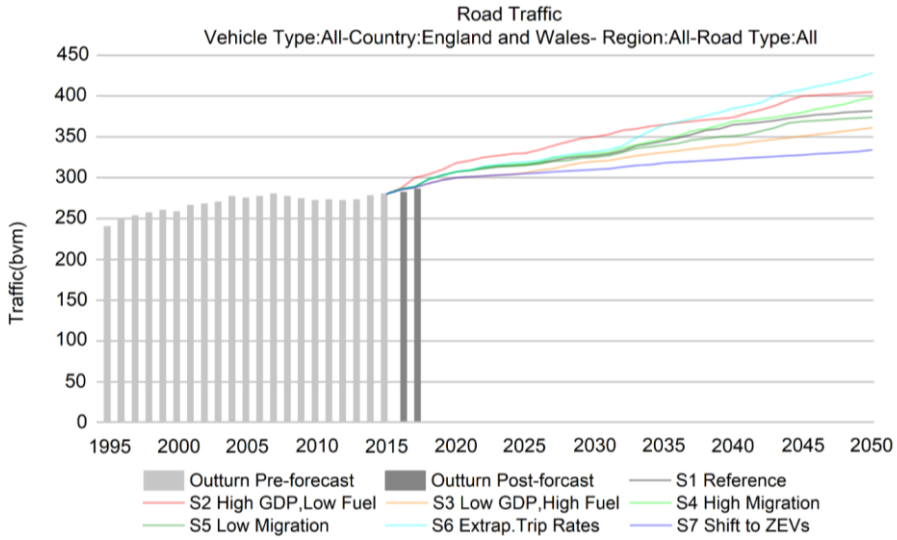


Figure 1.1: Vehicle miles forecasts for England & Wales (Historic & Forecast).

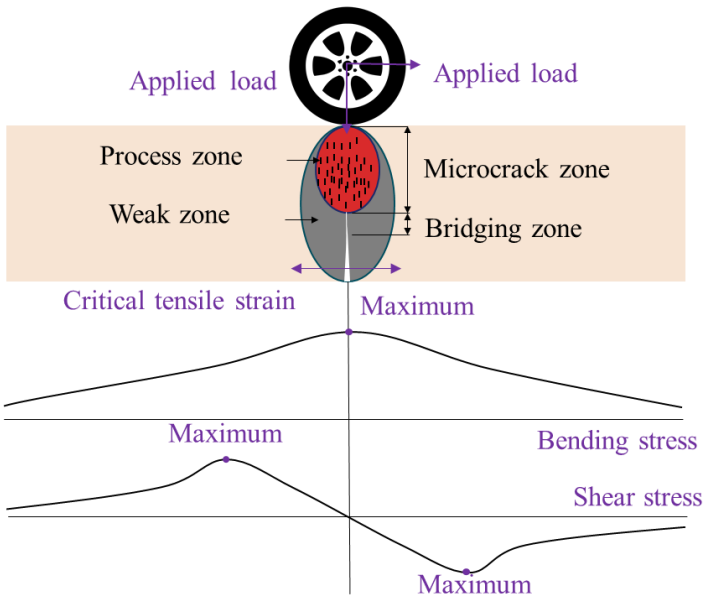


Figure 1.2: Load distribution and the bridging and the process zones.

1.2 Field and Laboratory Fatigue Tests

Various fatigue test methods are investigated to study the fatigue behaviours of asphalt pavements under specific traffic and environmental conditions, aiming to improve the fatigue resistance performance of asphalt concrete, so as to achieve the purpose of increasing service life of asphalt pavements. Fatigue test methods are divided into three main categories: (1) fatigue tests of the actual road surface under real vehicle load, represented by the famous AASHTO test road in the United States [4]; (2) fatigue tests of the full-scale pavement structure under simulated vehicle load, including the accelerated loading test, represented by the famous Heavy Vehicle Simulator (HVS) in South Africa [5]; (3) fatigue tests in the laboratory, in which, the asphalt mixture is made into a specimen of a certain shape, and then a fatigue test is carried out by simulating the strain-stress state of the asphalt pavement. The first two kinds of test methods can be used to simulate more real situations of pavement working conditions;

however, due to the high cost and long loading cycles, their application is limited. Although fatigue tests in the laboratory are more or less different from the field, they are still widely used to evaluate fatigue behaviour of asphalt concrete due to their low cost and short cycles.

Various laboratory methods have been used to measure fatigue performance of asphalt mixtures, including simple bending fatigue tests, supported bending tests, direct axial fatigue tests, indirect tensile fatigue tests, etc. Simple bending tests apply sinusoidal load on a prismatic beam (or a trapezoidal beam) under centre-point or third-point configuration [6, 7]. In supported bending tests, the specimen (beam or circular) is supported in several ways to simulate in-situ stress and modes of loading conditions [8]. Direct axial fatigue tests are applied using uniaxial sinusoidal (pulsating) loads to the specimen (circular or rectangular) [9]. The types of the load can be tension, compression or tension-compression. Indirect tensile fatigue tests apply a compressive load in a diametric direction on cylindrical specimens, to develop a uniform tensile stress along the vertical diametric plane [10]. In addition, the role of the wheel on the road surface is often simulated in a wheel tracking fatigue test, and various fracture tests are used to predict the fatigue life of the mixture based on fracture mechanics [11].

1.3 Research on Fatigue Behaviour at Micro Level

Asphalt concrete material is a multi-component heterogeneous material, and its fatigue behaviour is far more complicated than can be known completely, even the same batch of samples composed of the same raw material and gradation having different fatigue performance. In addition to the external factors considered by laboratory fatigue tests such as temperature and load conditions, fatigue performance of asphalt concrete is also affected by the content of asphalt binder, aggregates and air voids and their distributions.

Therefore, traditional fatigue tests are insufficient, and the use of advanced technology to observe the internal structure and analyse the structural changes during the failure process, is of great significance in studying the fatigue performance of asphalt concrete.

Fatigue cracking of asphalt concrete develops from small to large size. With the change of size and development rate of fatigue cracking in asphalt concrete, the attenuation law of dissipated energy and mechanical properties (stiffness) is also different. The study of dissipated energy in the fatigue failure process of asphalt concrete shows that the change of dissipated energy of asphalt concrete is related to the development of fatigue cracks. There are two turning points for fatigue crack development of asphalt concrete namely micro-crack initiation and the macro-crack generation point, which can more or less characterize the fatigue failure mechanism of asphalt concrete. However, dissipated energy is not a mechanical parameter that can be directly tested by experiment, and a calculation procedure is needed. However, the stiffness parameters of asphalt concrete can be directly measured, although the relationship between the stiffness parameters and the development of fatigue cracks is still not clear. In this thesis, the development mechanism of fatigue cracking of asphalt concrete is studied from the perspective of mechanical parameters.

In addition, there are various microscopic methods that can be used for characterizing the fatigue behaviour of asphalt concrete, such as molecular dynamics methods and the generalized particle dynamics method, scanning electron microscope (SEM), atomic force microscopy (AFM) and Computed Tomography (CT). On the Nano or atomic scale, molecular dynamics methods and the generalized particle dynamics method are used to research the interactions between molecules and atoms of aggregates, asphalt, water, and modifiers, based on the thermodynamic theory and force field theory. But a study conducted at this scale can hardly directly connect to the performance in real

pavements. On the other hand, the SEM and AFM can be applied to study the interfacial microcracks caused by imperfect bonding between the aggregate and the asphalt binder. However, they can be only used to investigate the surface micro morphology of asphalt concrete, and cannot see the cracks in the inner part of asphalt concrete. Meanwhile, CT technology provides an alternative method for studying the fatigue failure mechanism of asphalt concrete materials at micro level. In the early 1990s, the US Strategic Highway Research Program (SHRP) used CT technology to study the internal structure of core samples of mixtures. The work found that CT technology can reasonably and effectively quantitatively analyse the true distribution of the internal components of a core sample [12]. Industrial CT is mainly composed of the X-ray source and detector. The scanning technique uses the ability of short wavelength electromagnetic radiation (X-rays) to penetrate objects by measuring the X-ray intensity before and after it passes through the object. Based on CT technology, the crack tip geometry and internal structure of the asphalt mixture can be fully observed, and the crack propagation and damage evolution law at micro level can be understood.

CT technology can observe the crack growth through the image, and the results can be used to study the relationship between the internal microstructure and the macroscopic properties of asphalt concrete. For this reason, the combination of numerical analysis methods based on CT technology with laboratory tests has become popular among researchers. Pixels in a CT image can be converted into geometric information for the numerical simulation. Numerical models can simulate the failure mode and mechanical properties of materials under different test conditions. Numerical models can be validated with the results of laboratory tests, with the aim of finding a suitable model that can replace some of the laboratory tests. Current research on the numerical simulation of asphalt concrete mainly includes the finite element method (FEM) and the discrete element method (DEM).

1.4 Objectives of Research

It can be seen from the above background that asphalt concrete follows different mechanisms under different length scales, but there is also a correlation between different scales. Therefore, to better understand the fatigue resistance performance of asphalt pavements, the internal structure characteristics of asphalt concrete and the correlation of physical and geometric parameters between different scales also need to be revealed. The main purpose of this project is to study the fatigue cracking behaviour of asphalt concrete at different scales to gain insight into fatigue failure micro mechanisms.

The project is mainly focused on the micro mechanism of fatigue cracking in asphalt concrete. The objectives simply consist of the following parts:

- Model the stiffness development in asphalt concrete to obtain fatigue failure criteria, find factors affecting the criteria, link the stiffness development with crack development, and reveal the development mechanism of fatigue cracking in asphalt concrete from the perspective of mechanical parameters (stiffness).

- Characterise the fatigue damage in asphalt concrete using X-ray Computed Tomography (CT), and investigate fatigue damage evolution at the micro level.

- Simulate initiation and propagation of fatigue cracks in asphalt concrete applying zero-thickness cohesive elements, and verify the model with laboratory fatigue tests. Simulation results further explain micro mechanisms of fatigue cracking in asphalt concrete.

This project first conducted various laboratory fatigue tests to develop a method that

can be used to model the stiffness evolution in asphalt concrete. A logistic model was selected to represent the relationship between the stiffness and the number of cycles obtained from the two-point bending (2PB) fatigue tests. The measured stiffness reduction versus loading curves were determined for a range of asphalt mixtures in unaged, aged and moisture damaged conditions by testing at various temperatures and strains. Different mixtures tested by four-point bending (4PB) fatigue tests were also applied to demonstrate the applicability of the established method in more asphalt binder grades, mixture grades and test methods. By analysing the derivatives of the logistic model, it is possible to identify three transition points associated with fatigue progression. Energy-based methods were applied to verify the method established to identify transition points. The relationship between the stiffness development and the crack development was found by 4PB and wheel tracking fatigue tests (WTTs) based on the established method.

The second part of the research is based on the micro tests (X-ray CT) to characterise the fatigue damage in asphalt concrete; and investigate fatigue damage evolution at the micro level. To overcome the scale applicability of traditional theories and computational efficiency of the numerical simulation method, high resolution X-ray CT (with resolution of $0.014 \times 0.014 \times 0.014$ mm^3) applied on small size samples (20 mm diameter and 18 mm height) is carried out to visualize the detailed crack geometry of asphalt concrete. All samples were tested using the ITFT at 5 ℃ and were set to stop at given vertical deformations. The detailed X-ray CT images in the centre of the samples were used to characterise the fatigue cracking and air voids extension at different vertical deformations. By analysing air void content and surface area before and after loading, it is possible to investigate damage evolution in different directions at different vertical deformations. The X-ray CT images of samples, where the maximum change of air voids content occurs were used to investigate the effect of aggregate properties

on fatigue damage.

The final part of the research is the combination of numerical analysis methods based on X-ray CT with laboratory tests (ITFTs) to establish a numerical model that can simulate crack initiation and propagation of asphalt concrete under different test conditions. The clearly visible CT images were reconstructed with realistic aggregate morphology. The model embedded zero-thickness cohesive elements (CEs) both within asphalt mastic and at interfaces between mastic and aggregates. Viscoelastic input properties were measured by conducting a frequency sweep at multiple temperatures using the Dynamic Shear Rheometer (DSR); and the results were fitted by a Prony series. CEs input properties were determined by a bespoke tensile strength test mounted on a universal testing machine (UTM) at 5 ℃ and 25 ℃. Fractures in asphalt mixture samples at different deformation levels were compared to the fractures in the numerical simulations. The established model was applied to predict crack propagation until failure, as well as crack initiation and propagation at 25 ℃.

1.5 Scope of Research

The scope of the thesis consists of the literature review, the test methods applied in the project, followed by three main chapters that focus on the three objectives of the thesis, and the final chapter presenting conclusions and recommendations.

The literature review presents approaches to study fatigue behaviour in asphalt concrete, characterisation of fatigue behaviour in different designs and an introduction to the Logistic model and its application, which are useful for the achievement of the first objective. The literature review summarises the X-ray CT test methods and Digital Image Processing (DIP) methods which were applied in Chapter 5 to gain the second

objective. The literature review also describes the approaches to reconstruct the numerical simulation and theories of fracture processing zone and the Cohesive Zone Model (CZM), which are the basis of Chapter 6 to achieve the third objective. The materials and experimental programme chapter shows details of material applied and tests conducted in this project. The three main chapters are Chapters 4 – 6, which address topics of modelling the stiffness development in asphalt concrete to obtain fatigue failure criteria, characterisation of fatigue damage in asphalt concrete using X-ray CT and numerical modelling of fatigue cracking in asphalt concrete using cohesive elements. The results in this thesis aim to reveal the micro mechanism of fatigue cracking in asphalt concrete. In addition, the method established will be useful to predict the remaining fatigue life of asphalt pavement, and the numerical model developed can be applied to predict initiation and propagation of fatigue cracks under different conditions in future work.

2 Literature Review

This chapter investigates different approaches to study fatigue behaviour of asphalt concrete, including the phenomenological approach, fracture mechanics, dissipated energy approach and microstructural approaches. Different characterisations of fatigue behaviour in different designs were also compared with the influence of various factors on fatigue life included. In addition, the chapter explains the definition of logistic regression and its application in various fields. Theories and the application of X-ray computed tomography (CT), as well as different digital image processing (DIP) methods are also introduced in the chapter. Approaches to numerical simulation including the computer-generated approach and imaged-based approach are described in this chapter. Theories of fracture process zone and the cohesive zone model (CZM) are discussed, and various cohesive zone traction-separation relations are also listed. Finally, the methods to embed Cohesive Elements and the CZM application in viscoelastic materials are discussed.

2.1 Approaches to Study Fatigue Behaviour in Asphalt Concrete

A reasonable definition of fatigue behaviour is required to develop a fatigue life prediction model. In this section, four approaches mainly used to characterize fatigue behaviour are introduced: phenomenological approaches; fracture mechanics; dissipated energy approaches; and microstructural approaches.

2.1.1 Phenomenological Approach

Fatigue life is defined as the number of cycles that are subjected to repeated stresses (or strains) which lower than the material strength, leading to failure. To obtain fatigue life,

researchers have mainly carried out fatigue tests under two controlled modes: stress-controlled mode and strain-controlled mode. Pell (Eq. 2-1) [13] and Monismith (Eq. 2-2) [14] studied the number of cycles to failure (N_f) by conducting tests under these two modes, respectively. After that, researchers realized that there were other factors affecting the fatigue performance of asphalt mixture. Through numbers of fatigue tests, Monismith established a fatigue equation (Eq. 2-3) including the effect of initial asphalt mixture stiffness (E_0) to evaluate the fatigue performance of asphalt mixture [15].

$$N_f = K_1 \left(\frac{1}{\sigma_t}\right)^a \tag{2-1}$$

$$N_f = K_2 \left(\frac{1}{\varepsilon_t}\right)^b \tag{2-2}$$

$$N_f = K_2 \left(\frac{1}{\varepsilon_t}\right)^b \left(\frac{1}{E_0}\right)^c \tag{2-3}$$

where ε_t and σ_t are the tensile strain and stress; K_1, K_2, a, b and c are the regression constants obtained from laboratory tests.

Another phenomenological fatigue relationship often employed by researchers is Miner's hypothesis of linear damage accumulation [16] as seen in Eq. 2-4. A damage parameter D is defined as an internal state variable. The values of $D = 0$ and $D = 1$ refer to the undamaged and failure state, respectively.

$$D = \sum_i^T \frac{n_i}{N_i} = 1 \tag{2-4}$$

where T is the number of periods; n_i and N_i are the applied number and the allowable number of load applications at condition i, respectively.

The Phenomenological approach is easy to use; however, it has the weakness of relating fatigue behaviours to cracking behaviours, leading to less mechanics theories to support this approach. Therefore, an alternative approach based on fracture mechanics was put forward.

2.1.2 Fracture Mechanics

Inevitably defects or micro-cracks exist in asphalt mixtures. Therefore, some researchers believe that using fracture mechanics to describe the fatigue performance of asphalt mixtures is more in accordance with the actual state of an asphalt pavement. Mechanics was first used by Griffith [17] to study fracture behaviour and this has driven the development of fracture mechanics. After that, many researchers have used the stress intensity factor at the crack tip to explore crack propagation of specimens in fatigue tests and development of various cracks in asphalt pavement [18] [19] [20].

Fracture mechanics analysis assumes that the development process of cracks includes three stages: first, generation of initial cracks; second, stable propagation of cracks; third, unstable development of cracks. Fracture mechanics focuses on quantitative analysis of the second stage which is the main part of fatigue life (as shown in Figure 2.1). Paris law (Eq. 2-5) [21] is usually applied to analyse the relationship between crack growth rate ($da/\,dN$) and the range of stress intensity factor (ΔK) in fracture mechanics analysis.

$$\frac{da}{dN} = A\Delta K^n \tag{2-5}$$

where a is the crack length; N is the number of cycles of loading; A and n are material constants.

The Paris equation only considers the effect of ΔK on crack growth rate. To better reflect the influence of various factors on crack growth, researchers have improved the Paris equation by considering physical meaning. The effect of the maximum stress-intensity parameter (K_{max}) on crack growth rate was considered [22]. Walker's law is given in Eq.6. Donahue et al. [23] tried to add the threshold stress intensity factor (K_{th}) into the Paris equation (Eq. 2-7). Dowling and Begley [24] believed that the stress intensity factor was no longer effective under the condition of large deformation. Therefore, they used the dynamic J-integral to describe the fatigue crack growth rate (Eq. 2-8).

$$\frac{da}{dN} = AK_{max}^{m}\Delta K^{n} \tag{2-6}$$

$$\frac{da}{dN} = A(\Delta K - K_{th})^{n} \tag{2-7}$$

$$\frac{da}{dN} = A\Delta J^{n} \tag{2-8}$$

The fatigue life (N) can be calculated by Eq. 2-9 if all parameters in the Paris equation, the initial crack length (a_i) and the critical crack length (a_c) are known.

$$N = \int_{a_i}^{a_c} \frac{1}{A\Delta K^{n}}\, da \tag{2-9}$$

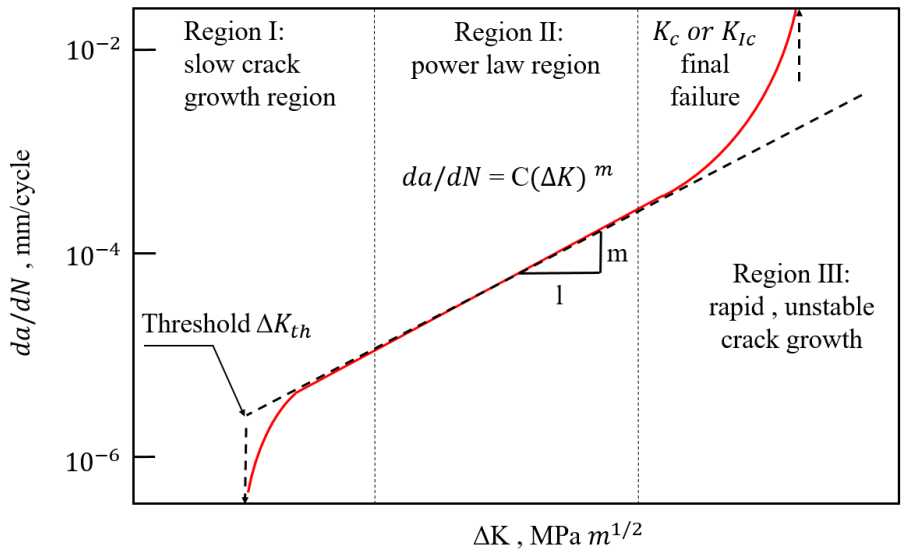


Figure 2.1: Three development stages of cracks and the da/dN versus ΔK curve.

The disadvantage of the fracture mechanics analysis method is that a large number of experimental data are needed to conclude the relationship between the extension length of cracks and stress intensity factors. The stress intensity factors are not constant with the increase of temperature. Fracture mechanics is suitable for brittle materials using in the stable propagation stage [25] [26].

2.1.3 Dissipated Energy Approach

An asphalt mixture is a kind of viscoelastic material, therefore, the stress-strain curve of which under repeated loading is not linear, leading to loading and unloading paths do not overlap, but a cycle, which is called a hysteresis loop (as shown in Figure 2.2). The hysteresis loop with different loading and unloading paths shows a certain difference between input and release energy, and area of the hysteresis loop is defined as dissipated energy.

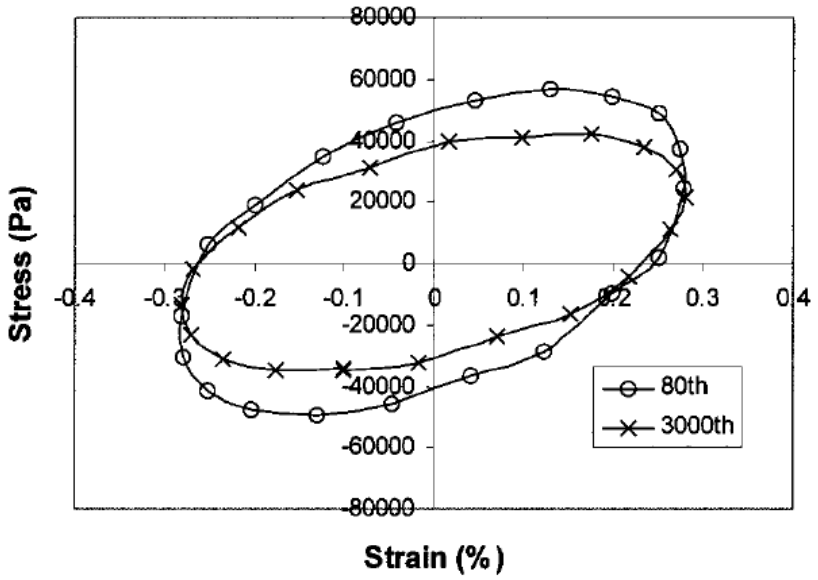


Figure 2.2: Hysteresis loop of asphalt concrete [27].

Except for heat energy generation and mechanical work, dissipated energy is mainly caused by damage in the interior of materials. Therefore, dissipated energy can be used to analyse the damage condition inside materials and can also be used to study the fatigue behaviour of asphalt mixture [28]. Dissipated energy per loading cycle per unit volume (W) is shown in Eq. 2-10 [29].

$$W = \pi\sigma\varepsilon \sin\varphi \tag{2-10}$$

where σ is stress level in cycle; ε is strain level in a cycle and φ is phase angle difference.

A range of energy-based approaches have subsequently been proposed as improved methods to characterise fatigue damage. Van Dijk put forward the concept of dissipated energy, and studied energy loss properties of asphalt mixture using fatigue tests [30]. He pointed out that the energy loss has nothing to do with the test method or test

condition, but there is a certain relationship between the cumulative dissipated energy (W_T) and the total number of load cycles (N_f), as shown in Eq. 2-11.

Then, the energy ratio (Ψ) was introduced as shown in Eq. 2-12. The initial dissipated energy (W_0) can be calculated from the initial stress (σ_0), the initial strain (ε_0) and the initial phase angle (φ_0), as shown in Eq. 2-13. Ψ is mainly related to the type of test and the stiffness of asphalt mixture. The value of Ψ is under 1 if the test is controlled by stress, while it is more than 1 if the test is controlled by strain.

An equation for predicting fatigue life (Eq. 2-14) was proposed by Van Dijk according to the relationship between N_f and W_T, and the relationship between Ψ and initial stiffness ($S = \sigma_0/\varepsilon_0$) [31].

$$W_T = A{N_f}^z \tag{2-11}$$

$$\Psi = \frac{N_f \times W_0}{W_T} \tag{2-12}$$

$$W_0 = \pi\sigma_0\varepsilon_0 \sin\varphi_0 \tag{2-13}$$

$$N_f = \left[\frac{\pi S \sin\varphi_0}{A\Psi}\right]^{\frac{1}{Z-1}} {\varepsilon_0}^{\frac{2}{Z-1}} \tag{2-14}$$

where A and z are material parameters determined by experiment.

However, only a proportion of the energy dissipation happening in asphalt materials during the loading-unloading process is due to fatigue damage. Further methodologies to isolate the energy dissipation due to damage and viscoelasticity. Ghuzlan and Carpenter used the Ratio of Dissipated Energy Change (RDEC) approach to define the fatigue failure (N_{fm}) in asphalt materials (Eq. 2-15), and this approach was later refined by Shen and Carpenter [32]. Ghuzlan and Carpenter described the link between RDEC and the number of load cycles in three regions. The plateau value (PV) of RDEC during

the steady state fatigue crack propagation zone (Region II) be utilised as a failure criterion.

$$\mathrm{RDEC} = \frac{W_{n+1} - W_n}{W_n} \tag{2-15}$$

Where W_n and W_{n+1} are dissipated energy produced in load cycle n and n+1, respectively.

Kim et al. and Daniel and Kim employed pseudo-strain instead of actual strain to model the evolution of damage in asphalt mixtures. Kim et al. then employed the concept of dissipated pseudo-strain energy (DPSE) to evaluate the fatigue cracking life of sand-asphalt mixtures [33] [34] [35] . The area of stress pseudo-strain hysteresis, which corresponds to the energy dissipated only as a result of damage, is computed as Eq. 2-16. The equivalent of Eq. 2-16 for a controlled-stress case is showed in Eq. 2-17 [36].

$$DPSE_N = \pi G_N^* \gamma_0^2 \sin(\theta_N - \varphi) \tag{2-16}$$

$$DPSE_N = \pi \frac{\tau_0^2}{G_N^*} \sin(\theta_N - \varphi) \tag{2-17}$$

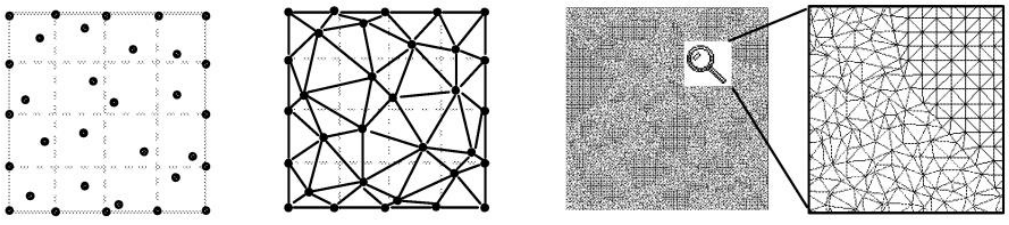
where $DPSE_N$, G_N^* and θ_N dissipated pseudo-strain energy, apparent dynamic shear modulus, and apparent phase angle, respectively, measured at cycle N, and γ_0, τ_0 and φ are strain and stress amplitudes, and viscoelastic phase angle, respectively.

Although these energy-based approaches greatly improve the ability to determine the appropriate failure criteria by relating criteria to crack initiation and propagation, they have a limitation in that the defined failure criteria cannot be directly connected to the stiffness development.

2.1.4 Microstructural Approach

Researchers have realized the importance of analysing the properties of asphalt mixture from the microstructural perspective since the 1990s [37]. Aims of studying the microstructure of asphalt mixtures are to explore the influence of microstructure on fatigue performance of asphalt mixtures, explain the mechanism of fatigue cracking from the microscopic point of view, and predict the service life of asphalt pavements more accurately. Research has been carried out using digital image processing (DIP) methods and nanoscale characterization methods for the characterisation of fatigue behaviours, as well as combined these two methods with virtual test methods for the further analysis of fatigue behaviours.

Virtual test methods like the finite element method (FEM) and discrete element method (DEM) have shown their value when applied to analyse asphalt microstructure. Feng proposed a lattice model for fatigue cracking of asphalt mixture [38]. The lattice model begins with lattice mesh grid that discretises the continuum microstructure into a network of truss elements (as shown in Figure 2.3). Dai et al. developed an extended finite element model (XFEM) to investigate micro morphology and micro crack properties of asphalt concrete [39]. Stolarska et al. used XFEM in the level set method (LSM) to trace micro cracks growth [40].



(a) (b) (c)

Figure 2.3: Lattice model: (a) random nodes inside base mesh; (b) lattice network formed by delaunay triangulation; and (c) lattice mesh [39].

FEM has drawbacks in characterising the inconsistency of the micro-properties, the complexity of internal contacts between materials and discontinuities in the internal stress field of materials. DEM appears to be an alternative method for micromechanical analysis. A bilinear cohesive zone model (Eq. 2-16; Figure 2.4) has been applied in DEM to simulate crack initiation and propagation in asphalt materials [41] [42].

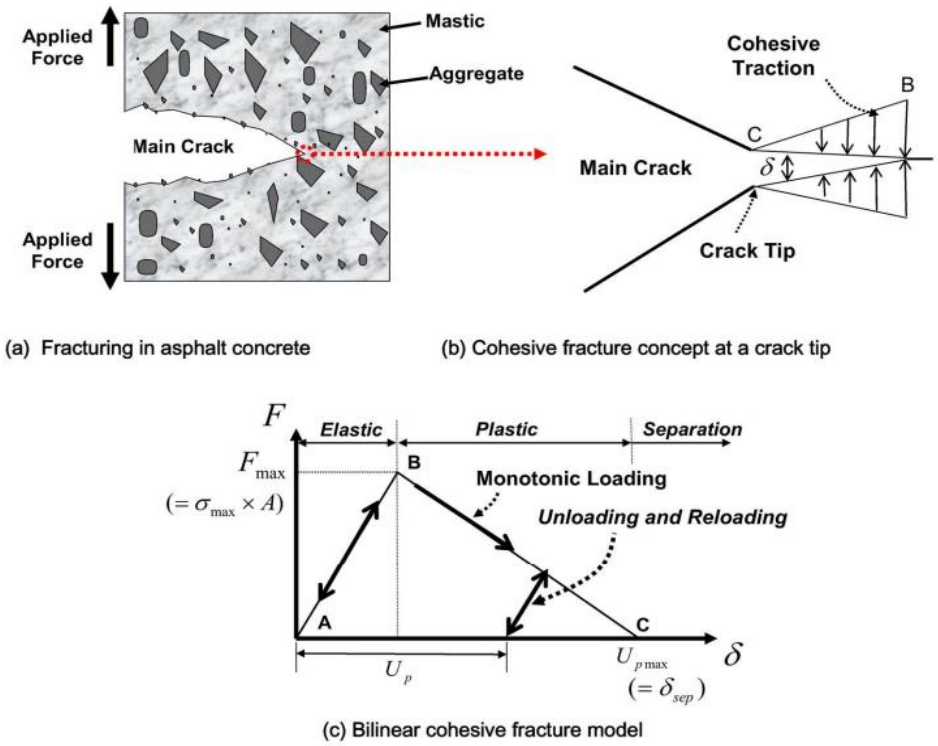


Figure 2.4: Bilinear cohesive zone fracture model [41] [42].

$$\sigma = \begin{cases} \delta & 0 \le \delta < 1 \\ 2 - \delta & 1 \le \delta \le 2 \\ 0 & \delta > 2 \end{cases} \qquad (2\text{-}16)$$

where σ is the cohesive strength, δ is the separation displacement, and the value of the cohesive energy (Φ) is 1.

DIP has been applied to study the properties of asphalt materials since it can accurately as well as non-destructively determine their microstructure. The morphology change of internal structure has been detected to investigate the fatigue damage of asphalt mixture using X-ray Computed Tomography (XCT) (as shown in Figure 2.5). It has been found that fatigue damage presents a linear relation with the complexity of air voids (Eq.14) (as shown in Figure 2.6). Geometric information of images obtained from DIP can be imported into virtual test tools to reconstruct a numerical model.

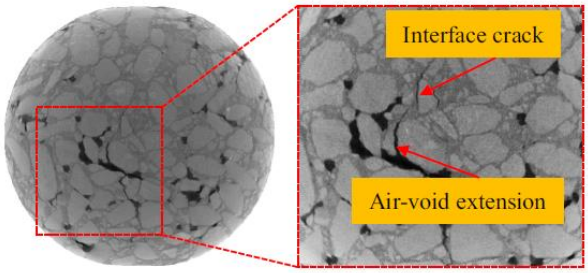


Figure 2.5: Damage state of asphalt mixture [43].

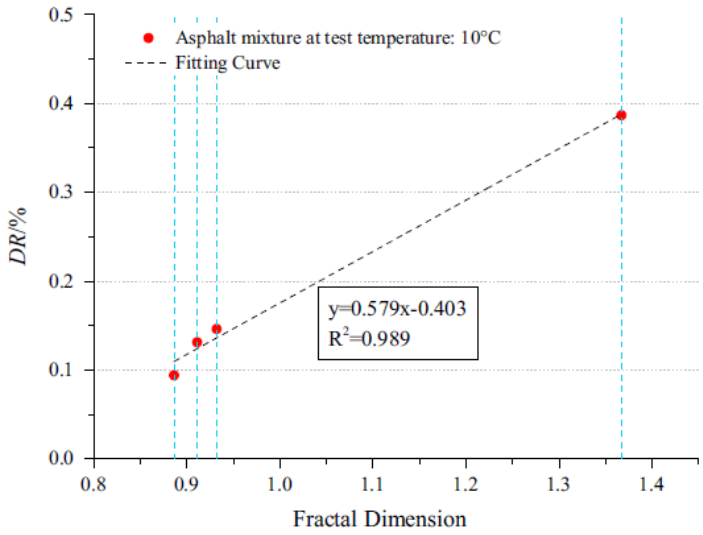


Figure 2.6: Damage ratio (DR) versus fractal dimension [43].

Nanoscale characterization methods open up a new prospect in the study of the microstructure of asphalt mixtures. Field emission scanning electron microscopy (FESEM) micrographs of cement kiln dust (CKD) and coal waste ash (CWA) mixtures compared to a non-additive (NA) mixture are shown in Figure 2.7 and Figure 2.8 [44]. The results show that specimens containing CKD and CWA have a rougher texture and a more pockmarked surface than the NA specimen. The crystalline network of CKD and CWA mixtures may have had a significant effect on mixture stiffness.

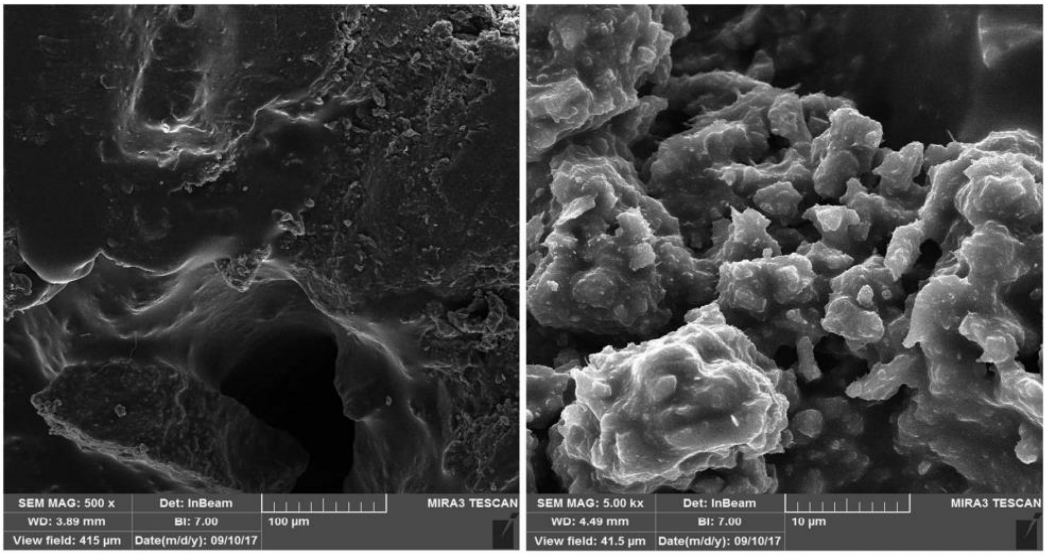


Figure 2.7: FESEM micrographs of NA at magnification of (a) 500× and (b) 5,000× [44].

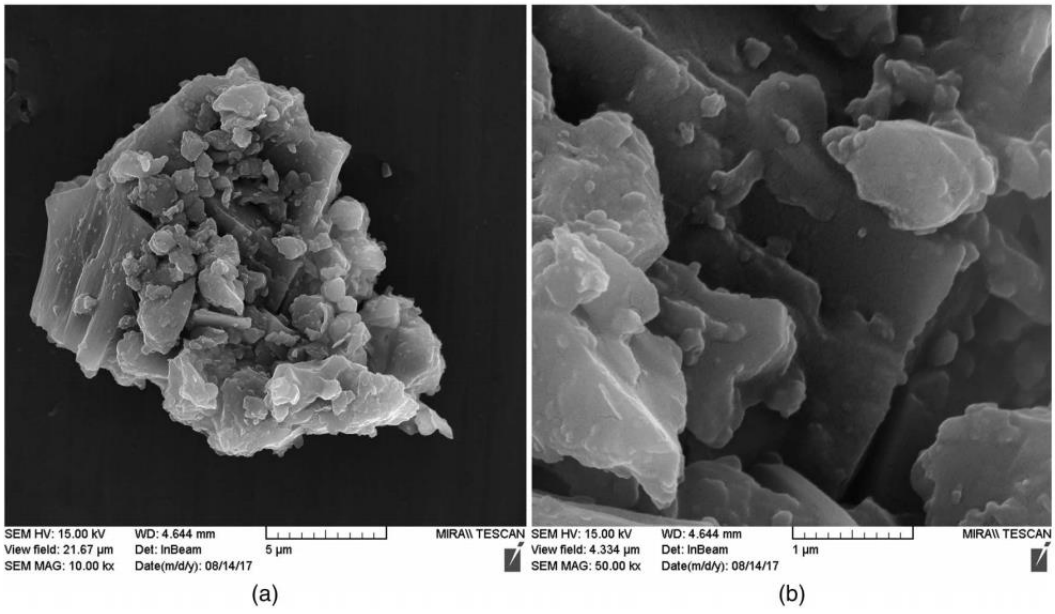


Figure 2.8: FESEM micrographs of CKD3%+CWA3% at magnification of (a) 10,000× and (b) 50,000× [44].

The microrheology and geometry obtained by atomic force microscopy (AFM) show the microstructural features of asphalt binders, and the information of phase images were combined with FEM to study the effect of asphalt binder microstructure on internal stress distribution (as shown in Figure 2.9 and Figure 2.10) [45].

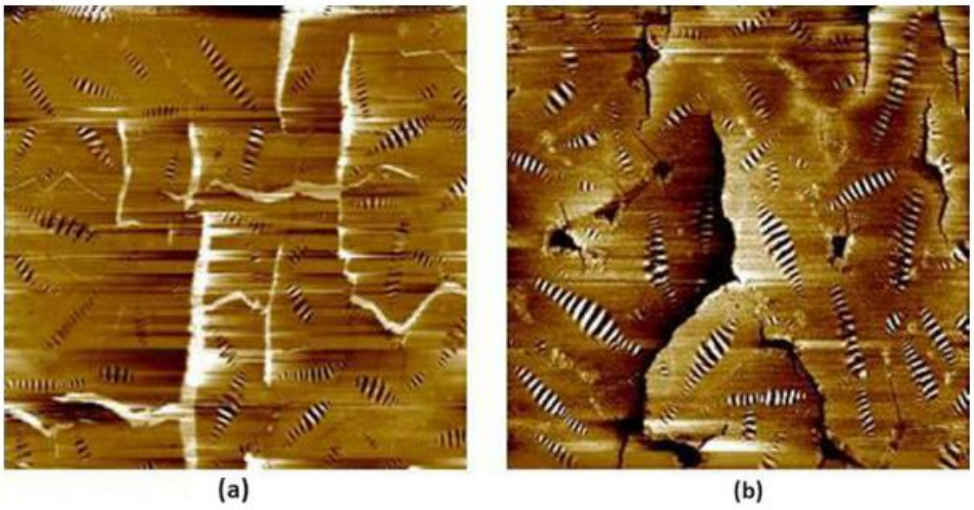


Figure 2.9: AFM phase images (a) asphalt binder A and (b) asphalt binder B (50 × 50 μm^2) after 5% strain.

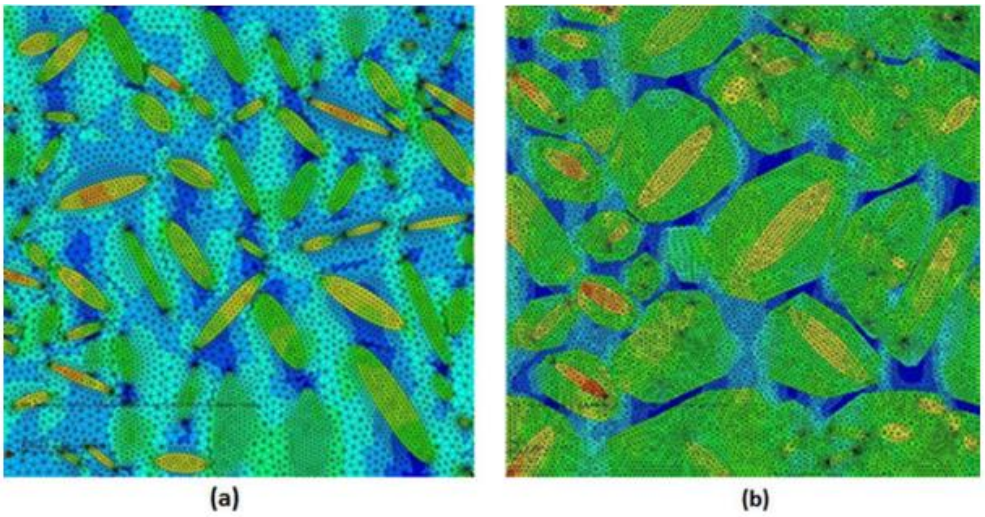


Figure 2.10: Tensile strain contours for FE simulations (a) asphalt binder A and (b) asphalt binder B (50 × 50 μm^2).

Molecular dynamics (MD) simulation is an effective approach to analyse the inter-structure of asphalt materials at nano-scale. Caro et al. [46] used the MD simulation to find the influence of moisture on adhesion between aggregate and asphalt binder, and

the moisture damage mechanisms is shown in Figure 2.11, where the blue area represent water vapour. Lu and Wang have used the MD simulation to model the tension process, and the results show that nano-voids keep growing rapidly during loading and shear localization was observed due to a weakened layer near the interface (as shown in Figure 2.12) [47] [48].

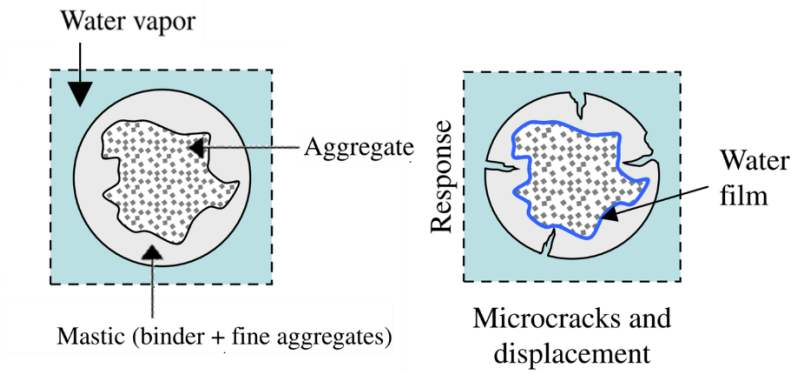


Figure 2.11: Water replacement at asphalt binder/aggregate interface [46].

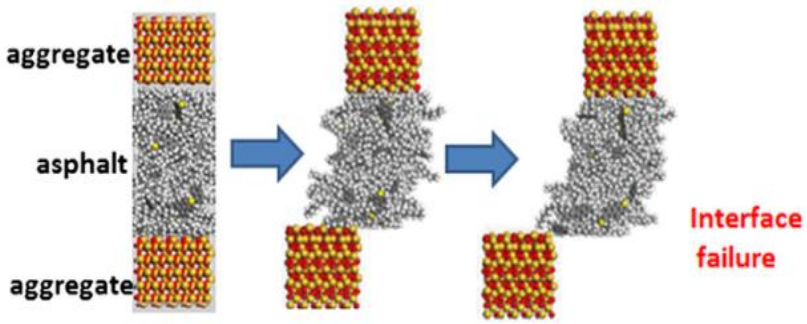


Figure 2.12: Tension loading process [47].

2.2 Characterisation of Fatigue Behaviour in Different Designs

In the past half century, researchers have made a lot of studies on fatigue properties of

asphalt pavement. Based on fatigue tests, the factors affecting fatigue properties of asphalt mixtures have been analysed, including asphalt binder type and content, aggregate type and gradation, air voids content, test temperature, loading frequency and rest periods, etc Many fatigue performance models of asphalt concrete have been established considering the above factors, some of which are adopted and applied in asphalt pavement structural design by various countries and institutions.

2.2.1 Transport and Road Research Laboratory (TRRL, U.K.) Fatigue Model

The TRRL fatigue model was based on field tests on flexible asphalt pavements [49], and the model calculated the dynamic strain on the basis of multi-layer elastic theory. According to 34 test roads with well-compacted base and 29 rolled asphalt pavements, laboratory fatigue tests were carried out under different temperatures and dynamic strains to obtain fatigue design curves. The fatigue life obtained from the laboratory was much lower than that in the field. Therefore, the model considered the traffic load characteristics (volume, rest periods etc.), temperature etc Accumulative fatigue damage was calculated using Miner's hypothesis, based on which the relationship between the results of indoor fatigue tests and fatigue life in the field was established by laboratory fatigue tests considering various mixtures. The fatigue life in standard axles (N_f) prediction of dense bitumen macadam (DBM) and hot rolled asphalt (HRA), with a reliability of 85% at a temperature of 20 ℃ was obtained, as shown in Eq. 2-17 and Eq. 2-18.

DBM (Pen 100):

$$N_f = (4.169 \times 10^{-10}) \left(\frac{1}{\varepsilon_r}\right)^{4.16} \quad (2\text{-}17)$$

HRA (Pen 50):

$$N_f = (1.660 \times 10^{-10}) \left(\frac{1}{\varepsilon_r}\right)^{4.32} \quad (2\text{-}18)$$

where ε_r is the horizontal tensile strain at the bottom of the bound layer.

2.2.2 The University of Nottingham (UoN, U.K.) Model

UoN developed a fatigue life prediction model using the log of tensile stain at the bottom of the asphalt layer (ε_t) against the log of traffic in millions in standard axles (N). Influences of the volume (V_b) and the initial softening point (SP_i) of asphalt binder are included, and the temperature considered in this equation is less than 30 $°C$. A shift factor is applied to account for difference in conditions between laboratory and field, which chooses 440 and 77 for failure and critical condition, respectively (see Brunton et al. [50]).

$$lg\varepsilon_t = \frac{14.39lgV_b + 24.2lgSP_i - k - lgN}{5.31lgV_b + 8.63lgSP_i - 15.8} \quad (2\text{-}19)$$

where k chooses 46.06 and 46.82 for life to failure and critical condition, respectively.

2.2.3 Superior Performing Asphalt Pavements (SUPERPAVE, U.S.) Fatigue Model

Strategic Highway Research Program (SHRP A-003A) predicted fatigue life (N_f) of a given pavement section under a given traffic load, as shown in Eq. 2-20 [51]. The equation considered effects of the voids filled with asphalt (VFA)， the tensile strain at the bottom of the asphalt layer (ε_t) and initial stiffness (S_0), which is measured from

the frequency sweep at constant height (FSCH) test at 10 Hz and 20 ℃.

$$N_f = 2.738 \times 10^5 e^{0.077VFA} {\varepsilon_t}^{-3.624} (S_0)^{-2.270} \quad (2\text{-}20)$$

SHRP A-404 developed an accelerated laboratory performance test to predict the fatigue life of asphalt mixtures, which is applied in pavement design. The influence considered in the equation includes the percentage of voids filled with asphalt binder (VFB), initial strain (ε_0) and initial stiffness (S_0), as shown in Eq. 2-21 and Eq. 2-22 [52]. The frequency of 10 Hz and the temperature of 20 ℃ are chosen for fatigue tests under strain-controlled mode with the applied strain between 200 and 1200 με.

$$N_f = 466.4 e^{0.052VFB} {\varepsilon_0}^{-3.948} (S_0)^{-2.270} \quad (2\text{-}21)$$

or

$$N_f = 6.72 e^{0.046VFB} (W_0)^{-2.047} \quad (2\text{-}22)$$

where W_0 is initial dissipated energy per cycle.

2.2.4 Asphalt Institute (AI, U.S.) Fatigue Model

The fatigue life prediction model of the AI is shown in Eq. 2-23 to Eq. 2-25 of the tensile strain at the bottom of the asphalt layer (ε_t), the dynamic modulus of mixtures (E_*), the air void (VV) and volume of asphalt binder in mixture (V_b), which are reflected by a correction coefficient (M). The Eq. 2-25 shows that the fatigue life decreases with the increase of air voids and volume of asphalt binder.

$$N_f = 18.4 \times 0.00432\mathrm{C}\varepsilon_t^{-3.291}|E_*|^{-0.854} \quad (2\text{-}23)$$

$$C = 10^M \quad (2\text{-}24)$$

$$M = 4.84 \times \left(\frac{V_b}{VV + V_b} - 0.6875\right) \quad (2\text{-}25)$$

where C is a function of air voids and volume of asphalt binder.

2.2.5 SHELL Pavement Design Model

The fatigue prediction model of asphalt mixtures used in SHELL pavement design is shown in Eq. 2-26 [53]. The model was obtained from wheel tracking tests (WTT); it contains factors such as the volume of asphalt binder in mixture (V_b), the maximum tensile strain (ε) and the dynamic modulus of mixtures (S_{mix}).

$$N_f = 4.91 \times 10^{-13}(0.86V_b + 1.08)\varepsilon^{-5}{S_{mix}}^{-1.8} \quad (2\text{-}26)$$

2.2.6 WesTrack (U.S.) Fatigue Model

WesTrack is a project which consists of a specially built track in the state of Nevada; based on its data, fatigue models of three aggregate gradation levels: fine, fine-plus, and coarse have been developed. The relationship between fatigue life under vehicle wheel tracks and tensile strain (stn), temperature (T), the air void (VV) and volume of asphalt binder in mixture (V_b) has been explored. The established fatigue models are shown in Eq. 2-27, Eq. 2-28 and Eq. 2-29 [54].

Fine:

$$\ln N_f = -27.0265 - 0.1439VV + 0.4148V_b + 4.6894 \ln stn \quad (2\text{-}27)$$

Fine-plus:

$$\ln N_f = -27.3409 - 0.143VV + 0.4219V_b + 0.0127T + 4.6918 \ln stn \quad (2\text{-}28)$$

Coarse:

$$\ln N_f = -27.6723 - 0.094VV + 0.6540V_b + 0.0331T - 4.5402 \ln stn \quad (2\text{-}29)$$

2.2.7 Specifications for Design of Highway Asphalt Pavement (CHN.) Model

The fatigue life (N_{f1}) prediction of asphalt mixtures in the Specifications for Design of Highway Asphalt Pavement (JTG D50-2017) [31] [32] is given by Eq. 2-30 [55].

$$N_{f1} = 6.32 \times 10^{15.96-0.29\beta} k_a k_b k_{T1}^{-1} (\frac{1}{\varepsilon_a})^{3.97} (\frac{1}{E_a})^{1.58} (VFA)^{2.72} \quad (2\text{-}30)$$

where β is the reliability index, k_a and k_{T1} are the seasonal frozen soil and the temperature adjustment coefficients, respectively, E_a is the dynamic compression modulus of mixtures at 20 ℃, VFA is the voids filled with asphalt binder in the compacted mixture; k_b is the fatigue loading mode coefficient which is calculated by Eq. 2-31 and ε_a is the tensile strain at asphalt layer bottom which is calculated by Eq. 2-32 and Eq. 2-33.

$$k_b = [\frac{1 + 0.3E_a^{0.43}(VFA)^{-0.85} e^{0.024h_a - 5.41}}{1 + e^{0.024h_a - 5.41}}]^{3.33} \quad (2\text{-}31)$$

where, h_a is the thickness of asphalt mixture layer.

$$\varepsilon_a = p\bar{\varepsilon}_a \tag{2-32}$$

$$\bar{\varepsilon}_a = f(\frac{h_1}{\delta}, \frac{h_2}{\delta}, \dots, \frac{h_{n-1}}{\delta}; \frac{E_2}{E_1}, \frac{E_3}{E_2}, \dots, \frac{E_0}{E_{n-1}}) \tag{2-33}$$

where, $\bar{\varepsilon}_a$ is the theoretical strain coefficient, p is the ground pressure of the tire under a standard axle load, δ is the equivalent circle radius, E_0 is the resilient modulus of subgrade top, $h_1, h_2, \dots, h_{n-1}$ are the thicknesses of each layer and $E_1, E_2, \dots, E_{n-1}$ are the modulus of each layer.

The purpose of establishing a fatigue prediction model is to explore the relationship between the stress or strain in an asphalt layer and the number of repeated loads leading to structural damage. It can be seen from the above fatigue prediction models that stress, strain and modulus are the main factors considered. Some researchers also introduced the volume characteristics of materials such as air voids, voids filled with asphalt binder, asphalt binder content, etc. and energy characteristics such as initial dissipated energy. The fatigue life of an asphalt pavement is not only affected by the asphalt mixture itself, but also by other factors such as environment. Therefore, environmental factors such as temperature and moisture are also considered.

2.3 The Logistic Model and its Application

Logistic regression is a popular machine learning algorithm, which can be used for various classification and for regression problems by means of predicting the categorical dependent variable with the help of independent variables. Unlike the linear regression model, logistic regression does not fit straight lines or hyperplanes, but use logistic equations to compress the output of linear equations between 0 and 1. A logical model describes the probability of an event for a given condition, for example, the probability of the event is 2 (the elasticity or plasticity), a specific equation (a logical

model) is used to explain the probability of a dichotomous variable (such as yes or no). A typical logistic equation is defined as Eq. 2-34; the curve of which is called sigmoid curve (S curve), as shown in Figure 2.13 [56].

$$\text{logistic}(\eta) = \frac{1}{1 + \exp(-\eta)} \tag{2-34}$$

where, η is the independent variable.

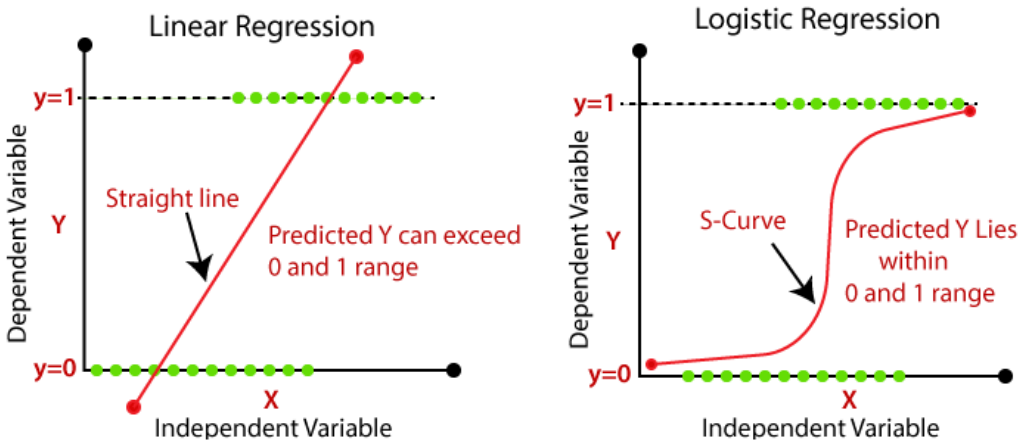


Figure 2.13: Difference between the linear regression and logistic regression [56].

Logistic regression was first established by statistician David Cox [57] in 1958 and is then widely used in various scientific fields [58] [59] [60] [61] [62] [63] [64], it is also applied in studying asphalt pavement performance, especially analysing the data obtained from the field. A logistic model was developed based on the standard maximum likelihood procedure, as a function of the volume and performance parameters of asphalt mixtures, which were collected in the field, as well as prepared in the laboratory. It was found that the logistic model specification is suitable for predicting the mixed probability of road deformation reaching the third stage [65]. Logistic regression has been used to find out the probability of the increase of low-

temperature cracks when high-modulus asphalt concrete is used instead of conventional asphalt concrete in pavements [66]. A logistic model has been developed to predict the probability of alligator cracking severity. Statistical conformance tests and empirical verification of independent data show that the developed model is accurate for generating the probability of road at a certain distress level [67].

2.4 X-ray Computed Tomography (CT) and Digital Image Processing (DIP)

2.4.1 X-ray CT

X-ray CT is an imaging technique that can generate images of the density distribution of an object's cross-section, so as to reveal the internal structure of the object. The X-ray CT scanner consists of an X-ray tube, a rotating table and a detector (Figure 2.14). Short-wavelength electromagnetic radiation (X-ray) penetrates the object on the rotating table, and the detector measures the intensity of the X-ray before and after passing through the object and reveals images. The intensity of the X-ray before and after passing through is different for the reason that part of the radiation is absorbed when initial X-ray radiation (I_0) passes through the object. The absorption is a function of the linear attenuation coefficient and the attenuation (μ), which is related to the density of the object (Figure 2.15) [68]. For example, different parts of the object have different densities, X-ray radiation will be absorbed differently when passing through, and the rest (I) penetrates through and is recorded by the detector array to produce images with different gray values. The greater the density difference between different parts of the object, the better each part of the object can be recognized. In general, the greater the density of an object, the more radiation it absorbs, but it is also affected by the energy and the atomic number of the element emitting the X-ray and the thickness of the object [69]. X-ray CT technology can be used to create three-dimensional (3D)

images of an object by scanning two-dimensional (2D) image slices from different angles [70] for better visualise the internal structure of an object, and was first used in civil engineering in the early 1990s [71-73]. Since significant achievements were made to visualise detailed images of aggregate and asphalt binder interfaces and the air void distribution in asphalt concrete [74-76], X-ray CT technology has been widely used in pavement engineering. Figure 2.16(a) shows a 2D image of an asphalt concrete sample produced in this project. Aggregates have the highest density, therefore is the brightest, while air voids have the lowest density, therefore, is the darkest; mastic (asphalt binder and fine aggregates) is in the middle range. A 3D image of the asphalt concrete sample can be generated from 2D image slices, as shown in Figure 2.16(b).

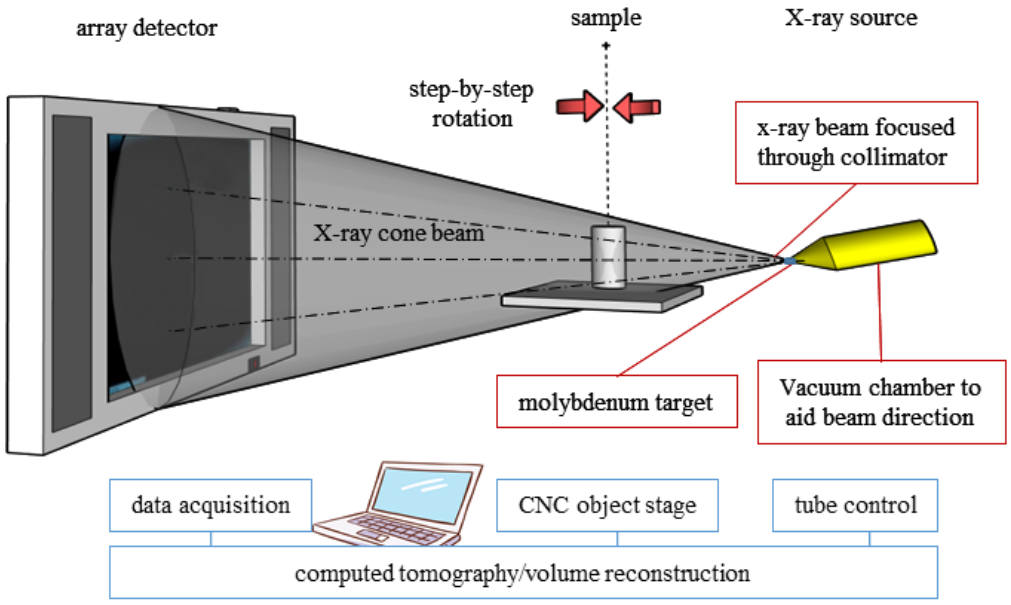


Figure 2.14: Schematic of industrial X-ray CT system.

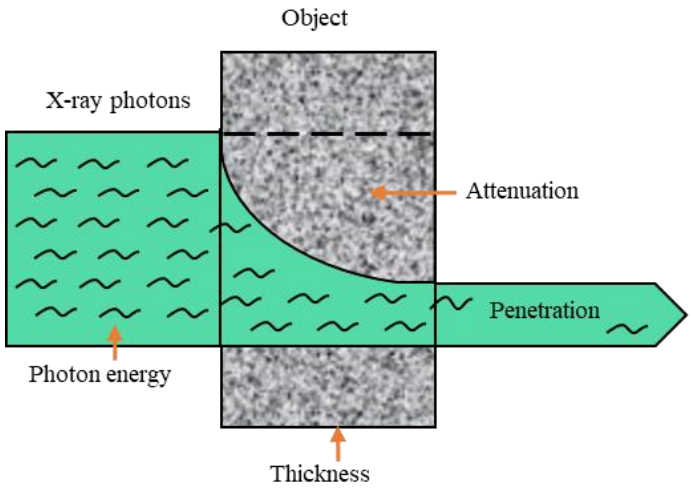


Figure 2.15: Schematic of X-ray radiation absorption.

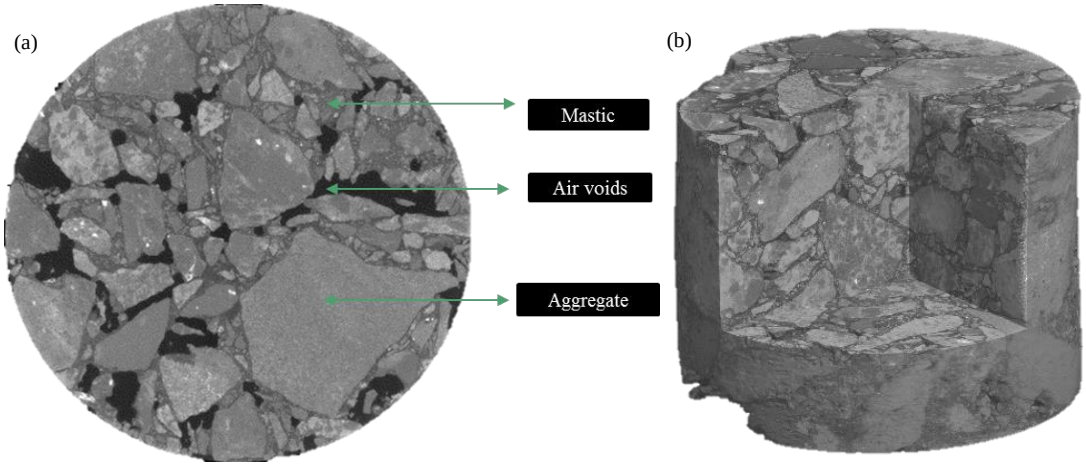


Figure 2.16: (a) X-ray CT 2D image of a mixture sample; (b) Reconstruction of the 3D CT model from 2D image slices.

2.4.2 DIP

DIP is a method to process X-ray CT images to achieve high quality internal images with distinguished area of interest (AOI) for further image analysis; it involves adjustments, such as contrast enhancement and noise reduction, gray intensity

thresholding and image segmentation. DIP is utilised not only for numerical model reconstruction, but also for comprehensive study of phase characteristics, including aggregate angularity and orientation, air void size and distribution, etc. [77, 78].

The Digital Image and Image Brightness Histogram

A digital image is a digital representation of an object, and image processing and analysis is achieved through the numerical computations on discrete elements [79]. Each graphic in a bitmap graphic format is treated as a collection of image elements, called pixels in a 2D image and voxels in a 3D image, and each element is assigned a specific colour. Pixels are little square elements that are stacked in rows and columns to form an image. Voxels, on the other hand, are little box elements created by extending a planar element into a volume element (Figure 2.17). The varied gray scales allocated to each pixel appear when the image is zoomed in on a specific location; the greater the number of pixels, the more information is provided. Bit depth refers to the amount of information that may be stored in a pixel, mainly includes binary (1-bit), multi-level gray (8-bit) and colour (24-bit). A 1-bit image is either black (pixel = 0) or white (pixel = 1) depending on the pixel value. Each pixel in an 8-bit image is given eight integers, with 0 representing black and 255 representing white. A 24-bit image is made up of three 8-bit integer arrays: red, blue, and green [80]. The image brightness histogram shows the quantity or frequency of pixels in an image, which is basic to determine threshold values for image segmentation, as illustrated in Figure 2.18.

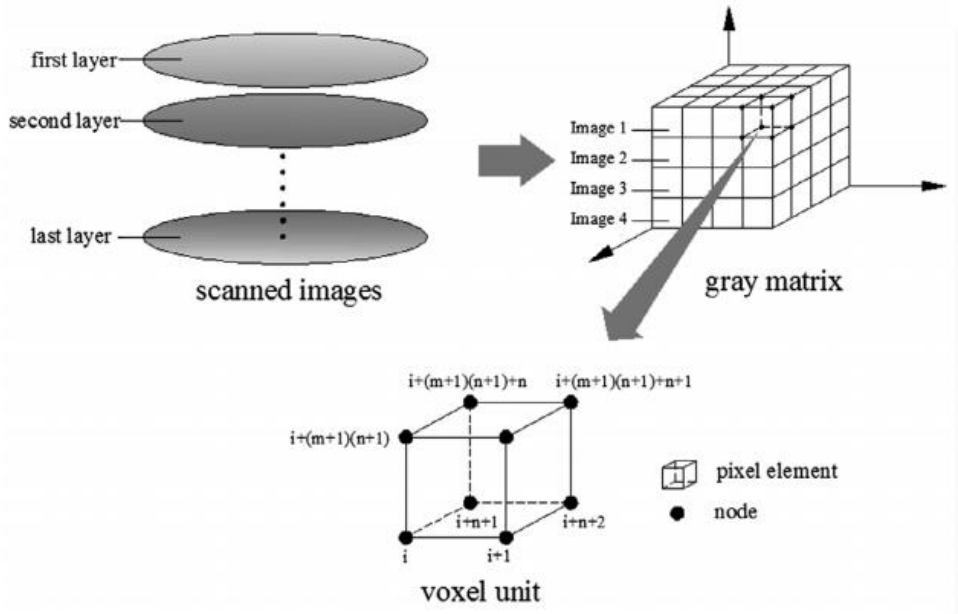


Figure 2.17: Transformation of a scanned digital image into a voxel matrix [79].

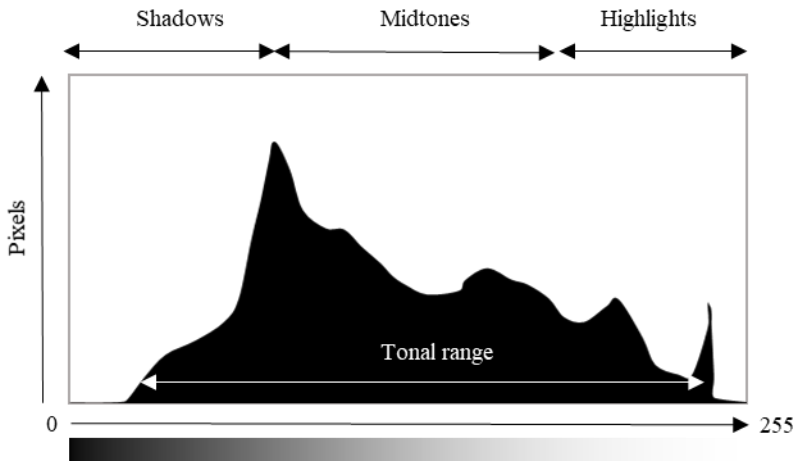


Figure 2.18: Image brightness histogram [81].

Contrast Enhancement and Noise Reduction

Images with good contrast and precise colour representation are essential for

thresholding and image segmentation. Contrast is the difference in image brightness between the average brightness and background brightness of an object. The contrast enhancement is beneficial for better visualise the image when compared to the original, and it has no effect on the sample threshold (Figure 2.19a-b). Normalisation is one form of contrast enhancement, which achieves a consistent brightness and contrast. Another kind is histogram equalisation, which generates images with the maximum possible contrast while preserving nearly all of the original image's features.

Due to inadequate light, digital images are frequently contaminated by noise, which will affect thresholding and image segmentation. Therefore, noise should be eliminated by filtering of an original image, includes smoothing and sharpening. The simplest filtering approach is smoothing, which is accomplished by taking the mean of the pixel values; it works well with images with minimal noise issues. When dealing with images with a lot of noise, a 2D or 3D median filter can get better results; it takes into account the pixel value that is exactly in the middle of the ascending series of pixel values (Figure 2.19c). The sharpening enhances the image's features by responding to sudden variations in pixel intensity, which is particularly beneficial for edge detection.

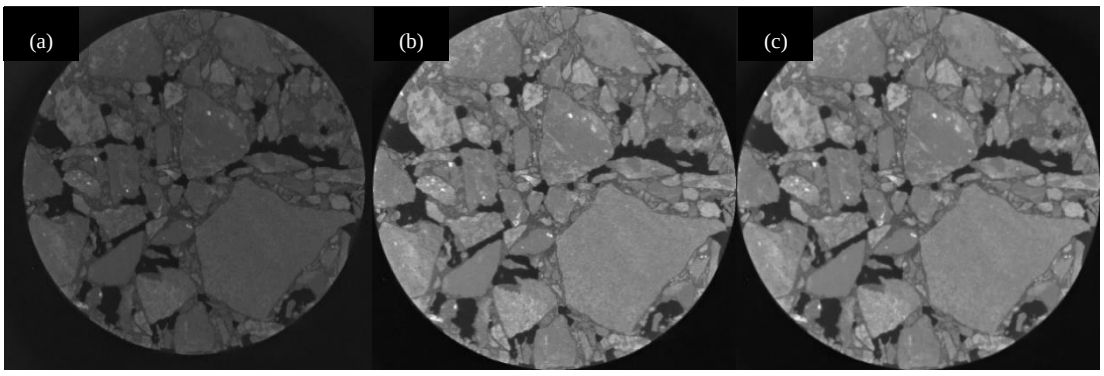


Figure 2.19: (a) Original X-ray CT image; (b) Contrast enhancement image; (c) Median filtered image of a mixture sample.

Gray Intensity Thresholding

To determine the range of potential threshold values in the area of interest (AOI), an image profile is created, by which the pixel intensity of various materials inside an image and possible group of pixels that represent the AOI can be identified, as illustrated in Figure 2.20. It shows that gray values of pixels are coloured individually to group ranges of gray values for the selected components in the mixture. Throughout the AOI, gaps in profiles indicate variations in the gray levels of adjacent pixels. This is a great way to describe the separation of two materials and a smaller gap implies that gray values for given materials are almost identical.

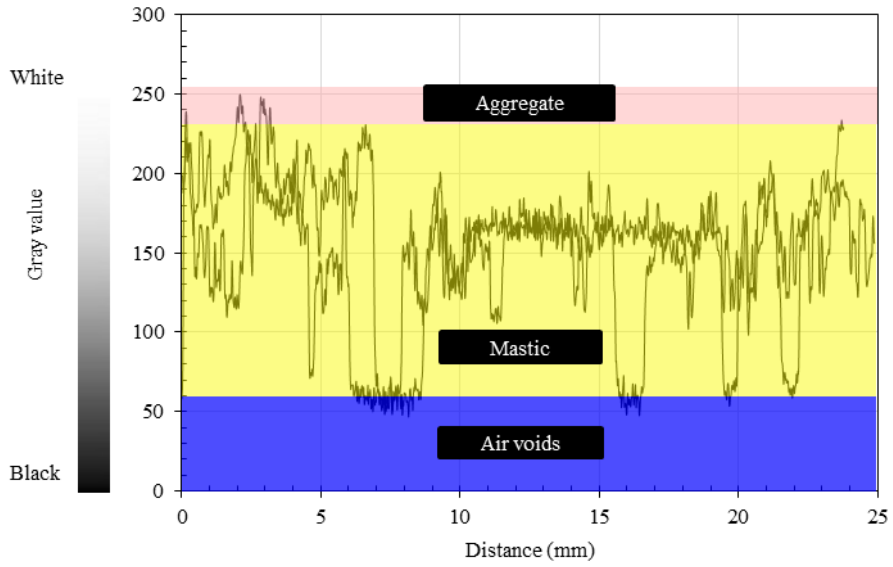


Figure 2.20: Image profile of a mixture sample.

Thresholding is used to separate the AOI from the background of an image based on pixel intensity. When the threshold value is compared to each pixel in an image, pixels with gray levels less than the threshold value are transformed to black, whereas pixels with gray levels more than the threshold value are transformed to white [82]. This study used histogram-based thresholding, which is based on the form of the histogram. The histogram of a mixture sample includes two different peaks (shown in Figure 2.21), and the gray value between the two peaks is used to determine the threshold value. As

illustrated in Figure 2.22, phase isolation (air void, mastic and aggregate,) is achieved by using different threshold values (approximately 60 and 230). CT images of varied slices and mixtures, as well as varied thresholding methods lead to different threshold values. By assigning each phase with a separate colour spectrum, a pseudo colour was given to the original image; it shows in Figure 2.23 that the image is well thresholded.

The picture is well thresholded in the X-ray image following pseudo colour transformation (Figure 2.23).

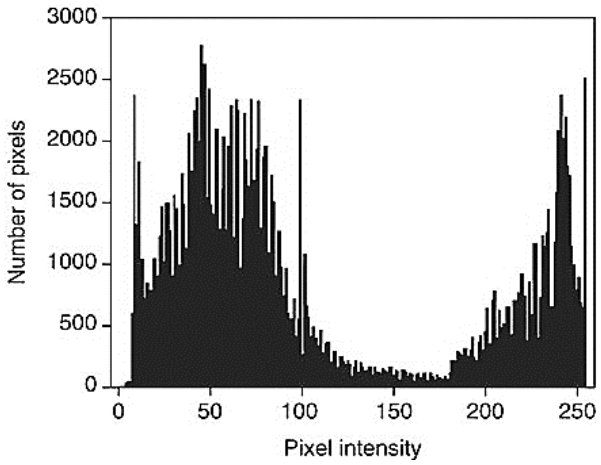


Figure 2.21: Histogram of a mixture sample.

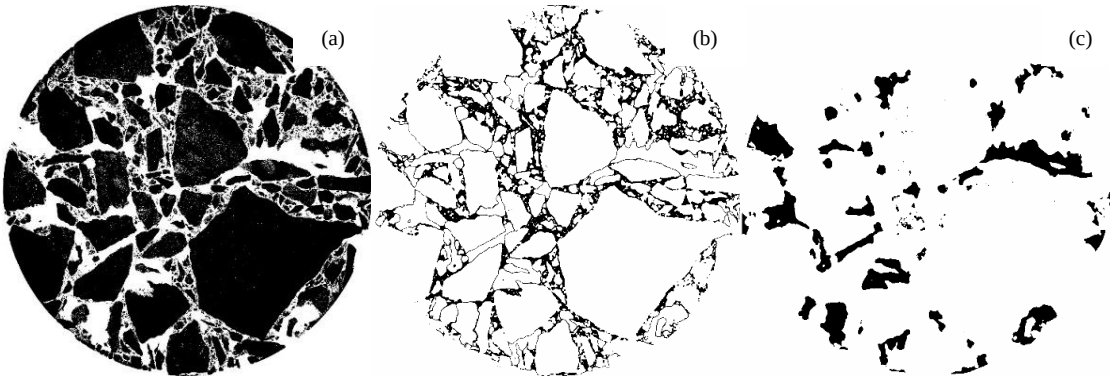


Figure 2.22: A mixture sample adjusting the threshold values (a) Aggregate; (b) Mastic and (c) Air voids.

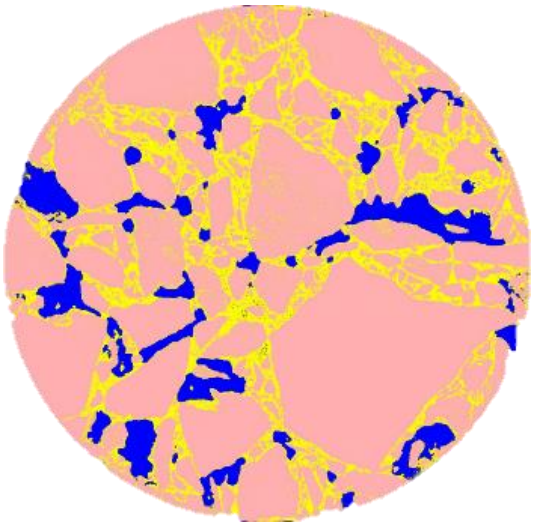


Figure 2.23: Image after pseudo colour transformation of a mixture sample.

Image segmentation with morphological operations

In some cases, AOI might be over or under segmented after thresholding, which is caused from tiny variation in grey levels leading to the border between two particles might be ambiguous. In a binary image, morphological operations, such as filtering,

holes filling, erosion, open, dilation and close combined etc., improve the detection of the exact area and form of a particle, as well as the border between two particles. Filtering is a technique for removing particles with less than a certain number of pixels, and holes filling is a technique for filling missing pixels in particles. Erosion with open operation erodes the aggregate form and separates two connected aggregates, whereas dilatation with close operation extends the aggregate form and connects separated aggregates. Image segmentation is improved by applying different morphological operations. An example of a mixture sample is used to show how different morphological operations work in processing an aggregate binary image (Figure 2.24).

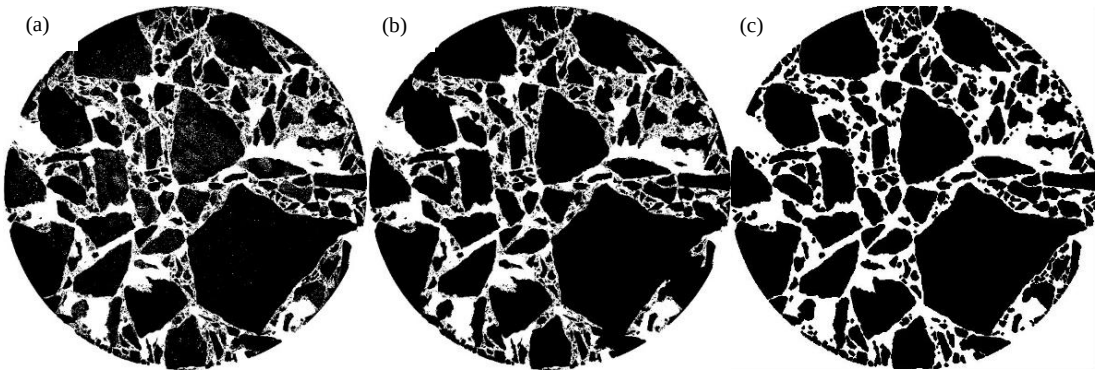


Figure 2.24: (a) Aggregate binary image; (b) After filter and holes filling; (c) After erosion with open and dilation with close.

2.5 Approaches for Reconstruction in Numerical Simulation

2.5.1 The Computer-generated Approach

The user-defined and the realistic aggregate models are two categories of the computer-generated approach. Numerical aggregates are created in the user-defined aggregate model, and the placement of aggregates in the matrix are determined by the user; whereas the placement of aggregates is extremely comparable to reality in the realistic

aggregate model.

User-defined aggregate particles can have an idealised or angular form. Idealised form, such as circle/ellipse or sphere/ellipsoid, are the most basic user-defined aggregate particles. Dai et al. [83] used optical images to build their idealised form of aggregate particles (comparable ellipses) for FEM, as illustrated in Figure 2.25. Idealised form can only be utilised when aggregate form is not an important factor for analysis [84-87].

Angular form of aggregate particles can better represent the shape of real aggregates compared to idealised form. Angular from in 2D was firstly utilised for unbound granular materials [88-91], for example, Liu and You [92] used particles created by truncating circles, to reconstruct 2D DEM for asphalt concrete. Angular from in 3D, such as Cylinder [93] and polyhedron [94, 95] were also created. Caballero et al. [55] used polyhedral from of aggregate particles to create 3D FEM in cement concrete, as illustrated in Figure 2.26. Yang et al. [96] presented an automated sphere growth technique for modelling aggregate morphologies using sphere clumps, as illustrated in Figure 2.27. They [97] then used their method to rebuild 3D DEM in asphalt concrete for fracture behaviour analysis.

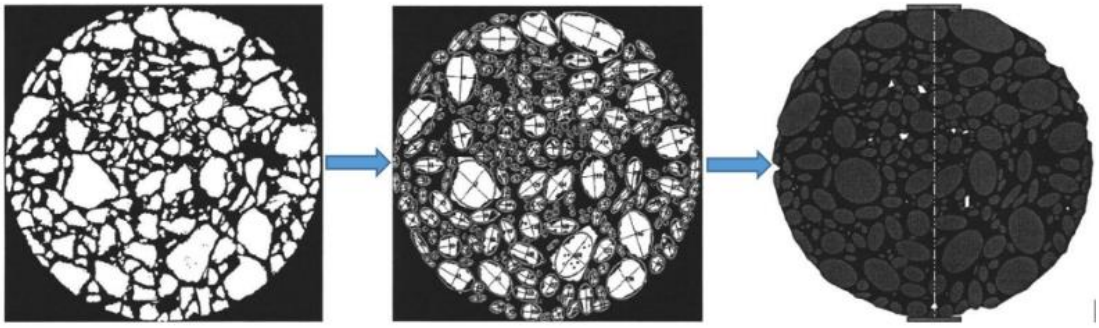


Figure 2.25: Idealised form of user-defined aggregate particles applied in FEM [83].

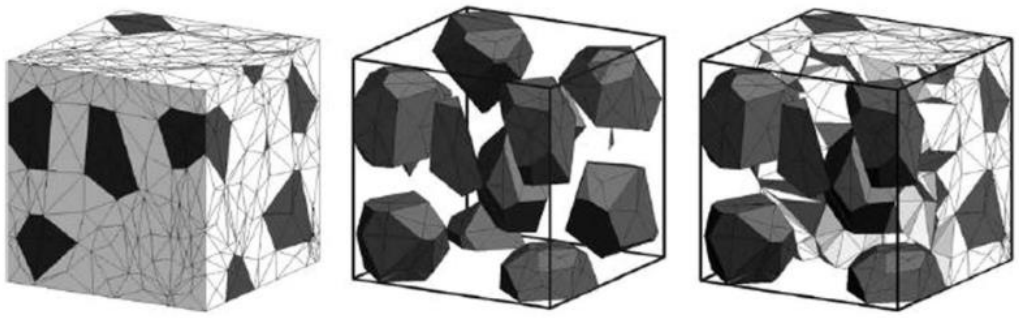


Figure 2.26: Angular form (polyhedral) of aggregate particles applied for 3D FEM in cement concrete [55].

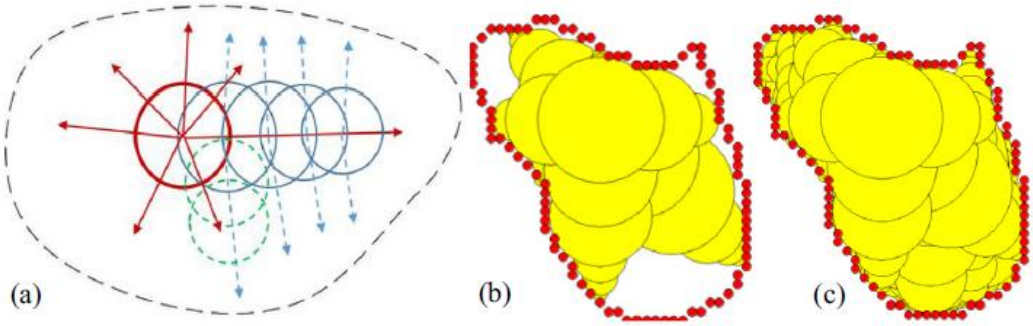


Figure 2.27: (a) Automated sphere growth technique, (b) sphere clump after the first growth, and (c) after the second growth [96].

The majority of studies acquire aggregate information based on digital scanning, and the obtained information are then saved and utilised to reconstruct stone-based composite in numerical modelling. When different mixtures are used for modelling, instead of scanning again, structure can be created by stored information, including aggregate shape and gradation, and binder and air voids content. Garboczi et al. [98, 99] were the first to develop realistic aggregate models based on surface geometry. They extracted individual aggregate particles from a multi-aggregate image, then acquired and stored 3D form and surface geometries by spherical harmonic mathematical

analysis. As show in Figure 2.28, the harmonic method is highly effective in capturing and storing aggregate surface information, and the saved information can be easily used to rebuild numerical models of stone-based composites. Overlapping between two particles has been a noteworthy problem in correct aggregate placement. Qian et al. [100] presented a take-and-place parking technique for aggregate models, which were created by applying spherical harmonic method on aggregate X-ray images. They also presented a contact equation-based technique to avoid the overlap of two particles (in Figure 2.29). The appropriate placement of aggregates into the binder matrix is a crucial problem in the realistic aggregate model, although the problem is constantly improving, it is still very different from the real aggregate placement in binder matrix.

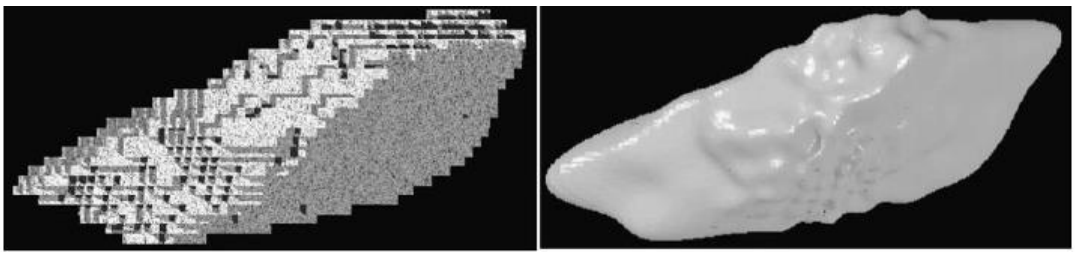


Figure 2.28: 3D model reconstructed from digital scanning (left) and from the spherical harmonic mathematical analysis (right) [98].

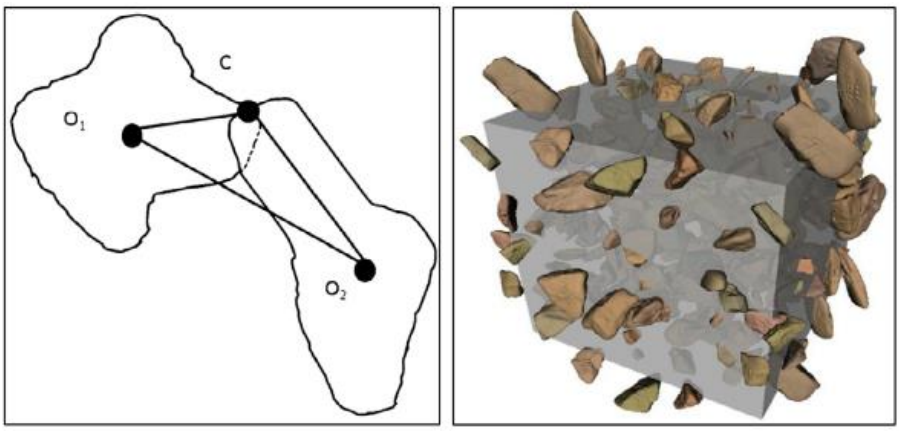


Figure 2.29: The particle overlapping detection method (left) and visualisation (right) [100].

2.5.2 The Image-based Approach

Processing on X-ray and optical images to get distinct phases, and then input geometric information of these phases in numerical simulation are basic methods for the image-based approach. The smallest size of phases achieved is concerned by researchers using the image-based approach. Aggregates as tiny as 0.3 mm were separated through image processing by Romero and Masad [101]. However, the smallest size of phases achieved is influenced by a variety of factors, such as the resolution of images and different image processing technologies. The Image-based approach is widely used to simulate and analyse various characteristics of asphalt concrete both in 2D and 3D simulation. Masad et al. [102] used image-based approach to reconstruct a 2D FEM of asphalt materials for the analysis of strain distribution, and Papagiannakis et al. [103] used the same approach to study the viscoelastic characteristics of asphalt concrete. Dai [104] simulated the dynamic modulus test in asphalt concrete by reconstructing 2D FEM from X-ray images. Three phases (aggregate, asphalt mastic and air voids) were identified, and the aggregate outlines were identified for further triangular meshing, as illustrated in Figure 2.30. Buttlar et al. [105-107] used 2D DEM rebuilt from optical images to replicate the complicated modulus test, hollow cylinder modulus test, and uniaxial

compression test. Image-based approach has been used to reconstruct 3D numerical models in order to capture more realistic numerical models. Wang [108] investigated the stress concentration factor and stress distributions by reconstructing a 3D FEM of asphalt concrete from the stacked slices of 2D numerical models. Zhang et al. [109] used X-ray CT imaging to reconstruct 3D FEM for the numerical simulation of the indirect tensile test. You et al. [110] [111, 112]built the 3D DEM to conduct virtual dynamic modulus testing in both 2D and 3D. Figure 2.31 and Figure 2.32 explain the processes for reconstructing 2D and 3D models, respectively. The image segmentation has a significant improvement when You et al. [113] used Avizo [114], an image processing programme, to recreate 3D FEM of asphalt concrete.

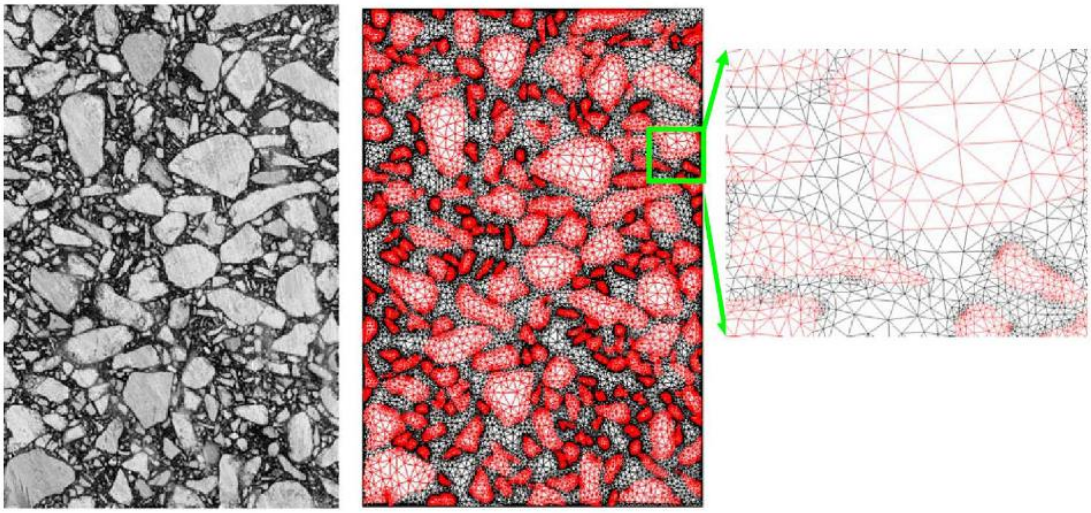


Figure 2.30: Image processing to identify three phases in 2D FEM [104].

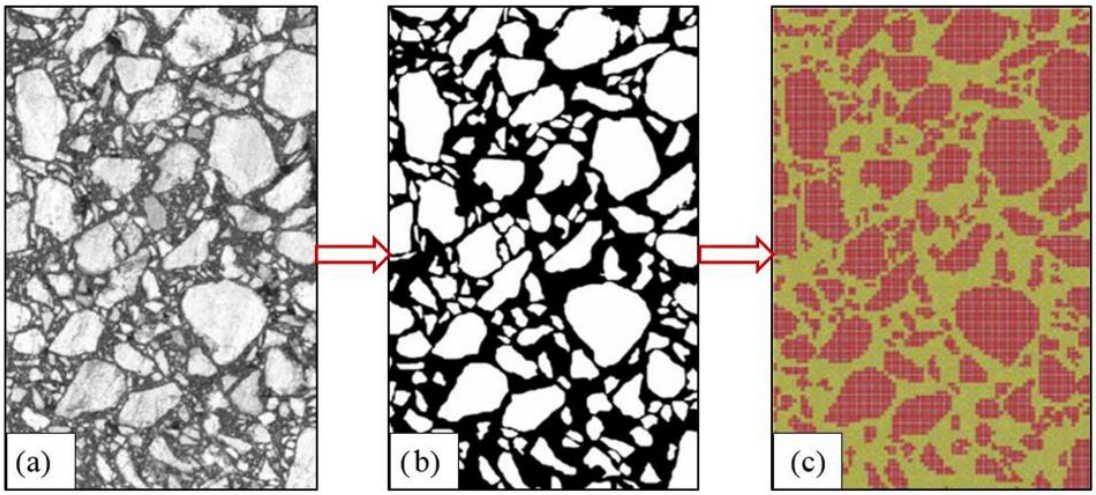


Figure 2.31: (a) Original image of asphalt concrete, (b) binary image, and (c) DEM simulation [109].

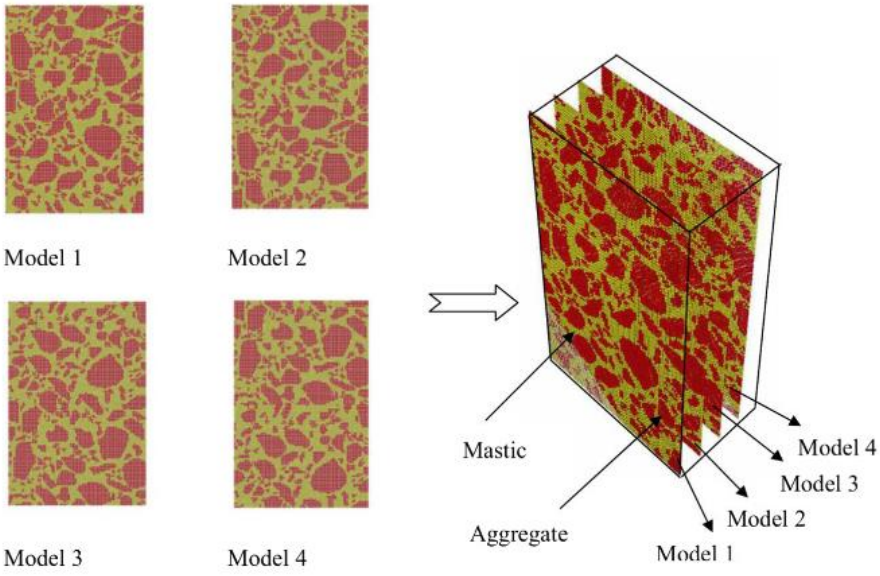


Figure 2.32: Reconstruct 3D DEM from 2D DEM [107].

2.6 Fracture Processing Behaviour and the Cohesive Zone Model (CZM) Theory

2.6.1 Fracture Process Zone

The fracture process zone is defined as a nonlinear zone that gradual softening and stress reduction as deformation increases. A non-softening nonlinear zone surrounds the nonlinear softening zone, representing material inelasticity [115]. Bazant and Planas categorised the fracture process of specific materials into three types: brittle, ductile, and quasi-brittle, as illustrated in Figure 2.33.

Figure 2.33(a) shows the first kind of fracture process, which is often seen in brittle materials, including glass, and brittle ceramics and metals. The nonlinear zone, including softening and nonlinear hardening zones, is small, and the fracture occurs virtually at the crack tip. In this fracture process, linear elastic fracture mechanics (LEFM) can be applied. Figure 2.33(b) shows the second kind of fracture process, which is often seen in ductile materials, including ductile metals and tough alloy. The softening zone is still small, while the hardening zone occupies the majority of the nonlinear zone. In this fracture process, elastic-plastic fracture mechanics (EPFM) can be applied. Figure 2.33(c) shows the third kind of fracture process, which often seen in quasi-brittle materials, including concrete, rock and cement bound. The hardening zone surrounds and is significantly smaller than the softening zone.

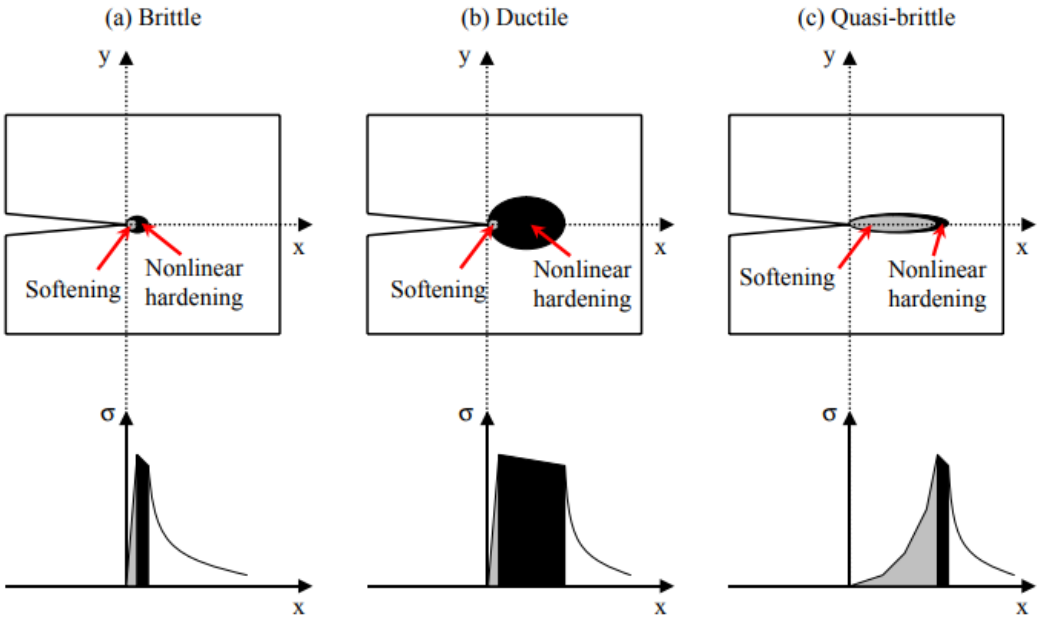


Figure 2.33: Concept of fracture process zone [115].

2.6.2 Cohesive Zone Model (CZM)

The CZM has gained considerable attention since it was used by Barenblatt [116, 117] and Dugdale [118] to study the properties of brittle materials and ductile materials, respectively. Figure 2.34 shows the concept of the CZM that it depicts the nonlinear fracture process zone ahead of a crack tip, where fracture is inhibited by cohesive tractions [119]. Figure 2.35 describes the four stages of cohesive crack propagation: elastic, initiation, softening, and failure. Stage I is called elastic, and the material in this stage has no damage, until the stress of the material meets the maximum stress, Stage II (crack initiation) begins. Stage III is defined as the nonlinear material softening that characterises damage progression, whereas Stage IV is defined as failure with a crucial crack opening width that represents new surfaces generated during fracture process. The whole process describes as: the traction (T) increases as the separation (Δ) grows, until reaches a maximum cohesive strength (σ_{max}), and it then decreases and finally vanishes at the critical separation (δ), resulting in fracture surfaces [120-122]. The

connection between cohesive zone (CZ) tractions and separations determines the form of the softening curve and establishes the CZ constitutive law.

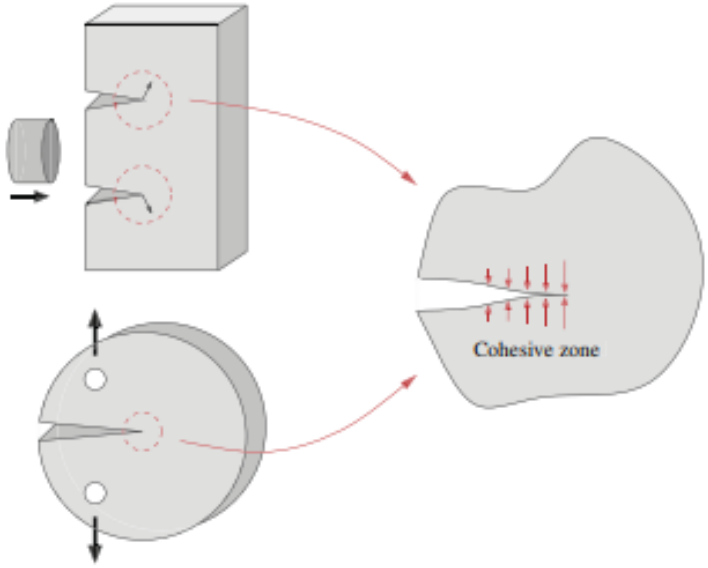


Figure 2.34: Concept of the CZM [119].

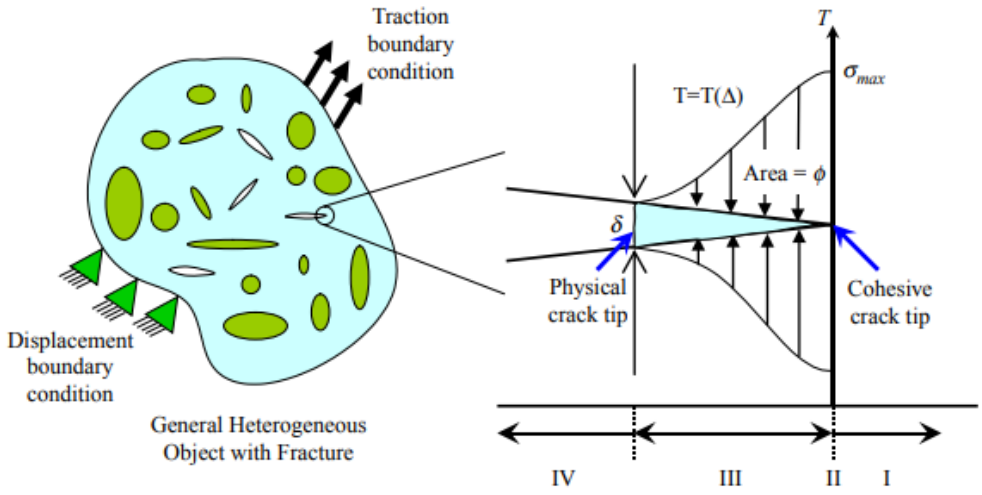


Figure 2.35: Mechanics of the CZM [120].

2.6.3 CZ Traction-separation Relationships

The CZM's traction-separation relationships, as a function of traction (T) and separation (Δ), can be recognised as various equations, as shown in Figure 2.36. Non-potential and potential models are used to classify CZ traction-separation relationships.

Cohesive interactions are easy to construct in non-potential models since a symmetric system is not needed. Paulino [123] investigated the dynamic failure of homogeneous and functionally graded materials (FGMs) using a bilinear traction-separation relationship. Yang and Thouless [124] simulated mixed-mode fracture of plastically deforming adhesion using a trapezoidal traction-separation relationship. Van den Bosch et al. [125] presented an exponential traction-separation relationship and evaluated the separation in mixed-mode circumstances.

At the continuum or atomistic level, the potential model is linked with physical field characteristics as a function of location (e.g. gravity, strain energy and magnetic energy).

Figure 2.37a illustrates a typical atomistic potentials [126]. A potential model has a minimum at some point because the interaction force, thus, the potential required to complete dissociation of an interaction (Ψ_0) is limited, illustrated as the area under the derivate of potential (Ψ) versus traction in Figure 2.37b. When the traction becomes critical (l_{cr}), the interaction hits a limit. The first derivative of potential (Ψ') shows the convex and the concave from before and after the limit point, which represents the traction across fracture surfaces, whereas the second derivative (Ψ'') represents the constitutive relationship (shear modulus). Needleman [127] developed a potential model based on a polynomial equation to model void nucleation via debonding. He [128] then devised anther potential model based on the exponential period to account for shear displacements. Rose et al. [129] proposed a potential model based on an exponential equation to characterise the normal interaction, while a periodic equation to characterise the shear interaction.

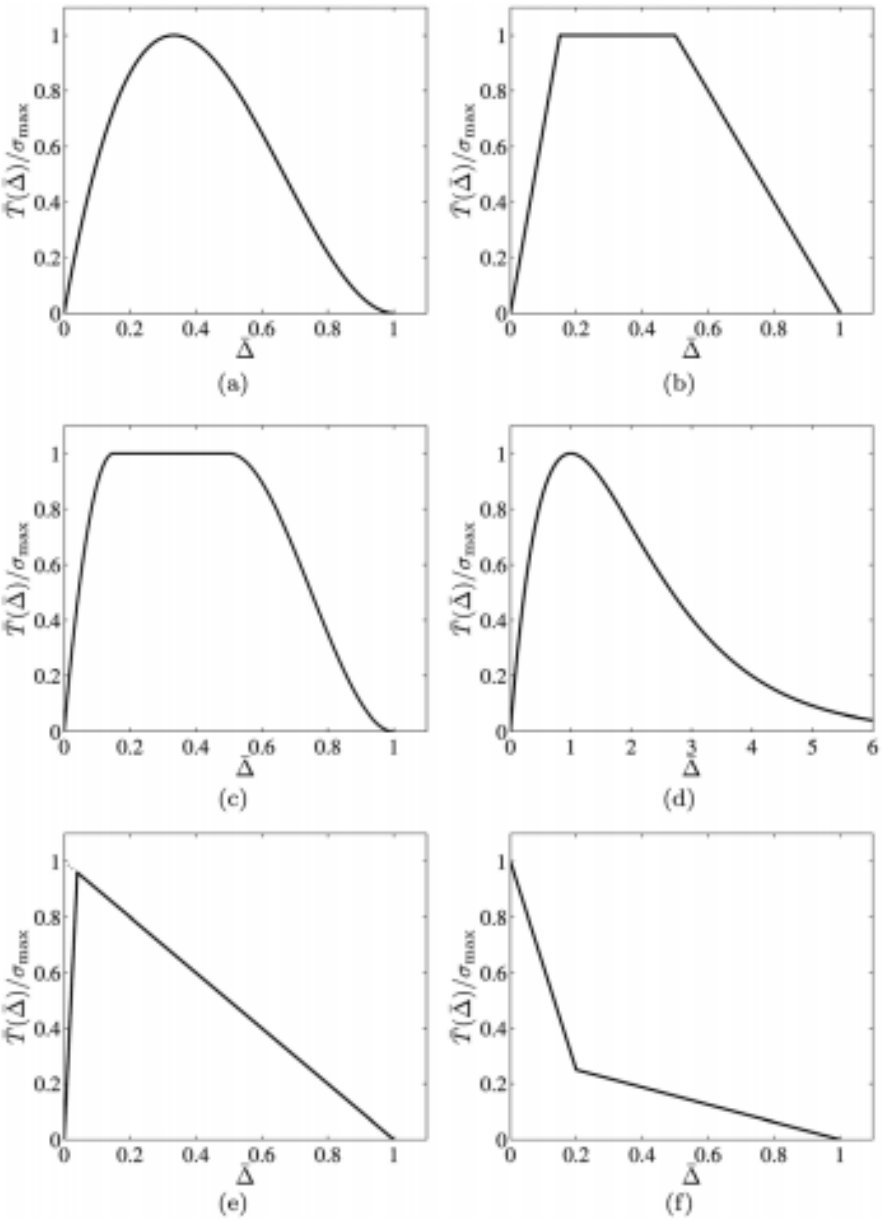


Figure 2.36: Traction-separation relationships: (a) cubic polynomial[130], (b) trapezoidal[131], (c) smoothed trapezoidal[132], (d) exponential[133], (e) linear softening [134-136] and (f) bilinear softening [134-136].

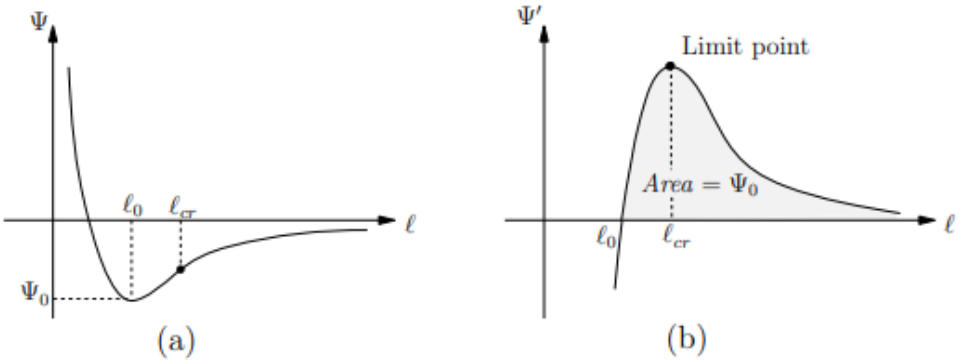


Figure 2.37: (a) Typical atomistic potential (Ψ) and (b) its derivative (Ψ') [126].

2.6.4 Methods to Embed Cohesive Elements

The artificial initial stiffness in the CZM characterises the pre-fracture response. Intrinsic models consider artificial initial stiffness by embedding cohesive elements (CEs) before numerical simulations, while extrinsic models assume initial rigidity.

Figure 2.38 describes the intrinsic CZM traction-separation relationship as a function of T_n and Δ_n, which contains an elastic stage between zero and critical separation. When separation becomes critical (δ_{nc}), the cohesive traction approaches the cohesive strength (σ_{max}), which correlates to crack initiation. Intrinsic CZM has been used for a variety of materials, including plain concrete [137], and asphalt concrete [138], because of its simplicity and easy incorporation of FEM. However, because numerous CEs needed be placed in FE meshes in advance, using intrinsic CZM may be computationally costly.

Figure 2.39 illustrates the extrinsic CZM traction-separation relationship, which has no elastic stage Separation happens when the traction exceeds the material's cohesive strength, and the traction continuously decreases as separation progresses. The extrinsic CZM provides different outcomes than the intrinsic CZM, however [139], it may have

problems of time continuity during CEs activation and FE meshes inaccuracy during cracks modelling [133, 140].

Cohesive elements are established on the surface cut out from a whole structure, the established cohesive elements share the joint with other elements on the same surface, and use the joint to transfer force and displacement. The cohesive elements can be regarded as two surfaces separated by a thickness. In some cases, the interface can be very thin, for example, the thickness of interfaces between cohesive elements chose zero (zero-thickness CEs) for crack modelling [141].

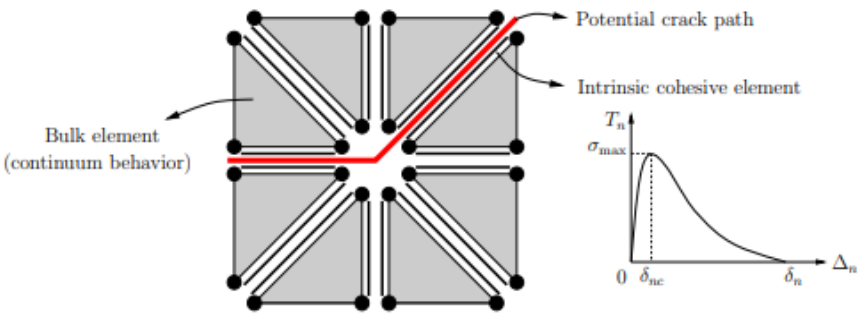


Figure 2.38: Intrinsic CZM.

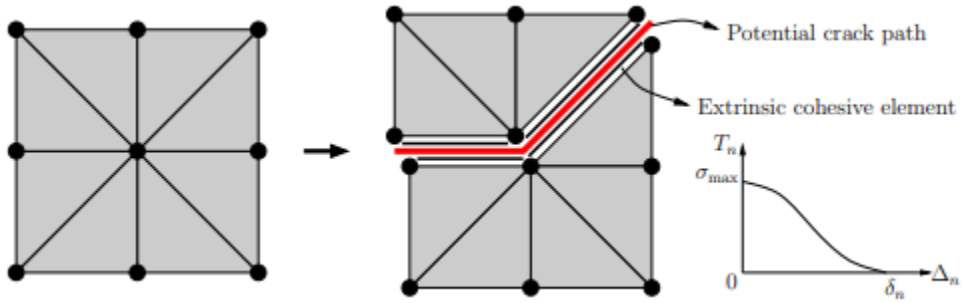


Figure 2.39: Extrinsic CZM.

2.6.5 CZM Application in Viscoelastic Materials

As mentioned in previous sections, the CZM has been utilised in a variety of applications and materials to offer an excellent framework for modelling strength, stiffness, and failure. In this section, applications of CZM in viscoelastic materials have been introduced.

The first application CZM in asphalt materials is by Jeng et al. [142, 143] to simulate crack resistance and propagation in flexible pavements overlays. Following that, researchers focused on CZM to see whether it might better depict the fracturing process of asphalt materials. The rate-dependent CZM suggested by Xu et al. [144] contains rate-dependent material characteristics that are derived by experiments and numerical analysis. Using a potential CZM, Paulino et al. [123] and Song et al. [138] simulated mode I and mixed-mode crack propagation of laboratory fracture tests, and investigated various fracture behaviours in conjunction with laboratory tests. Song et al. [145] used a bilinear CZM to simulate mixed-mode crack propagation in asphalt concrete and successfully minimise the false compliance inherent in the intrinsic cohesive law. Allen and Searcy [146] used a hereditary integral method with a traction-separation function

of bulk materials. The nonlinear viscoelastic CZM considering heterogeneity was used by Kim et al. [147-149] [150] to predict the cracking and damage behaviour of asphalt mixtures at intermediate temperatures. As illustrated in Figure 2.40, phases of mastic and aggregate have independent material characteristics obtained from experiments.

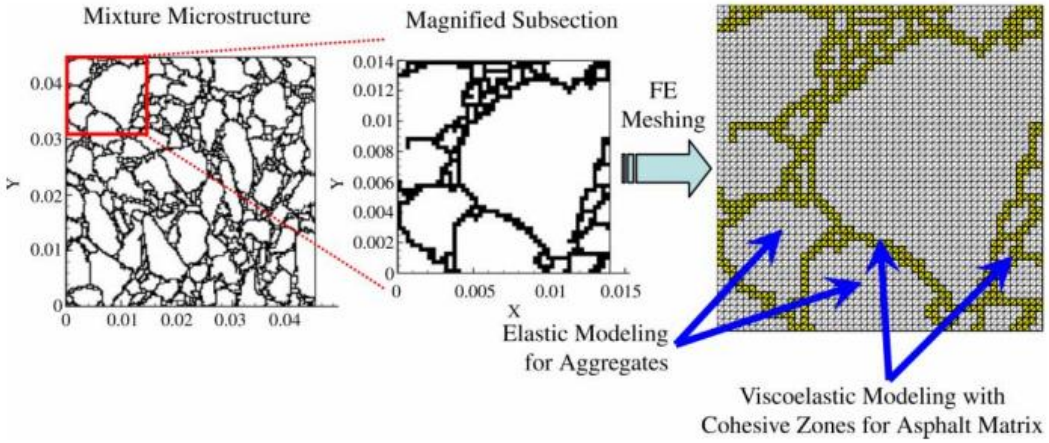


Figure 2.40: FEM using intrinsic CZM [150].

CZM-based 3D FEM models have recently gained popularity. Keyvan Zare Rami et al [151] proposed a computational model of asphalt mixtures utilising multiple 2D FE microstructures (Figure 2.42) as an alternative method to model 3D fracture response. An autonomous method was created to efficiently produce numerous 2D X-ray CT images, and a FE meshing module was created for CEs embedment in asphalt mixtures. The results show that multiple 2D microstructures are capable of representing the complicated 3D microstructures efficiently and accurately, lowering the experimental and computing costs of 3D microstructure. Pengfei Liu et al [152] developed a 3D FEM applying bilinear traction-separation law for adhesive fracture behaviours in mastic-aggregate interfaces, based on X-ray CT images. Figure 2.41 illustrates 3D FEM with mesh and boundary conditions and aggregate angularities used in simulations. It is discovered that the aggregate angularity has a substantial impact on mechanical

behaviour of asphalt mixtures. Figure 2.44 illustrates a notched concrete beam divided into homogeneous, and heterogeneous parts with two different 3-phase (aggregate, cement matrix, and interfacial transitional zones) regions [153]. A 3D FEM was built based on X-ray CT scans, with cohesive elements incorporated in the cement matrix and interfacial transitional zones. Compared numerical analysis with laboratory tests, a good agreement in terms of vertical force against fracture mouth opening displacement evolution and crack geometry were found.

For simulation based on CZM, one important input parameter is cohesive strength. The cohesive strength of a material is the strength of bonding between the particles or surfaces that make up that material, which is more specifically the inherent shear strength of a plane across which there is no normal stress [154]. Different test methods has been conducted to measure this parameter. Some researchers applied existing test methods, such as bitumen bond strength test (BBS) [155], three-point semi-circular bend test (3PSCBT) [156], indirect tensile test (IDT) and the single-edge notched beam SE(B) test [157], a convenient disk-shaped compact tension DC(T) test [41]. Others designed their own test methods to test cohesive strength. The HC-40 hydraulic force measurement device and the self-designed test die were used to test the low-temperature cohesive strength of asphalt mortars [158]. A designed tensile testing rig mounted on an Instron testing machine was applied to determine the aggregate–mastic interfacial bond strength [159].

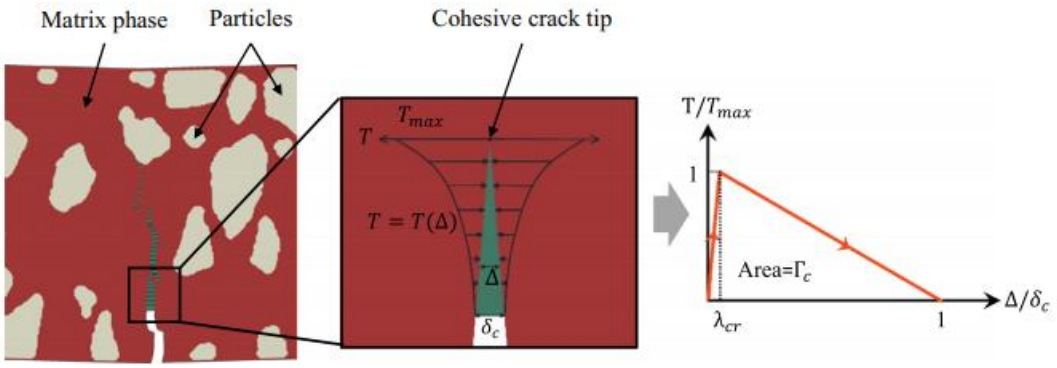


Figure 2.42: Bilinear CZM and 2D microstructures [151].



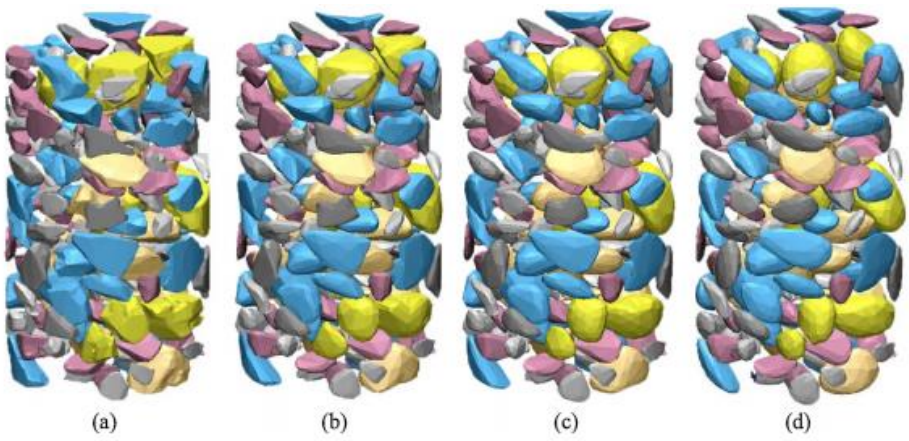


Figure 2.43: 3D FEM with mesh and boundary conditions and aggregates with different angularities: (a) 3DTS = 0.395, (b) 0.410, (c) 0.425 and (d) 0.440 [152].

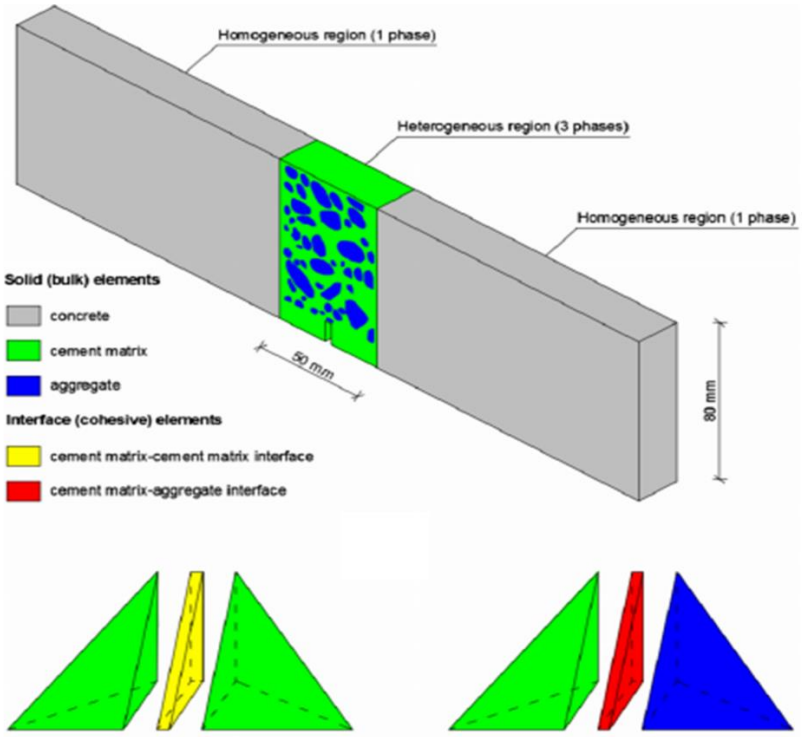


Figure 2.44: Concrete beam divided into homogeneous, and heterogeneous parts with two different 3-phase regions [153].

2.7 Summary

Section 2.1 describes approaches for studying fatigue behaviour of asphalt concrete, including phenomenological approaches; fracture mechanics; dissipated energy approaches; and microstructural approaches. Based on these contents, Chapter 4 combines the benefits of both approaches (phenomenological and energy-based) by developing a method that can be used to model the stiffness evolution in asphalt concrete. Chapter 4 further explains the relationship between stiffness development and crack development, which relates fatigue damage with fracture mechanics. The results of Chapter 4 lead to studies in Chapters 5 and 6, reflecting the in-depth study of fatigue mechanisms from macro to micro level.

Section 2.2 explains the characterisation of fatigue behaviour in different designs. Based on these contents, different influencing factors are considered in fatigue experiments in this thesis: asphalt binder type, aggregate grade, fatigue test type, test temperature and strain, ageing and moisture damage.

Section 2.3 introduces the Logistic model and its application, based on which, a logistic model is selected to represent the relationship between the log of the stiffness (E) and the log of the number of cycles (N) obtained from the 2PB fatigue test.

Section 2.4 and 2.5 describes X-ray CT and DIP, and approaches for reconstruction in numerical simulation, respectively. Based on these contents, the micro mechanism of fatigue behaviors is investigated in Chapter 5, and in Chapter 6 a 2D FEM is established to simulate crack initiation and propagation of asphalt concrete at the micro level based

on X-ray CT images.

Section 2.6 introduces the fracture processing behaviour and the CZM theory. Based on these contents, the 2D FEM built in Chapter 6 considers the following: a heterogeneous model with two phases (aggregates and asphalt mastic), viscoelastic properties of asphalt mastic, embedment of zero-thickness CEs both in asphalt mastic and interfaces between mastic and aggregates.

3 Materials and Experimental Programme

3.1 Introduction

In this project, various tests conducted to characterise fatigue resistance properties of asphalt concrete (AC) were introduced. The Dynamic Shear Rheometer (DSR) was applied for characterising the rheological properties of the asphalt mastic and calculating its viscoelastic parameters. Thermal oxidative ageing tests and moisture damage tests were used to condition the mixtures. Two point bending (2PB) tests, four point bending (4PB) tests, wheel track fatigue tests (WTT) and indirect tensile fatigue tests (ITFT) were used to characterise fatigue performance of asphalt concrete. Detailed fatigue cracking behaviours were observed by X-ray Computed Tomography (CT). Details of material applied and tests conducted in this project are shown in the following sections.

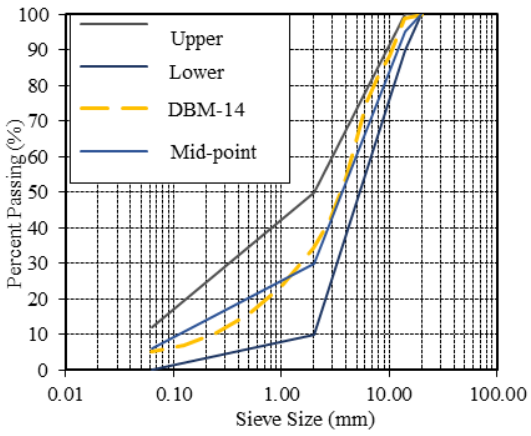
3.2 Raw Materials and Mixture Design

A 40/60 penetration grade asphalt binder was used, the technical parameters of which are shown in Table 3.1. In addition, crumb rubber modified asphalt binder (CRMB) was applied to investigate the fatigue behaviour of asphalt concrete with different types of asphalt binder. Aggregates used in this project are granite collected from Bardon Hill quarry, Leicestershire, UK. Asphalt mixtures with nominal maximum aggregate size (NMAs) of 10 mm and 14 mm were chosen. The composite aggregate gradations of dense bituminous mixture with NMAs of 14 mm (DBM-14) and 10 mm (DBM -10) and stone mastic asphalt with NMA of 10 mm (SMA-10) are shown in Figure 3.1(a)-(c). The thickness of the asphalt binder film is determined by the asphalt binder volume and the aggregate specific surface area (SSA). The relationship of them can be

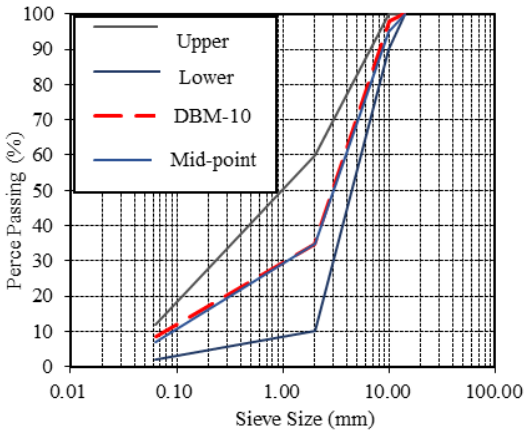
described as: Asphalt binder volume = Aggregate SSA × Thickness of the asphalt binder film. To make sure the film thickness of asphalt binder in the mastic is the same with that in the asphalt mixture, the asphalt binder content in asphalt mastic was calculated as: Asphalt binder volume = Filler SSA × Thickness of the asphalt binder film. Equations and SSA coefficients can be found in the "Technical Specifications for Construction of Highway Asphalt pavements" JTG F400-2004, China. The asphalt mastic applied comprises of filler (smaller than 0.063 mm) and Pen40/60 asphalt binder, the asphalt mastic design is shown in Table 3.2.

Table 3.1 Properties of asphalt binder.

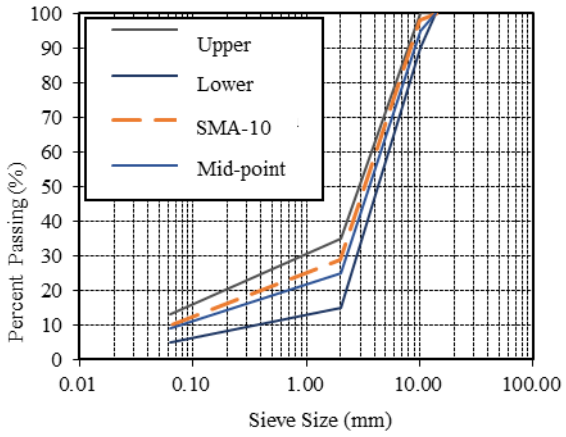
Properties	Pen 40/60	Test methods
Specific gravity	1.030	BS 2000-549:2007 [160]
Penetration (25 ℃, 5 s, 100 g)/0.1 mm	43	BS EN 1426:2015 [161]
Softening point/℃	51.0	BS EN 1427:2015 [162]
Viscosity, 135℃/Pa.s	0.441	BS EN 13302:2018 [163]



(a)



(b)



(c)

Figure 3.1: Gradations of (a) DBM-14, (b) DBM-10 and (c) SMA-10 of Hot Mix Asphalt (HMA).

Table 3.2: The asphalt mastic design.

Components	Mass ratio (%)
< 0.063 mm	73
Asphalt binder	27

3.3 Mixing and Compaction

Asphalt mixtures were compacted by a roller compactor; mixing and compaction procedures of the asphalt mixtures were chosen from BS EN 12697-35: 2016 [164] and BS EN 12697-33: 2019 (Figure 3.2 and Figure 3.3). Mixing and compacting temperatures of HMA were controlled at around 160 ℃ (Figure 3.4). Hot mixtures were poured into pre-heated moulds and compacted to the required slab thickness.



Figure 3.2: Mixing procedure (BS EN 12697-35: 2016) [164].

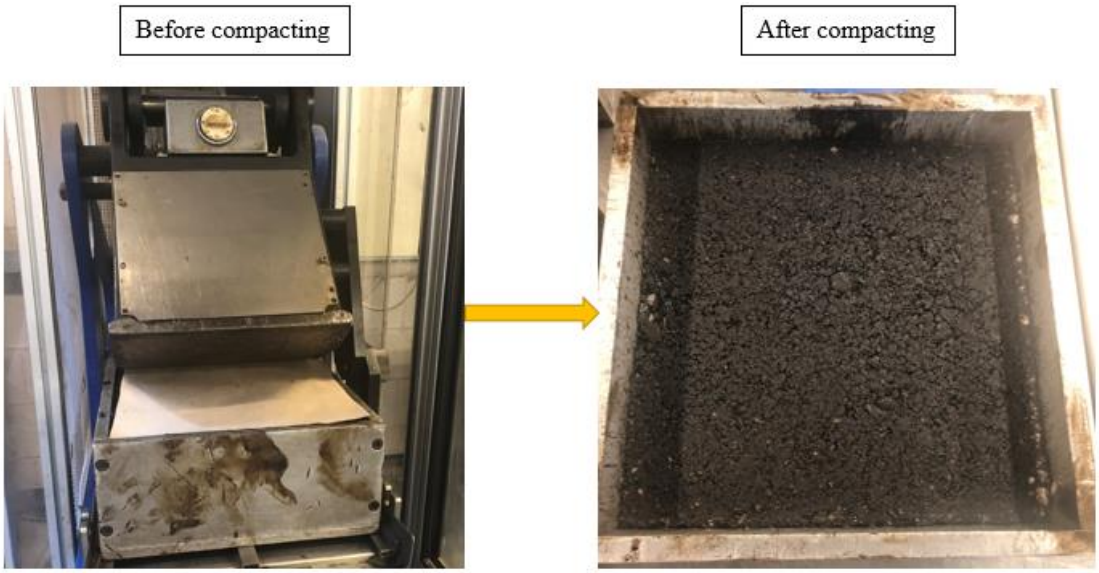


Figure 3.3: Compaction of asphalt concrete (BS EN 12697-33: 2003) [165].



Figure 3.4 : Testing compaction temperature.

3.4 Dynamic Shear Rheometer (DSR) Test

The complex modulus and phase angle of the asphalt mastic were measured by conducting a frequency sweep at multiple temperatures (5, 10, 15, 20, 25 and 30 ℃) using the DSR test. At each temperature, eleven values were collected by running a frequency sweep (0.1% controlled, strain 0.1 Hz to 10 Hz). For all temperatures, an 8 mm DSR head geometry and 2-mm gap geometry were used (Figure 3.5) [166].

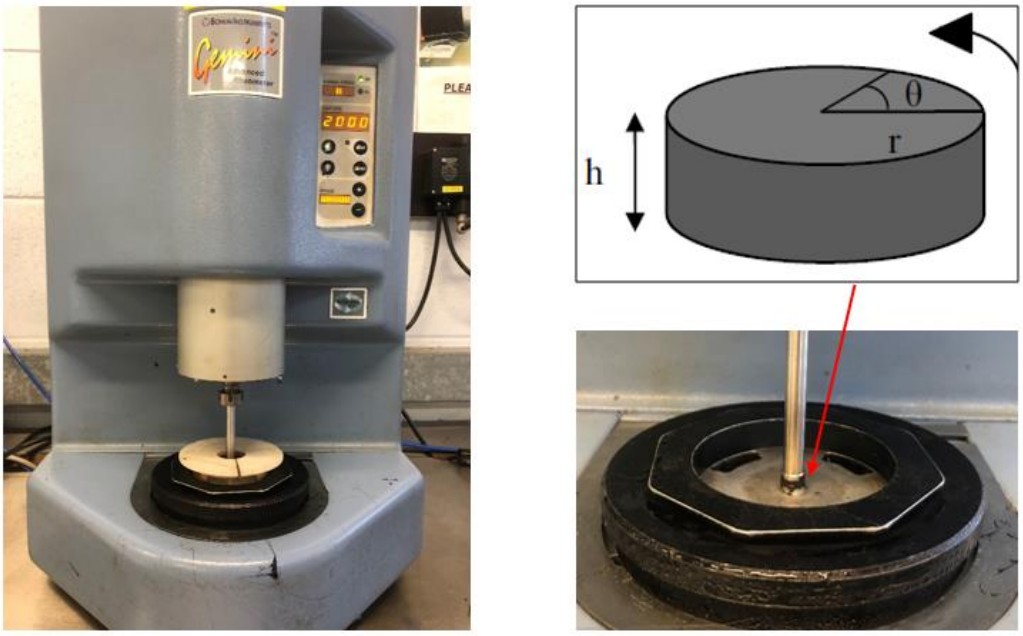


Figure 3.5 : DSR test set-up.

3.5 Thermal Oxidative Ageing Test

The test method for short-term ageing of the asphalt mixture was to put loose material in an oven at 135 ± 1 ℃ for 4 hours. For long-term ageing, the compacted specimens were put in an oven at 85 ± 3 ℃ for 5 days according to TS 12697-52:2017 [167]. The oven setting is presented in Figure 3.6. After the ageing, the oven is turned off and left to cool to room temperature, and the specimens are then removed. All the specimens were placed in a temperature-controlled cabinet at 20 ℃ for at least 6 hours before testing. The materials after short-term and long-term ageing can be seen in Figure 3.6 (a) and (b), respectively.

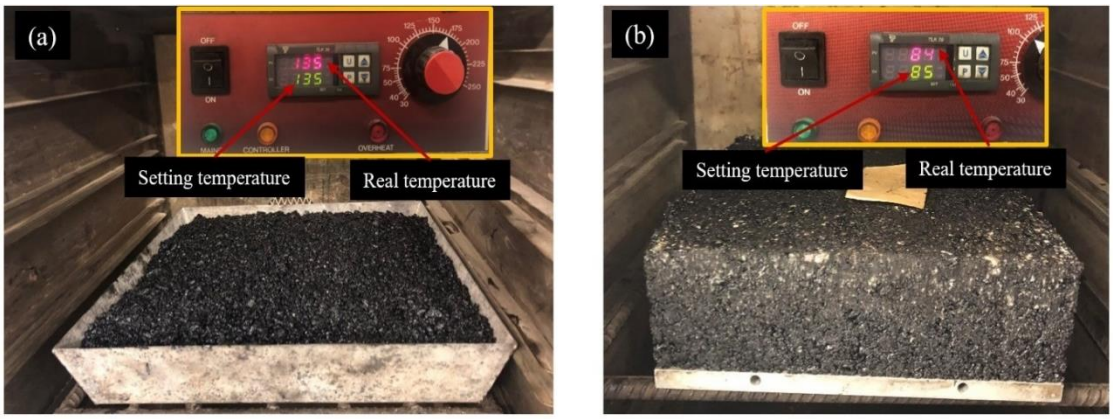


Figure 3.6: Oven setting and the materials after the (a) Short-term ageing and (b) Long-term ageing.

3.6 Moisture Damage Test

The moisture damage test used in this research is described in BS EN 12697-12:2018 [168]. The vacuum procedure was conducted under a residual pressure of 6.7 ±0.3 kPa for 30 ±5 minutes before the specimens were placed in a water bath. A thermostatically controlled water bath is capable of maintaining the prescribed conditioning temperature in the vicinity of the specimens. The bath is equipped with a perforated shelf, placed on spacers above the bottom. The capacity of the bath is such that the test specimens can be stored with the upper surface more than 20 mm below the water surface. The specimens were put in a water bath at 40 ±2 ℃ for a period of 72 ±2 hours, as shown in Figure 3.7.

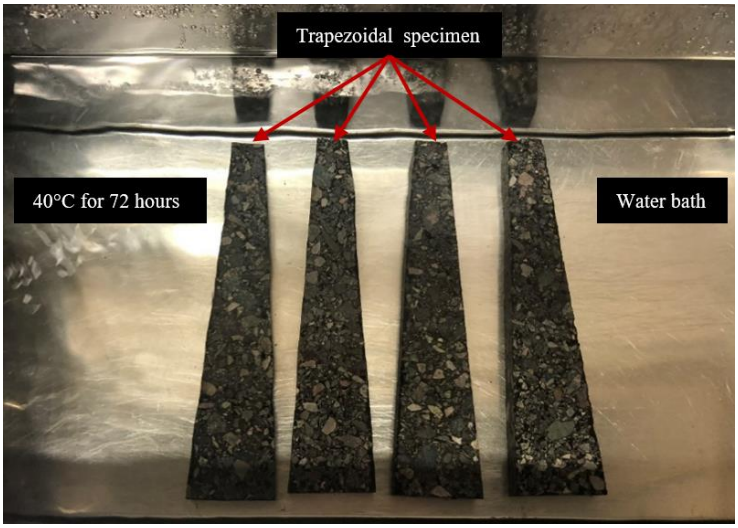


Figure 3.7: Water bath for moisture conditioning of specimens.

3.7 Two Point Bending (2PB) Test

Fatigue tests in this project were mainly carried out using the 2PB equipment. The test consists of applying a continuous sinusoidal waveform at the top of a trapezoidal specimen. To prepare the samples for 2PB, trapezoidal specimens were manufactured from slabs with dimensions: 305 mm length, 305 mm width and 85 mm depth. Twelve specimens were produced from one slab using the process shown in Figure 3.8(a). Dimensions of the 2PB specimens are shown in Table 3.3. The dimensions required for a 14 mm size DBM are taken from BS EN 12697-24 2018 [169]. The samples were glued to metal plates using epoxy resin to enable them to be fitted to the test apparatus (see Figure 3.8(b)). The bottom base is fixed so that the specimen is mounted as a vertical cantilever, allowing a sinusoidal displacement to be applied to the top of the specimen. During a fatigue test, the failure usually occurs at 4/9 of the height of the specimen from the bottom, where the tensile stress is a maximum, as shown in Figure 3.9 [170].

The 2PB tests were conducted under strain-controlled mode using sinusoidal loading;

load loading mode can be seen in Figure 3.10. The specimens were subjected to different strain levels - 150, 200 and 250 με at different temperatures - 0, 5, 10 and 20 ℃ at a frequency of 15 Hz. All samples were conditioned for 4 hours before the start of the tests. The sample stiffness at the 100th cycle is defined as the initial stiffness. In this study, the failure criteria were studied at different reductions of the initial stiffness value. The test was set to stop once the stiffness reached 10% of the initial stiffness value. The equipment tests two specimens at each strain level. Figure 3.8(c) shows the test equipment and the samples ready for testing.

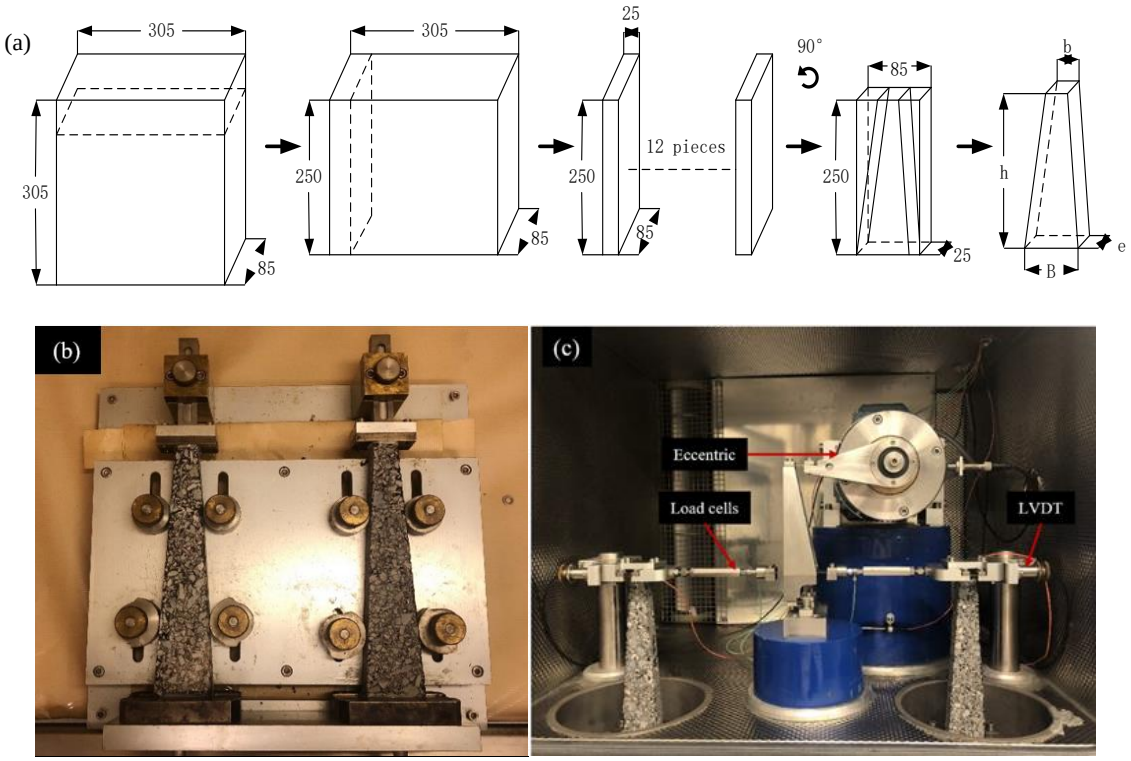


Figure 3.8: Sample preparation and setting of 2PB: (a) Schematic diagram of preparation of trapezoidal specimens; (b) Gluing of samples and (c) Setting procedure of samples.

Table 3.3: Dimensions of the 2PB specimens: BS EN 12697-24: 2004.

Dimensions of the specimens (see Figure 3.8(a))	Type of mixture: D ≤ 14 mm
B	56 ± 1 mm
b	25 ± 1 mm
e	25 ± 1 mm
h	250 ±1 mm

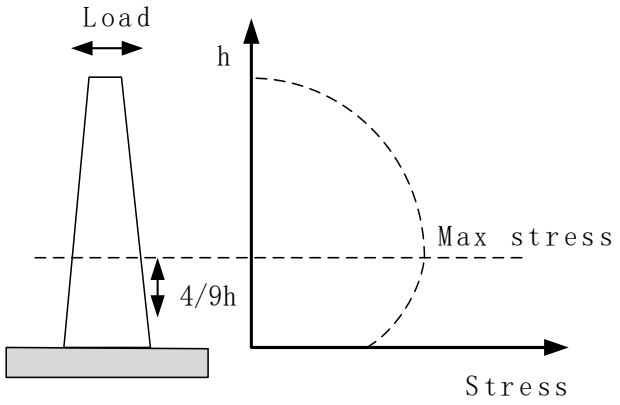


Figure 3.9: Stress in the 2PB samples [170].

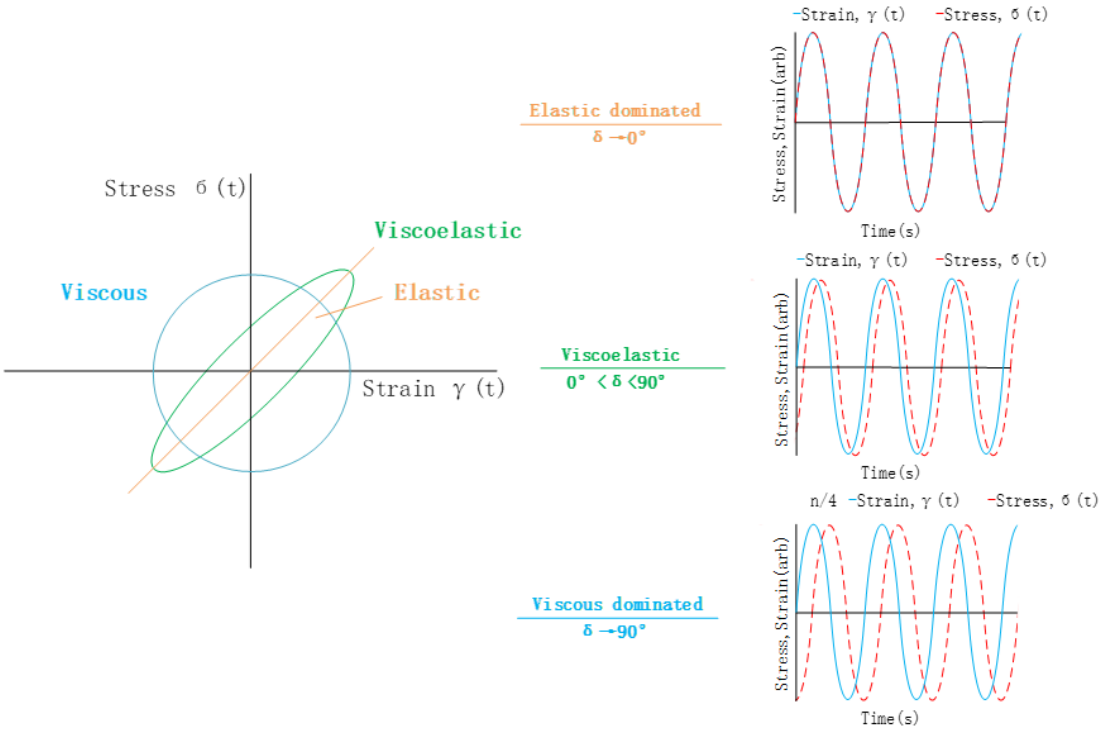
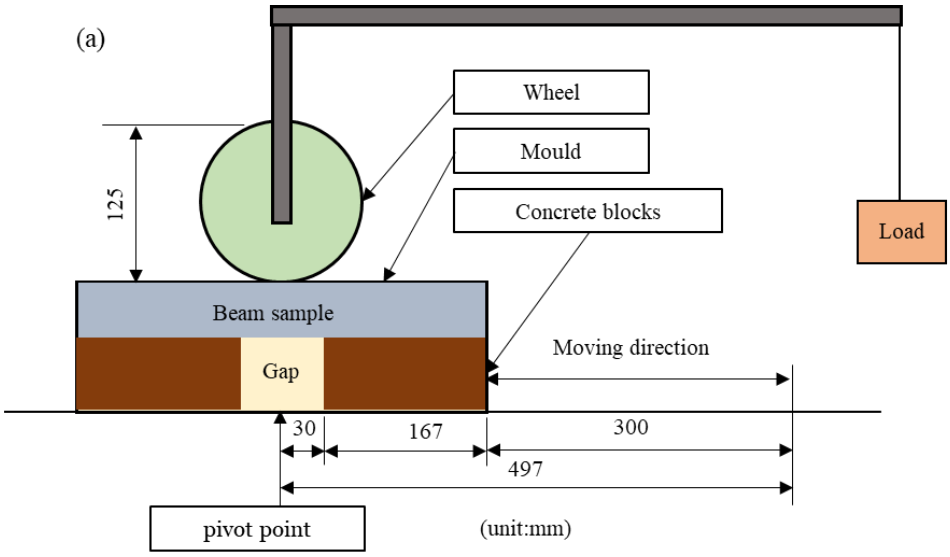
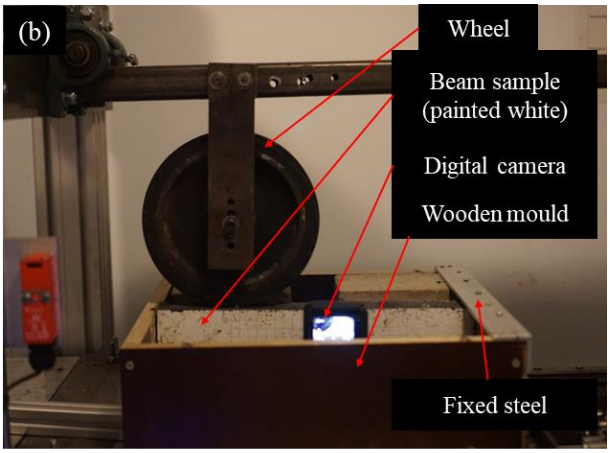


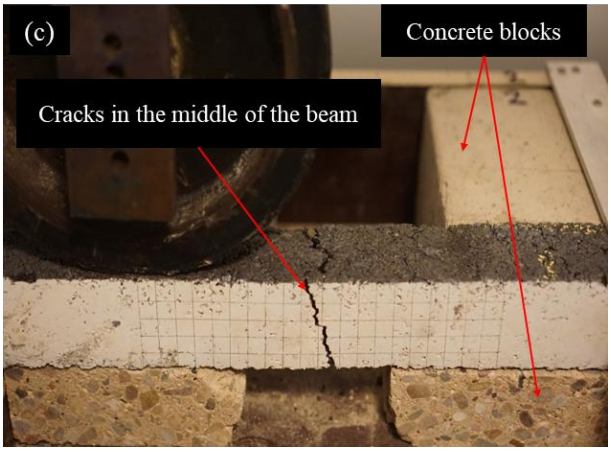
Figure 3.10: Loading mode of 2PB tests.

3.8 Wheel Tracking Fatigue Test (WTT)

The WTTs were performed by applying a moving load at a rate of 25 passes per minute (2.4 Hz) to white and grid-marked beam samples (Figure 3.11) [171]. Fatigue tests were conducted at a temperature of 10 ℃ with a load level of 1.44 kN. The WTT machine consists of a loaded wheel that bears on a beam sample housed in a wooden mould, and diagram of the mould is shown in Figure 3.11c. Two concrete blocks were placed underneath the beam samples to ensure that the pivot point experienced the maximum tensile stress. A digital camera was set to monitor crack growth at the bottom of the beam. Concrete blocks were put in the mould to stop beam samples from moving side by side, which can affect the results of cracking length. The steel was attached to one side of the wooden mould to prevent the beam sample from warping excessively after deformation.


(a)
Wheel
Mould
Concrete blocks
Load
125
Beam sample
Gap
Moving direction
30
167
300
497
pivot point
(unit:mm)


(b)
Wheel
Beam sample
(painted white)
Digital camera
Wooden mould
Fixed steel


(c)
Concrete blocks
Cracks in the middle of the beam

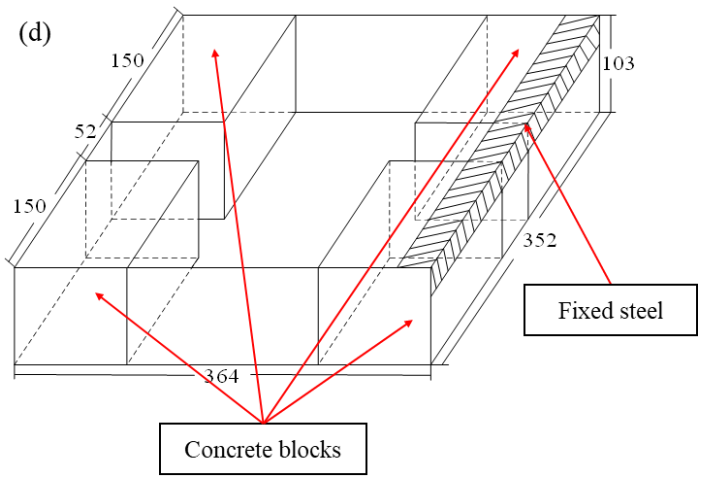


Figure 3.11: (a) Arrangement of the WTT; (b) WTT set-up; (c) Fracture in the middle of the beam sample and (d) Diagram of the mould.

3.9 Four Point Bending (4PB) Test

The test consists of applying a continuous sinusoidal waveform at the top of a prismatic specimen by means of two load points. The specimen is restrained at four points by means of four clamps. Free translation and rotations are allowed at all load and reaction points. Deformation is calculated by means of three LVDTs (Linear Variable Differential Transformers) located at three different points (Figure 3.12).

The 4PB tests in this project were mainly used to demonstrate the applicability of the stiffness change tendency method (SCTM) obtained from 2PB tests. Firstly, the 4PB tests were applied to calculate the stiffness of beam samples after certain number of cycles (after WTT testing). To fit both WTT machine and 4PB test machine, dimensions of beam samples used were designed as 360 mm length, 50 mm width and 50 mm height. Beam samples were manufactured from slabs with dimensions: 400 mm length, 300 mm width and 50 mm height. The beam samples were tested under strain-controlled mode at a strain level of 400 με at 10 ℃ at a frequency of 10 Hz. Secondly, three

different mixtures, DBM-10 + CRMB, DBM-14 + Pen 40/60 and SMA-10 + Pen 40/60, were tested by 4PB tests to demonstrate the applicability of the SCTM with different asphalt binder grades, mixture grades and test methods. The beams were tested under strain-controlled mode at a strain level of 270 με at 10 ℃, and with a frequency of 15 Hz. The fatigue test was conducted according to the BS EN 12697-24: 2018 [169].

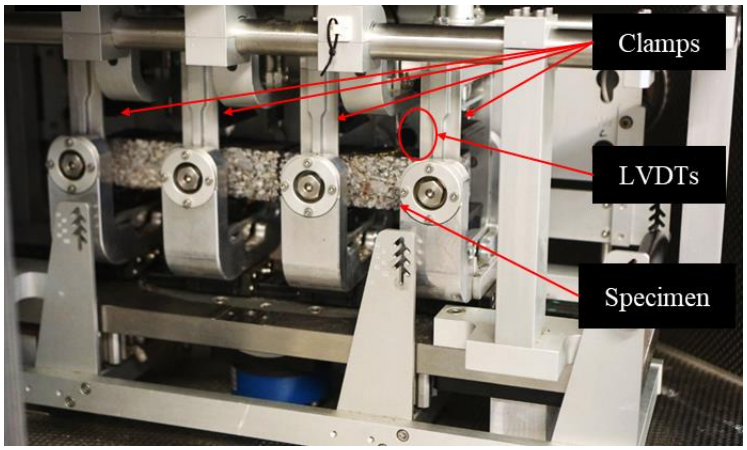


Figure 3.12: Set-up of the 4PB test.

3.10 Indirect Tensile Fatigue Test (ITFT)

Specimens of dimensions 20 mm diameter by 18 mm height were made for use in the ITFT equipment, the cutting procedure and the prepared samples are shown in Figure 3.13. The specimens were conditioned at the test temperature of 5 ± 1 ℃, and then positioned perpendicularly, between the top and bottom loading strips (Figure 3.14a). Figure 3.14b illustrates a repeated controlled stress pulse applied at a rate of 40 pulses per minute at a load of 0.8 kN. The cumulative vertical deformation versus the number of load cycles was recorded. Tests stopped automatically when the vertical deformation exceeded the set values of 0.4, 0.6, 0.8, 0.9, 1.1 and 1.4 mm. As the specimen is not the standard size, a strain gauge was applied on the specimen with the 1.4 mm vertical

deformation to record the strain level.

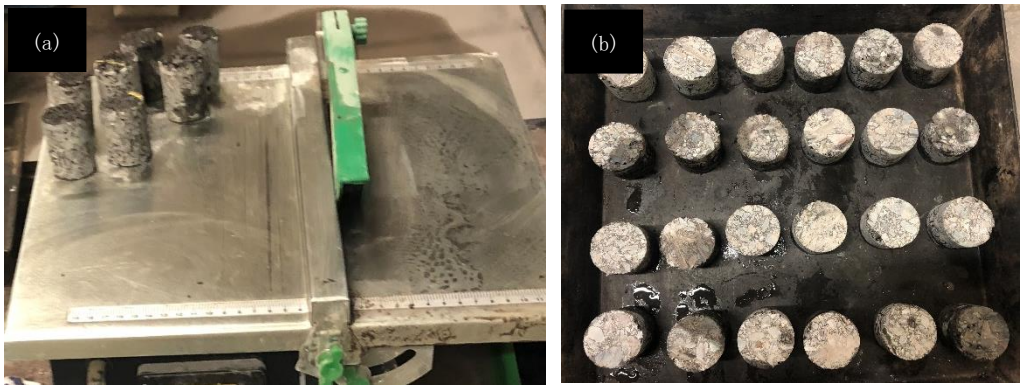
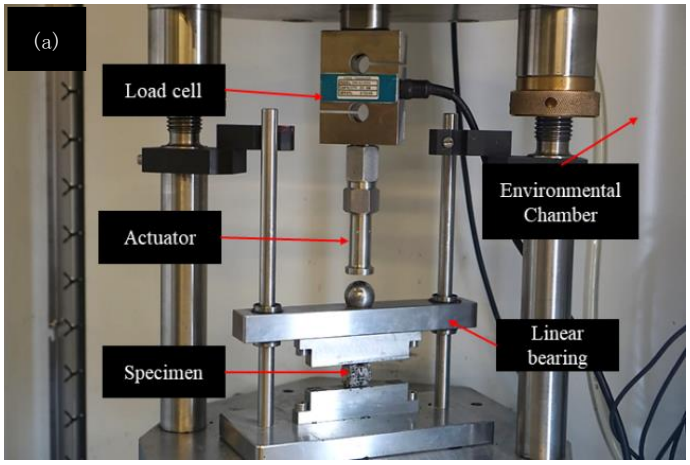


Figure 3.13: (a) Cutting procedure; (b) Prepared samples.



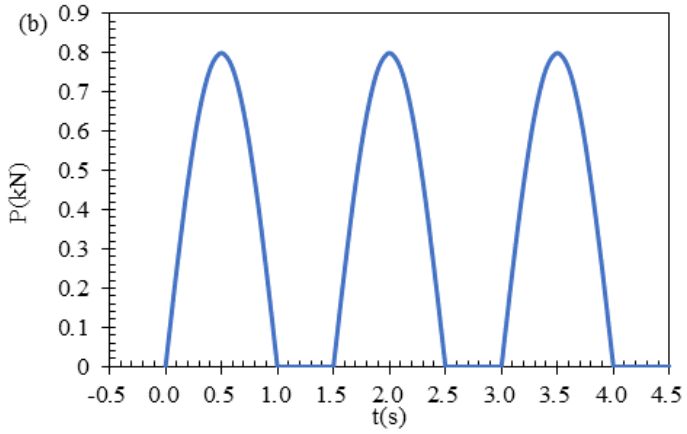


Figure 3.14: (a) Indirect tensile fatigue test set-up; (b) Schematic diagram of the load during the ITFT.

3.11 X-ray Computed Tomography (CT)

For the microstructure analysis, the specimens were X-rayed before and after the ITFT test. The scanner consists of an X-ray tube, a rotation stage and a detector (Figure 3.15). The X-ray CT scanning was conducted under a penetration of 180 kV and a contrast of 80 mA with the resulting resolution of 0.014 mm. During scanning, the small sample (Figure 3.15) is shifted vertically and the entire procedure is repeated to generate additional 2D image slices. The images were processed using the VGStudio Max software [172].

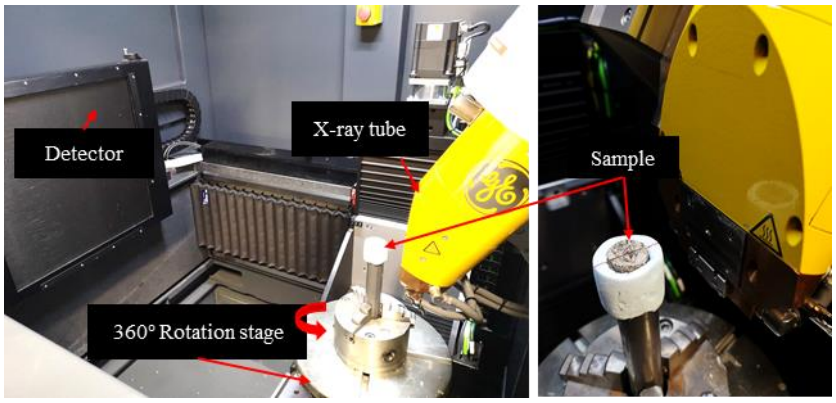


Figure 3.15: X-ray CT equipment set-up.

3.12 Bespoke Tensile Strength Test

The maximum cohesive strength (tensile strength) of the mastic was determined with a bespoke tensile test mounted on a universal testing machine (UTM), as shown in Figure 3.16 [159]. A mould was specially designed to produce the dog bone-shaped specimen, as illustrated in Figure 3.16a. Both the asphalt mastic and mould were heated in an oven before pouring the mastic into the mould; and screws were tightened up to fix the mastic in the mould. The mould must be coated with a release agent (a mixture of glycerin and talcum powder) in advance to facilitate the demoulding of the mastic. The two ends of the test sample were fixed on the UTM and the samples were demoulded after sample conditioning (this process prevents the asphalt from deforming at high temperatures). All samples were conditioned at 5 ℃ and 25 ℃, respectively for 4 h before testing, and then a constant cross-head speed of 20 mm/min was applied. Five replicate specimens were tested to obtain the cohesive strength and the fracture energy.

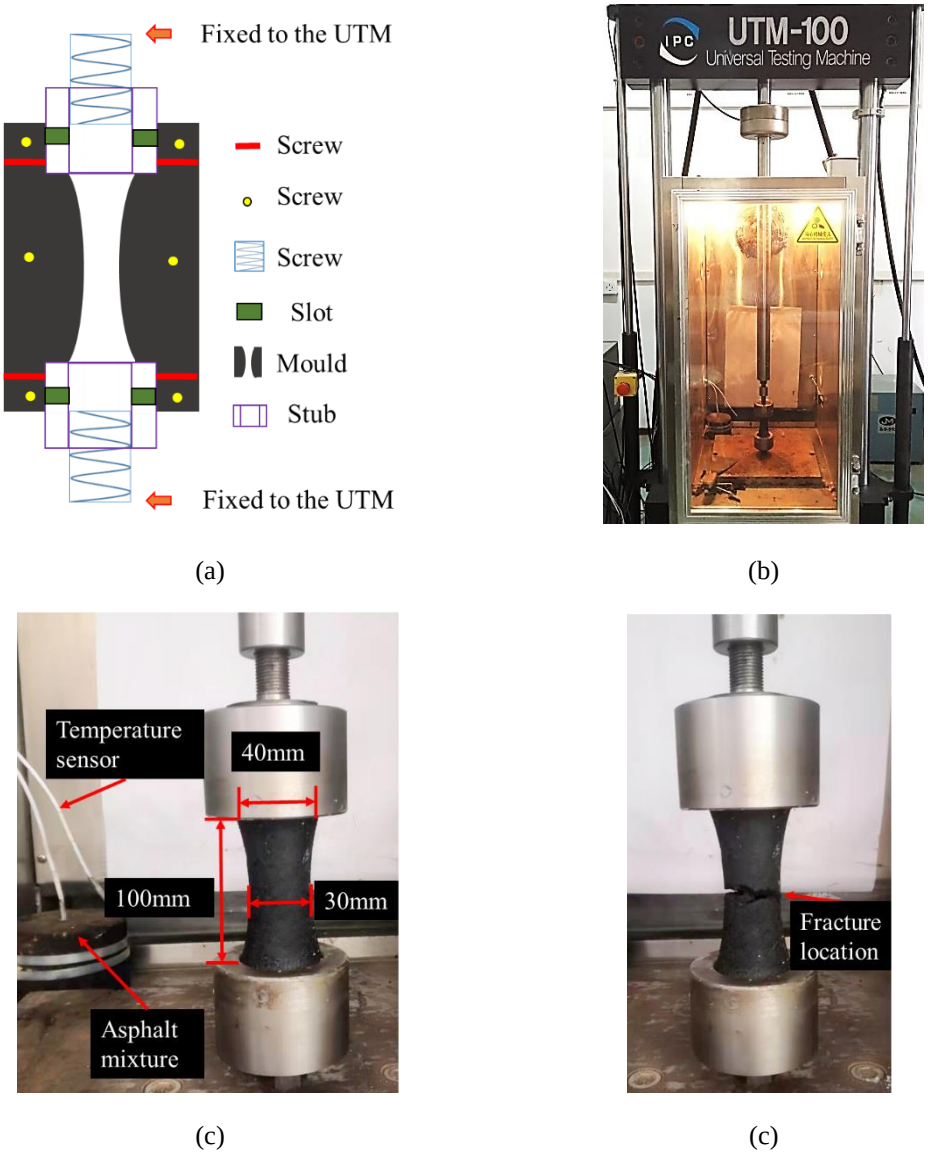


Figure 3.16: Asphalt mastic tensile strength test (a) the specially designed mould; (b) the UTM machine set-up; (c) the dog bone-shaped specimen dimensions; and (d) Fracture location.

3.13 Summary

This chapter has introduced the materials and testing programmes applied in the project, including detailed material properties, mixing and compaction methods, sample preparation, testing conditions and testing procedures for each test. These materials and methods will be used in Chapters 4 to 6 to explore micro mechanism of fatigue cracking in asphalt concrete.

4 Modelling the stiffness Development and Links to Crack Development

4.1 Introduction

Considerable research has been undertaken to explore methods to reduce the effect of fatigue damage and prolong the pavement life. Critical to this is the accurate identification of the key stages in the development of fatigue performance deterioration and the appropriate definition and selection of failure criteria [173] [174-177].Within the literature, various approaches have been used to define fatigue damage and analyse fatigue performance. Traditionally, fatigue failure is defined using a phenomenological approach with the fatigue failure criterion being defined as the number of loading cycles corresponding to a 50% stiffness reduction [178]. The traditional fatigue failure criterion is easy for calculation and prediction of the fatigue life, but results in the loss of information regarding fatigue behaviour characteristics. It is realized that a typical fatigue curve (stiffness versus number of cycles under strain-controlled mode) is presented by a “S” shaped curve with four distinct regions (internal heating, micro-crack formation, crack formation and propagation, and sample breakdown) separated by three transition points [179] [180]. It is then suggested that the first and second transition points are possibly associated with microcracking and macrocracking in the material, respectively [34]. But the method of how to determine the transition points on the stiffness reduction curve, and how to relate the transition points to different fatigue cracking processes are still not very clear.

A range of energy-based approaches have subsequently been proposed as improved methods to characterise fatigue damage. The cumulative dissipated energy (CDE) approach and initial dissipated energy (IDE) approach are two of the earliest examples

of this [180] [181]. However, only the relative amount of energy dissipation happening in the asphalt materials during the loading-unloading process is due to fatigue damage. Further methodologies to isolate the energy dissipation due to damage and viscoelasticity including the ratio of dissipated energy change (RDEC), dissipated pseudo-strain energy (DPSE) and rate of DPSE approaches were subsequently developed [182-184]. Different from the traditional method, energy-based approaches are independent of test conditions and mode of loading when nonlinearity in material response is not significant. More importantly, by calculating the plot of dissipated energy versus number of cycles, three stages that were clearly separated by two transition points were found. The transition points were then used as fatigue criteria that were defined and calculated using the energy-based approaches. Pronk and Hopman [185] used the energy ratio (ER) to define the number of cycles at a critical fatigue point (N_1) where the relationship between the ER and the number of cycles becomes nonlinear, for controlled strain fatigue tests. Pronk [186] then suggested that N_1 could be defined as the number of cycles at which cracks are considered to initiate. Ghuzlan and Carpenter [183] used the RDEC to define macroscopic failure (N_{fm}), which is related to crack propagation. The RDEC method was refined by Shen and Carpenter to calculate the value of N_{fm} [187]. Although these energy-based approaches greatly improve the ability to determine the appropriate failure criteria by relating criteria to crack initiation and propagation, they have a limitation in that the defined failure criteria cannot be directly connected to the stiffness (force-deformation) development.

This chapter combines the benefits of both approaches (phenomenological and energy-based) by developing a method that can be used to model the stiffness evolution in asphalt concrete, determine critical laboratory fatigue failure points to characterise different fatigue damage stages, and relate the fatigue failure points to different fatigue cracking processes. This aim is achieved by selecting a logistic model to represent the

relationship between the log of the stiffness (E) and the log of the number of cycles (N) obtained from 2PB fatigue tests to form a stiffness change tendency method (SCTM). The measured stiffness reduction versus loading curves were determined for a range of asphalt mixtures in unaged, aged and moisture damaged conditions by testing at various temperatures and strains. Three different mixtures including DBM-10 with crumb rubber modified asphalt binder (CRMB), DBM-14 with Pen40/60 asphalt binder and SMA-10 with Pen40/60 asphalt binder were tested by 4PB fatigue tests to demonstrate the applicability of the SCTM across more asphalt binder grades, mixture grades and test methods. By analysing the derivatives of the logistic model, it is possible to identify three transition points associated with fatigue progression. The number of loading cycles associated with the first two transition points in the SCTM (N_{p1} and N_{p2}) were compared to the value of N_1 and N_{fm} obtained from two energy-based approaches (the ER and RDEC approaches), aiming to relate N_{p1} and N_{p2} to crack initiation and propagation. The numbers of loading cycles associated with the transition points (N_{p1}, N_{p2} and N_{p3}) in the SCTM are found to be affected by factors such as the strain level, temperature, and ageing and moisture. To prove whether the fatigue criteria calculated by the SCTM can be reflected in the plot of crack length versus number of cycles, and to further explain the relationship between the stiffness development and crack development, the 4PB fatigue tests is used to measure the stiffness of beam samples corresponding to different numbers of cycles in WTTs.

4.2 Programme

To develop the SCTM, curves of measured stiffness reduction versus loading cycles were determined by considering different conditions, including aged and moisture damaged, different test methods, different test temperatures and strains, and different types of mixtures, as shown in Table 4.1. One sample set contains four repeated 2PB

tests with the results being averaged. A scheme for the testing programme is shown in Figure 4.1. The thermal oxidative ageing test and moisture damage test were applied for conditioning samples used in 2PB tests.

Table 4.1: Testing samples and conditions.

Sample set	Test Method	Asphalt binder	Mixture type	Temperature (℃)	Strain (με)	Condition
1	2PB	Pen 40/60	DBM-14	0	200	Unaged
2	2PB	Pen 40/60	DBM-14	5	200	Unaged
3	2PB	Pen 40/60	DBM-14	10	200	Unaged
4	2PB	Pen 40/60	DBM-14	20	200	Unaged
5	2PB	Pen 40/60	DBM-14	10	150	Unaged
6	2PB	Pen 40/60	DBM-14	10	250	Unaged
7	2PB	Pen 40/60	DBM-14	10	200	Aged
8	2PB	Pen 40/60	DBM-14	10	150	Aged
9	4PB	Pen 40/60	DEM-10	10	250	Aged
10	2PB	Pen 40/60	DBM-14	0	200	Aged
11	2PB	Pen 40/60	DBM-14	5	200	Aged
12	2PB	Pen 40/60	DBM-14	20	200	Aged
13	2PB	Pen 40/60	DBM-14	10	200	Moisture damaged
14	2PB	Pen 40/60	DBM-14	10	200	Aged + moisture damaged
15	2PB	Pen 40/60	DBM-14	10	150	Aged + moisture damaged
16	2PB	Pen 40/60	DBM-14	10	250	Aged + moisture damaged
17	2PB	Pen 40/60	DBM-14	0	200	Aged + moisture damaged
18	4PB	Pen 40/60	DEM-10	5	200	Aged + moisture damaged

19	2PB	Pen 40/60	DBM-14	20	200	Aged + moisture damaged
20	4PB	Pen 40/60	DEM-10	10	270	unaged
21	4PB	CRMB	DEM-10	10	270	unaged
22	4PB	Pen 40/60	SMA-10	10	270	unaged

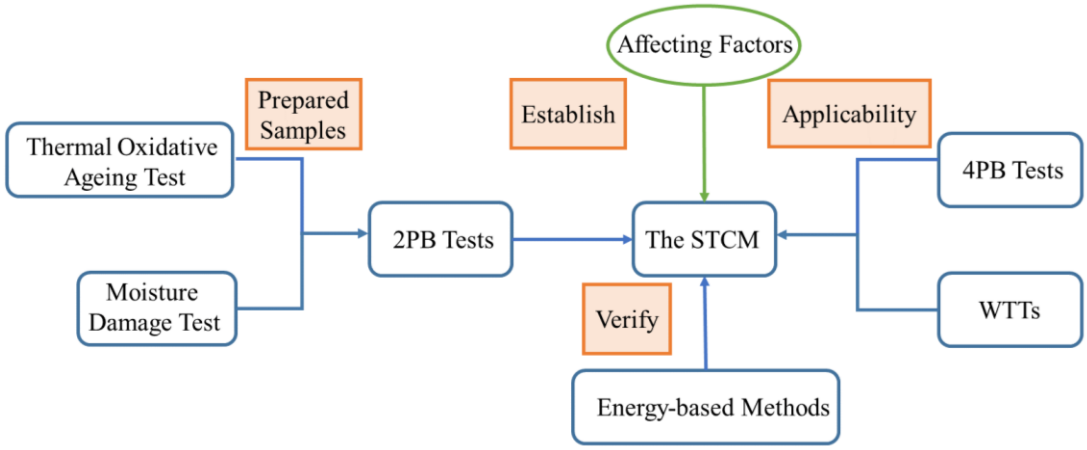


Figure 4.1: Scheme for testing programme.

4.3 Determination of Fatigue Failure Criteria by Energy-based Approaches

4.3.1 Dissipated Energy Approach

To assess the accuracy of modelling stiffness development, the ER and RDEC approaches are applied to validate the results obtained from the SCTM. The data collected at 10 ℃ under 150 με is chosen as an example; the phenomenological stiffness versus the number of cycles on logarithmic scales is applied to show the position of N_{f50} as a comparison (Figure 4.2).

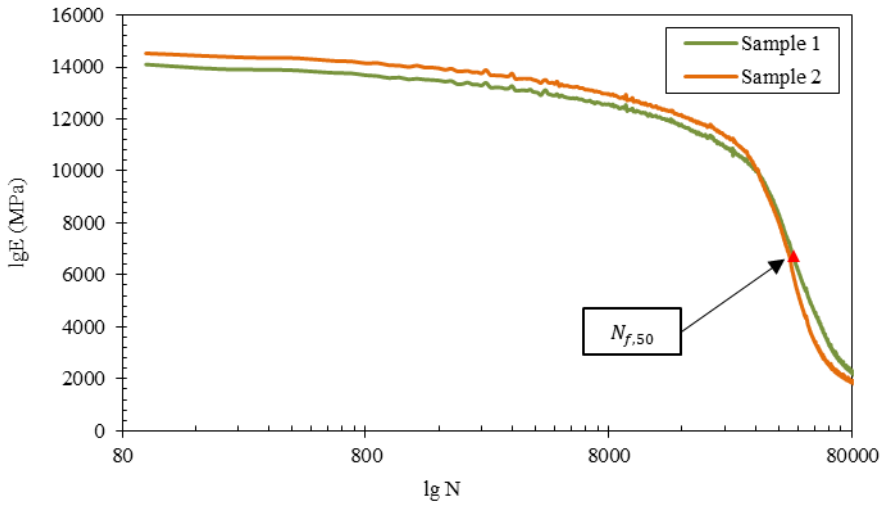


Figure 4.2: lgE versus lgN (10 °C, 150 με).

The basis of the ER and RDEC approaches is to calculate the dissipated energy cycle per unit volume (W), shown in Eq. 4-1 [29]. It is known that an asphalt mixture is a viscoelastic material, therefore its stress-strain curve under repeated loading is non-linear. The loading and unloading paths do not overlap, instead they form loops, known as hysteresis loops [175]. The area of the hysteresis loop is defined as the dissipated energy [177].

$$W = \pi\sigma\varepsilon \sin\varphi, \tag{4-1}$$

where σ is the stress level in each cycle; ε is the strain level in each cycle and φ is the phase angle in each cycle.

4.3.2 Energy Ratio (ER) Approach

For asphalt mixtures under strain controlled loading mode, the dissipated energy evolution will follow three stages connected by two transitions [187], as shown in

Figure 4.3. The first stage is considered as a no damage or minimal damage region. The ER approach can be used to calculate the value of the first transition point (N_1). N_1, is defined as the point of crack initiation [174]. At this point the ER changes from a good linear relationship to a significantly noisier relationship, as shown in Figure 4.4. ER is the ratio between the initial dissipated energy (W_0) multiplied by the cycle number (n) and the dissipated energy in the n^{th} cycle (W_n), shown in Eq. 4-2 [180].

$$ER = \frac{nW_0}{W_n} = \frac{n(\pi\sigma_0\varepsilon_0 \sin\varphi_0)}{(\pi\sigma_n\varepsilon_n \sin\varphi_n)}, \quad (4\text{-}2)$$

*w*here σ_0, ε_0 and φ_0 are stress, strain and phase angle in the initial cycle and σ_n, ε_n and φ_n are stress, strain and phase angle in the nth cycle.

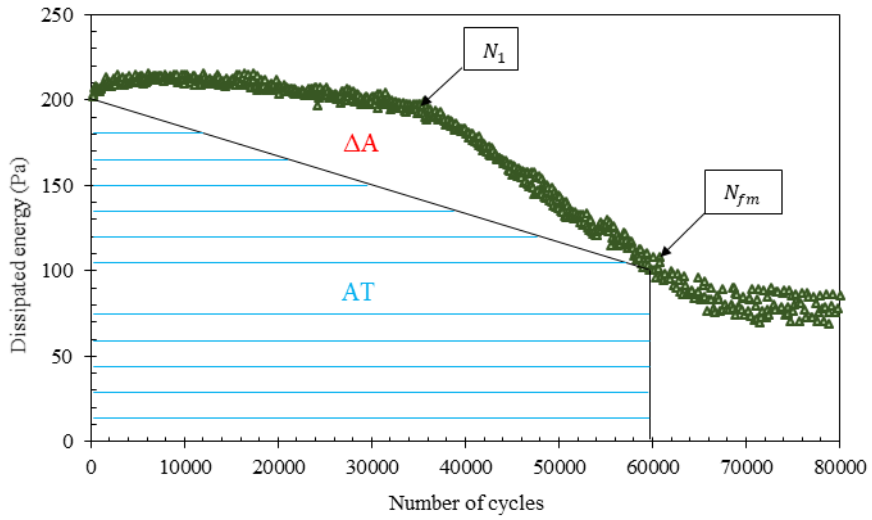


Figure 4.3 Dissipated energy versus number of load cycles (10 ℃, 150 με).

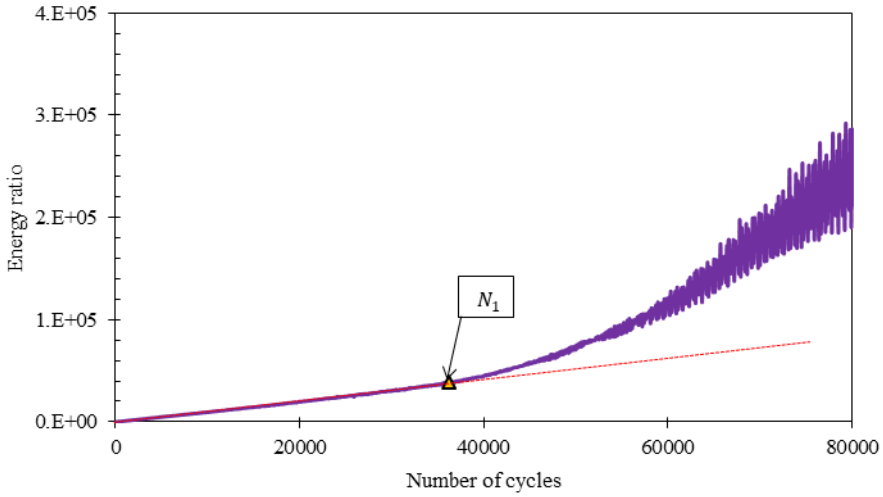


Figure 4.4: ER versus number of load cycles (10 ℃, 150 με).

4.3.3 Ratio of Dissipated Energy Change (RDEC) Approach

After the first transition point, the dissipated energy curve enters the second stage (the plateau stage) where the dissipated energy drops at a relatively constant rate, until the third stage where the dissipated energy curve has a significantly different slope (Figure 4.3). The transition point between the second and the third stage is related to macrocrack propagation [183]. Ghuzlan and Carpenter [183] used the RDEC approach

to define N_{fm} as macroscopic failure, according to Figure 4.5 and Eq. 4-3. The RDEC approach was refined by Shen and Carpenter [187] to calculate N_{fm}, the cycle number corresponding to the maximum ΔA (Equation 4-4 to 4-6).

$$\text{RDEC} = \frac{W_{n+1} - W_n}{W_n}, \tag{4-3}$$

where RDEC is the ratio of the dissipated energy change per load cycle, W_n is the dissipated energy produced in load cycle n and W_{n+1} is the dissipated energy produced in load cycle $n + 1$.

$$\Delta\text{A} = |AT - SDE|, \tag{4-4}$$

$$\text{SDE} = \sum_{0}^{n} DE, \tag{4-5}$$

$$AT = \frac{(DE_0 + DE_i) \times n}{2}, \tag{4-6}$$

where n is the cycle number, DE_0 is the initial dissipated energy and DE_i is the dissipated energy at cycle n. SDE is the area under the dissipated energy curve, AT is the trapezoidal area and ΔA is the difference between SDE and AT, as shown in Figure 4.3.

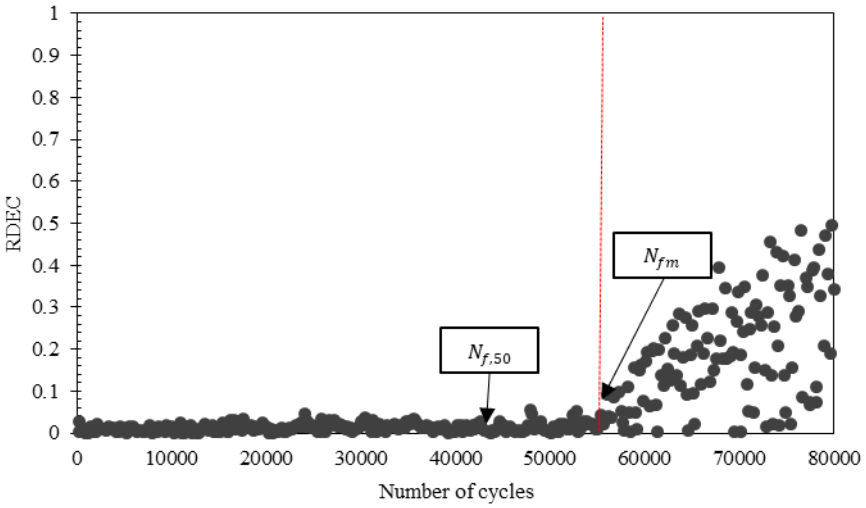


Figure 4.5: RDEC versus number of load cycles (10 ℃, 150 με).

4.4 Development of the stiffness Change Tendency Method (SCTM)

4.4.1 The SCTM Definition

A typical plot of the "S" shape stiffness reduction curve is shown in Figure 4.6. Four stages are defined by researchers based on three transition points (P1, P2 and P3), relating to different damage progression [34, 180, 188]. Prior to P1, the asphalt stiffness is high and decreases relatively stable from the initial stiffness. After P1, the reduction in stiffness rapidly increases until the second transition point P2, at P2 the rate of loss of stiffness is maximum. Then, the reduction in stiffness decreases and the stiffness approaches zero after P3. In regions III and IV, the road would probably already have failed. The SCTM is developed to model stiffness change and determine transition points.

Typical logistic curves and the base logistic equation are shown in Figure 4.7; two asymptotes 0 and 1 can be seen. Changing the value of μ shifts the function in the x direction; changing the value of γ impacts the gradient of the function [189]. It can be

seen that, the shape of the typical curves in Figure 4.7 are similar to the stiffness reduction curve in Figure 4.6. Therefore, the logistic model is used to determine the relationship between the log of the stiffness (E) and the log of the number of cycles (N) by transforming the base logistic equation to obtain Figure 4.7. The constants A, B and C are determined using regression methods in the SAS software. Two asymptotes A1 and A2 can be seen in Figure 4.8. A1 can be seen to represent the initial stiffness when the sample deformation is highly elastic. A2 represents the stiffness as the number of cycles tends to infinity and the sample fails. The second derivative of the logistic model represents the changing rate of the gradient of the function, therefore, and can be used to calculate the exact transition points P1, P2 and P3 [190, 191]. These are represented by the maximum, minimum and equilibrium of the second derivative of Eq. 4-7 (“lgE’’), as shown in Figure 4.8.

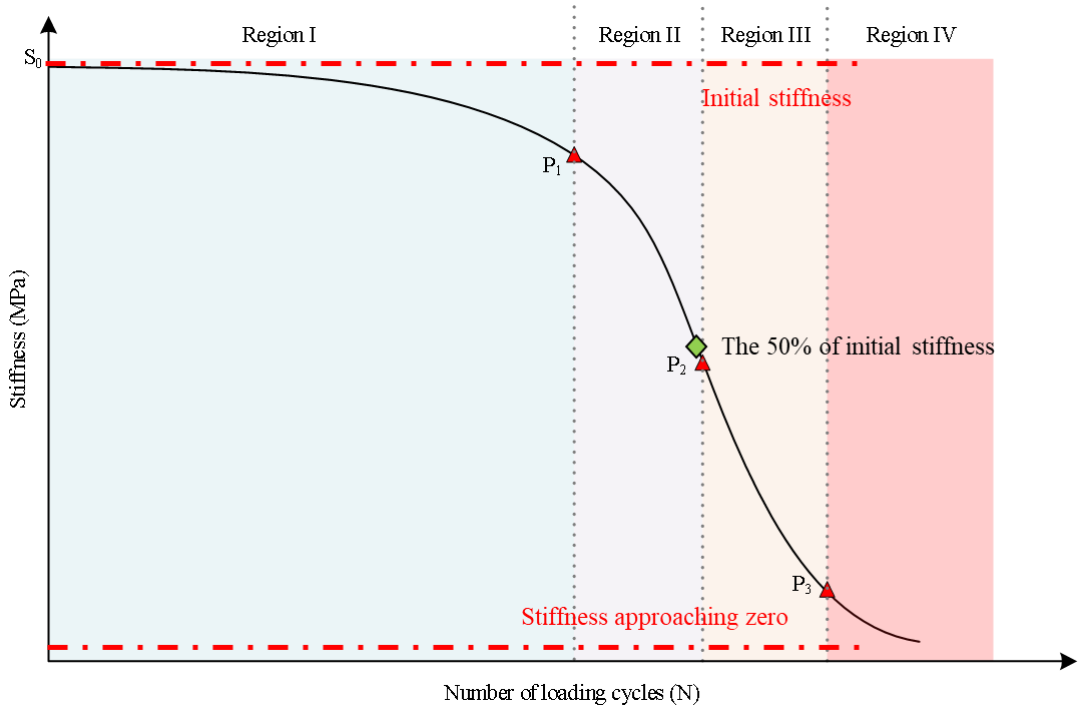


Figure 4.6: Four regions of a stiffness reduction curve, based on three transition points.

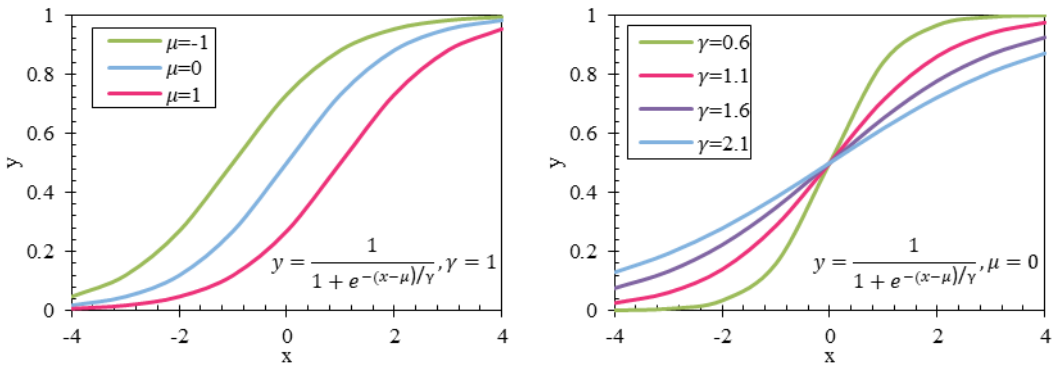


Figure 4.7: Typical curves of the logistic regression.

$$lgE = \mathrm{A} - \frac{(lgN)^B}{C^B + (lgN)^B}, \tag{4-7}$$

where E is the stiffness (MPa), N is the number of cycles, A, B and C are constants.

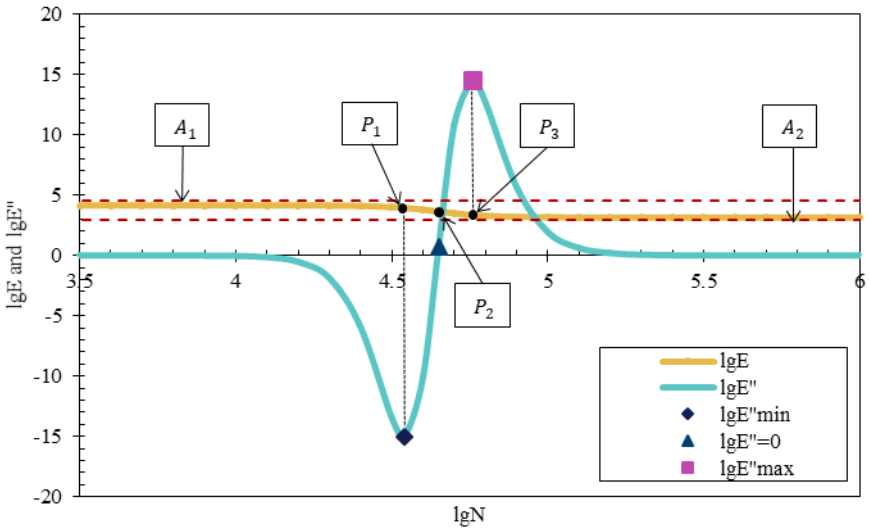


Figure 4.8: Fitting logistic equation and it's the second derivative.

4.4.2 The SCTM Analysis

Samples were subjected to four repeated tests per test condition; with the results being averaged. Based on the data points (shown in blue in Figure 4.9 and Figure 4.10) obtained from the tests, a logistical model of the form in Eq. 4-7 is fitted to the data with the constants A, B and C being determined using SAS software. The constants determined using the SAS software are shown in Table 4.2 alongside their R^2 values. The R^2 values show that in all cases there is good agreement between the laboratory data and the fitted logistic model, confirming that the logistic model it is a suitable model to model the stiffness reduction curve. Visual comparison of Figure 4.9 and Figure 4.10 shows the equation does not quite match at the beginning of some curves. The initial drop in stiffness at the beginning of the stiffness reduction curves, which may be partly due to temperature increase, are not considered by the equation. The derivatives of the logistic model are shown in Table 4.3 alongside the stiffness Ratio ($SR = E/S_0$). This illustrates that the stiffness ratio at the three transition points is similar across all samples. P1 occurs between 48% and 68% of the initial stiffness (S_0).

The stiffness ratio at P2 ranges between 22% and 35% of S_0, and at P3 ranges between 12% and 17% of S_0.

Based on the fitted logistic model, three transition points (P1, P2 & P3 in Figure 4.9 and Figure 4.10) associated with fatigue progression were determined to characterise the different fatigue damage stages. The stiffness reduction in region I (prior to P1) is observed to be slow. The stiffness drops sharply during region II (between P1 and P2), after region II the rate of loss of stiffness decreases until P3.

The values of the stiffness and corresponding number of cycles at each failure point is affected by factors such as temperature, ageing and moisture damage. Seen from Table 4.3 (sample sets 1-4), under the same strain level, at the higher the temperature, the later the failure point occurs. E_{p1}, E_{p2} and E_{p3} happen at 52%, 22% and 12% of S_0 at 20 ℃, respectively, while at 0 ℃, they happen at 68%, 31% and 17% of S_0, respectively. Similarly, seen from Figure 4.9 (a) and (b), the higher the temperature, the greater the corresponding number of cycles at the failure point. N_{p1}, N_{p2} and N_{p3} at 20 ℃ are 55000, 72500 and 93400, while at 0 ℃, these are 22400, 41100 and 72500, respectively. Figure 4.9 (c) and (d) show that fatigue performance deteriorates after ageing and moisture damage compared to undamaged condition. Moisture damage has a greater impact on fatigue performance with aged samples experiencing 35500 cycles while moisture damage samples experienced 19100 cycles at 15% initial stiffness. However, the value of P1 for the moisture damaged samples occurs at a lower stiffness value compared to the aged samples.

The fitting results are presented in Figure 4.10 alongside the data obtained for the 4PB tests. As with the 2PB, a good likeness is observed and the R^2 values of all fitted models are close to unity, demonstrating that the SCTM is applicable to be used to model

stiffness development of different asphalt mixtures and different test methods. The 4PB fatigue tests of the three bituminous mixtures in Figure 4.10 were stopped at 20% of the initial stiffness of the samples, however, the value of N_{P3} can still be calculated using the SCTM. In future study, the SCTM is able to predict fatigue failure points and remaining fatigue life as long as part of the fatigue test data is known, removing the need for time intensive laboratory testing. The results of more temperatures, strains and conditions are shown in Appendix A.

Table 4.2 Fitting results for the Logistic model.

Sample set	Logistic model constants			R^2
	A	B	C	
1	4.32	23.55	4.63	0.94
2	4.23	46.4	4.27	0.88
3	4.15	57.57	4.65	0.86
4	3.77	56.10	4.86	0.82
5	4.10	37.96	4.77	0.91
6	4.00	57.41	4.33	0.80
7	4.18	27.74	4.36	0.88
8	4.18	35.00	4.74	0.91
9	4.17	24.28	4.07	0.86
10	4.40	13.95	4.29	0.84
11	4.24	22.67	4.09	0.91
12	3.92	44.30	4.76	0.80
13	4.06	39.91	4.15	0.86
14	4.20	22.31	4.74	0.88
15	4.24	27.67	4.33	0.87
16	4.20	22.29	4.03	0.88

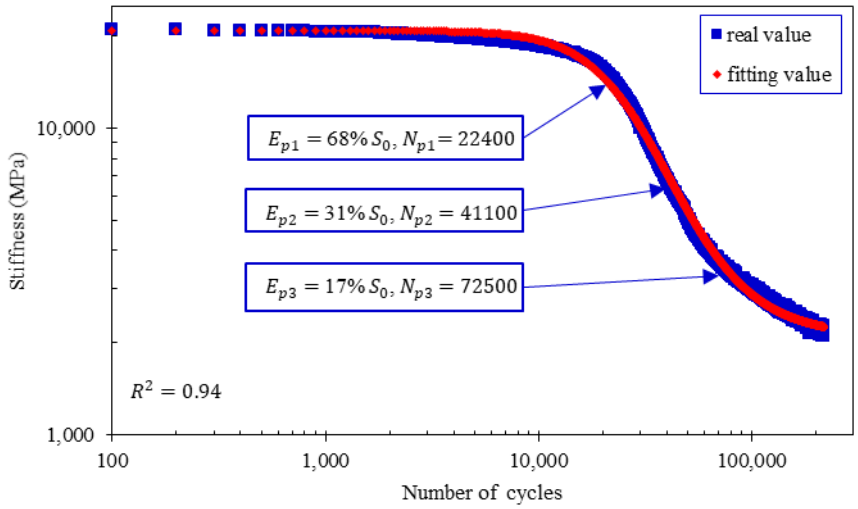
17	4.33	19.78	4.14	0.90
18	4.28	32.37	4.06	0.91
19	3.89	31.38	4.70	0.85
20	4.06	19.10	3.90	0.88
21	4.11	16.42	3.85	0.87
22	4.08	22.00	3.93	0.89

Table 4.3 Results of second derivative function and the corresponding stiffness ratio (SR).

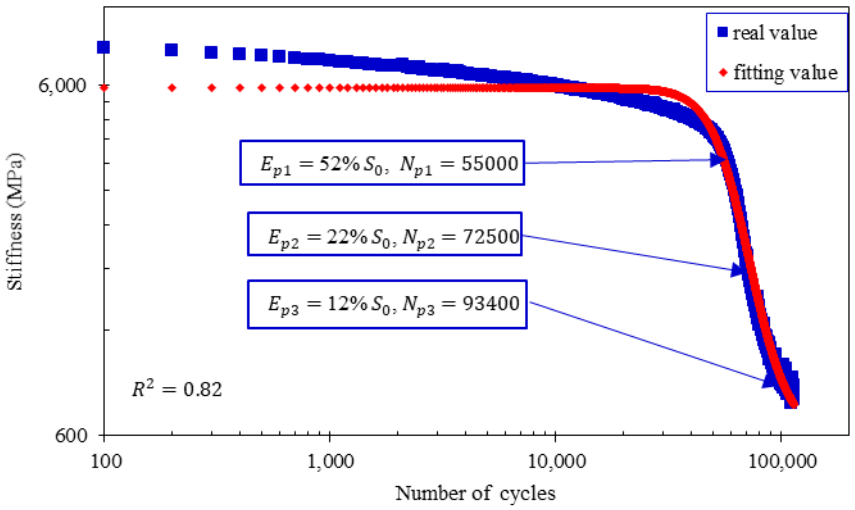
Sample set	lgE''_{min}	$lgE''=0$	lgE''_{max}	E_{p1} (MPa)	E_{p2} (MPa)	E_{p3} (MPa)	S_0 (MPa)	SR $_{p1}$	SR $_{p2}$	SR $_{p3}$
1	4.35	4.61	4.86	14447	6632	3686	21099	68%	31%	17%
2	4.15	4.27	4.38	11189	5015	2825	18868	59%	27%	15%
3	4.54	4.65	4.76	9367	4225	2215	17105	55%	25%	13%
4	4.74	4.86	4.97	3965	1700	935	7633	52%	22%	12%
5	4.60	4.76	4.93	8340	4333	2039	14102	59%	31%	15%
6	4.23	4.33	4.43	6512	3608	1646	13667	48%	26%	12%
7	4.00	4.14	4.28	10900	4395	2592	17126	55%	26%	14%
8	4.56	4.73	4.91	10405	4594	2505	16109	65%	29%	16%
9	3.83	4.05	4.28	10824	4463	2476	16212	67%	28%	15%
10	3.85	4.25	4.65	17821	7485	4288	25301	70%	30%	17%
11	3.85	4.05	4.30	11183	6213	3109	19252	58%	32%	16%
12	4.60	4.75	4.90	5368	2026	1199	10911	49%	19%	11%
13	4.15	4.35	4.55	7727	3654	1933	13931	64%	26%	15%
14	4.45	4.70	5.00	11588	5475	2929	15859	73%	35%	18%
15	4.10	4.30	4.50	11898	6059	2952	18560	64%	33%	16%
16	3.75	4.00	4.25	11772	5828	2788	16272	72%	36%	17%
17	3.85	4.10	4.40	15537	7269	2670	21281	735	34%	17%
18	3.90	4.05	4.20	12643	5773	3325	20385	62%	28%	16%

19	4.50	4.70	4.90	4960	2540	1284	9479	52%	27%	14%
20	3.59	3.87	4.15	7623	4327	1986	12234	62%	35%	16%
21	3.52	3.83	4.14	8018	4169	2202	13343	60%	31%	17%
22	3.68	3.91	4.15	8196	4287	2063	12649	65%	34%	16%

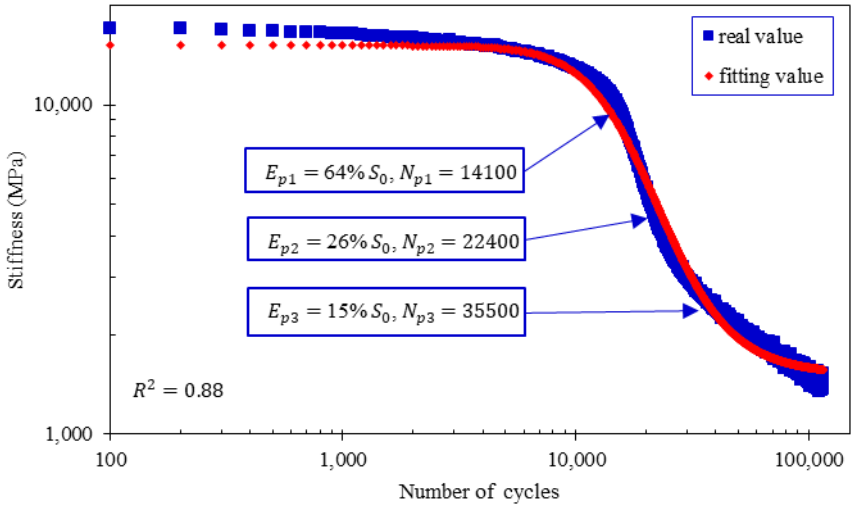
(a)



(b)



(c)



(d)

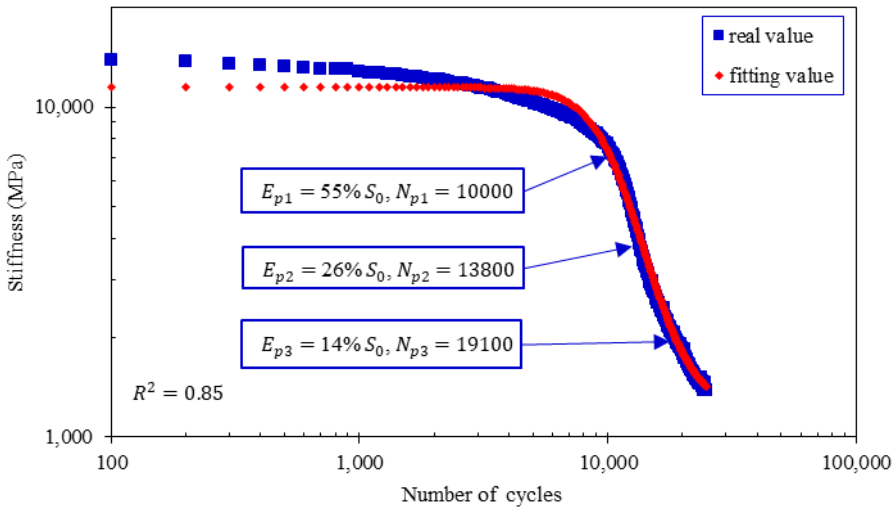
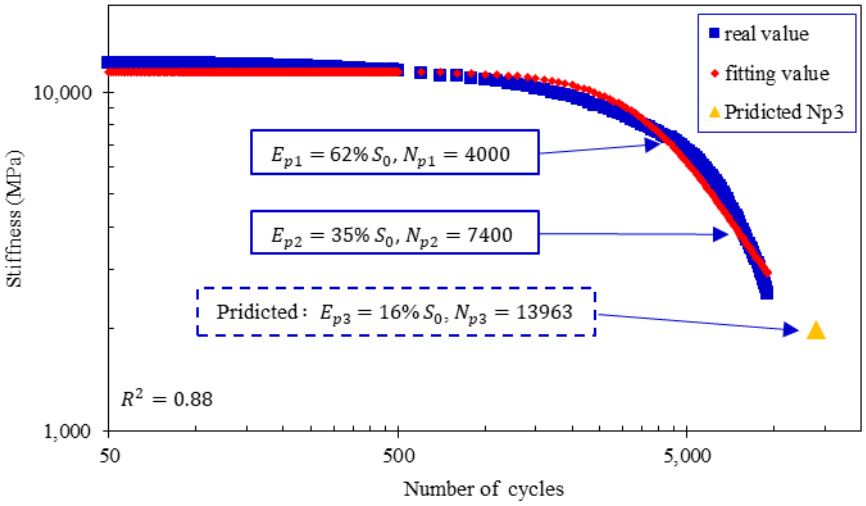
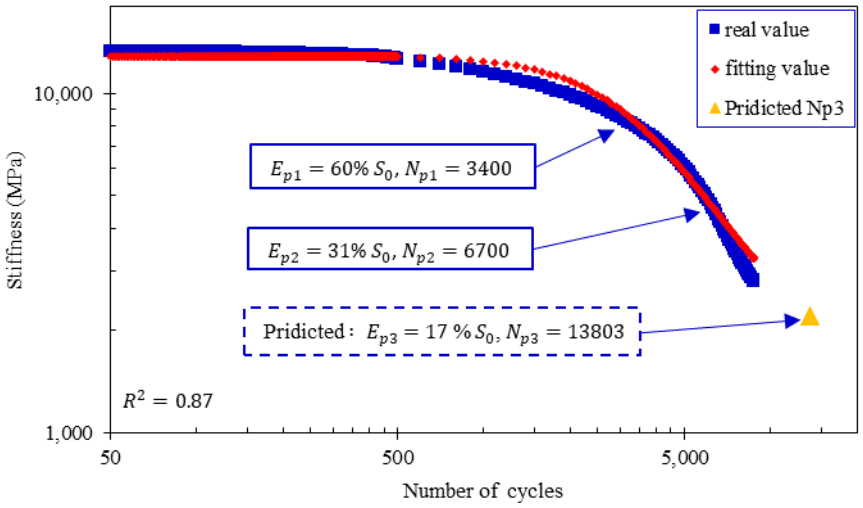


Figure 4.9: Fitting results under different temperatures, strains and conditions of 2PB tests: (a) 0 ℃ and 200 με; (b) 20 ℃ and 200 με; (c) 10 ℃ and 200 με aged; (d) 10 ℃ and 200 με moisture damaged.

(a)


real value
fitting value
Pridicted Np3
$E_{p1} = 62\% S_0, N_{p1} = 4000$
$E_{p2} = 35\% S_0, N_{p2} = 7400$
Pridicted: $E_{p3} = 16\% S_0, N_{p3} = 13963$
$R^2 = 0.88$
10,000
1,000
50
500
5,000
Stiffness (MPa)
Number of cycles

(b)


real value
fitting value
Pridicted Np3
$E_{p1} = 60\% S_0, N_{p1} = 3400$
$E_{p2} = 31\% S_0, N_{p2} = 6700$
Pridicted: $E_{p3} = 17\% S_0, N_{p3} = 13803$
$R^2 = 0.87$
10,000
1,000
50
500
5,000
Stiffness (MPa)
Number of cycles

(c)

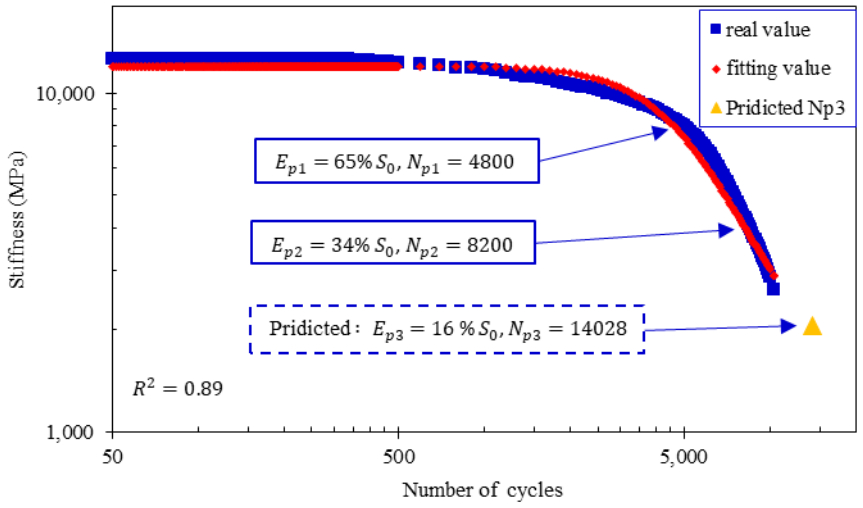
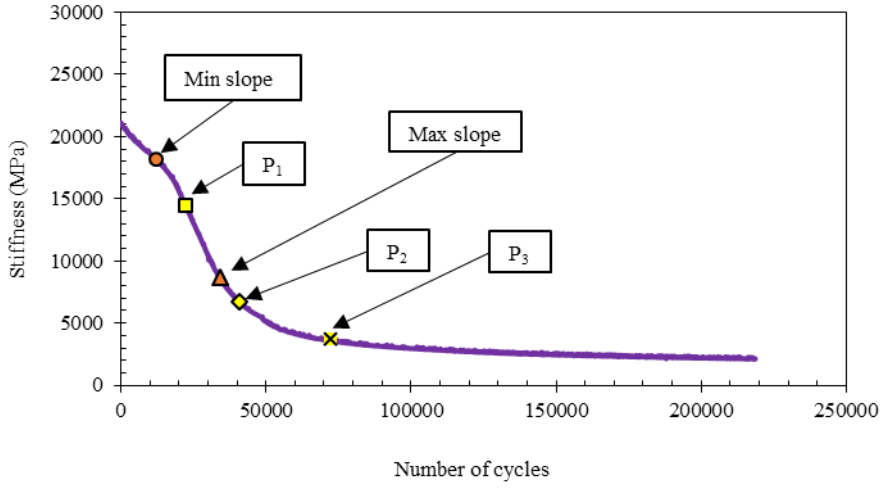

real value
fitting value
Pridicted Np3
$E_{p1} = 65\% S_0, N_{p1} = 4800$
$E_{p2} = 34\% S_0, N_{p2} = 8200$
Pridicted: $E_{p3} = 16\% S_0, N_{p3} = 14028$
$R^2 = 0.89$
10,000
1,000
50
500
5,000
Stiffness (MPa)
Number of cycles

Figure 4.10: Fitting results of different asphalt mixtures at 10 ℃ under 270 με of 4PB tests (a) DBM-14+Pen40/60; (b) DBM-10+ CRMB; (c) SMA-10+Pen40/60.

(a)



(b)

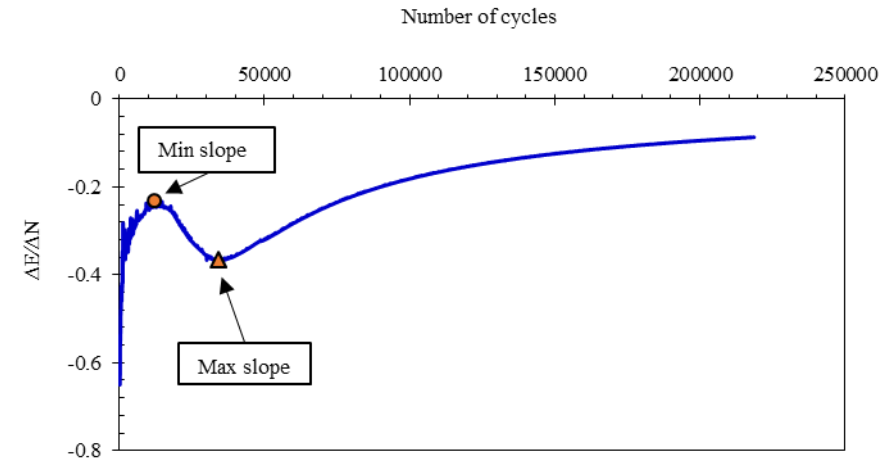


Figure 4.11: A comparison example at 0 ℃ and 200 με: (a) stiffness versus number of cycles and (b) calculation of curvature = ΔE/ΔN.

Calculation of curvature = ΔE/ΔN at 0 ℃ and 200 με is used to compare with the results calculated based on the logistic model. There are two points show in Figure 4.11b, the

first point is ΔE/ΔN decrease to the minimum then increase, and the second is ΔE/ΔN increase to maximum then decrease again. The positions of two points can be found in Figure 4.11a, together with three transition points calculated based on the logistic model. The first two transition points calculated based on the logistic model are larger than the two points calculated from ΔE/ΔN, for the reason that curve of ΔE/ΔN calculates the maximum and minimum of the slope without considering the rate of change of the slope. When calculating the rate of change of the slope with discrete data, there might appear no extreme points. Therefore, this thesis applied the logical model to fit the discrete data to ensure that three transition points can be calculated.

Unlike the traditional 50% initial stiffness, the transition point happens variably in the stiffness reduction curve, therefore, it is necessary to evaluate the fatigue performance with regard to the unit stiffness loss. The quotient of the number of cycles and the stiffness loss, $\Omega = \frac{N}{(S_0 - E)}$, of represented sample sets (set 1-7, set 13 and set 20-22), was calculated to determine the number of cycles per unit stiffness loss. In other words, Ω expresses how easily stiffness is lost and can be used to evaluate fatigue performance; the more cycles required for a unit stiffness loss, the better the fatigue performance. As shown in the Figure 4.12, for most sample sets, Ωp2 is the smallest, which indicates that stiffness loss is greater at P2, the stiffness reduction curve also shows that the stiffness decreases quickest near P2. Generally, Ω decreased as the temperature increased and the strain decreased. For 2PB tests, fatigue performance under 200 με at 20 ℃ is the best as Ω is the largest, whereas fatigue performance after moisture damage is the worst and has the smallest Ω value. Ω value of 4PB tests are smaller than that of 2PB tests, fatigue performance of SMA-10+Pen40/60 is the best as Ω is the largest.

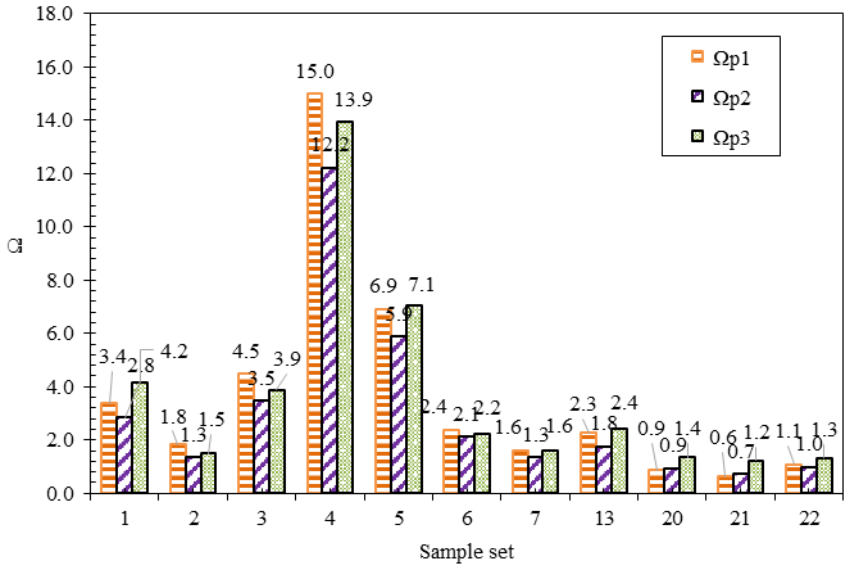


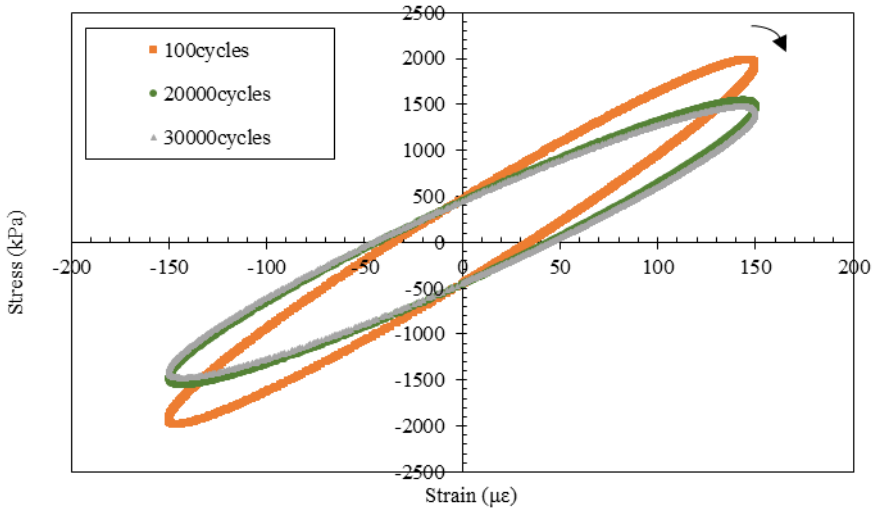
Figure 4.12: Number of cycles per unit stiffness loss, Ω, at P1, P2 and P3.

4.5 Validation of the SCTM

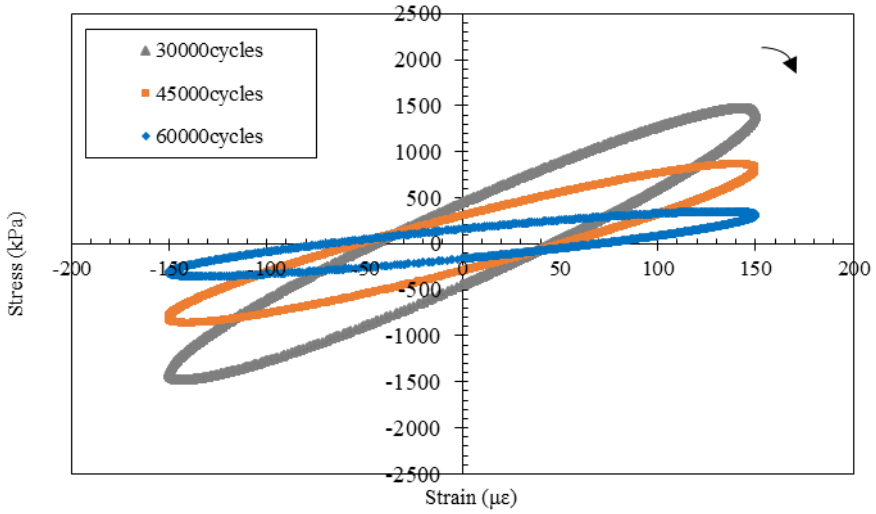
4.5.1 Dissipated Energy Approach

Hysteresis loops were calculated to explore the energy change law for different numbers of cycles in a strain-controlled mode. The damage accumulates and the dissipated energy decreases as the number of loading cycles is increased. The first stage is the no damage or minimal damage region, during which the material's stress-strain hysteresis loop remains similar and there is no apparent change in dissipated energy as seen in Figure 4.13a. In the second stage, the dissipated energy steadily decreases, which is reflected in the clockwise movement and decrease in area of the stress-strain hysteresis loop (Figure 4.13b). Most fatigue failure criteria are defined at this stage as it is where macro damage happens. In the third stage, the change in dissipated energy (the stress-strain hysteresis loop) once again becomes minimal; however, the area of the stress-strain hysteresis loop is decreased significantly compared to stage 1 (Figure 4.13c).

(a)


100cycles
20000cycles
30000cycles
Stress (kPa)
Strain (με)
2500
2000
1500
1000
500
0
-500
-1000
-1500
-2000
-2500
-200
-150
-100
-50
0
50
100
150
200

(b)


30000cycles
45000cycles
60000cycles
Stress (kPa)
Strain (με)
2500
2000
1500
1000
500
0
-500
-1000
-1500
-2000
-2500
-200
-150
-100
-50
0
50
100
150
200

(c)

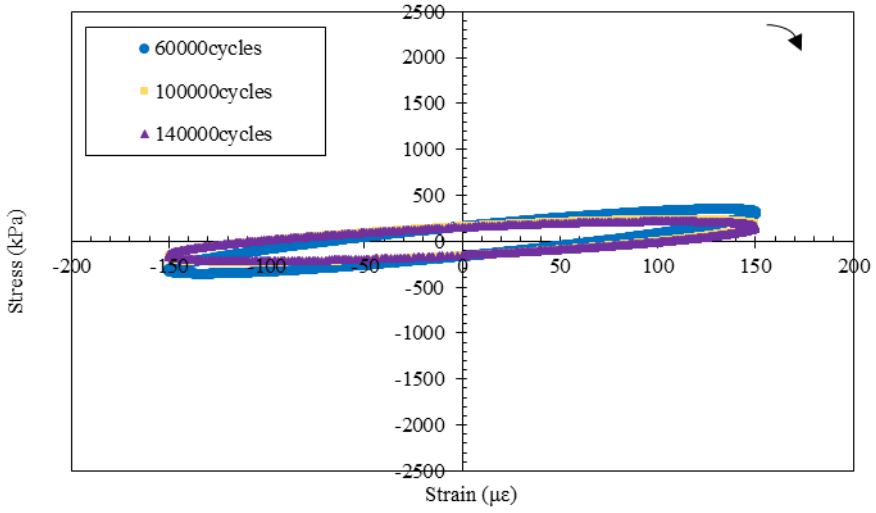

60000cycles
100000cycles
140000cycles
Stress (kPa)
Strain (με)
2500
2000
1500
1000
500
0
-500
-1000
-1500
-2000
-2500
-200
-150
-100
-50
0
50
100
150
200

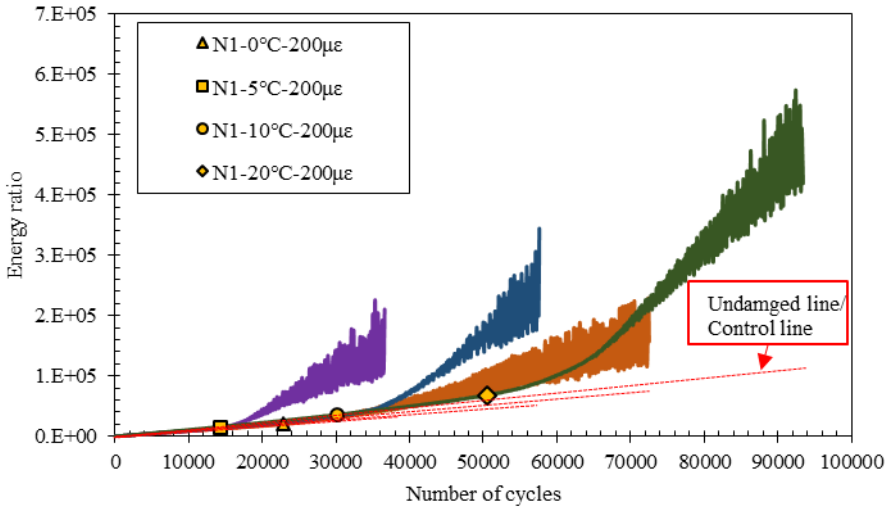
Figure 4.13: Stress-strain hysteresis loops change (10 ℃, 150 με) for controlled strain 2PB test: (a) first stage; (b) second stage and (c) third stage.

4.5.2 ER Approach

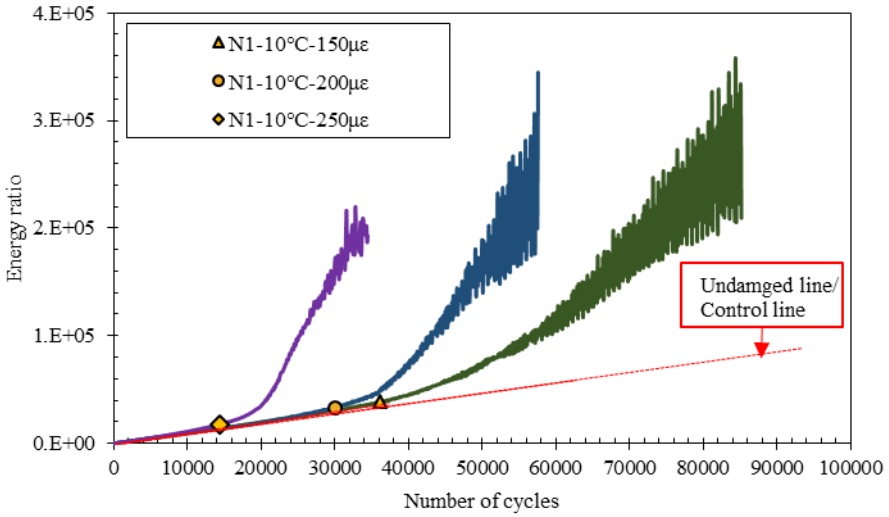
Seen in the plot of ER versus number of cycles in the strain-controlled mode (Figure 4.14), the ER is initially a straight line with a rapid increase after a given number of cycles. N_1 is the inflection point where the ER curve deviates from the linear section (undamaged line in (Figure 4.14)). The value of N_1 is affected by factors including temperature, strain, ageing and moisture damage. It can be seen from Figure 4.14a-c that N_1 generally increases as the temperature increases and decreases with strain increase. Fatigue damage is caused by a combination of various factors, and this combined effect is more complicated at low temperatures. The possible reason that N_1 is smaller at 5 ℃ than that at 0 ℃ is under low strain, changes in stiffness affect the strain. Similar results can be found in a literature study that under 1200 με, the difference between the fatigue life of different mixtures at 0 ℃ and 20 ℃ is greater than that under 300 με. In particular, under 300 με, the fatigue life of two mixtures is better at 0 ℃ than 20 ℃ [192]. More experiments are needed for validation to find the worst-case temperature.

Ageing and moisture damage cause different reduction rates of N_1, but the impact of moisture damage is more significant. Figure 4.14d shows ER versus number of load cycles for controlled strain 4PB test of different mixtures. The N_1 of SMA-10+ Pen40/60 is the largest whereas the N_1 of DBM-10+ CRMB is the smallest, showing that the value of N_1 is also affected by the asphalt binder type and mixture type. N_1 calculated under all conditions gave a similar undamaged control line thereby confirming that the control line of *ER* vs *N* curves is independent of all the factors investigated.

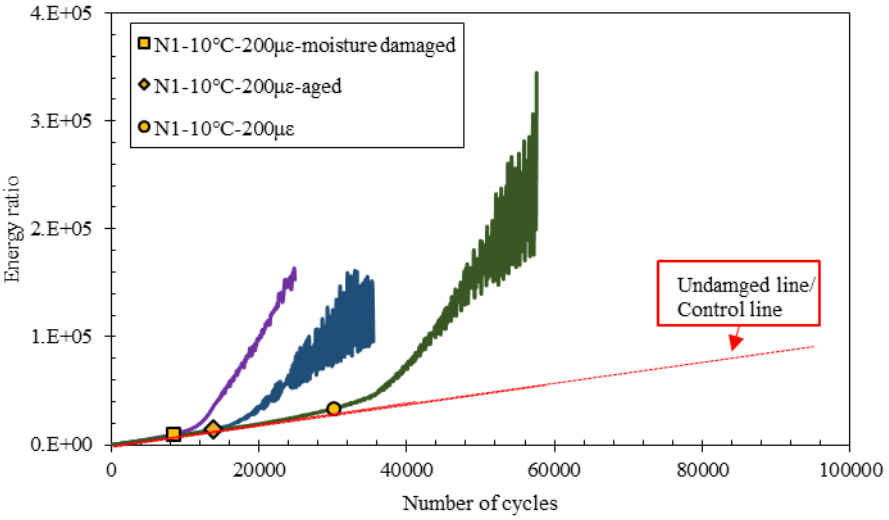
(a)


N1-0°C-200με
N1-5°C-200με
N1-10°C-200με
N1-20°C-200με
Energy ratio
Number of cycles
Undamged line/
Control line

(b)


N1-10°C-150με
N1-10°C-200με
N1-10°C-250με
Energy ratio
Number of cycles
Undamged line/
Control line

(c)


N1-10°C-200με-moisture damaged
N1-10°C-200με-aged
N1-10°C-200με
Energy ratio
Number of cycles
Undamged line/
Control line

(d)

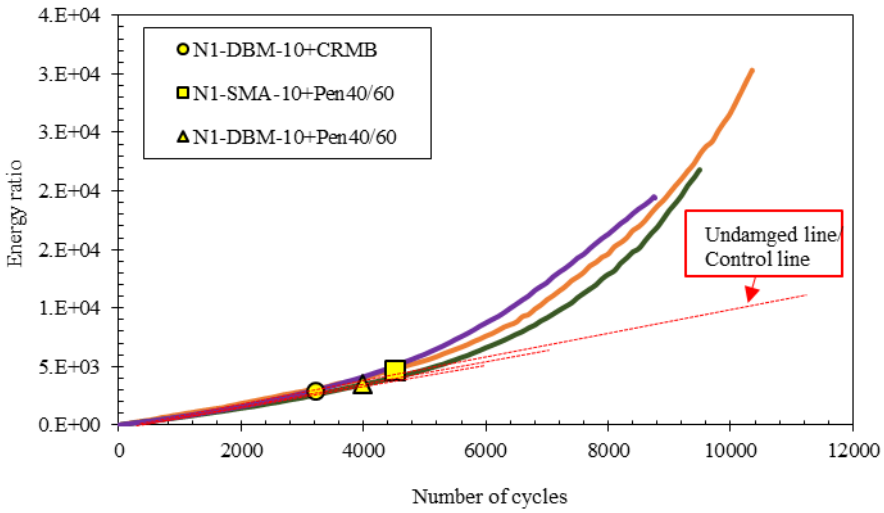
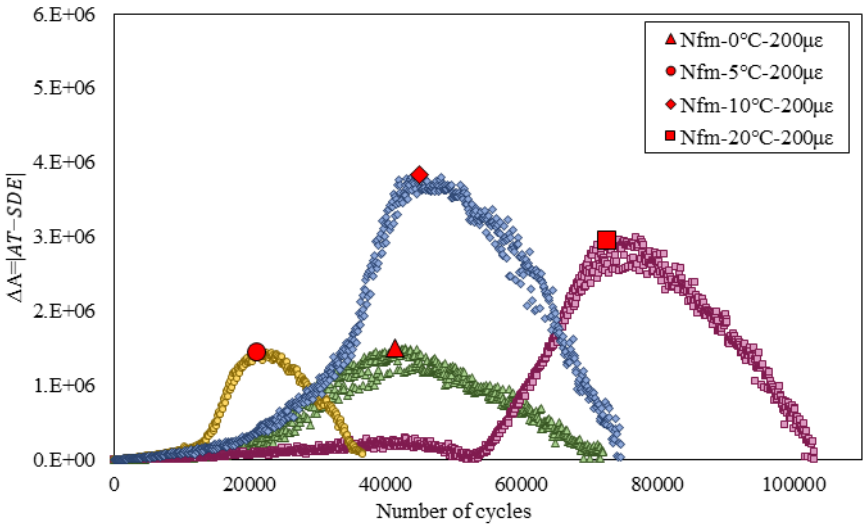


Figure 4.14: Energy ratio versus number of load cycles for controlled strain 2PB test: (a) at different temperatures; (b) under different strains; (c) under different conditions; and for 4PB test: (d) of different mixtures.

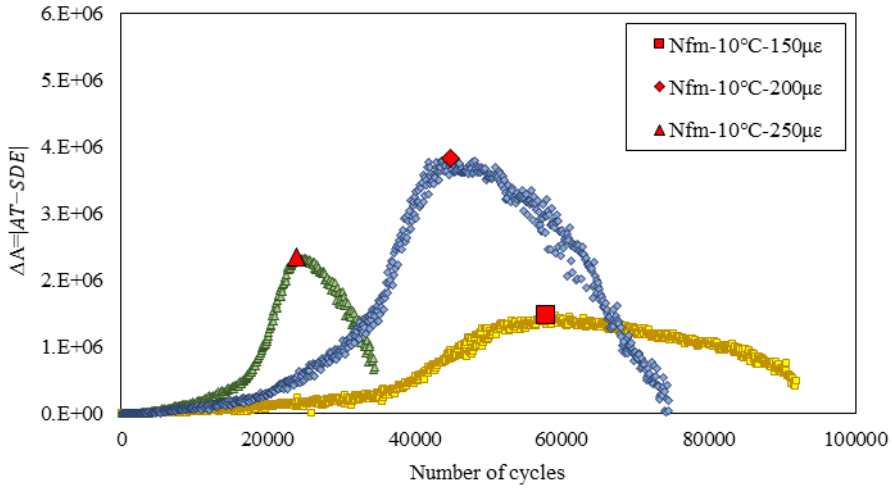
4.5.3 RDEC Approach

The results of the second transition point (N_{fm}) are shown in Figure 4.15. Under strain-controlled loading mode, the area ΔA is initially very small but increases with loading cycles. There is a point where the area ΔA is maximised and this point corresponds to N_{fm}, where macroscopic failure occurs, after which the area ΔA decreases. The value of N_{fm} is also affected by the factors in the same way as N_1, it generally increases as the temperature increases and decreases with strain increase. Ageing and moisture damage also cause a decrease in N_{fm}, where the impact of moisture damage is more significant. The value of N_{fm} is also affected by the asphalt binder type and mixture type. Unlike N_1, the dissipated energy decline rate at N_{fm} is maximum. At this point cracks are propagating rapidly, which is considered to be the true point of failure.

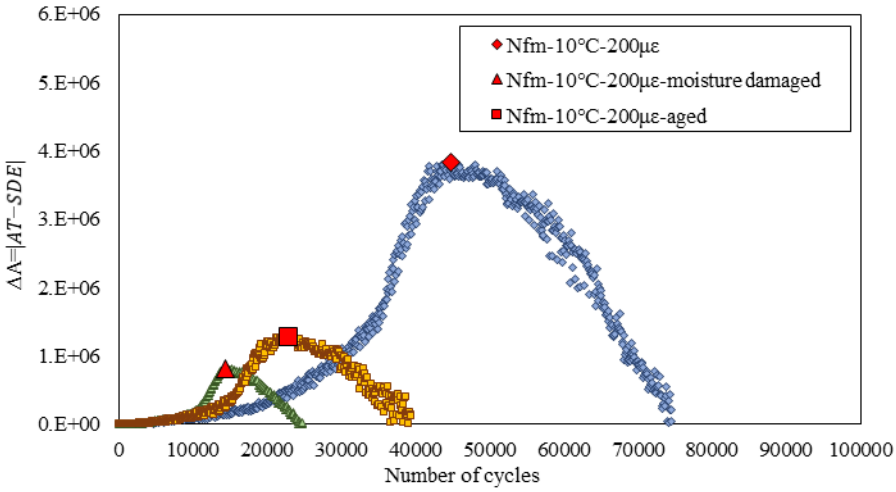
(a)


Nfm-0°C-200με
Nfm-5°C-200με
Nfm-10°C-200με
Nfm-20°C-200με
ΔA=|AT−SDE|
Number of cycles

(b)


Nfm-10°C-150με
Nfm-10°C-200με
Nfm-10°C-250με
ΔA=|AT−SDE|
Number of cycles

(c)


Nfm-10°C-200με
Nfm-10°C-200με-moisture damaged
Nfm-10°C-200με-aged
ΔA=|AT−SDE|
Number of cycles

(d)

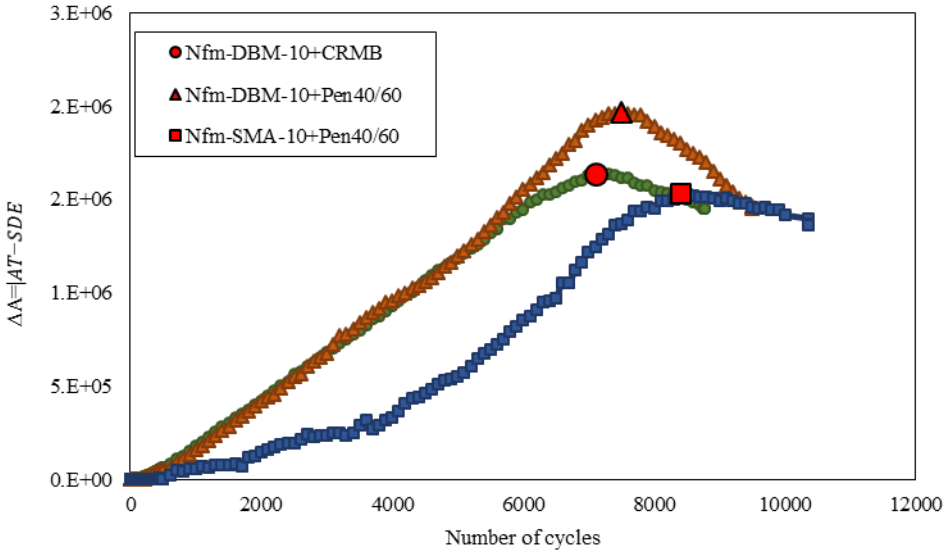


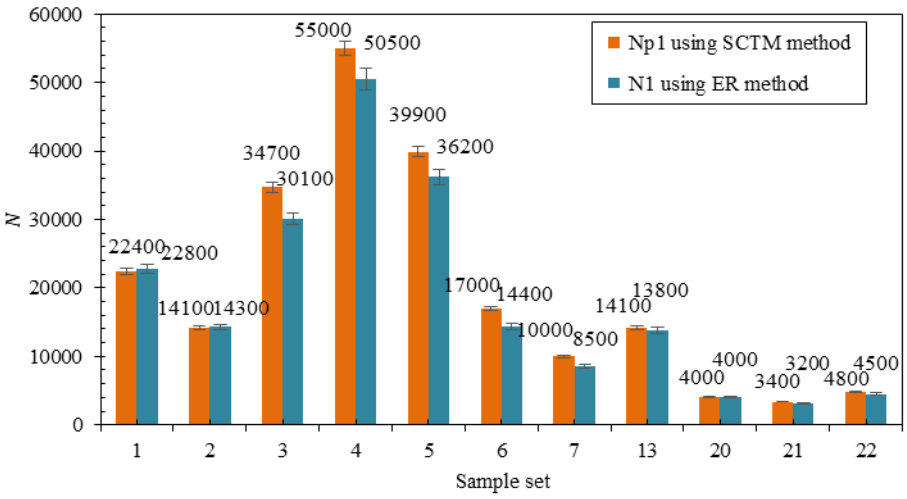
Figure 4.15: ΔA versus number of cycles for controlled strain 2PB test: (a) At different temperatures, (b) Under different strains; (c) Under different conditions and for 4PB test: (d) of different mixtures.

4.5.4 Comparison between Fatigue Failure Criteria obtained from the SCTM and the Energy-based methods

This research compares the number of loading cycles at P1 and P2 in the SCTM with the values of N_1 and N_{fm} obtained from the two different energy-based methods (the ER method and the RDEC method). The results obtained from the two different energy-based methods and SCTM are shown in Figure 4.16. The figure shows that differences between P1 and the micro cracking point are generally greater than those between P2 and the macro-crack generation point. For different conditions, including aged and moisture damaged, different test methods, different test temperatures and strains, and different types of mixtures, the results calculated by the SCTM are similar to those calculated by the energy-based methods. The one-way analysis of variance (ANOVA) has been applied to show the difference between the proposed method and the two energy methods. The results indicate that there are no statistically significant differences between the SCTM and the two energy methods, as determined by one-way

ANOVA ($F < F_{crit}$, P-value > 0.05 for all sample sets), confirming that the SCTM is indeed appropriate to model stiffness loss and be used as a means to calculate the fatigue failure criteria. P1 can be viewed as the number of cycles to micro-crack initiation and propagation. The region prior to P1 is the micro-crack formation region. P2 can be defined as the macro-crack generation point; the true failure point is at P2.

(a)



(b)

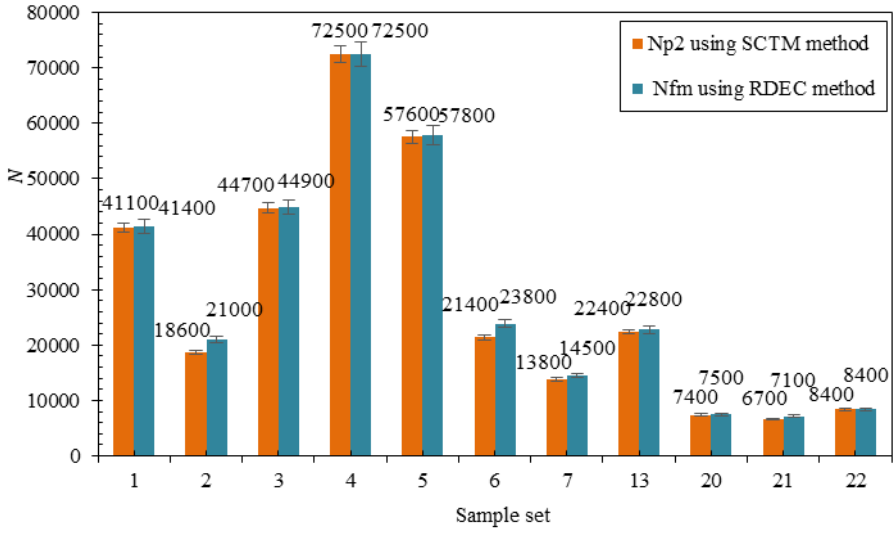


Figure 4.16: Comparison of fatigue failure criteria gained from different methods: (a) N_{p1} and N_1; and (b) N_{p1} and N_{fm}.

4.6 Factors Affecting the Fatigue Failure Criteria obtained by the SCTM

The fatigue performance of asphalt mixtures is affected by many factors. The internal factors include asphalt type, asphalt content, aggregate gradation, aggregate type, modifier type, filler type and air voids, etc. Asphalt binder is generally divided into four components: aromatic, saturated, resin and asphaltene. Different components have different molecular chain structures, which makes the internal structure of asphalt binder different, therefore affecting the performance of asphalt.

Apart from the effects of the asphalt material itself, the external factors, like loading mode, loading frequency, temperature and rest periods, etc., have a more direct impact on the fatigue performance of asphalt mixtures. This project will mainly study the external factors affecting fatigue life, including various stain levels, temperatures, ageing and moisture. The fatigue life is calculated by the STCM based on three transition points on stiffness reduction curves. The fatigue lives at the three transition points correspond to the fatigue lives when cracks initiate, propagate and break through respectively.

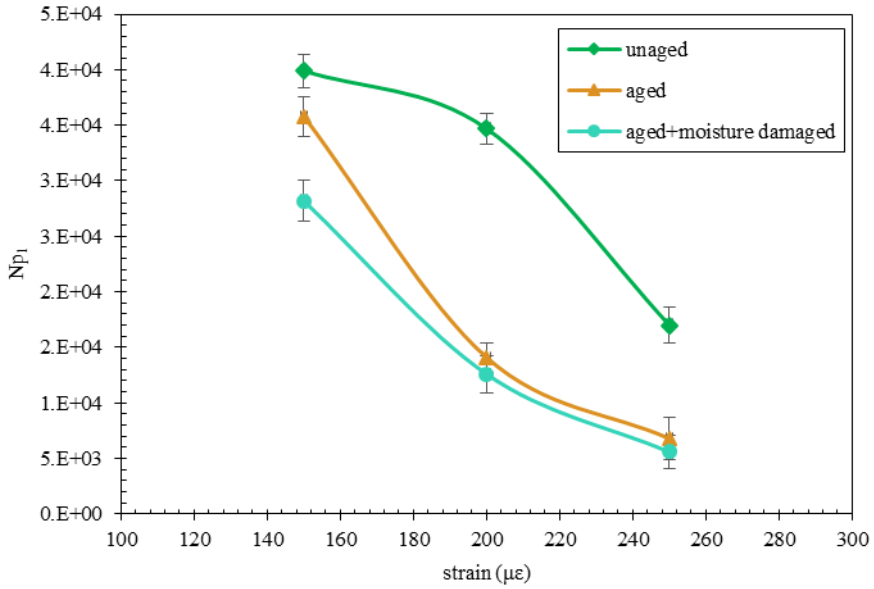
4.6.1 Strain Level

The study of fatigue life of asphalt mixtures under different strain/stress levels is important to find influences of various traffic scenarios on the service life of asphalt pavement. Unaged, aged and aged + moisture damaged specimens were tested by 2PB tests at three different strain levels (150, 200 and 250 με) at a temperature of 10 °C at a frequency of 15 Hz. The results of the fatigue life (N_{p1}, N_{p2} and N_{p3}) of unaged, aged and aged + moisture damaged specimens at different strain levels are shown in Figure

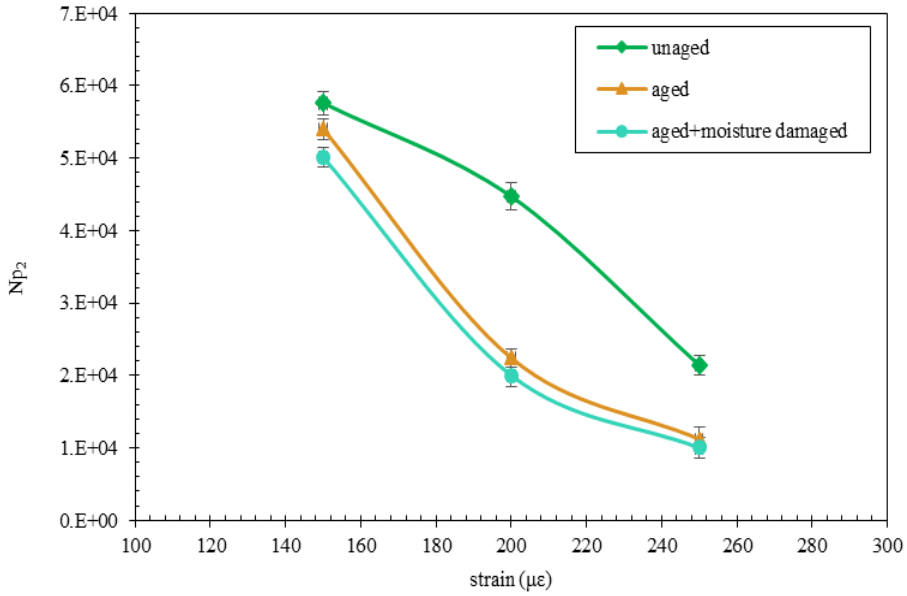
4.17. The results show that with the increase of strain, N_{p1}, N_{p2} and N_{p3} of unaged, aged and aged + moisture damaged specimens decrease continuously but with different decrease rates.

For unaged specimens, the decrease rate of N_{p1} and N_{p2} increases first, then drops, while N_{p3} decreases linear. For aged and aged + moisture damaged specimens, the decrease rate of fatigue life decreases first, then increases. It is concluded that the influence of increasing strain on the unaged specimens is greater than that on the aged and aged + moisture damaged specimens.

(a)



(b)



(c)

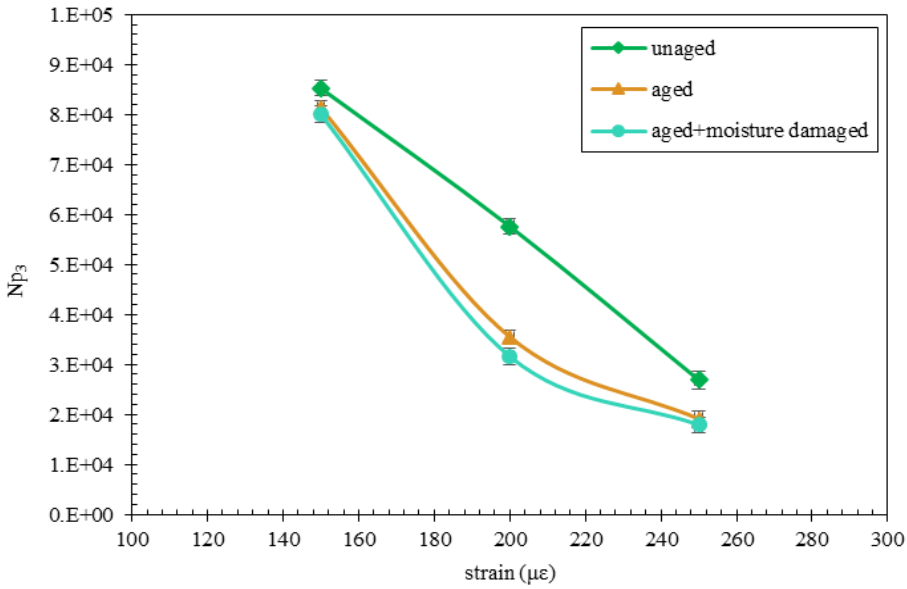


Figure 4.17: Results of (a) Np1, (b) Np2 and (c) Np3 of unaged, aged and aged + moisture damaged specimens at different strain levels.

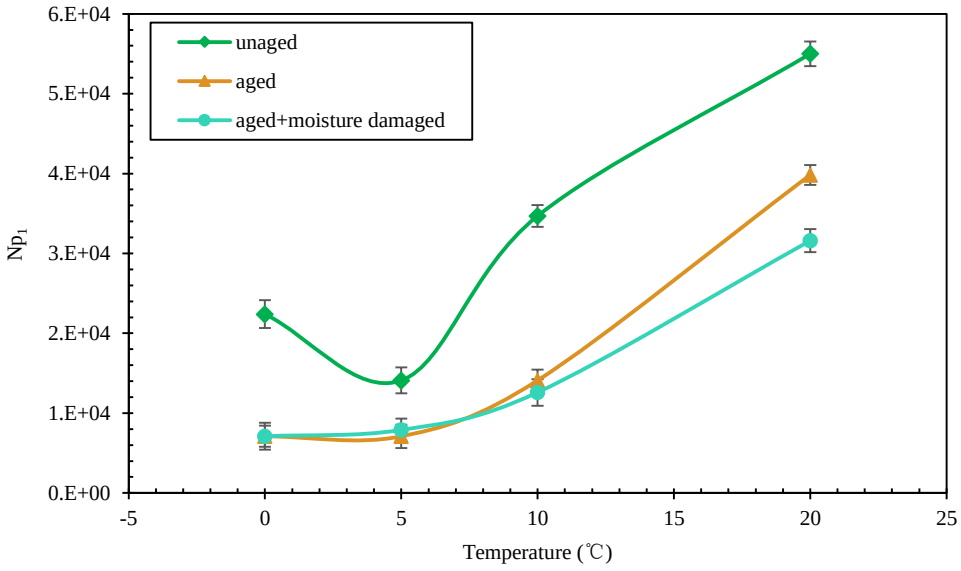
4.6.2 Temperature

The fatigue behaviour of asphalt mixtures in their unaged, aged and moisture damaged conditions was revealed using 2PB tests under a controlled strain level of 200 με at different temperatures 0, 5, 10 and 20 ℃ at a frequency of 15 Hz. The results of the

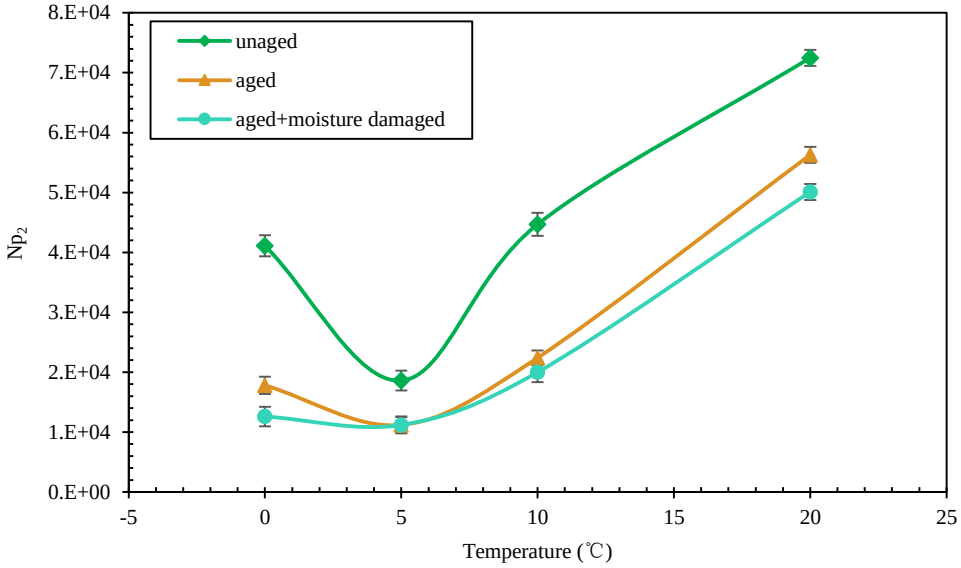
fatigue life (N_{p1}, N_{p2} and N_{p3}) of unaged, aged and moisture damaged specimens at different temperatures are shown in Figure 4.18.

It can be seen that with the increase of temperature, N_{p1}, N_{p2} and N_{p3} of unaged, aged and aged + moisture damaged specimens decrease at first and then increase continuously. Generally, the increase of temperature can improve the fatigue resistance of asphalt mixtures, as asphalt mixtures become brittle and easier to crack at low temperature. Figure 4.19 shows the initial stiffness of unaged, aged and aged + moisture damaged specimens at different temperatures. The aged specimens have highest initial stiffness, however, fatigue life is not the shortest. It implies that there is a worst-case temperature for fatigue life of asphalt pavements since changes in stiffness affect the strain. The worst-case temperature is not exactly at 5 ℃ where the minimum is shown in the figures and more experiments are needed for validation.

(a)



(b)



(c)

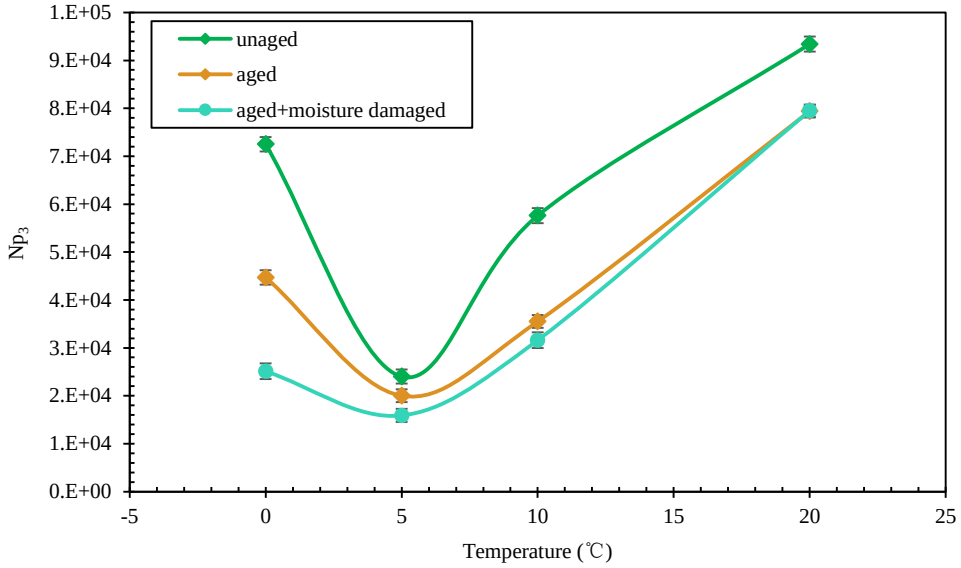


Figure 4.18: The results of (a) Np1, (b) Np2 and (c) Np3 of unaged, aged and aged + moisture damaged specimens at different temperatures.

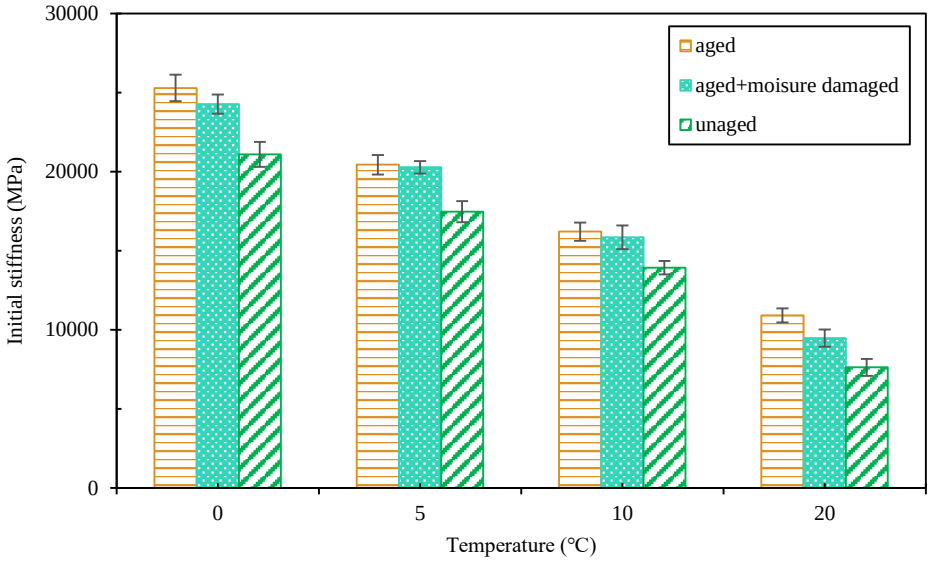


Figure 4.19: Initial stiffness of unaged, aged and aged + moisture damaged specimen at different temperatures.

4.6.3 Ageing and Moisture

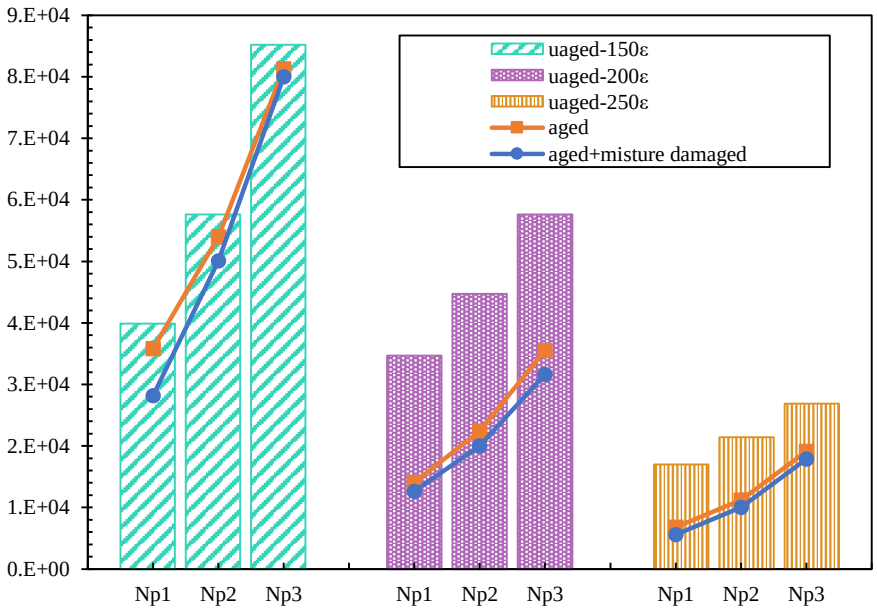
In Figure 4.20a, the fatigue life of both aged and aged + moisture damaged specimens at different strain levels decrease significantly compared to unaged specimens; and the decrease of aged + moisture damage specimens is slightly larger. It can also be seen that the effect of ageing and moisture damage is less obvious at the strain of 150 με compared to higher strain levels (200 and 250 με).

Figure 4.20b shows that the fatigue life of both aged and aged + moisture damaged specimens at different temperatures decrease significantly; as above, the fatigue life of aged + moisture damage specimens drop slightly quicker.

The relationship between the fatigue life of aged, aged + moisture damaged specimens (Nf aged, Nf aged + moisture damaged) and the fatigue life of unaged (Nf unaged)

specimens was calculated, aiming to obtain ageing and moisture modified indexes compared to the unaged condition. Figure 4.21 shows a good linear relationship between Nf aged, Nf aged + moisture damaged and Nf unaged. Therefore, when the Nf unaged of samples is obtained in the laboratory, the fatigue life after ageing and moisture damage can be calculated using aging and moisture modified indexes, which time-consuming ageing and moisture damage tests. More different mixture types are worth taking into consideration in future for better fitting the index.

(a)



(b)

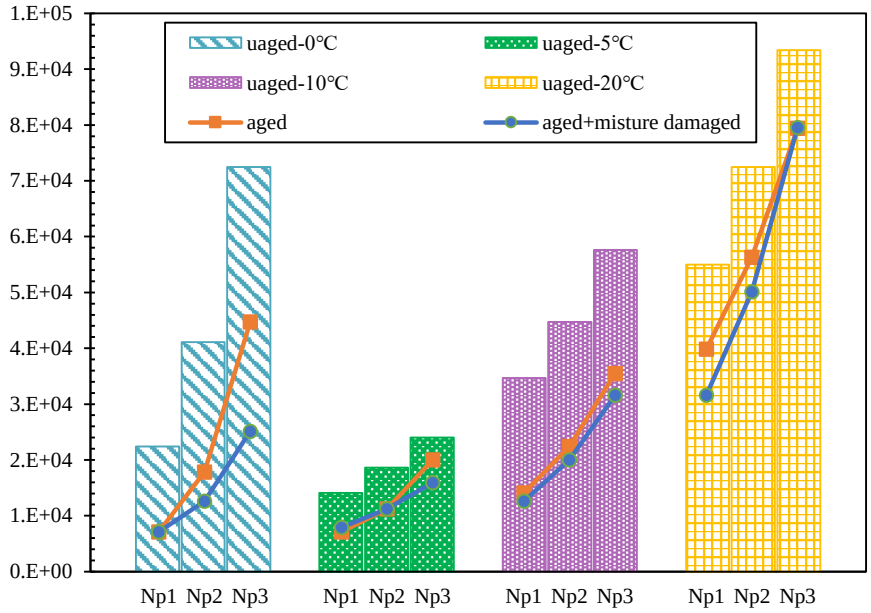


Figure 4.20: The change of Np1, Np2 and Np3 of unaged, aged and moisture damaged specimens (a) at different strain levels and (b) at different temperatures.

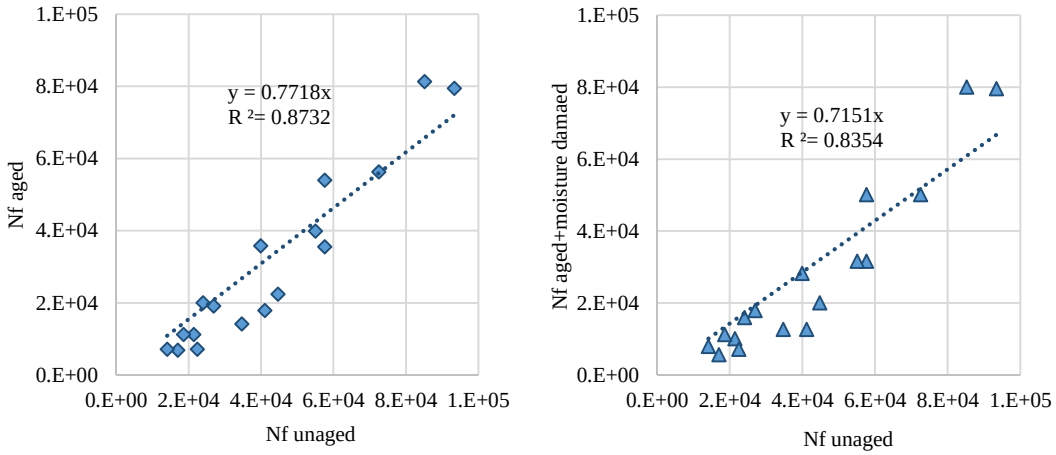


Figure 4.21: Ageing and moisture modified indexes.

4.6.4 Relating the Stiffness Development to Crack Development

Relationships between crack development observed through the digital camera, and the number of cycles obtained by WTTs are shown in Figure 4.22a. It is found that the

crack length increases slowly with the growth of the number of cycles at first, and then the growth rate increases rapidly for a short while. Although the growth rate increases here, the crack length is still relatively short. After this, the growth rate tends to be stable for a while, then the growth rate increases rapidly again until the specimen fractures. Take beam3# as an example, with different numbers of cycles, the details of crack development are shown in Figure 4.22b. It can be observed that cracks begin to generate at Point1# and develop at Point3#, which are the same as P1 and P2 defined in the SCTM.

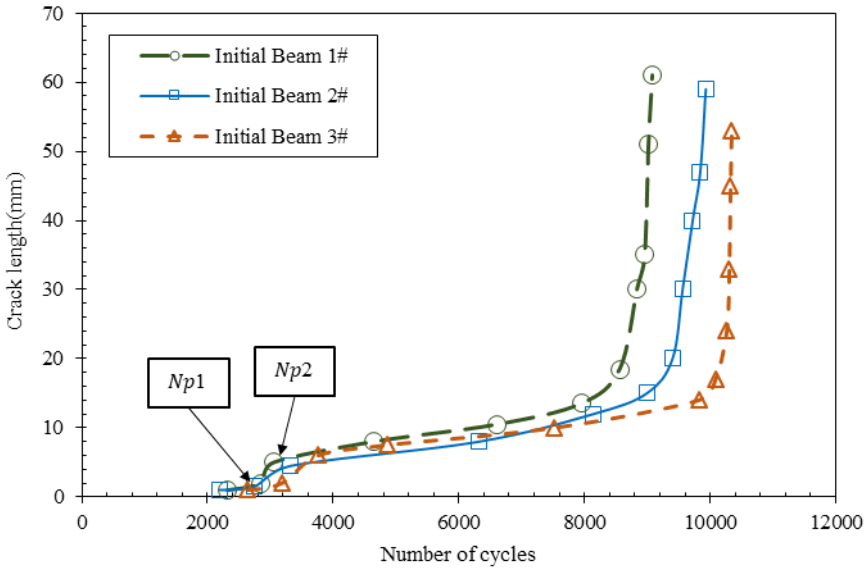
The 4PB initial stiffness test was used to measure the stiffness of beam samples by stopping WTTs at different numbers of cycles and testing corresponding stiffness, drawn as a plot of stiffness versus number of cycle shown in Figure 4.23, to prove whether the fatigue criteria calculated by the SCTM can be reflected in the Figure 4.22, and to further explain the relationship between stiffness development and crack development. The SCTM is used to model stiffness development, calculate the fatigue criteria, and compare the number of cycles at transition points with those where cracks initiate and propagate in Figure 4.22. The figure shows that SCTM is a good approximation to model stiffness development based on test data from 4PB tests and WTTs.

According to crack geometry at certain numbers of cycles obtained by the digital camera (Figure 4.23), the cracks of beams 1#, 2# and 3# occurred after P1 (calculated by STCM). The closer the point to P1, the shorter the crack development length, for example, the crack length observed from beam 3# is shorter than those observed from beam 1# and beam 2#. The cracks of beam 1#, 2# and 3# have propagated after P2 (calculated by STCM). The farther the point from P2, the longer the crack development length and the faster the development rate, for example, the crack lengths observed

from beam 1# and beam 2# are longer than that observed from beam 3#.

Taking beam3# as an example (Figure 4.23c and Figure 4.22b), the N_{P1} and N_{p2} calculated by the SCTM (2630 and 3801, respectively) are similar to the number of cycles at Point1# and Point3# observed through the digital camera (2640 and 3670, respectively). The N_{P1} and N_{P2} calculated by the SCTM are marked in Figure 4.22a. N_{P1} of all beams is close to the number of cycles where the crack length first starts to increase rapidly, and N_{P2} of all beams is close to the number of cycles where the crack length starts to increase steadily and continuously. Thus, the SCTM can be used to link the stiffness development to crack development, as well as calculate the number of cycles where the crack length starts to increase rapidly (cracks initiate) and where the crack length starts to increase steadily and continuously (cracks propagate). The P1 and P2 calculated by the SCTM are proved to be related to the crack initiation and propagation respectively, which was also proved by energy-based methods in Section 4.5.

(a)



(b)

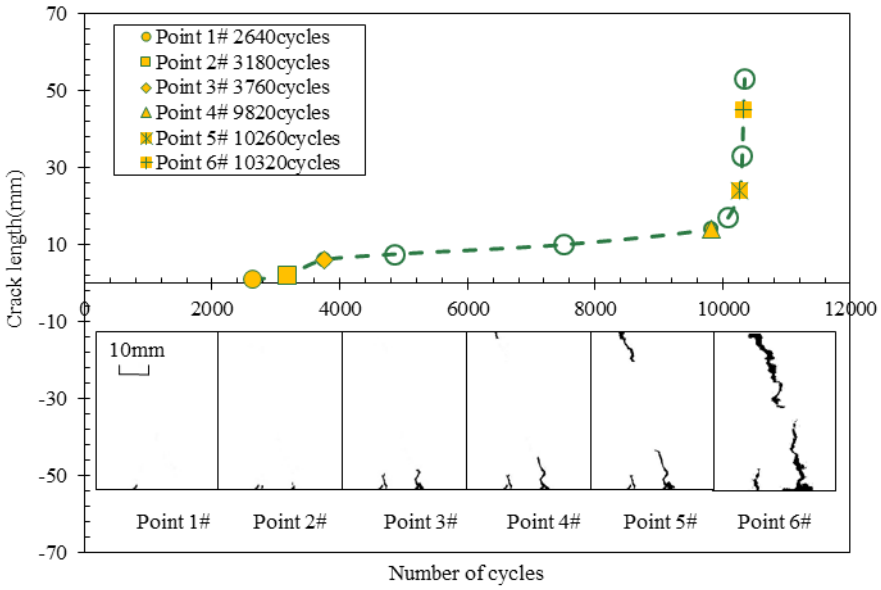
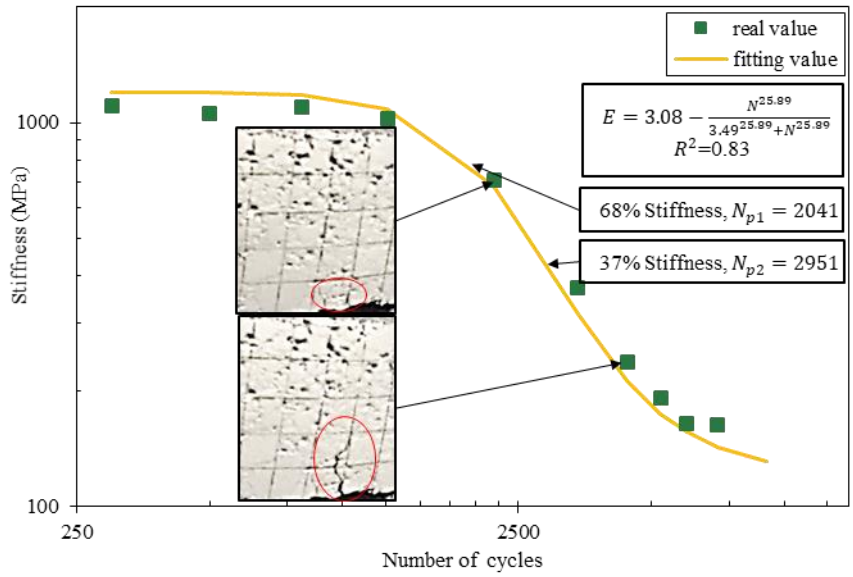
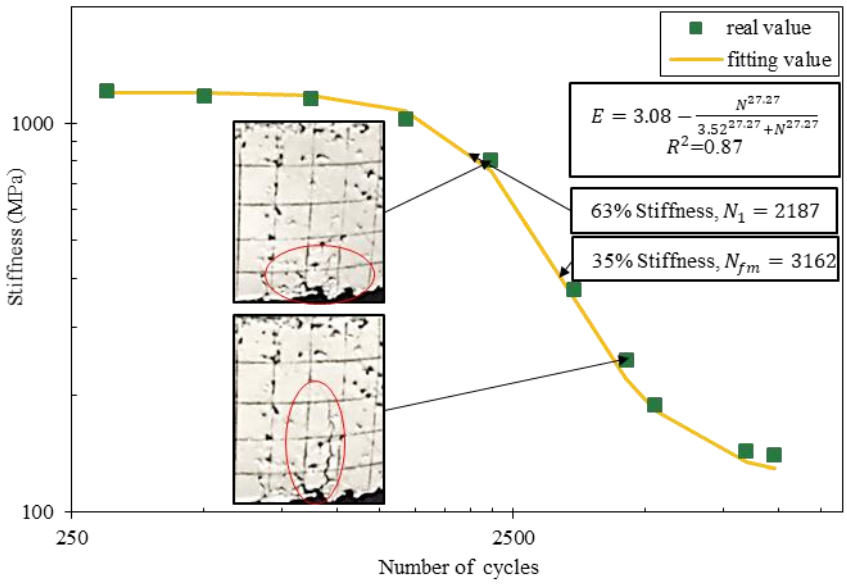


Figure 4.22: Fatigue crack development of (a) the beams; (b) at different stages of beam 3#.

(a)



(b)



(c)

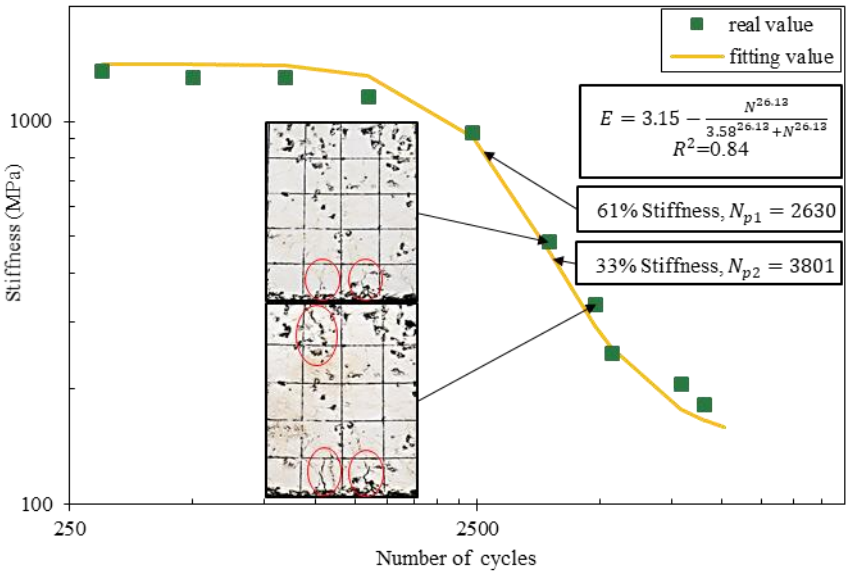


Figure 4.23: Relation between stiffness development and fatigue crack development of the (a) beam1#; (b) beam2# and (c) beam3#.

4.7 Conclusions

The main conclusions of this chapter are as follows:

1. There is good agreement between the stiffness (E) of asphalt concrete from tests

and that the logistic model proposed, confirming that the logistic model is feasible to characterise the relationship between E and the number of cycles (N).

2. The SCTM is developed to model stiffness evolution of asphalt concrete, and identify various fatigue damage stages by three transition points (P1, P2 and P3).

3. The SCTM illustrates that stiffness ratios at the three transition points are similar across all samples, confirming that no matter what the condition, fatigue failure happens at similar stiffness ratios.

4. The number of cycles at the fatigue failure points is affected by factors, such as temperature, strain level, ageing conditions, and the SCTM can be used to calculate the fatigue life after ageing and moisture damage using aging and moisture modified indexes.

5. The number of loading cycles at the transition points P1 and P2 (N_{p1} and N_{p2}) in the SCTM has a good match with the values of N_1 and N_{fm} obtained in the energy-based methods.

6. P1 can be viewed as the number of cycles to micro-crack initiation and propagation. The region prior to P1 is the micro-crack formation region. P2 can be defined as the macro-crack generation point.

7. It is feasible to use the SCTM to model stiffness development of different asphalt concretes and test methods. It can be applied to predict the fatigue transition points and remaining fatigue life of asphalt concrete.

8. The SCTM can be used to link the stiffness development to crack development, and calculate the number of cycles where the crack length starts to increase rapidly (cracks initiate) and where the crack length starts to increase steadily and

continuously (cracks propagate), it reveals the mechanism of fatigue crack of asphalt concrete basing on the mechanical parameter.

9. The SCTM combines the benefits of both the phenomenological approach and energy-based approach, it can characterise different fatigue damage stages, and allow all critical fatigue failure criteria to be determined using a single methodology.

5 Characterisation of Fatigue Damage in Asphalt Concrete in Micro Level

5.1 Introduction

The internal structure of asphalt concrete has been the focus of various research studies [193]. The anisotropy of the microstructure causes complex mechanical responses to variables such as temperature and loading, which in turn influences the performance of asphalt concrete [194]. Visualising the internal structure is critical in determining microstructural damage mechanisms and relating to the performance of asphalt concrete. Nonetheless, traditional laboratory and field tests generally do not allow visualisation of the internal structure of an asphalt mixture. Digital imaging techniques have been proposed as a solution to this issue and have been shown by a number of researchers [75, 195, 196] to be effective for evaluating the internal structure of asphalt concrete.

Over the last decade, there has been significant improvement in the capabilities of digital imaging techniques with technology development and advances in equipment availability [197]. Tomographic images obtained from X-ray computed tomography (CT) have been used to successfully research the microstructure of asphalt concrete [198]. The X-ray CT technique is able to visualise the damage evolution inside an asphalt mixture specimen as well as the internal structure of the materials in three-dimensions (3D) [199-201]. Further structural analysis including aggregate orientations and air voids content distribution can be used to segment asphalt concrete composition from tomographic images through digital image processing (DIP). This can be done using techniques such as contrast enhancement, noise reduction, gray intensity thresholding and binarization [73, 202].

Recent literature has had two main focuses; firstly, showing the significant role of air voids and aggregate properties on the mechanical behaviour of asphalt pavements [203-209] and secondly, in developing 2D and 3D microstructure numerical models [104, 109, 150-153]. However, few studies have applied X-ray CT for characterising fatigue damage [210, 211]. In one such study, damage was defined by Song using X-ray CT images which were scanned at 1mm intervals [212]. X-ray CT was also used by Khan and Collop [213] to quantify the damage induced during constant strain rate and fatigue tests. They concluded that the damage increased with increasing strain and there is a greater increase in damage (increased air voids content) for specimens tested at higher temperatures and lower strain rates. The disadvantage of X-ray CT is that it is difficult to obtain high resolution images with large asphalt mixture samples. Detailed microcrack evolution is often not visible in low resolution and low resolution also results in inaccurate data as the thresholding might be affected.

This chapter applies high-resolution X-ray CT (with resolution of 0.014 mm) to investigate the fatigue damage evolution of asphalt concretes at the micro-level. To achieve this aim, samples (20 mm diameter and 18mm height) were specially designed to visualise detailed fatigue crack geometry. All samples were tested using the Indirect Tensile Fatigue Test (ITFT) at 5 ℃ under a repeated controlled stress pulse applied at a rate of 40 pulses per minute at a load of 0.8 kN, and were set to stop at given vertical deformations of 0.4, 0.6, 0.8, 0.9, 1.1 and 1.4 mm. The detailed X-ray CT images in the centre of the samples were used to characterise the fatigue cracking and air voids increase at different vertical deformations. By analysing air void content and surface area distributions before and after loading, it is possible to investigate damage evolution in different directions at different vertical deformations. The X-ray CT images of samples, where the maximum change of air voids content occurs were used to investigate effects of the aggregate size and the distance between aggregates on fatigue

damage.

5.2 Programme

Preparation of the special designed sample can be seen in Chapter 3. Three trial samples were tested; results (Table 5.1) show that three sample failed when the vertical deformations were approximately 2mm, and the number of cycles at failure were similar, proving that the special size sample is also suitable for ITFTs. Before ITFTs, specimens were placed in the environmental chamber and conditioned at 5 ℃ for 4 hours. After the test, in order to avoid changes (i.e. crack healing) before CT scanning, all the specimens were stored at -5 ℃. CT scans were then performed on specimens.

The scheme for the testing programme is shown in Figure 5.1. 2D image slices generated by X-ray CT were firstly used for the calculation of air voids content and air voids surface area, with the images processed by DIP. 2D image slices were also applied to reconstruct a 3D model to calculate volume and surface parameters, with the 3D model adjusted threshold values by DIP. The curves of vertical deformations versus number of cycles, were compared to fatigue cracking geometry at different vertical deformations. Details of image analysis methods, the applied coordinate axis, the image area for calculation, calculation equations for volume and surface area parameters, and fatigue damage evolution laws will be shown in the following sections.

Table 5.1 Results of the trial samples.

Sample ID	Damage deformation (mm)	Damage number of cycles (time)
1	1.98	19430
2	2.00	21512
3	2.04	23548

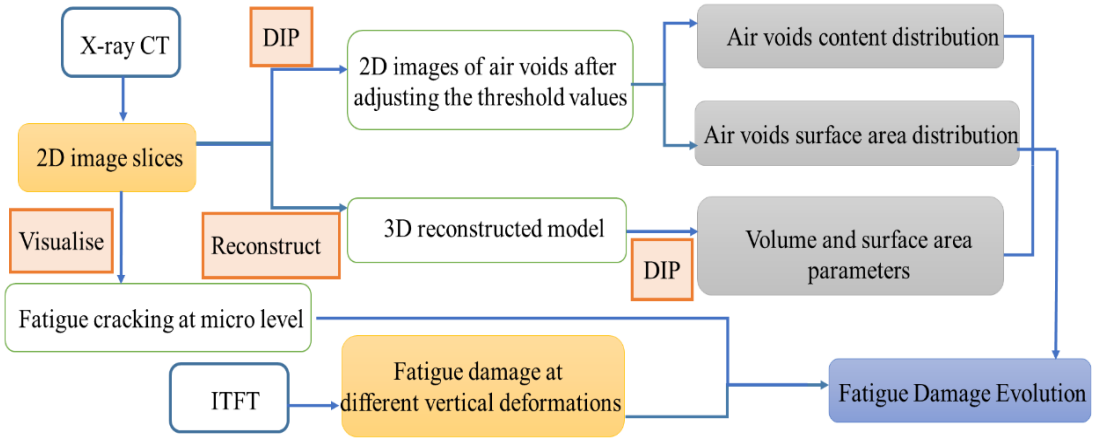


Figure 5.1 Scheme for testing programme.

5.3 Image Analysis Methods

5.3.1 Digital Image Processing (DIP)

Figure 5.2 illustrates the processing procedure used with the CT X-ray images. Specially designed samples with diameter of 20 mm and height of 18 mm were shown in Figure 5.2a. Figure 5.2b shows a typical 2D image from an asphalt mixture specimen, the brightest region represents aggregates, followed by the mastic (asphalt binder and filler) and the darkest regions represent air voids. The 2D slices can be rendered to produce a 3D image as shown in Figure 5.2h. In this study, DIP is used to process X-ray CT images, including adjustments to improve the image quality, such as gray intensity thresholding and image segmentation. An image profile was generated to identify the range of possible threshold values in the Area of Interest (AOI). As shown in Figure 5.2c, pixels (gray values) are shaded separately in different colours to group the ranges of gray values for the specified materials in the mixture. These gray values are used to identify those pixels that belong to the AOI for detecting the threshold values. Thresholding is carried out to isolate the AOI within an image from the background

based on pixel intensity. Phase (aggregates, mastic and air voids) isolation was achieved by applying different threshold values, as shown in Figure 5.2e-g. A pseudo colour was applied to the original image to view the material phases, by assigning each of them a different colour spectrum (Figure 5.2d).

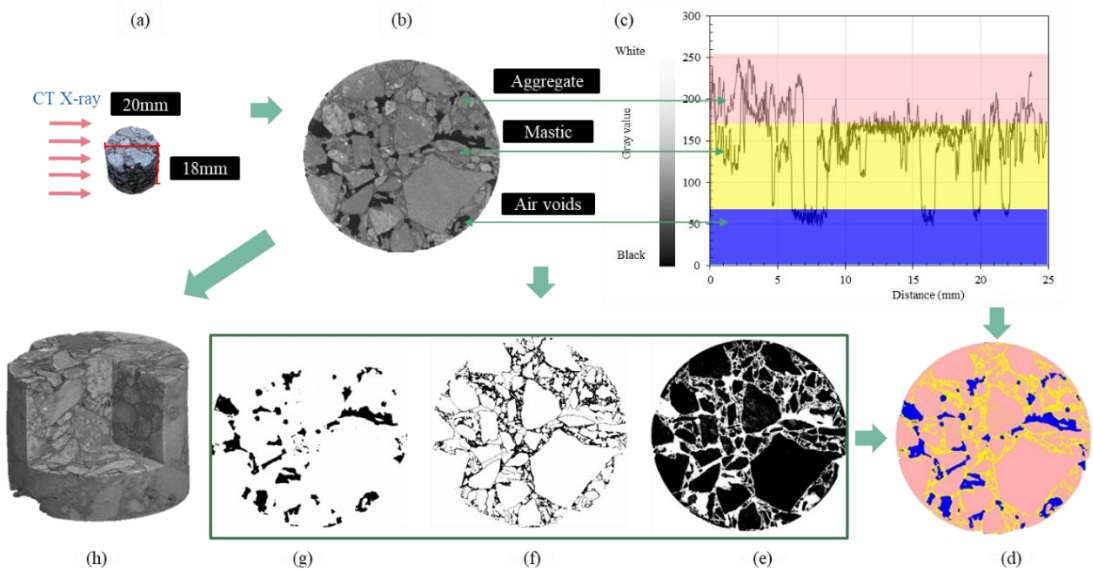


Figure 5.2: CT X-ray image processing; (a) The geometry and dimensions of samples; (b) Central CT slice image; (c) AOI extracted by gray value; (d) After pseudo colour transformation; the phase (e) Aggregates; (f) Mastic and (g) Air voids after adjusting the threshold values; (h) 3D reconstruction from 2D slices.

5.3.2 The Coordinate Axis and the Image Area for Calculation

Six asphalt specimens were analysed at different vertical deformations to establish the air voids distribution, where the Y-axis is the loading direction and the X and Z axes are in the horizontal plane with the Z-axis in the direction of the specimen height. To make sure the calculated area is the same for each slice, the image area as shown in Figure 5.3 is applied to calculate air voids distribution.

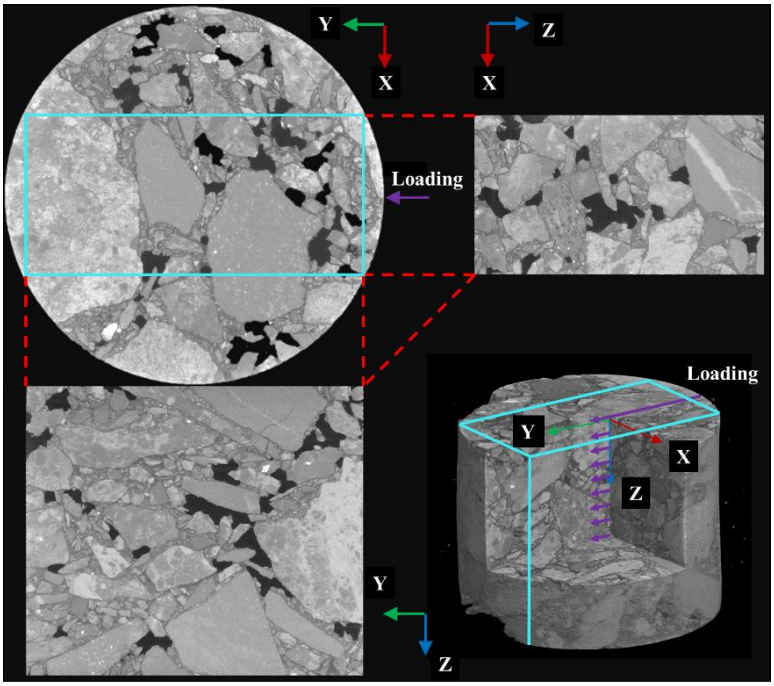


Figure 5.3: The coordinate axis and the image area for calculation.

5.3.3 Calculation Equations for Volume and Surface Area Parameters

The volume and surface area parameters of air voids were calculated to determine the damage evolution and fatigue resistance properties of the sample. Total sample volume (SV, mm^3) air voids volume (AVV, mm^3) and air voids surface area (AVSA, mm^2) before and after loading were calculated by software VGStudio Max 3.0.0. Air voids content (AVC, %), air voids content change (AVCC, %) and air voids content increase (AVCI, %) were calculated according to Eq. 5-1 to Eq. 5-3. Surface area change (AVSAC, mm^2) and surface area increase (AVSAI, %) of air voids were calculated by Eq. 5-4 to Eq. 5-5.

$$AVC = \frac{AVV}{SV} \times 100\% \quad (5\text{-}1)$$

$$AVCC = AVC_{after} - AVC_{pre} \quad (5\text{-}2)$$

$$AVCI = \frac{AVC_{after} - AVC_{pre}}{AVC_{pre}} \times 100\% \quad (5\text{-}3)$$

$$AVSAC = AVSA_{after} - AVSA_{pre} \quad (5\text{-}4)$$

$$AVSAI = \frac{AVSA_{after} - AVSA_{pre}}{AVSA_{pre}} \times 100\% \quad (5\text{-}5)$$

where C_{pre}, AVC_{after} $AVSA_{pre}$ and $AVSA_{after}$ are air voids content and air voids surface area before and after loading.

5.4 Fatigue Damage Evolution

To explore the damage evaluation, the number of loading cycles vs. the vertical deformation was recorded as shown in Figure 5.4a. It can be seen that there are three distinct stages which represent the different fatigue damage stages. In the first stage, deformation develops rapidly before slowing down. In the second stage, vertical deformation develops approximately linearly while finally in the third stage, the deformation becomes rapid once again.

Strain gauge with the full scale of 1με was glued in the centre of the sample during ITFTs to find relationship between the vertical deformation and the strain level. In Figure 5.4b, the strain vs. time curve changes from a smooth relationship to a significantly noisier relationship at the transition point (Time = 1578 s, Strain = 3960 × 10^{-6}), which is caused by cracks initiating near the strain gauge. The time (1578 s) corresponds to the vertical deformation 0.47 mm in Figure 5.4c, and also to the first stage in Figure 5.4a. The strain vs. time curve increases significantly at the point (Time = 4494 s, Strain = 13411 × 10^{-6}), for the reason that the strain gauge exceeds the full

scale value when cracks propagate quickly. The time (4494 s) corresponds to the vertical deformation 0.76 mm in Figure 5.4c, and also to the second stage in Figure 5.4a.

To explore how cracks initiate and propagate in each stage, images in the centre of the samples were captured. The main failure mode of asphalt at low temperatures is debonding at the surface between aggregates and mastic, which is an adhesive failure (Figure 5.5). Figure 5.5a and b correspond to the first stage, where deformation is relatively small. A number of microcracks initiate at the aggregate–mastic interfaces. In fracture mechanics, the first stages are known as pre-cracking and transition. The process where stresses begin to accumulate in the sample to form microcracks is called pre-cracking and the process when micro-cracking begins to occur and propagate is called transition. Transition happens when the peak load of the sample occurs in the microcrack nucleation [214]. Figure 5.5c and d correspond to the second stage, where deformation increases linearly. Air voids expand in a small range and several microcracks connect together. This stage is defined as stable cracking. During this stage, microcracks propagate steadily causing the vertical deformation also to increase steadily. Figure 5.5e and f correspond to the third stage, where air voids expand rapidly, and at the same time cracks develop quickly. This stage is defined as full cracking. With the vertical deformation increasing rapidly, macrocracks initiate and propagate until the sample becomes fully damaged.

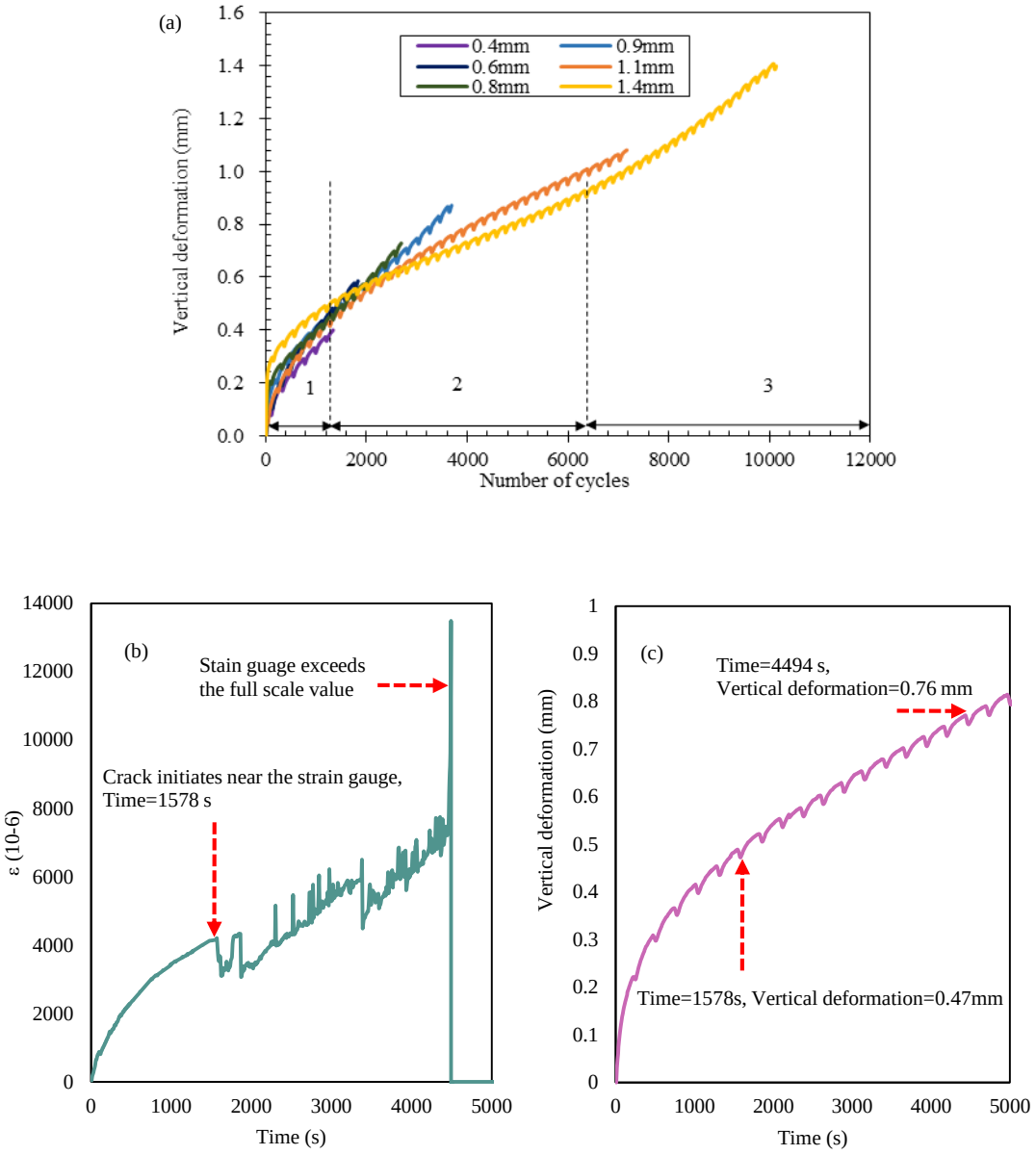


Figure 5.4: (a) Vertical deformation vs. number of cycles showing three different fatigue damage stages; (b) Strain vs. time curve and (c) Vertical deformation vs. time curve.

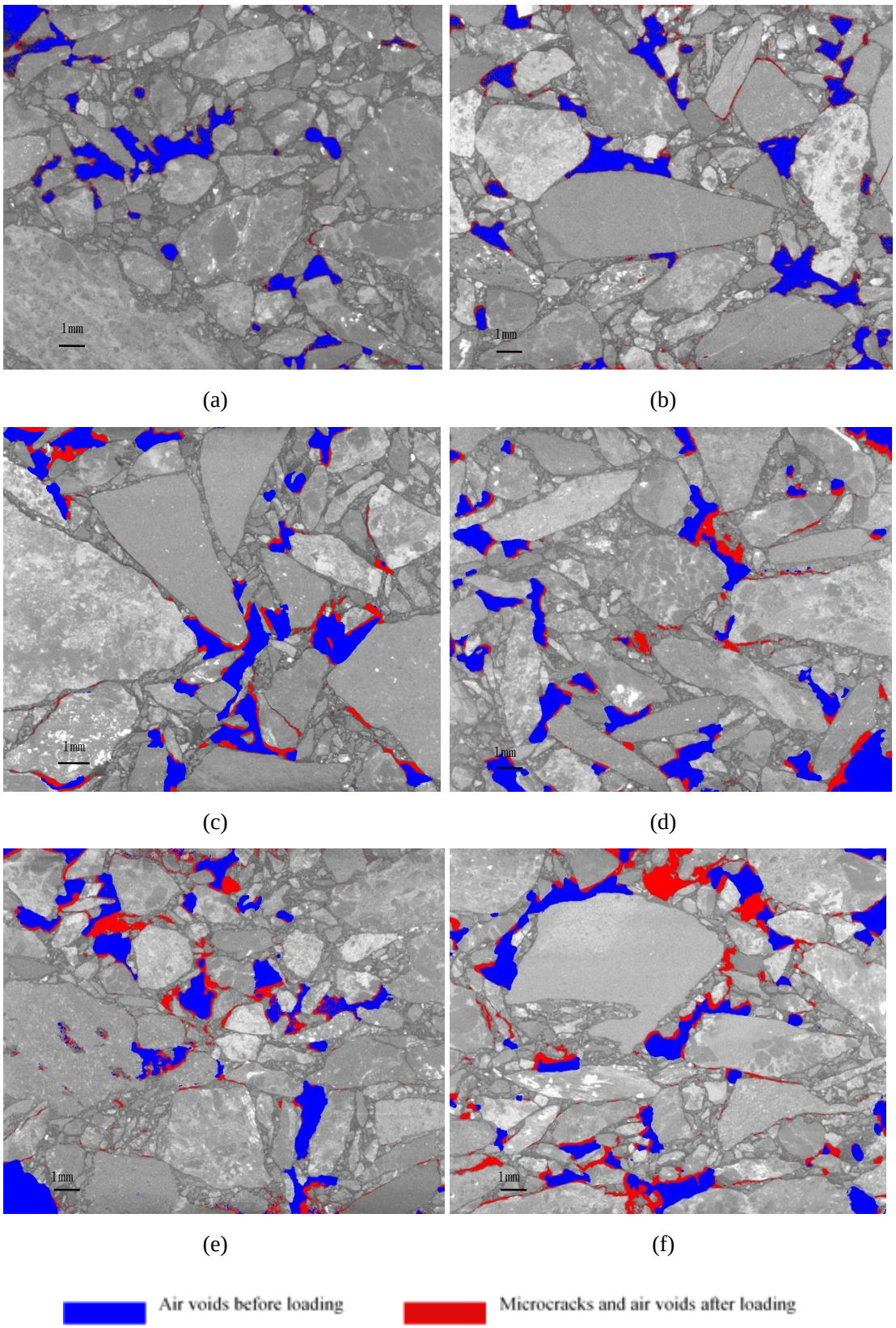

1 mm
(a)
1 mm
(b)
1 mm
(c)
1 mm
(d)
1 mm
(e)
1 mm
(f)
Air voids before loading
Microcracks and air voids after loading

Figure 5.5: Air voids of unloaded samples and microcracks of loaded samples under different vertical deformation: (a) 0.4 mm; (b) 0.6 mm; (c) 0.8 mm; (d) 0.9 mm; (e) 1.1 mm and (f) 1.4 mm.

5.5 Air Voids Content Distribution

The air voids content (AVC, %) distribution in the X and Y directions was calculated. The average AVC was calculated per 100 X-ray CT images (100 intervals). Due to the limitation of space, just three examples are shown in Figure 5.6, more examples of air voids distribution can be found in Appendix B. In the figure, the purple line represents the AVC before loading and the blue line is after vertical deformation. For the results calculated, for both the X and Y directions, the change of the AVC after loading becomes more obvious with the increase of vertical deformation. The change of the AVC can reflect the fatigue damage evolution. Increase in the AVC in the Y direction was calculated. Two examples and the corresponding images at the position of the max and min increase in the AVC are shown in Figure 5.7, more examples can be found in Appendix C. When vertical deformation is 0.4 mm, the increase values in the AVC are mainly negative, and the max and min increase in the AVC occurred at the edge, proving that the specimen is in volumetric compression. When the vertical deformation is 0.6 mm, the increase values in the AVC are mainly positive. The max increase in the AVC occurred in the middle part of the sample, showing the specimen to be undergoing tensile strain [215]. Similar results were concluded for the other vertical deformations (0.8, 0.9, 1.1 and 1.4 mm). This means that the specially designed sample is mainly in compression when the deformation is relatively small, while the sample becomes tensile and cracks develop faster as deformation increases.

To capture crack geometry, images of the slices representing the maximum and minimum increase in the AVC in the Y direction at six different vertical deformations

were collected; these are shown in Figure 5.7 - Figure 5.9. It can be seen that air voids are squeezed or stretched, and cracks are observed developing at these positions. Figure 5.7 and Figure 5.8 illustrate the images at the position of the minimum increase in the AVC. Air voids can be seen squeezed at these positions and the larger the vertical deformation, the more the air voids are squeezed. Although the samples were compressed at these positions and the dominant damage is in the form of air voids being squeezed, the cracks still developed in accordance with the law found in Section 5.4, which is that microcracks initiate at small deformation (Figure 5.7), then develop steadily (Figure 5.8a and b) and finally connect together to form macrocracks (Figure 5.8c and d). Figure 5.7 and 5.9 show the images at the position of the maximum increase in the AVC. Air voids can be seen stretched at these positions, and the larger the vertical deformation, the more the air voids are stretched. The dominant damage is in the form of cracks when samples were under tensile stress.

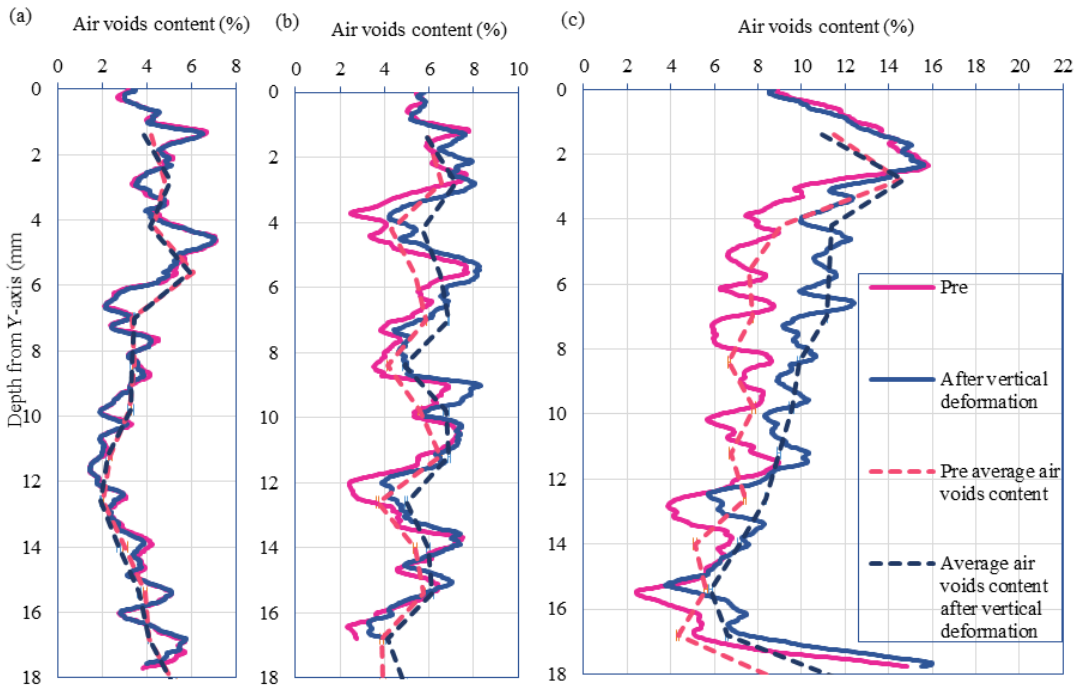


Figure 5.6: Air voids distribution in Y direction at (a) 0.4 mm; (b) 0.9 mm; (c) 1.4 mm vertical deformation.

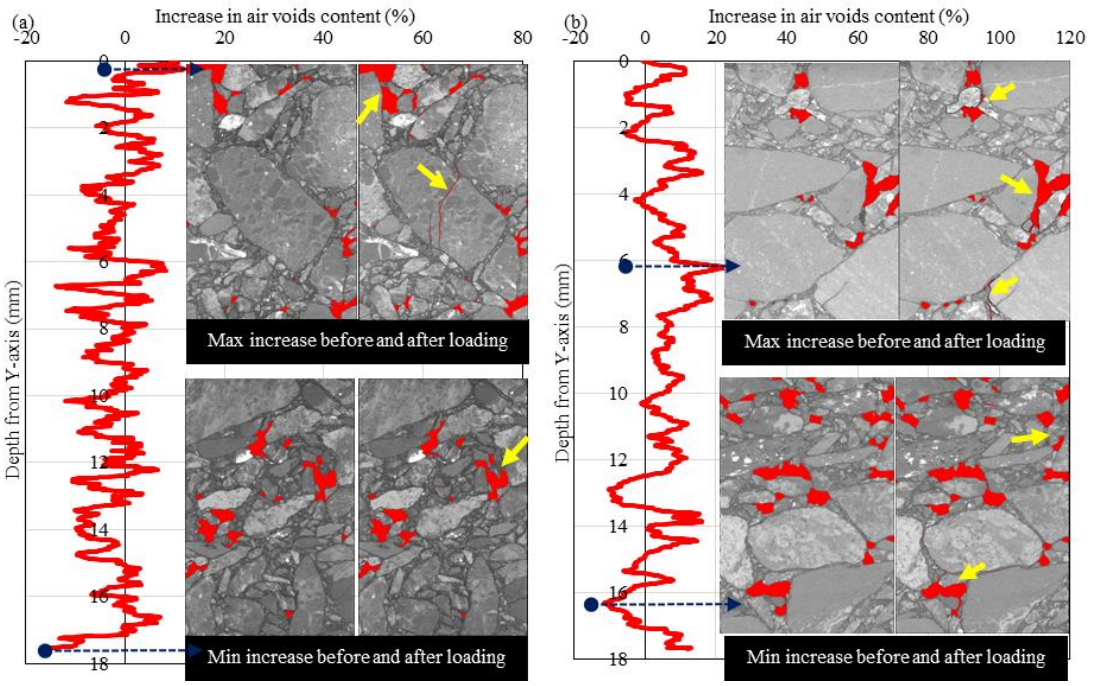
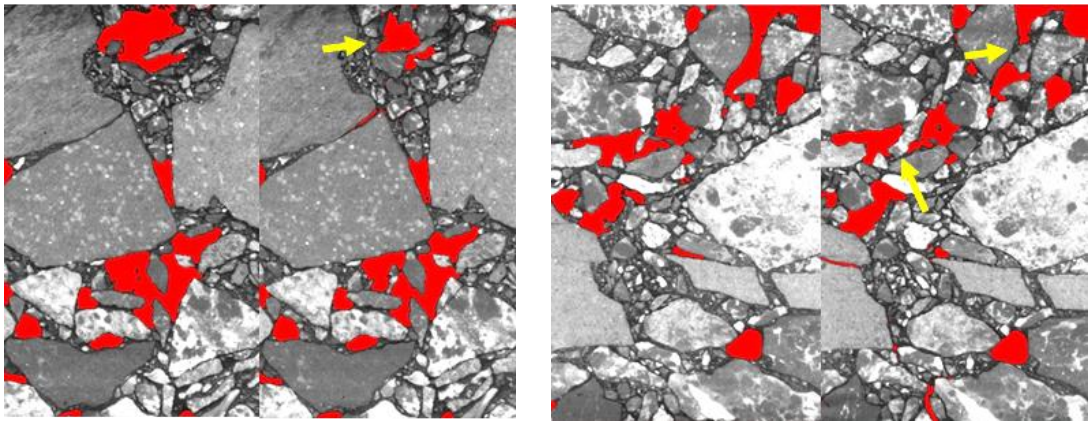
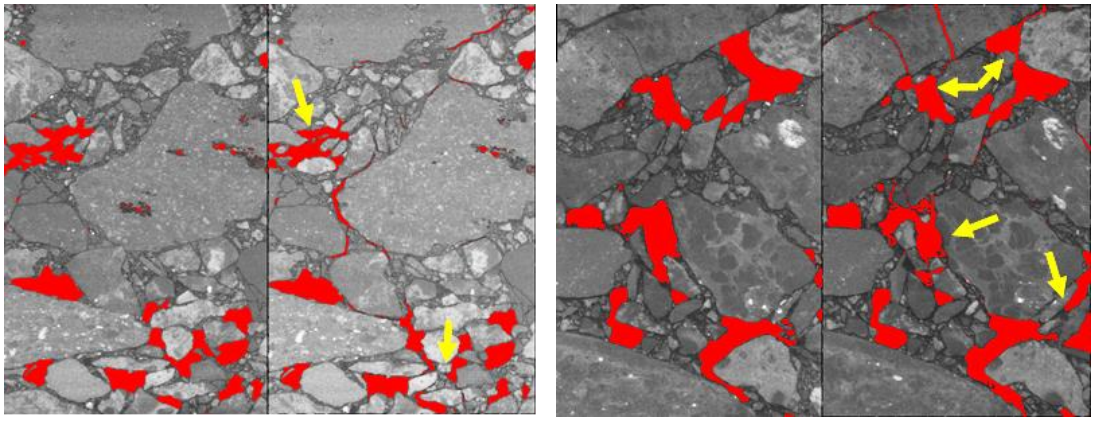


Figure 5.7: Increase in air voids content at (a) 0.4 mm and (b) 0.6 mm vertical deformation and the images of slices at the position of the max and min increase in air voids content in Y direction.

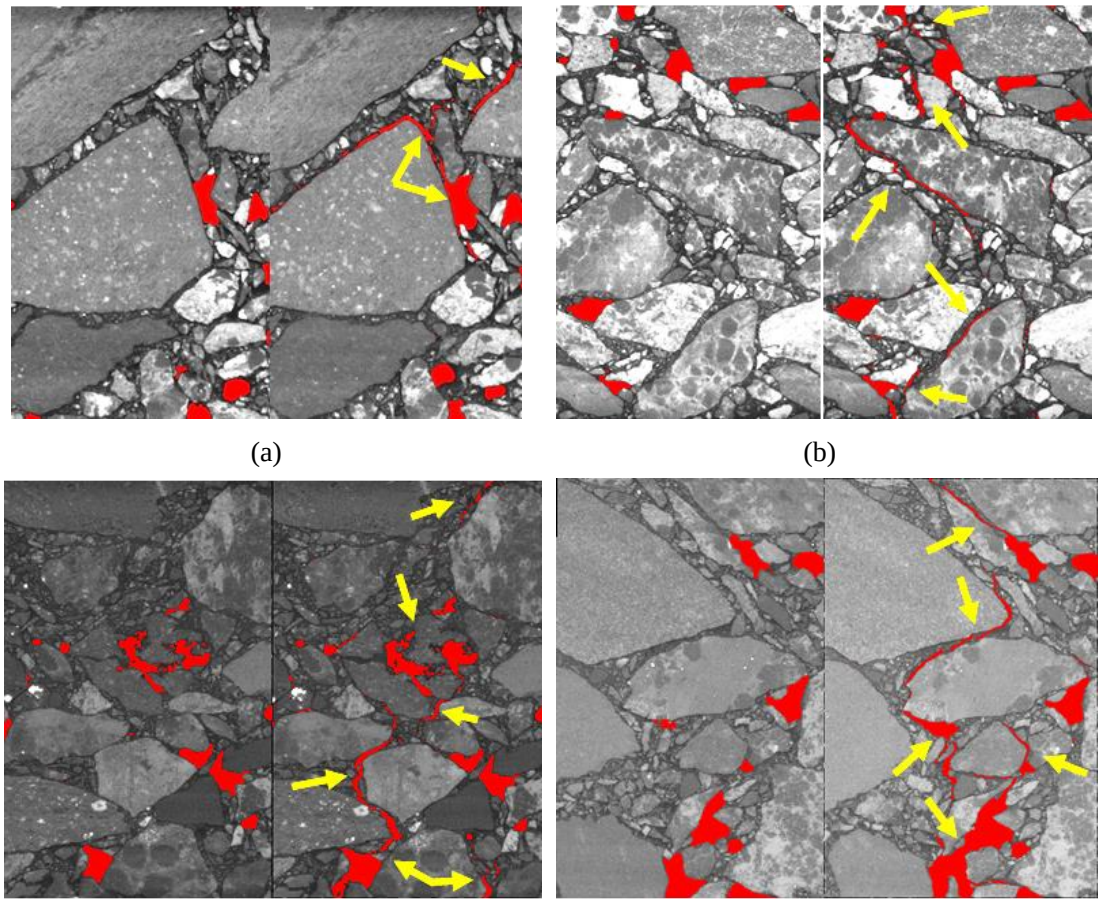


(a) (b)



(c) (d)

Figure 5.8: The images at the position of the min increase in air voids content at (a) 0.8 mm, (b) 0.9 mm, (c) 1.1 mm and (d) 1.4 mm in Y direction.



(a) (b)

(c) (d)

Figure 5.9: Images at the position of the max increase in air voids content at (a) 0.8 mm, (b) 0.9 mm, (c) 1.1 mm and (d) 1.4 mm in Y direction.

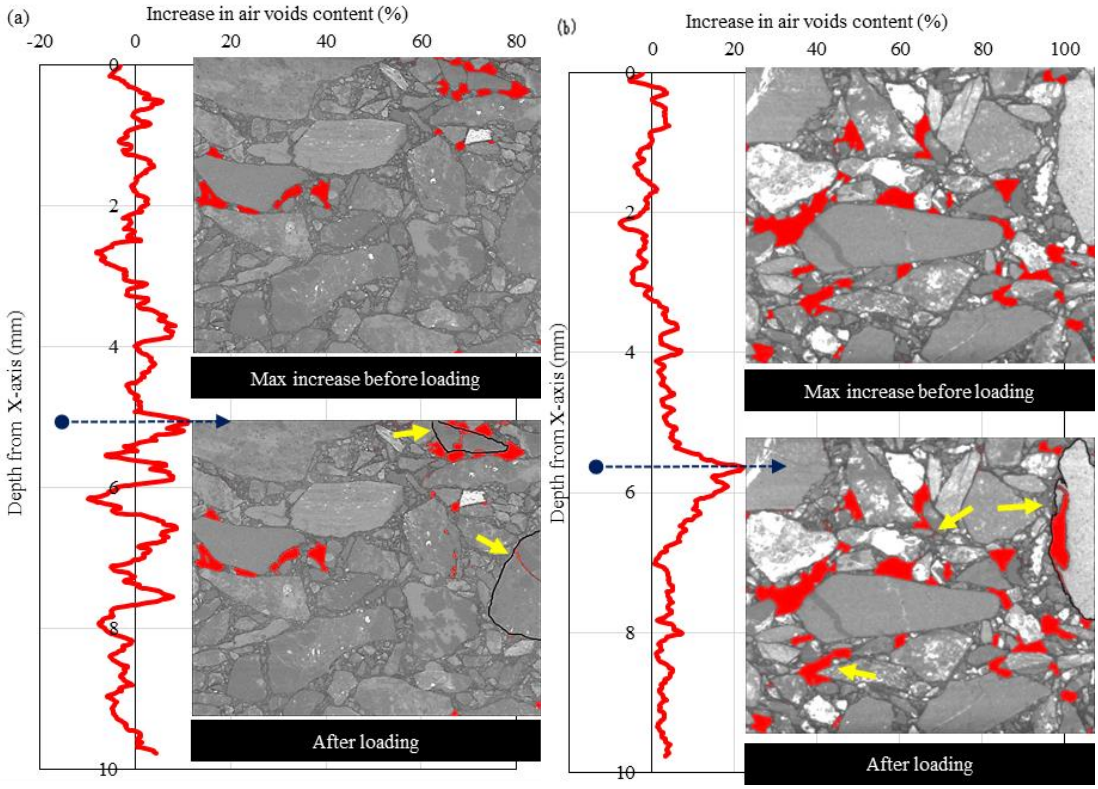
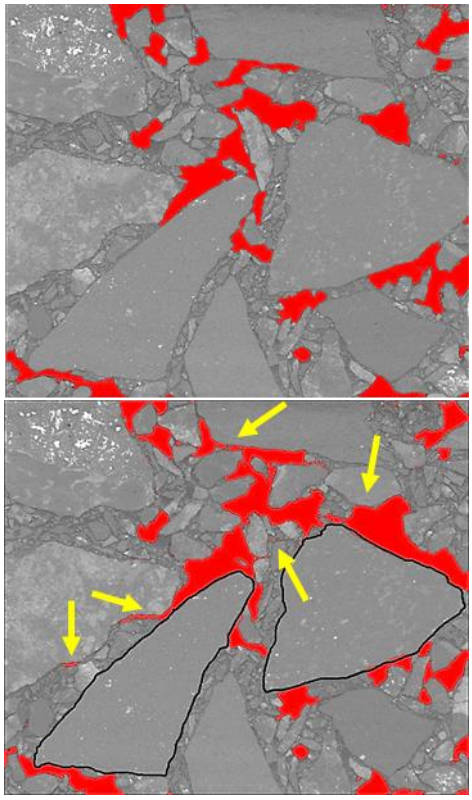
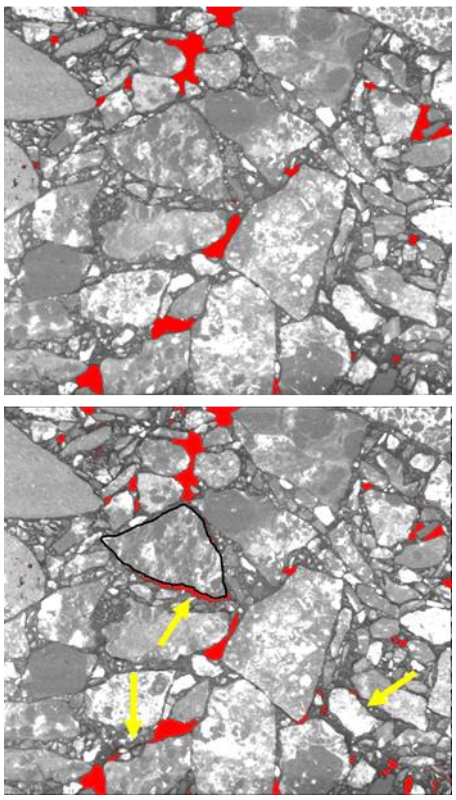


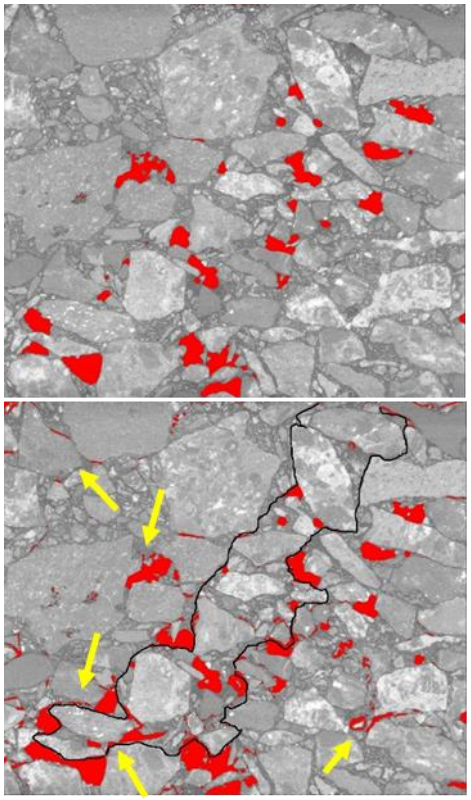
Figure 5.10: Increase in air voids content at (a) 0.4 mm and (b) 0.6 mm vertical deformation and the images at the position of the max and min increase in air voids content in X direction.



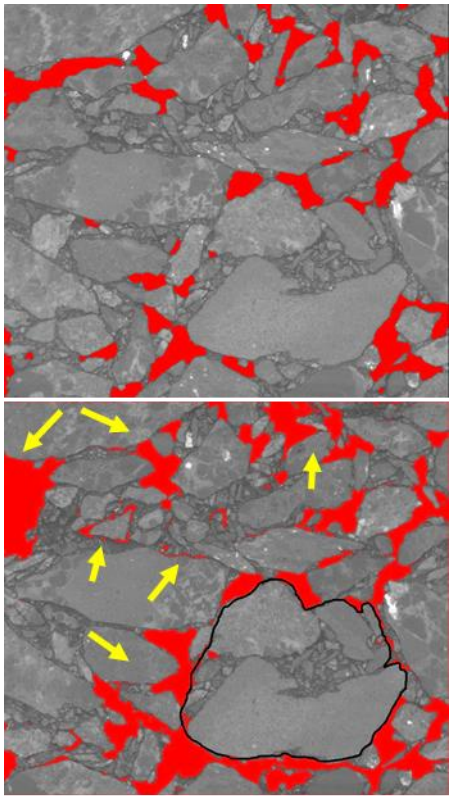
(a)



(b)

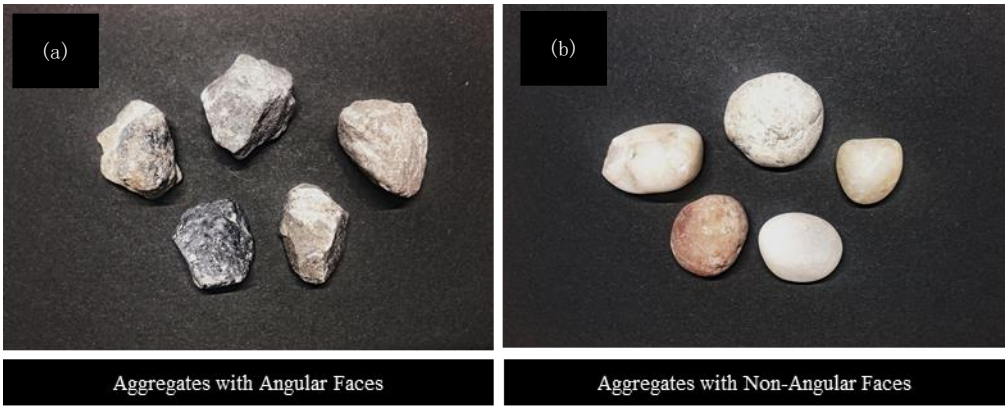


(c)



(d)

Figure 5.11: The images at the position of the max increase in air voids content at (a) 0.8 mm, (b) 0.9 mm, (c) 1.1 mm and (d) 1.4 mm in X direction.



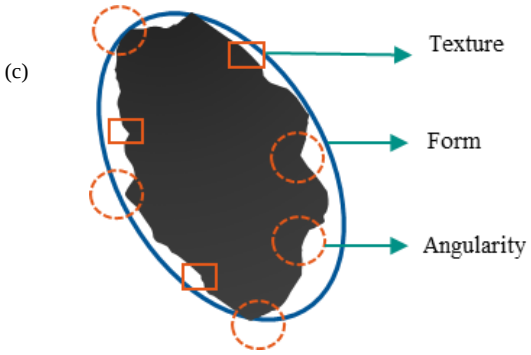


Figure 5.12: Illustration of morphological characteristic of aggregates: (a) angular and non-angular aggregate; (b) aggregate with many fractured faces; (c) shape characterization [216].

To further understand crack initiation and propagation, images at the positions where the maximum increase in the AVC occurred in the X direction were also taken; these are shown in Figure 5.10 – Figure 5.11 and were used for comparison to the results in the Y direction. In the X direction (Figure 5.10) it can be concluded that the change of air voids after loading becomes more obvious with the increase of vertical deformation, and the largest change in the AVC also appears in the middle part of the sample, which

agrees with the maximum tension occurring in the middle of the sample.

The impact of the form of the aggregates on fatigue cracking is also explored here. Flat and elongated particles are defined where the dimension ratio (width to thickness or length to width) exceeds 3:1 [216]. It has been determined that flat and elongated coarse aggregate particles have some influence on the performance of asphalt concretes, as such particles tend to break down [217]. Asphalt mixtures containing 30% or more flat particles have been shown to have poor properties compared to mixtures with lower percentages of flat particles [218]. In this chapter, cracks were found to have initiated and propagated adjacent to flat and elongated aggregates, as shown in Figure 5.8d and Figure 5.10b. Cracks were also observed initiating and propagating in interfaces between the mastic and flat and elongated aggregates, as shown in Figure 5.7a, Figure 5.9b and Figure 5.9d. Air voids also tend to expand at interfaces between mastic and flat and elongated aggregates, as shown in Figure 5.9d and Figure 5.9b.

The irregular shape of aggregates may lead to stress concentrations in asphalt mixtures, consequently causing the initiation and propagation of microcracks, which will finally change the macrostructure and microstructure of the material leading to a deterioration of the mixture's overall strength. Fractured faces, angularity and texture are often described as irregularities with examples of these shown in Figure 5.12. Angularity describes the edge sharpness of aggregate particles. The larger the angularity of aggregate, the sharper its edges. The texture expresses the relative surface roughness of aggregate particles [219]. The images captured in this paper show that cracks often occurred at interfaces between mastic and non-angular aggregates, as shown in Figure 5.7b, Figure 5.8c and Figure 5.9b. Cracks were also observed to occur within non-angular aggregates, as shown in Figure 5.10a. Reasonable angularity and texture ensures enough interlock friction between aggregates. However, when the angularity

continues to increase, cracks tend to initiate and propagate, as shown in Figure 5.9a-c and Figure 5.11a-b. Figure 5.7a shows cracks also tend to develop within aggregates with very angular but less textured surfaces. Fatigue cracking behaviour also became more complicated with vertical deformation increase, as shown in Figure 5.11c-d. The development of cracks follows the principles described above, but the increased vertical deformation results in coarse aggregates with smooth surfaces moving with the surrounding binder and fine aggregates.

5.6 Air Voids Surface Area Distribution

The air voids surface area (AVSA, mm^2) distribution at 0.4 mm vertical deformation is shown in Figure 5.13. It can be seen that air voids with surface area less than 0.3 mm^2 account for the majority of the voids. The number of air voids decreases exponentially when the surface area is larger than 0.3 mm^2. The number of air voids with a surface area larger than 2.3 mm^2, which is 1/3 of the maximum surface area (6.9 mm^2), is very small. The AVSAI in three ranges (less than 0.3 mm^2, 0.3 mm^2 – 1/3 of the maximum AVSA and larger than 1/3 of the maximum AVSA) were calculated, as shown in Figure 5.14. The AVSAI when the area is less than 0.3 mm^2 is stable and sustained as the vertical deformation increases. There is no obvious AVSAI in the range (0.3 mm^2 – 1/3 of the maximum AVSA). When the area is larger than 1/3 of the maximum AVSA, AVSAI grows rapidly as the vertical deformation is increased. It was found that air voids with large surface areas (macrocracks) are easier to expand and develop when the vertical deformation is large; however, air voids with small surface area (microcracks) continue initiating and propagating no matter whether the deformation is large or small. Previous research has defined the fracture processes, making it easier to understand the damage evolution laws; however, both the visualisation using high resolution x-ray CT images (Figure 5.7 – Figure 5.11) and the results of AVSA distribution analysis proves

that microcracks develop continuously throughout the whole fatigue process.

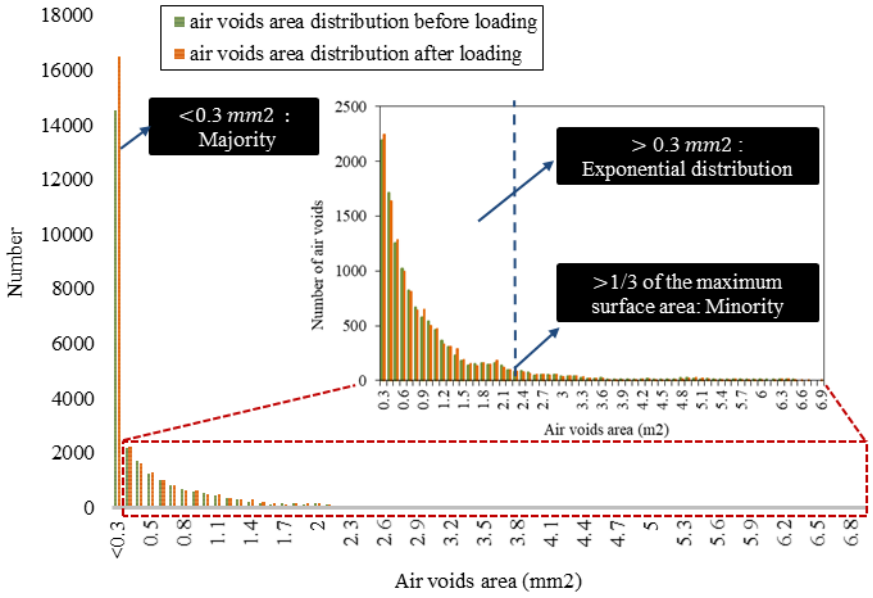


Figure 5.13: Air voids surface area distribution of the whole sample (at 0.4mm vertical deformation).

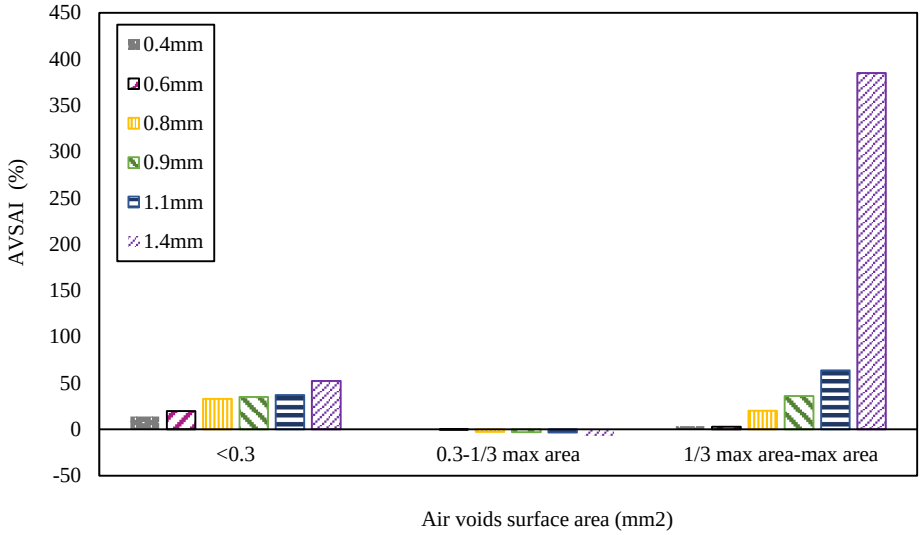


Figure 5.14: Increase rate of the air voids surface area at three ranges.

5.7 Volume and Surface Area Parameters

Generally, the volume and surface area of air voids in asphalt concrete can be used to characterise the damage status of asphalt concrete, the higher the volume and surface area of air voids, the more serious the damage is in the asphalt concrete [212, 213, 220]. The volume and surface area parameters of samples with different vertical deformations are shown in Table 5.2. It can be seen from Table 5.2 that the air voids content change (AVCC) becomes more obvious with the increase of vertical deformation (0.14% at 0.4mm while 1.5% at 1.4 mm), which demonstrates that the damage continues to accumulate. The air voids content of asphalt concrete basically increases with the increase of vertical deformation from 0.4 mm to 1.1 mm; however, it slows down when the deformation is higher than 1.1 mm. The reason is that the samples have probably effectively failed at the relatively larger deformations of both 1.1 mm and 1.4 mm.

In addition, the same tendency can be found for the air voids surface area change (AVSAC). With increasing vertical deformation, the AVSAC becomes more obvious (45.43 mm^2 at 0.4mm while 1228.90 mm^2 at 1.4 mm). The air voids surface area increase (AVSAI) basically increases with the increase of vertical deformation; however, the change rate increases suddenly at 0.6 mm (21.92%) and decreases after 1.1 mm. This indicates that the cracks develop rapidly at 0.6 mm, and sample failure occurs after the deformation is higher than 1.1 mm.

Table 5.2: Volume and area parameters of samples.

Sample ID	Vertical deformation (mm)	AVC_{pre} (%)	AVC_{after} (%)	$AVCC$ (%)	$AVCI$ (%)	$AVSA_{pre}$ (mm^2)	$AVSA_{after}$ (mm^2)	$AVSAC$ (mm^2)	$AVSAI$ (%)
1	0.4	3.05	3.19	0.14	4.59	1976.63	2022.06	45.43	2.30
2	0.6	5.54	5.90	0.36	6.50	2490.83	3036.81	545.99	21.92
3	0.8	6.55	7.19	0.63	9.77	3744.35	4313.69	569.34	15.21
4	0.9	4.35	5.24	0.89	20.38	2179.39	2950.45	771.06	35.38
5	1.1	3.54	4.56	1.02	28.89	1994.41	3049.32	1054.91	52.89
6	1.4	5.40	6.91	1.51	27.96	2447.90	3676.80	1228.90	50.20

5.8 Conclusions

The main conclusions of this chapter are as follows:

1. High-resolution imaging of CT scans of small-size indirect tensile fatigue specimens shows that the main failure mode at 5 ℃ is debonding at the interfaces of aggregates and mastic, which belongs to an adhesive failure mode.

2. The fatigue damage process of asphalt concrete consists of three distinct stages. At the first stage, deformation develops rapidly before slowing down, only a few microcracks occur at the aggregate–mastic interfaces; at the second stage, the vertical deformation of asphalt concrete develops approximately linearly, the microcracks spread continuously, and some microcracks connect; at in the third stage, the deformation becomes rapid once again, the air voids grow rapidly, and microcracks emerge swiftly.

3. The sample is mainly in compression when the deformation is relatively small.

However, it changes to a predominantly tensile strain with the increase of deformation, and cracks develop faster as deformation increases. The maximum increase in the AVC (fatigue damage) often occurs near the middle area of the sample.

4. Both the visualisation based on X-ray CT images and the results of AVSA distribution indicate that the microcracks (characterized as small size air voids) develop continuously throughout the entire fatigue process.

5. The AVCC value becomes more obvious with increasing vertical deformation. The AVCI basically increases with the increase of vertical deformation; however, it slows down when the deformation becomes very large and the reason is that the samples have effectively failed. The same tendency can be found for the AVSAC and AVSAI values with increasing vertical deformation.

6 Numerical Modelling of Fatigue Cracking in Asphalt Concrete Using Cohesive Elements

6.1 Introduction

The fracture resistance of asphalt materials significantly influences the service life of asphalt pavements [173]. Fracture mechanics approaches have received increasing attention for studying fracture processes and damage evolution. Most traditional fracture mechanics approaches assume the existence of infinitely sharp crack tips leading to stress singularities, preceding the crack tips. However, neither the sharpness of the crack nor the stress singularity of the crack tip is observed in laboratory tests [138]. An alternative approach, called the Cohesive Zone Model (CZM), has proved to be an efficient tool to model crack development and can be easily implemented in numerical simulations. In early work, asphalt in numerical simulation based on the CZM was considered as a homogeneous material. Paulino et al. [123] proposed an intrinsic cohesive model for asphalt concrete, which is based on the energy potential approach of Xu and Needleman [221]. Song et al. [222] employed a bilinear CZM in conjunction with a viscoelastic bulk material to investigate fracture behaviour of asphalt concrete. Crack propagation in the Indirect Tension Test (IDT) was simulated with cohesive parameters calibrated from the single-edge notch beam test.

To make the CZM more consistent with reality, heterogeneous models have then been developed to model the different material phases (aggregates, air voids and asphalt matrix) [223]. There are two main types of heterogeneous model, the computer-generated and the image-based. The computer-generated model constructs the asphalt mixture by generating numerical aggregates and asphalt mastic [224]. Many researchers have tried to establish aggregate shape libraries and apply them in

numerical simulation [96, 225]. The computer-generated model has the disadvantage of producing an unrealistic representation of asphalt mixture heterogeneity as the method has limits when accounting for irregular aggregate shapes and distribution. Image-based models often apply an X-ray computed tomography (CT) scanner or high-resolution camera to capture cross sectional or surface images of asphalt mixtures. The images are then transferred into a geometrical model by digital image processing (DIP) techniques [214]. Masad et al. reconstructed a 2D finite element (FE) model for asphalt mixture to analyse its strain distribution [102]. Sun et al. built a 2D FE model to simulate the local-scale damage initiation and evolution and the global-scale top-down cracking performance [226]. Recently, researchers have tried to reconstruct three dimensional (3D) numerical models based on X-ray CT images. Wang [108] reconstructed a 3D FE model to investigate the stress distributions and stress concentration factor. You et al. [111] reconstructed 2D and 3D DE models for dynamic modulus tests and compared the results from both models. A 3D FE model was developed by Hu et al. to determine the effect of different types of aggregate on the internal structure in the asphalt mixture [227, 228]. Most research has embedded cohesive elements (CE) at interfaces between aggregate and mastic, but few can be found applying CEs within the asphalt mastic [151]. The image-based model has the disadvantage of generating fine aggregates with small size (the common size used by researchers is 2.36 mm or larger) mainly because of the size of the test samples, the resolution of the CT scanner and the considerations of computational efficiency. Because of this disadvantage, most simulations research into macro-crack generation and development, rather than crack initiation and propagation of micro-cracks.

This thesis has established a 2D FE model considering two phases (aggregates and asphalt mastic) and applying zero-thickness cohesive elements (CEs) in asphalt mastic and interfaces between mastic and aggregates, aiming to simulate crack initiation and

propagation of asphalt concrete at the micro level. High resolution X-ray CT scans were applied on the specially designed small asphalt concrete samples (20 mm diameter and 18 mm height) to visualize microcracks in asphalt concretes, and to reconstruct more realistic aggregate morphology – as presented in Chapter 5.

6.2 Programme

The scheme for the programme is shown in Figure 6.1. The specially designed samples, described in Chapter 5, were tested by ITFTs and scanned by X-ray CT before and after loading. The images of all samples before loading were transferred into binary images using DIP techniques. A 2D FE model was reconstructed from binary images and the model embedded with zero-thickness CEs both in asphalt mastic and at interfaces between mastic and aggregates. Parameters input in the model include viscoelastic properties, which were derived from DSR tests and the results are fitted by a Prony series; CEs properties were determined by a bespoke tensile strength test carried out in a universal testing machine (UTM); load conditions, which were calculated based on the force response of the whole sample; and aggregate properties, referenced to the literature. Crack paths of asphalt mixture samples at different deformation levels at 5 ℃ in ITFTs were compared to those in the FE model in numerical simulation tests. The established 2D model was then applied to predict crack initiation and propagation at 25 ℃. The details are shown in the following sections.

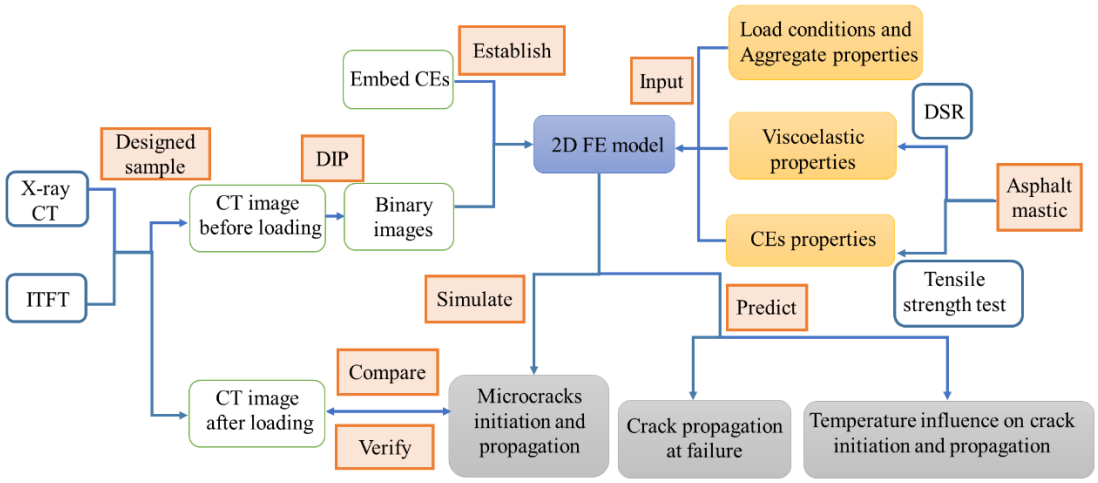


Figure 6.1: Scheme for testing/modelling programme.

6.3 Background

6.3.1 Viscoelastic Model

Asphalt binder is a thermoplastic liquid that behaves as a viscoelastic material, which exhibits both viscous and elastic behaviour depending on the temperature and the time of loading, and displays a time dependent relationship between applied stress or strain and resultant strain or stress [229]. In this study, the asphalt mastic is regarded as a linear viscoelastic material in FE simulation. The constitutive law for isotropic viscoelasticity is presented as volumetric and deviatoric components of stress and strain tensors, and the relations under multi-axial states of stress are shown in Eq. 6-1 and Eq. 6-2 [230]. The complex modulus and phase angle of the asphalt mastic were measured using DSR tests. The temperature dependency of the data was defined by using the Williams, Landel and Ferry (WLF) equation [231], expressed in Eq. 6-3.

$$\sigma_{kk} = 3\int_0^t K(t-\xi)\frac{\partial \varepsilon_{kk}}{\partial \xi}d\xi \qquad (6\text{-}1)$$

$$s_{ij} = 2\int_0^t G(t-\xi)\frac{\partial e_{ij}}{\partial \xi}d\xi \quad (6\text{-}2)$$

where $\sigma_{kk} = \sigma_{11} + \sigma_{22} + \sigma_{33}$ is first invariant of stress tensor that is the volumetric component of stress; $\varepsilon_{kk} = \varepsilon_{11} + \varepsilon_{22} + \varepsilon_{33}$ is volumetric strain; K is relaxation bulk modulus; t is current time of interest; ξ is integration variable that is a time before the current time; $s_{ij} = \sigma_{ij} - 1/3\sigma_{kk}\delta_{ij}$ is deviatoric stress tensor and δ_{ij} is Kronecker delta; $e_{ij} = \varepsilon_{ij} - 1/3\varepsilon_{kk}\delta_{ij}$ is deviatoric strain tensor; G is relaxation shear modulus.

$$\log a_T = \frac{-C_1(T - T_{ref})}{C_2 + (T - T_{ref})} \quad (6\text{-}3)$$

where a_T is the time temperature shift factor, C_1 and C_2 are regression coefficients, T_{ref} is the reference temperature, (5 ℃ and 25 ℃ in this study, aiming to predict the cracking behaviour at 25 ℃ and compare it with that at 5 ℃), and T is the test temperature. Regression coefficients C_1 and C_2 were calculated by fitting the WLF equation to the calculated shift factors with the aid of the Solver function in the Excel spreadsheet.

One of the mechanical models applied to predict viscoelastic properties is the Maxwell model, which is represented by connected springs and dashpots, as illustrated in Figure 6.2. The generalized Maxwell model is a set of Maxwell elements connected in parallel, which is used in this study to simulate the mastic time dependency. G and K in Eq. 6-1 and Eq. 6-2 are defined using the Prony series representation, expressed in Eq. 6-4 and Eq. 6- 5, all relaxation is assumed to occur in the shear mode. It is possible to obtain the values of storage modulus (G') and loss modulus (G''), which are represented as functions of frequency (ω) in Eq. 6-6 and Eq. 6-7. By fitting Eq. 6-6 and Eq. 6-7 to the measured G' and G'' data from DSR tests, the parameters of FE modelling can be

determined [232].

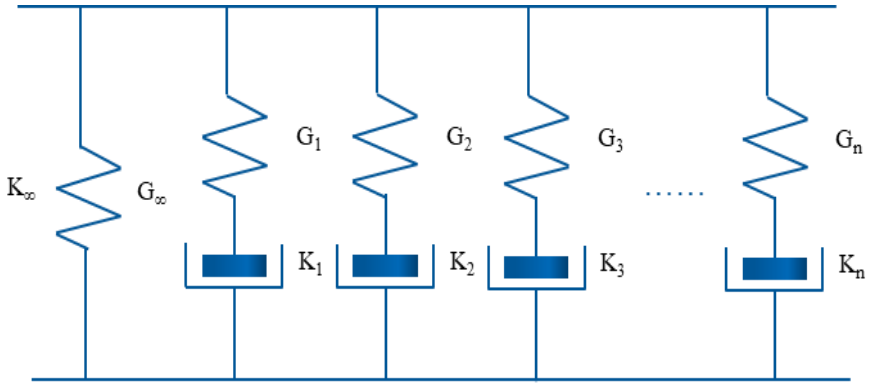


Figure 6.2: Schematic of the generalized Maxwell model.

$$\mathrm{G}(\xi) = G_\infty + \sum_{i=1}^{n} G_i \exp(-\xi/\tau_i) \tag{6-4}$$

$$\mathrm{K}(\xi) = K_\infty + \sum_{i=1}^{n} K_i \exp(-\xi/\tau_i) \tag{6-5}$$

where G_∞ and K_∞ are long-term shear modulus and bulk modulus, respectively, which are finite values when $\xi \to \infty$. G_i and K_i are the spring constant and dashpot, respectively, τ_i is the relaxation time of the element, and a variable number of Prony series parameters ending in n.

$$\mathrm{G}'(\omega) = G_\infty + \sum_{i=1}^{n_G} \frac{G_i \omega^2 {\tau_i}^2}{1 + \omega^2 {\tau_i}^2} \tag{6-6}$$

$$\mathrm{G}''(\omega) = \sum_{i=1}^{n_G} \frac{G_i \omega^2 {\tau_i}^2}{1 + \omega^2 {\tau_i}^2} \tag{6-7}$$

6.3.2 Bilinear Cohesive Zone Model (CZM)

A bilinear traction–separation law is applied to define the constitutive response of the

CE, as shown in Figure 6.3. The pre-peak region represents the elastic part of the intrinsic cohesive law whereas the softening portion after the peak load accounts for various forms of damage occurring. The parameter λ_{cr} is non-dimensional in which the traction (t) is the maximum traction (t_{cr}). The point (λ_{cr}, t_{cr}) separates the elastic and softening region, and after this point the stiffness begins to degrade up to zero. A quadratic interaction function regarding the nominal stress ratios is defined in Eq. 6-8. The cohesive fracture energy (G_c) is computed by equating the area under the displacement-traction curve (see Figure 6.4), as shown in Equation 6-9. A local scalar damage variable D is defined to quantify the progress of the damage-state of the element (Eq. 6-10) [222] [233], which has six different damage for traction separation laws included in ABAQUS to choose. When defining the mechanical properties of CEs in ABAQUS, it needs to determine the specific shape of the constitutive model, including cohesive elements stiffness, ultimate strength and critical fracture energy, which were obtained from laboratory tests in the thesis.

$$(\frac{\delta_n}{\delta_c})^2 + (\frac{\delta_S}{\delta_c})^2 = 1 \text{ and } {t_n}^2 + {t_s}^2 = 1 \tag{6-8}$$

$$G_c = \frac{1}{2}\delta_c \sigma_c \tag{6-9}$$

$$D = \frac{\delta_c(\delta_{max} - \delta_i)}{\delta_{max}(\delta_c - \delta_i)} \tag{6-10}$$

where δ_n and δ_S denote a normal displacement opening and shear sliding, respectively; t_n and t_s are normal and shear tractions, respectively; σ_c represents material strength. δ_c, δ_{max} and δ_i are critical displacements, namely complete separation, maximum separation at damage evolution and separation at damage initiation. $\delta_{max} - \delta_i$ is the effective displacement, which is the relative displacement when traction stress is at its peak.

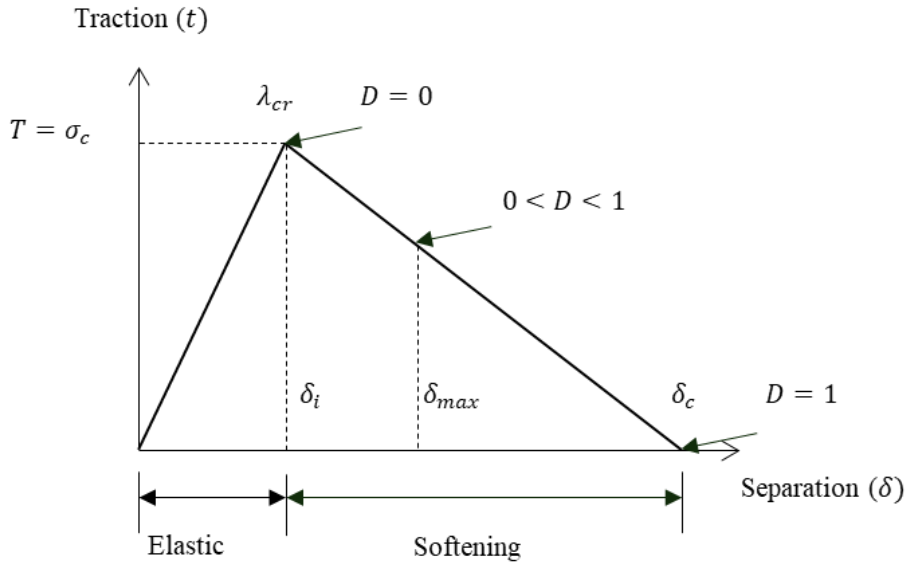


Figure 6.3: A typical bilinear traction-separation law (normal component).

6.3.3 Generate Zero-thickness Cohesive Interface Elements

The bilinear traction-separation law presented before is incorporated into the ABAQUS user element (UEL), in which functions of displacements, cohesive parameters and internal variables are defined [222] [233]. Transformation between global and local coordinates is necessary and the cohesive law represents a local separation-traction relationship. The 4-noded cohesive element is shown in Figure 6.4. The parameter θ represents the angle between global and local coordinates. X and Y denote global coordinates, while *s* and *n* indicate local coordinates. Nodes 1 and 2 are located on the bottom of the element whereas nodes 3 and 4 are located on the top of the element. Each node has two degrees of freedom. The global displacement vector (u_g) of the nodes belonging to the cohesive element can be expressed in Eq. 6-11. The global relative displacements (δ_X and δ_Y) between top and bottom nodes can be obtained in Eq. 6-12. The relative global displacement at Gauss points can be seen in Eq. 6-13. The matrix *R* defines the orthogonal transformation from global reference frame (X,Y) to

the element specific, local coordinate system (*s*,*n*), and the relative local displacement vector, shear sliding (δ_s) and normal (δ_n), is obtained in Eq. 6-14.

$$u_g = [u_X^1 \ u_Y^1 \ u_X^2 \ u_Y^2 \ u_X^3 \ u_Y^3 \ u_X^4 \ u_Y^4]^T \tag{6-11}$$

$$\begin{pmatrix} \delta_X^{(1,4)} \\ \delta_Y^{(1,4)} \\ \delta_X^{(2,3)} \\ \delta_Y^{(2,3)} \end{pmatrix} = \mathrm{L}u_g, \mathrm{L} = \begin{bmatrix} 1 & 0 & 0 & 0 & 0 & 0 & -1 & 0 \\ 0 & 1 & 0 & 0 & 0 & 0 & 0 & -1 \\ 0 & 0 & 1 & 0 & -1 & 0 & 0 & 0 \\ 0 & 0 & 0 & 1 & 0 & -1 & 0 & 0 \end{bmatrix} \tag{6-12}$$

$$\begin{pmatrix} \delta_X \\ \delta_Y \end{pmatrix} = \begin{bmatrix} N_1 & 0 & N_2 & 0 \\ 0 & N_1 & 0 & N_2 \end{bmatrix} \begin{pmatrix} \delta_X^{(1,4)} \\ \delta_Y^{(1,4)} \\ \delta_X^{(2,3)} \\ \delta_Y^{(2,3)} \end{pmatrix} = N \begin{pmatrix} \delta_X^{(1,4)} \\ \delta_Y^{(1,4)} \\ \delta_X^{(2,3)} \\ \delta_Y^{(2,3)} \end{pmatrix} = \mathrm{NL}u_g \tag{6-13}$$

$$\begin{pmatrix} \delta_s \\ \delta_n \end{pmatrix} = Bu_g = RNLu_g \tag{6-14}$$

where u_X^1 and u_Y^1 denote global displacements of node 1 along X and Y directions, respectively; $\delta_X^{(1,4)}$ represents the opening displacement between nodes 1 and 4 along global X direction; L is the operator matrix.

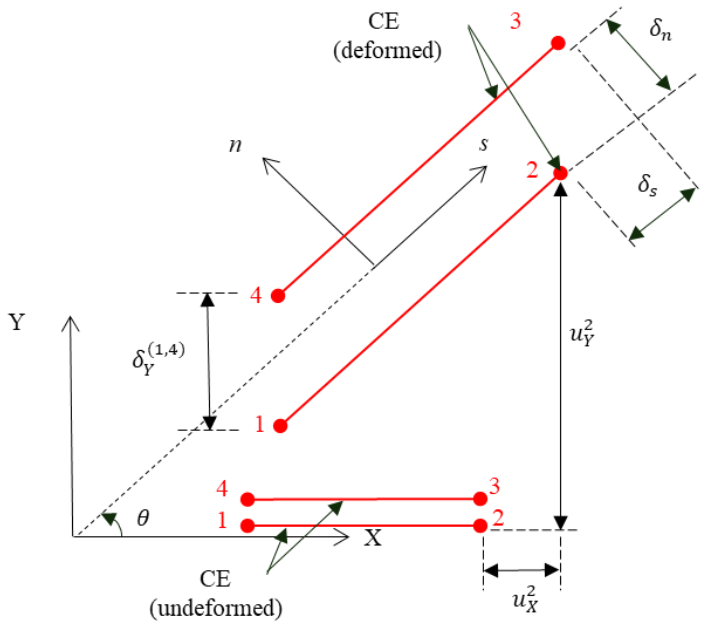


Figure 6.4: Schematic depiction of a 4-noded cohesive element.

6.4 Microstructures Reconstruction Based on X-Ray CT Images

6.4.1 Microstructure Acquisition using DIP

After thresholding of CT images, due to the small difference in gray levels, the boundary between particles in contact may be not very clear. Therefore, MATLAB was used to further process CT images for better microstructural reconstruction. 'Filtering' and 'hole-filling' were applied to reduce the noise and remove the smaller clutter of the images. 'Erosion' was combined with the 'open' operation to erode the aggregate shape and separate two connected aggregates, while the 'dilation combined with the close' operation expands the aggregate region to connect separated aggregates together. The method of watershed transform was used to segment the images. The aggregate images were clearly visible, which provided the foundation for the reconstruction of the 2D aggregate model for FEM analysis.

6.4.2 Numerical Model Generation

The method to choose images for numerical model generation is shown in Figure 6.5. A CT image in the middle section of the image stack from CT scans was picked, and the middle part of the CT image was chosen for numerical model generation, the dimensions of the image chosen is about length of 8.5mm and width of 7mm. This process aims to obtain smaller size aggregates and to model more detailed simulation of cracking behaviour. The process of numerical model generation is shown in Figure 6.6 in which Sample 1# (set to stop at 0.9mm vertical deformation in the ITFT) was chosen as an example [169]. The smallest aggregate size applied in this study is 0.05 mm. The two-phase (aggregate and mastic) binary image was gained from the original CT images by ImageJ and MATLAB, as shown in Figure 6.6 a and b. After getting the morphology of the aggregate, images were processed by MATLAB coding to get a geometric image of the sample, and the coordinates of each point were extracted for meshing, as shown in Figure 6.6c. The MATLAB code [234] was used to mesh the geometry image of the sample and output in nodes form that ABAQUS software can read (inp file), as shown in Figure 6.6d.

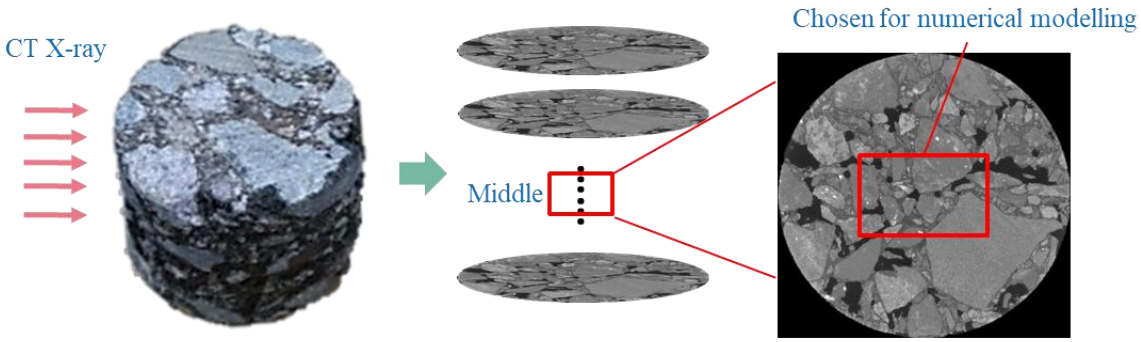


Figure 6.5: Method to choose images for numerical model generation.

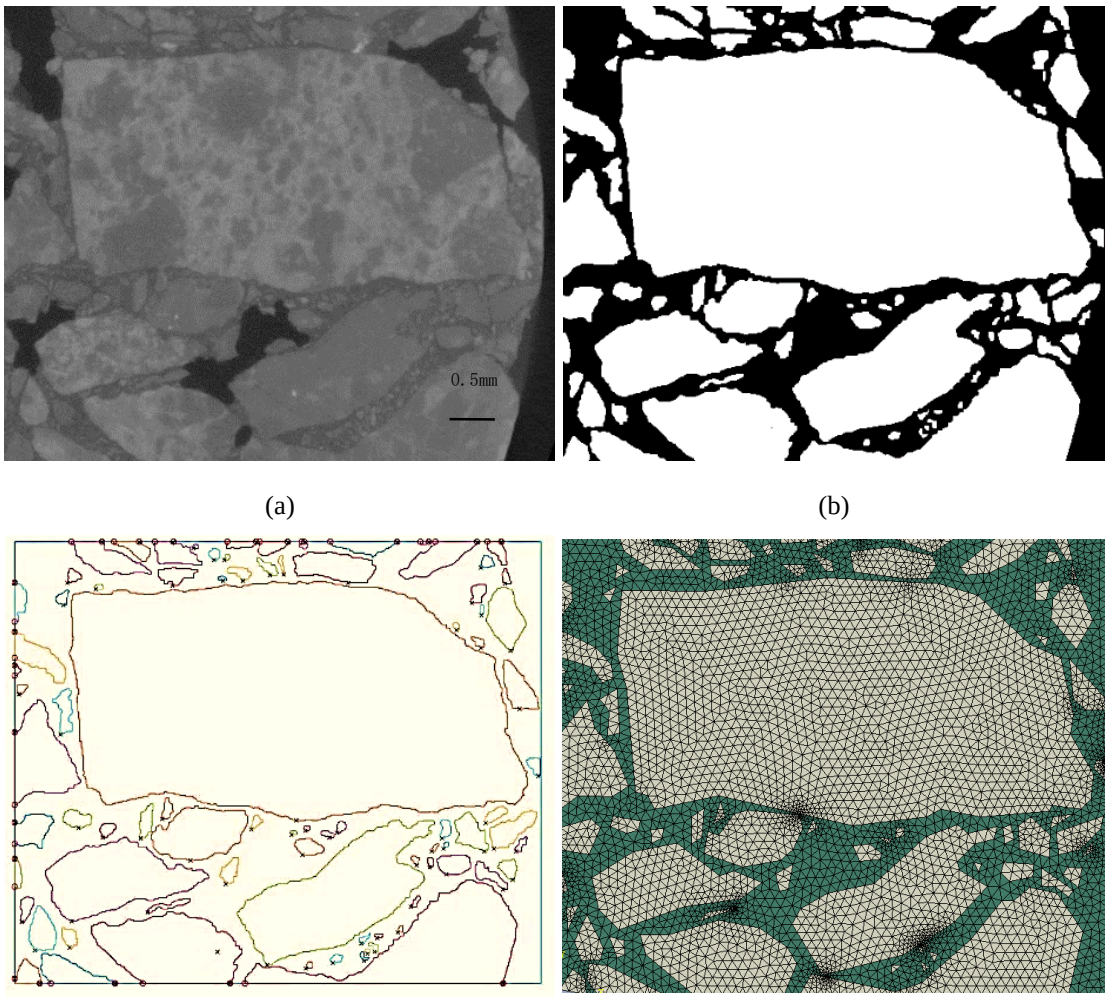
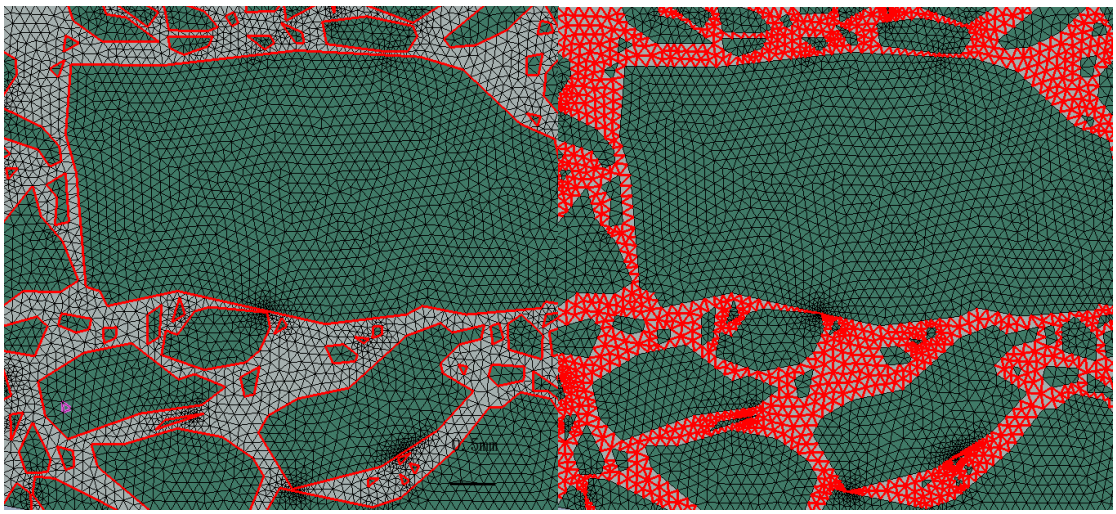


Figure 6.6: (a) Original CT image; (b) Two-phase (aggregate and mastic) binary image and (c) Geometry image; (d) FE mesh image.

6.4.3 Cohesive Element Embedment

A inp. file containing the relevant information of nodes and element connectivity was input into ABAQUS. In the interests of computational efficiency, only a two-dimensional microstructure of the asphalt mastic was taken into consideration in this study. A user-defined element (UEL) subroutine mentioned before was developed to embed cohesive elements between elements at interfaces between aggregates and mastic and within mastic, and then applied in ABAQUS, the cohesive elements were

marked in red as shown in Figure 6.7. The material properties of cohesive elements were defined by the bilinear cohesive model, details of which are mentioned in the following sections [235] [236] [237].



(a) (b)

Figure 6.7: Embedding 2D cohesive zone elements (a) In interfaces between aggregates and mastic and (b) Within mastic.

6.5 Parameters for Numerical Modelling of Fatigue Cracking in Asphalt Concrete

6.5.1 Viscoelastic Model Parameters

The complex modulus and phase angle of asphalt mastic were measured by conducting a frequency sweep at multiple temperatures (5, 10, 15, 20, 25 and 30 ℃) using the DSR test [166]. The asphalt mastic properties were defined as linear viscoelastic materials, and the master curve of the mastic was used as an input in ABAQUS. The master curves applying the Williams, Landel and Ferry (WLF) equation were constructed as shown in Figure 6.8; the data from the master curves were then used to fit Prony series. The viscoelastic property of the mastic was expressed in the form of Prony series

coefficients based on a generalized Maxwell model. ABAQUS input parameters are τ_i (relaxation time), $g_i = G_i/G_0$ (g_i is shear relaxation modulus ratio and G_0 is G(ξ) when ξ=0 in Equation 6-4), G_∞ (long-term shear modulus) and k_i (bulk relaxation modulus ratio, the value here is 0), which were obtained from the Prony series coefficients, and are shown in Table 6.1.

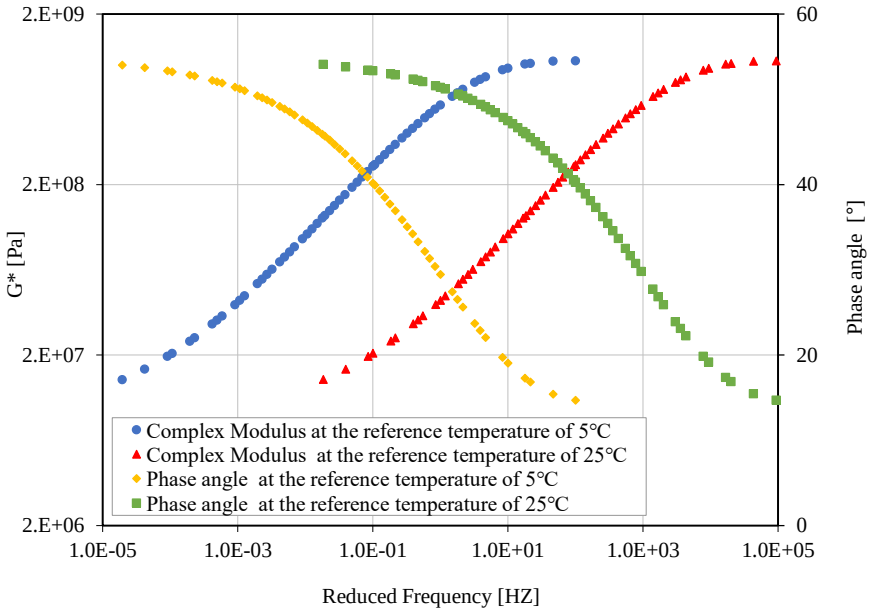


Figure 6.8: The master curves with 5 ℃ and 25 ℃ as the reference temperature.

Table 6.1: Prony series coefficients of asphalt mastic at 5 ℃ and 25 ℃.

i	5 ℃		25 ℃	
	τ_i (s)	g_i	τ_i (s)	g_i
1	0.003	5.49E-01	0.003	8.45E-01
2	0.2	2.26E-01	0.2	1.18E-01
3	2	1.21E-01	2	1.28E-02
4	6	9.13E-03	6	6.14E-03
5	10	3.45E-02	10	8.57E-03
6	30	2.06E-06	30	2.40E-03
7	60	4.54E-02	60	6.34E-03
8	3000	1.32E-02	3000	2.41E-07
-	G_∞ (MPa)	2.88E+06	G_∞ (MPa)	2.82E+03

6.5.2 Cohesive Element (CE) Properties

The maximum cohesive strength (tensile strength) of the mastic and the fracture energy were determined with a bespoke tensile test mounted on a UTM. All samples were conditioned at 5 ℃ and 25 ℃, respectively for 4 h before testing, and a constant cross-head speed of 20 mm/min was applied. Force versus displacement curves of the tensile strength test at 5 ℃ and 25 ℃ are shown in Figure 6.9. Under the constant cross-head speed of 20 mm/min in the UTM, the force increased from 0 to the peak load and then decreased to 0 until the specimen failed. The peak load at 25 ℃ is smaller than that at 5 ℃, while the deformation at failure is larger compared to 5 ℃. Due to the viscoelastic properties of asphalt mastic, the force increases more slowly as the temperature increases and damage of the specimen slows down at the same time. The maximum cohesive strength was computed as the ratio of the peak load divided by the cross-sectional area of the butt joint. The fracture energy was computed as the area under the force–displacement curve divided by the cross-sectional area of the butt-joint. An initial CE stiffness was identified based on the viscoelastic properties, making sure the main failure mode is cracking rather than permanent deformation. The results shown in Table 6.2 were used as the parameters in FE modelling. The aggregate–mastic adhesive strength (bond strength) was assumed to be slightly smaller than the maximum cohesive strength [224].

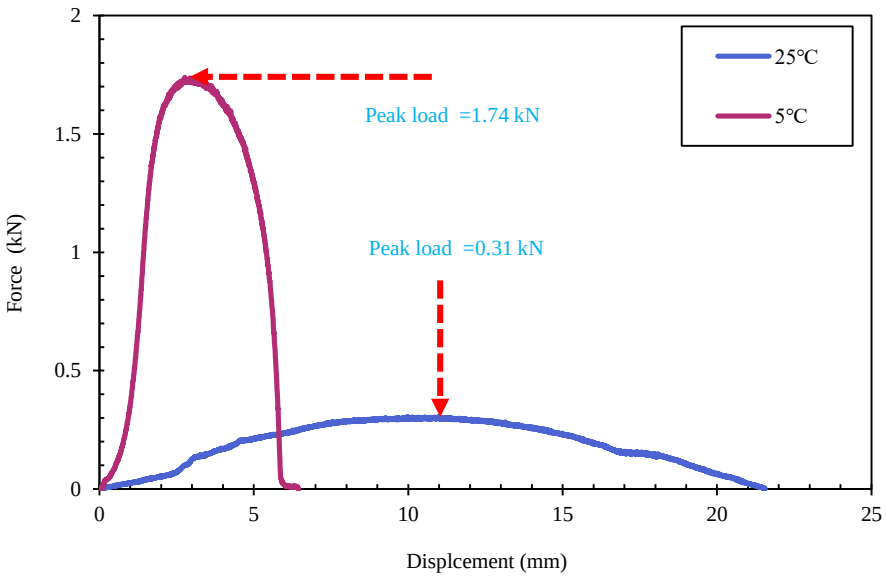


Figure 6.9: Force versus displacement curves of the tensile strength test at 5 ℃ and 25 ℃.

Table 6.2: Parameters input in FE modelling at 5 ℃ and 25 ℃.

Temperature (℃)	5 ℃	25 ℃
Adhesive strength (MPa)	2.10	0.40
Maximum cohesive strength (Mpa)	2.46	0.68
Fracture energy (kJ/m^2)	9.64	8.87
Cohesive elements stiffness (MPa)	800	600

6.5.3 Aggregates Properties and Load Parameters

The Figure 6.10a illustrates ITFTs which applied a repeated controlled stress pulse at a rate of 40 pulses per minute under the load of 0.8 kN. As mentioned before, to model details of microcrack initiation and generation, the middle part of the sample was chosen for modelling. Therefore, the force response of the chosen part needs to be calculated from simulation analysis of the whole sample. By applying the same load as in ITFTs to the whole sample in simulation, the load applied in FE modelling was obtained by averaging the stress of ten nodes as the load amplitude of the chosen part,

showed in Figure 6.10c and d. The boundary conditions applied are under compressive stress at left and right boundary, tensile stress at top and bottom boundary (in Figure 6.10b – note 90° change in orientation relative to the test). The aggregate input parameters are a Young's modulus of 55,000 MPa and a Poisson's ratio of 0.2 [227].

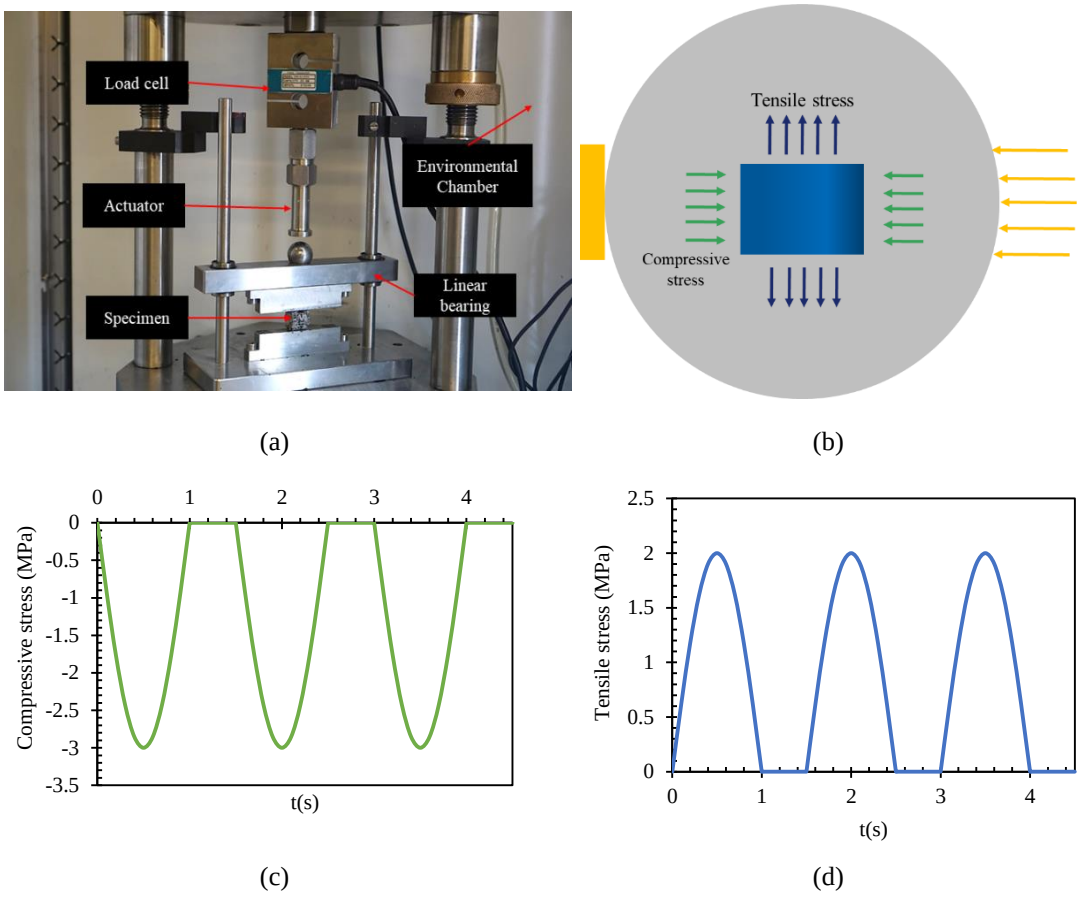


Figure 6.10: (a) ITFT set-up; (b) Load conditions applied in ITFTs and Load conditions applied in the numerical modelling (c) and (d).

6.6 Crack Initiation and Propagation

Sample1# (set to stop at 0.9mm vertical deformation in the ITFT) and Sample 2# (set to stop at 1.4 mm vertical deformation in the ITFT) were used as examples for simulations. The simulation was conducted at a temperature of 5 °C. Figure 6.11 shows the transverse tensile stress (S_{11}) distribution of Sample 1# and Sample 2# at 100 cycles.

It predicts that both samples are mainly under compression (negative values) at an early damage stage (100 cycles) at low temperature. Stress concentration is found to occur around where the aggregate is relatively large, as shown in Figure 6.11a. Due to the heterogeneous nature of the AC microstructure, the larger aggregates exhibit higher compressive or tensile stresses, which lead to significant stress concentrations [226]. Stress concentration is also observed where two aggregates are close to each other, seen in Figure 6.11b. The tensile stress is transmitted through both the aggregate phase and the mastic phase. The mastic plays a role of filling the gaps between the aggregates; as the amount of the mastic increases, an increasingly homogeneous transmission of the stress is expected [238]. When the distance between aggregates is small, the aggregates are nearly in contact, and the amount of mastic decreases in the region, causing the stress concentration. The crack tip is determined with the damage value of the cohesive element, which indicates the degree of stiffness reduction in the cohesive element (Figure 6.11c-d). Crack tips often occur at stress concentrations and cracks then initiate at these regions. When cracks expand, stress concentration at the initial crack tip is released, and the high tensile stress regions gradually move to the newly formed crack-tip region [239]. It is concluded that factors such as aggregate size and distance between aggregates can affect the crack initiation; the larger the aggregate is, the closer the distance between aggregates is, the more the stress will be concentrated and cracking will initiate.

Microcrack initiation and propagation of Sample 1# and Sample 2# at different fatigue damage levels are shown in Figure 6.12. Microcracks are distributed mainly along the compressive loading direction, which is consistent with the crack path observed in ITFTs. Three microcrack development phenomena are observed in both Sample 1# and Sample 2#, which are: microcracks are generated at interfaces between aggregate and mastic, and then microcracks propagate steadily, some microcracks connect with each

other to form larger cracks, which are similar to the crack development phenomena observed at macro level. Macrocracks are formed with microcracks constantly being initiated and propagated. With macrocracks generating continuously, mechanical properties of asphalt concrete at macro level will change, which is the combined effect of microcracks and macrocracks.

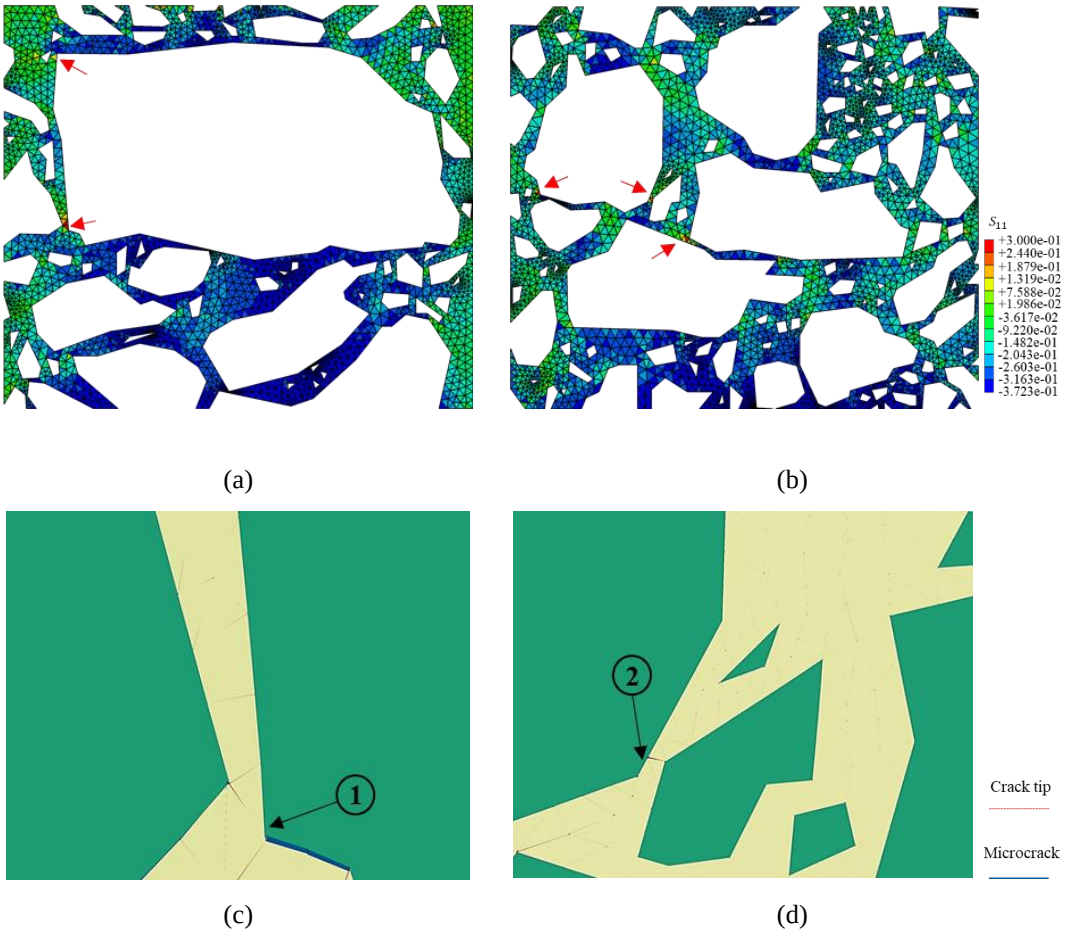


Figure 6.11: Transverse tensile stress of (a) Sample 1# and (b) Sample 2# at 100 cycles at 5 °C, and examples of the crack tip of (c) Sample 1# and (d) Sample 2#.

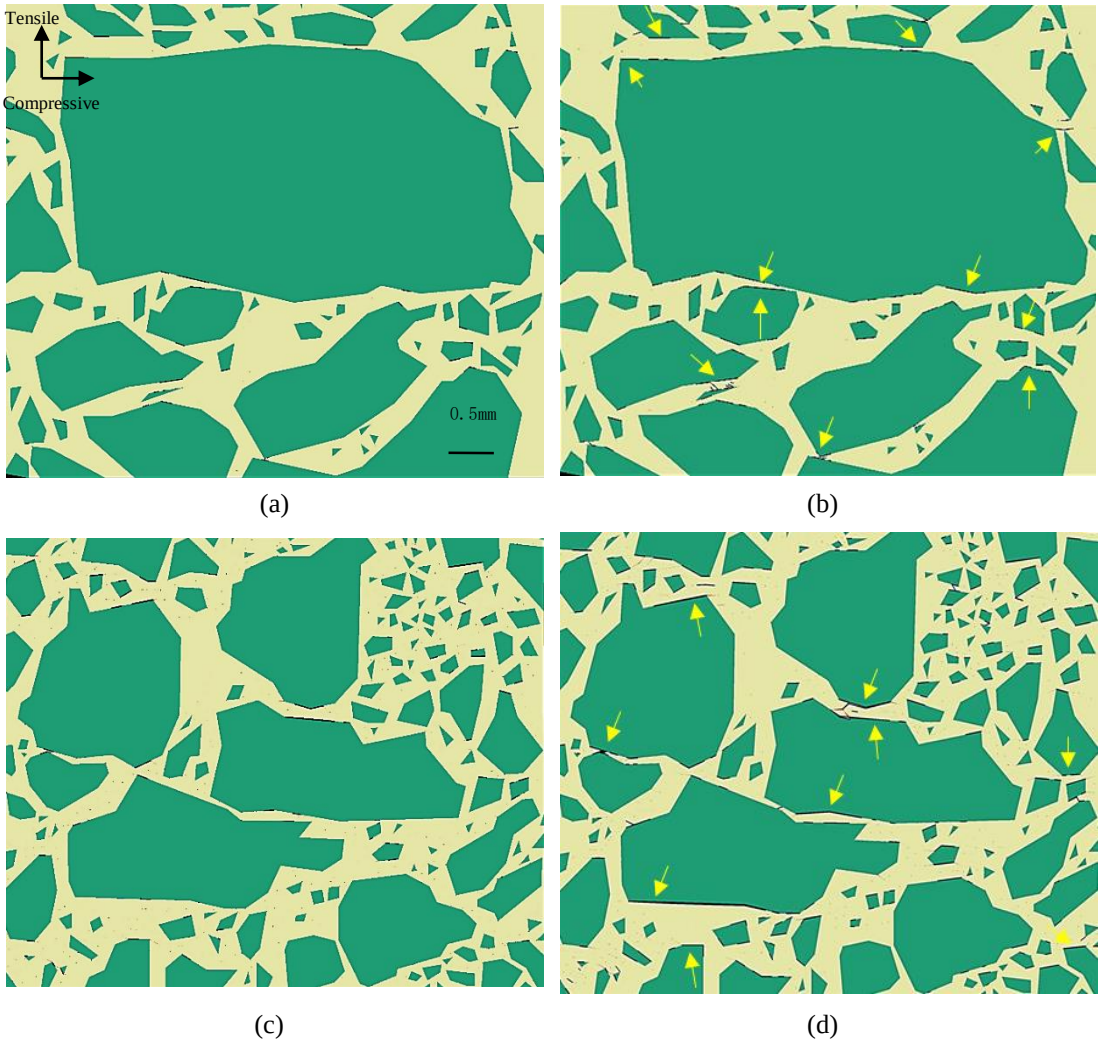


Figure 6.12: Crack initiation of (a) Sample 1# and (c) Sample 2# and propagation of (b) Sample 1# and (b) Sample 2# at 5 ℃.

6.7 Comparison between the Numerical Simulation and Experimental Results

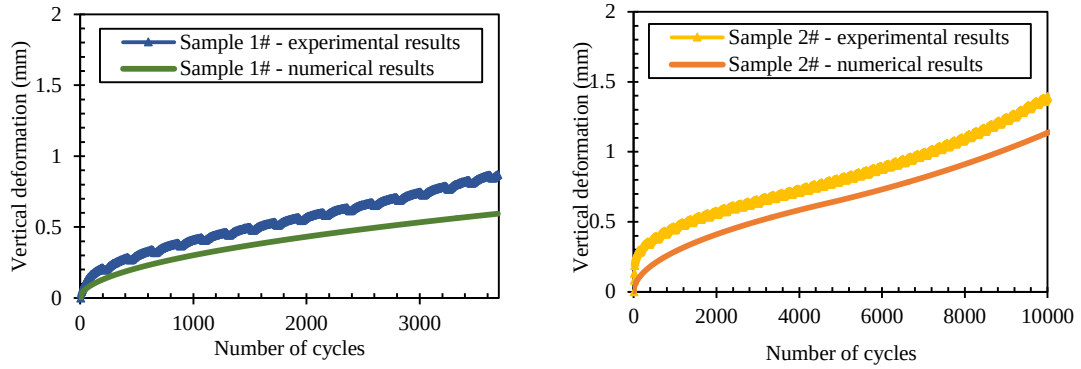
Figure 6.13 shows a comparison of the vertical deformation versus number of cycles of Sample 1# and Sample 2# between experimental and numerical results. The results show that the simulation results of both Sample 1# and Sample 2# have the same changing trend as the experimental results, proving the mechanical response of the model can approximately represent the real state in the experiment. Firstly, deformation develops rapidly, then the development speed slows down (observed in Figure 6.13a

and b), and finally the increase of deformation becomes rapid once again (observed in Figure 6.13b). The deformation simulated by the model is smaller than the deformation obtained in the experiment, for the reason that the model took only the central part of the specimen for simulation; in reality, the deformation in the central part of the specimen is less than that of the whole specimen in the experiment.

In the experiment, the number of cycles when the vertical deformation reaches 0.9 mm is 3690, while the same number of cycles in the simulation gives a deformation of 0.6 mm; the crack path of Sample 1# loaded to the same number of cycles in the simulation is shown in Figure 6.14b. It is observed that cracks develop at interfaces between the largest aggregate and the mastic, and these crack lengths are longer compared other cracks. In addition, where the aggregate distance is closer, the cracks develop more densely. Similar crack paths can also be observed in Figure 6.14a (the X-ray CT image of Sample 1# obtained in the experiment). In the experiment, the number of cycles for 1.4 mm vertical deformation is 10040, while the same number of cycles in the simulation gave a deformation of 1.1 mm; the crack path of Sample 2# loaded to the same number of cycles in the simulation is shown in Figure 6.14d. Compared to Sample 1#, Sample 2# has more cracks and the width of the cracks is wider, due to the increased number of loading cycles. It is observed that the crack development is mainly concentrated near the centre line of the load, and a long main crack tends to be produced. At the interfaces between the relatively large aggregates and the mastic, cracks are also observed to be developing. Similar crack paths can also be observed in Figure 6.14c (the X-ray CT image of Sample 2# obtained in the experiment).

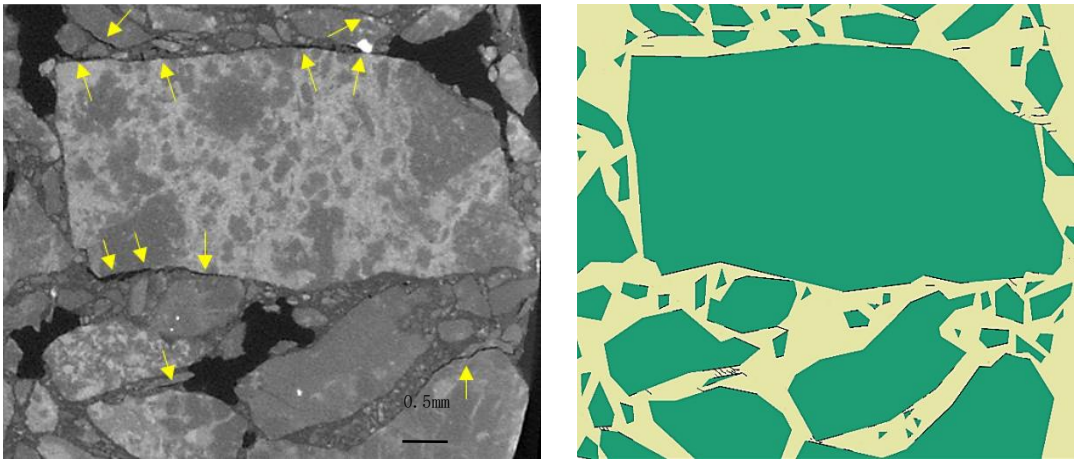
For both Sample 1# and Sample 2#, the numerical results produce more micro cracks in mastic than the experimental results. Theoretically, during crack development, tiny cracks will be initiated continuously, however, due to the limitations of current

technology, tiny cracks cannot be completely observed. It is concluded that the numerical and experimental crack paths are basically the same, including the crack geometry, the crack initiation position and propagation path. The 2D-FEM can approximately represent the real cracking behaviour in asphalt concrete.

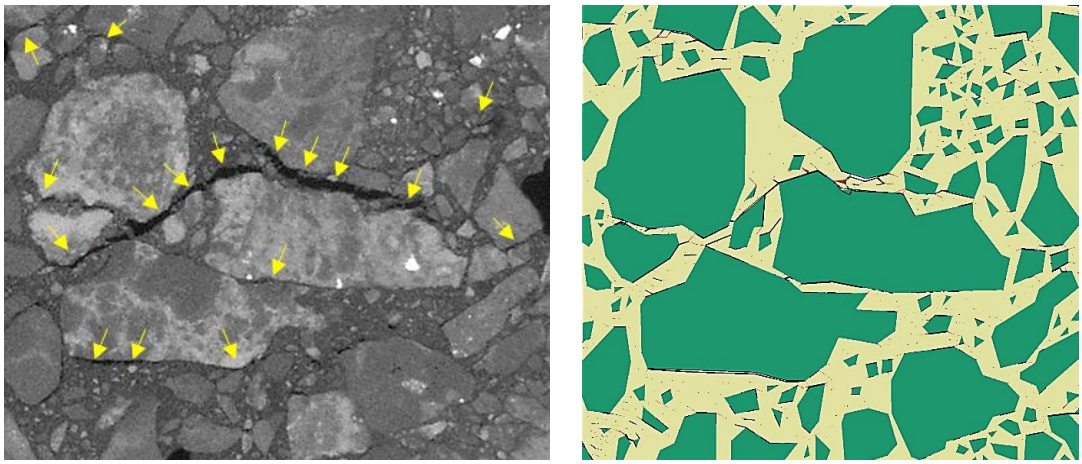


(a) (b)

Figure 6.13: Comparison of the vertical deformation versus number of cycles of (a) Sample 1#, and (b) Sample 2# between experimental and numerical results at 5 ℃.



(a) (b)



(c) (d)

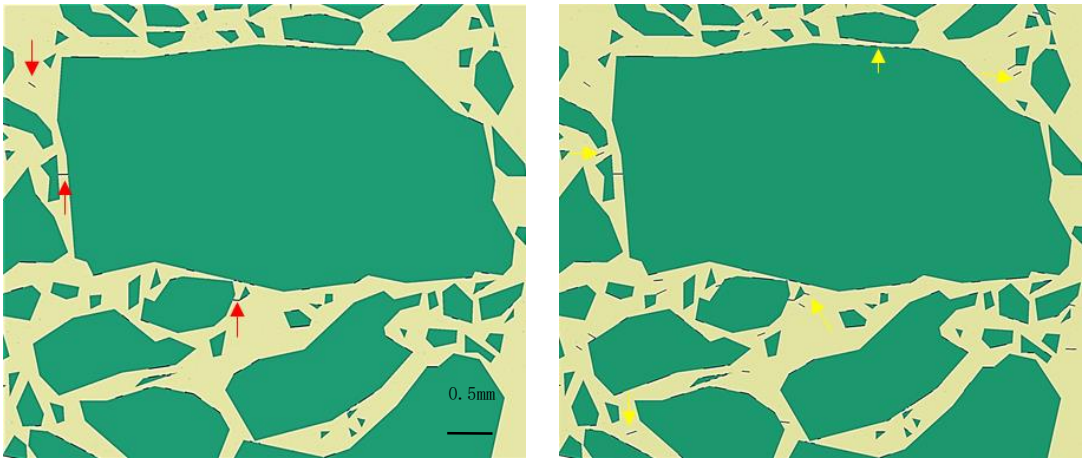
Figure 6.14: Comparison of crack paths of (a) (b) Sample 1#, and (c) (d) Sample 2# between experimental and numerical results.

6.8 Influence of Temperature on Fatigue Cracking Behaviours

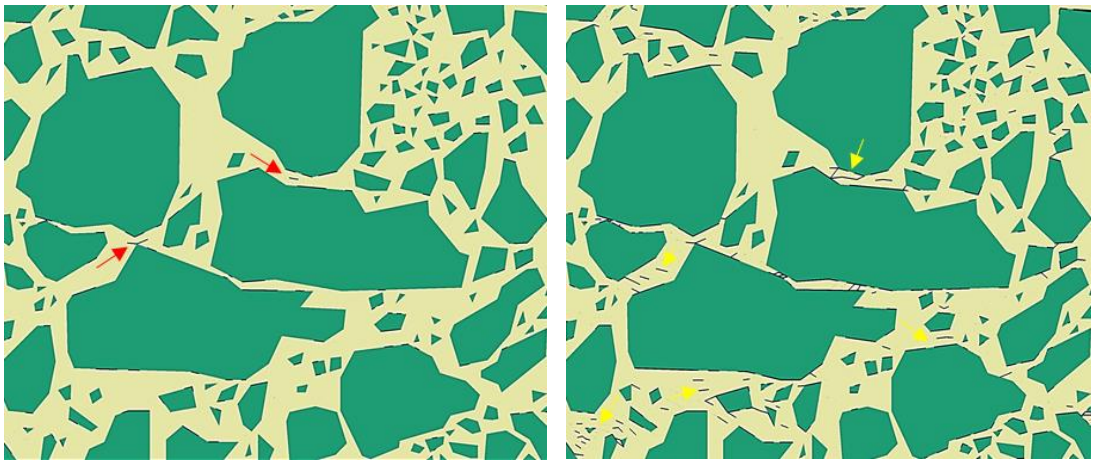
The model established in the thesis has been applied to simulate microcrack initiation and propagation of Sample 1# and Sample 2# at 25 ℃. The crack initiation and propagation of Sample 1# at 25 ℃ are shown in Figure 6.15a and b. Comparing with Figure 6.12a and b, the cracks are not only initiated at interfaces between aggregates and the mastic but also inside the mastic. With the increase of the number of cycles, cracks propagate at the contact surface and at the same time also propagate within the mastic, resulting in the length of cracks initiated at interfaces between aggregates and the mastic being shorter at 25 ℃ compared to 5 ℃. Unlike at low temperature, more new microcracks are also initiated in the mastic. Similar observations are also gained from the crack initiation and propagation of Sample 2# at 25 ℃ in Figure 6.15c and d.

It is concluded that, after microcracks initiating in asphalt concrete, the size and number of microcracks start to increase with the increase of loading cycles; microcracks are then connected together and form the macrocracks. After this, the sizes and numbers of macrocracks increase with increasing loading cycles; meanwhile, new microcracks are

still being initiated continuously. Therefore, the fatigue cracking in asphalt concrete is a combination of cracking in both micro and macro level, and cracking behaviours in these two levels influence each other. At higher temperature, the initiation time of macrocracks in asphalt concrete is delayed and the propagation rate slows down. It is because that, a larger number of microcracks tend to initiate in mastic at higher temperatures where the mastic is less brittle, resulting in less microcracks propagate to connect with each other to form macrocracks. This is phenomenon is the same with the research of Baek [240], which investigated the cracking mechanism of asphalt concrete overlayer with the numerical simulation method; the results shown that asphalt concrete is not easy to crack at a higher temperature due to it can dissipate more energy, and the crack initiation time of asphalt concrete is delayed and crack propagation rate slows down.



(a) (b)



(c) (d)

Figure 6.15: Microcrack initiation of (a) Sample 1# and (c) Sample 2# and propagation of (b) Sample 1# and (b) Sample 2# at 25 °C.

6.9 Conclusions

The main conclusions of this chapter are as follows:

1. Higher resolution X-ray CT scanning is a suitable method to visualize detailed crack geometry of asphalt concrete, and the realistic aggregate morphology in FE model of two phases (aggregate and mastic) can be reconstructed from the CT images.

2. The bespoke tensile test mounted on a UTM is a proper approach to obtain the maximum cohesive strength and the fracture energy of asphalt mastics which can be used for FE modelling.

3. The model zero-thickness cohesive elements are embedded both in asphalt mastic and at interfaces between mastic and aggregates of FE model, the results show that the numerical and experimental crack paths and mechanical response are basically the same. The 2D-FEM developed can approximately represent the real cracking behaviour in asphalt concrete.

4. Basing on this model, the factors such as aggregate size and distance between aggregates can affect the crack initiation, and the larger the aggregate or the closer the distance between aggregates, the more the stress will be concentrated and cracking will initiate.

5. Fatigue cracking in asphalt concrete occurs as a result of interaction between micro- and macro-scale cracks. Macrocracks are formed concurrently with the initiation and propagation of microcracks.

6. More energy is used for microcracks initiating in mastic at high temperature, leading to less microcracks being developed and connected with each other to form macrocracks.

7 Conclusions and Recommendations

7.1 Conclusions

The project investigated micro mechanism of fatigue cracking in asphalt concrete， the main conclusions of this project included the following three parts:

1. The stiffness development during fatigue damage of asphalt concrete was studied with different methods, and also be linked to crack development, which is used to revel the damage mechanical mechanism of asphalt concrete. The results show that:

(1) Logistic model is a good model to characterise the relationship between the stiffness (E) and the number of cycles (N). Three transition points (P1, P2 & P3) associated with fatigue progression were determined to characterise the different fatigue damage stages of asphalt concrete. The stiffness ratio at the three transition points is similar across all samples.

(2) The SCTM is applicable to be used to model stiffness development of different asphalt mixtures and different test methods, it can be used to link the stiffness development to cracks development, and determine the number of cycles where the crack length starts to increase rapidly (cracks initiate) and where the crack length starts to increase steadily and continuously (cracks propagate).

(3) The P1 and P2 calculated by the SCTM are proved to be related to the crack initiation and propagation respectively. P1 is viewed as the number of cycles to micro-crack initiation and propagation. The region prior to P1 is the micro-crack formation region. P2 is defined as the macro-crack generation point.

2. The fatigue damage in asphalt concrete of asphalt concrete was characterised in the micro level with the high-resolution X-ray CT, the results show that:

(1) There is a close relationship between the vertical deformation and the strain level, the fatigue damage process consists of three distinct stages. At the first stage, deformation develops rapidly before slowing down, only a few microcracks occur at the aggregate–mastic interfaces; at the second stage, the vertical deformation of asphalt concrete develops approximately linearly, the microcracks spread continuously, and some microcracks connect; at the third stage, the deformation becomes rapid once again, the air voids grow rapidly, and microcracks emerge swiftly.

(2) Flat and elongated particles and the irregular shape of aggregates may lead to stress concentrations in asphalt concrete, and causing the initiation and propagation of microcracks. The AVC development law shows that the sample is mainly in compression at relatively small deformation, then changes to a predominantly tensile strain with the increase of deformation, and cracks develop faster as deformation increases. The maximum increase in the AVC (fatigue damage) often occurs near the middle of the sample.

(3) The small size air voids (microcracks) develop continuously throughout the entire fatigue process, which leads to the increase of AVC.

3. A numerical modelling of fatigue cracking in asphalt concrete was constructed using cohesive elements. The results show that:

(1) The 2D FE model of asphalt concrete can be conducted to investigate the crack asphalt concrete initiation and propagation. The crack geometry, the crack initiation position and propagation path of numerical model and experimental

samples are basically the same, indicates that the numerical model constructed can approximately represent the real cracking behaviour in asphalt concrete.

(2) Macrocracks were formed with microcracks constantly being initiated and propagated. The factors such as aggregate size, distance between aggregates, and the temperature can affect the crack initiation and propagation of asphalt concrete. The larger the aggregate is, the closer the distance between aggregates is, the easier the stress will be concentrated and crack will initiate. Meanwhile, at high temperature, microcracks tend to initiate and propagate in mastic, with the microcracks propagating, new microcracks are still being initiated continuously. More energy is used for microcracks initiating in mastic at high temperature, leading to less microcracks developed and connected with each other to form macrocracks.

7.2 Recommendations and Future work

The following work is recommended in this project:

1. The SCTM can be useful in a simulation of pavement deterioration by prediction of remaining fatigue life of asphalt concrete, as long as part of the fatigue test data is known. Depending on the relationship between stiffness development and crack development on pavements, the crack development on pavements can be predicted by testing the stiffness of core specimens on pavements.

2. In the future, the relationship between the development of microcracks and macrocracks can be analysed, as well as the combined effect of microcracks and macrocracks on the stiffness deterioration of the specimen. In addition, the influence of the aggregate distribution, the distance between aggregates, and aggregate size on the initiation and propagation of microcracks can be further

analysed quantitatively.

3. One important point of the simulation using cohesive elements is to obtain effective cohesive strength of the mastic. In the past, the tensile strength is obtained through ITFTs or semi-circular bending tests of the asphalt mixture to represent cohesive strength of the mastic, while there is a certain difference between two. This thesis found a proper approach that is the bespoke tensile test mounted on UTM, to obtain the maximum cohesive strength and the fracture energy of asphalt mastics. In future study, the test method can be used to test the cohesive strength under various conditions to meet needs of different CZM-based simulations, such as applied on water damaged or aged specimens, or changing the test temperature, or changing the properties of the mastic like binder type and gradation etc..

4. The numerical model developed can approximately represent the real cracking behaviour in asphalt concrete. In the future, the simulated parameters can be changed, including the aggregate type, the binder type, the aggregate gradation, the load conditions, the temperature conditions, etc., to further study the micro-cracking mechanism to improve the material's fatigue resistance performance.

References

[1] Moving Britain Ahead. Road Traffic Forecasts 2018, Department for Transport, 2018.

[2] L. Raad, J.L. Figueroa, LOAD RESPONSE OF TRANSPORTATION SUPPORT SYSTEMS, Transportation Engineering Journal, 106(1) (1980) 111-128.

[3] X.Z. Hu, F.H. Wittmann, Fracture energy and fracture process zone, Materials & Structures, 25(6) (1992) 319-326.

[4] R.L. Carvalho, C.W. Schwartz, Comparisons of flexible pavement designs: AASHTO empirical versus NCHRP project 1–37A mechanistic–empirical, Transportation Research Record, 1947(1) (2006) 167-174.

[5] J.H. Maree, C.R. Freeme, E.G. Kleyn, HEAVY-VEHICLE SIMULATOR TESTING IN SOUTH AFRICA, Benefit Cost Analysis, (1900).

[6] L.D. Poulikakos, M. Pittet, A.G. Dumont, M.N. Partl, Comparison of the two point bending and four point bending test methods for aged asphalt concrete field samples, Materials & Structures, (2014).

[7] S. Kumar, S.V. Barai, Structures, Determining the double-Kfracture parameters for three-point bending notched concrete beams using weight function, Fatigue & Fracture of Engineering Materials, 33(10) (2010) 645-660.

[8] T.B. Moghaddam, M.R. Karim, M. Abdelaziz, A review on fatigue and rutting performance of asphalt mixes, entific research & essays, 6(4)(4) (2011) 670-682.

[9] E. Arambula, M.E. Kutay, Tension-compression fatigue test evaluation using fracture mechanics and field data, Road materials & pavement design, 10(1) (2009) 83-108.

[10] S. Said, J. Vieira, H. Hakim, O. Eriksson, R. Nilsson, A. Cocurullo, Interlaboratory experiment of asphalt concrete using indirect tensile fatigue test, Eurasphalt &

Eurobitume Congress, 5th, 2012, Istanbul, Turkey, 2012.

[11] N. Thom, Asphalt cracking: a Nottingham perspective, Engenaria Civil/Civil Engineering, 26 (2006) 75-84.

[12] D.J. Kulash, Update on the Strategic Highway Research Program (SHRP), (1992).

[13] P.S. Pell, CHARACTERIZATION OF FATIGUE BEHAVIOR, CHARACTERIZATION OF FATIGUE BEHAVIOR1973.

[14] C.L. Monismith, J.A. Epps, D.A. Kasianchuk, D.B. Mclean, Asphalt Mixture Behaviour in Repeated Flexure (with Discussion and Closure), 1970.

[15] C.L. Monismith, J.A. Epps, F.N. Finn, IMPROVED ASPHALT MIX DESIGN (WITH DISCUSSION), Association of Asphalt Paving Technologists Proc,, 1985.

[16] M.A. Miner, Cumulative damage in fatigue, Journal of Applied Mechanics, (1945).

[17] A.A. Griffith, The Phenomena of Rupture and Flow in Solids, Philosophical Transactions of The Royal Society A Mathematical Physical & Engineering Sciences, A221(4) (1920) 163-198.

[18] K. Majidzadeh, E. Kauffmann, D. Ramsamooj, Application of fracture mechanics in the analysis of pavement fatigue, Association of Asphalt Paving Technologists Proc,, 1971.

[19] S. Sulaiman, A. Stock, The use of fracture mechanics for the evaluation of asphalt mixes (with discussion), Journal of the Association of Asphalt Paving Technologists, 64 (1995).

[20] M. Jacobs, P. Hopman, A. Molenaar, Application of fracture mechanics principles to analyze cracking in asphalt concrete (with discussion), Journal of the Association of Asphalt Paving Technologists, 65 (1996).

[21] P. Paris, A critical analysis of crack propagation laws, Journal of Basic Engineering, 85 (1963).

[22] E.K. Walker, The Effect of Stress Ratio During Crack Propagation and Fatigue for 2024-T3 and 7075-T6 Aluminum, (1970).

[23] R.J. Donahue, H.M. Clark, P. Atanmo, R. Kumble, A.J. Mcevily, Crack opening displacement and the rate of fatigue crack growth, International Journal of Fracture Mechanics, 8(2) (1972) 209-219.

[24] N.E.J.A.S. Dowling, Fatigue crack growth during gross plasticity and the J-integral, 590 (1976).

[25] S. Najjar, A.M. Moghaddam, A. Sahaf, M. Aliha, Low temperature fracture resistance of cement emulsified asphalt mortar under mixed mode I/III loading, Theoretical & Applied Fracture Mechanics 110(2) (2020) 102800.

[26] S. Pirmohammad, M.R. Ayatollahi, Fracture resistance of asphalt concrete under different loading modes and temperature conditions - ScienceDirect, Construction & Building Materials 53(1) (2014) 235-242.

[27] K.A. Ghuzlan, S.H. Carpenter, Energy-derived, damage-based failure criterion for fatigue testing, Transportation research record, 1723(1) (2000) 141-149.

[28] Y.-R. Kim, D. Little, R. Lytton, Fatigue and healing characterization of asphalt mixtures, Journal of Materials in Civil Engineering, 15(1) (2003) 75-83.

[29] G.M. Rowe, Application of the dissipated energy concept to fatigue cracking in asphalt pavements, University of Nottingham,, 1996.

[30] W. Van Dijk, H. Moreaud, A. Quedeville, P. Uge, The fatigue of bitumen and bituminous mixes, Presented at the Third International Conference on the Structural Design of Asphalt Pavements, Grosvenor House, Park Lane, London, England, Sept. 11-15, 1972., 1972.

[31] W. Van Dijk, W. Visser, Energy approach to fatigue for pavement design,

Association of Asphalt Paving Technologists Proc,, 1977.

[32] S. Shen, S.H. Carpenter, Dissipated energy concepts for HMA performance: fatigue and healing, Citeseer2006.

[33] Y.R. Kim, H.-J. Lee, D.N. Little, Fatigue characterization of asphalt concrete using viscoelasticity and continuum damage theory (with discussion), Journal of the Association of Asphalt Paving Technologists 66 (1997).

[34] Y.R. Kim, D.N. Little, R. Lytton, J. D'Angelo, R. Davis, G. Rowe, G. Reinke, M. Marasteanu, E. Masad, R. Roque, Use of dynamic mechanical analysis (DMA) to evaluate the fatigue and healing potential of asphalt binders in sand asphalt mixtures, Asphalt Paving Technology: Association of Asphalt Paving Technologists-Proceedings of the Technical Sessions, Association of Asphalt Paving Technologist, 2002, pp. 176-206.

[35] J.S. Daniel, Y.R. Kim, S. Brown, G. Rowe, G. Reinke, Development of a simplified fatigue test and analysis procedure using a viscoelastic, continuum damage model, Asphalt Paving Technology: Association of Asphalt Paving Technologists-Proceedings of the Technical Sessions, 2002.

[36] E. Masad, V.T.F.C. Branco, D.N. Little, R. Lytton, A unified method for the analysis of controlled-strain and controlled-stress fatigue testing, International Journal of Pavement Engineering 9(4) (2008) 233-246.

[37] Z.Q. Yue, W. Bekking, I. Morin, Application of digital image processing to quantitative study of asphalt concrete microstructure, Transportation Research Record, 1492 (1995) 53-60.

[38] Z. Feng, P. Zhang, M.N. Guddati, Y.R. Kim, The development and evaluation of a virtual testing procedure for the prediction of the cracking performance of hot mix asphalt, Pavements and Materials: Testing and Modeling in Multiple Length Scales2010, pp. 142-158.

[39] Q. Dai, K. Ng, An extended finite element model for characterization of concrete fracture properties with compact tension tests, Pavements and materials: Testing and modeling in multiple length scales,2010, pp. 159-169.

[40] M. Stolarska, D.L. Chopp, N. Moës, T. Belytschko, Modelling crack growth by level sets in the extended finite element method, International journal for numerical methods in Engineering, 51(8) (2001) 943-960.

[41] H. Kim, M.P. Wagoner, W.G. Buttlar, Simulation of fracture behavior in asphalt concrete using a heterogeneous cohesive zone discrete element model, Journal of materials in civil engineering, 20(8) (2008) 552-563.

[42] L. Wang, Mechanics of asphalt: microstructure and micromechanics, McGraw-Hill Education2011.

[43] J. Hu, P. Liu, D. Wang, M. Oeser, Y. Tan, Investigation on fatigue damage of asphalt mixture with different air-voids using microstructural analysis, Construction & Building Materials, 125 (2016) 936-945.

[44] M. Amouzadeh Omrani, A. Modarres, Stiffness and fatigue behavior of emulsified cold recycled mixture containing waste powder additives: mechanical and microstructural analysis, Journal of Materials in Civil Engineering, 31(6) (2019) 04019061.

[45] R. Jahangir, D. Little, A. Bhasin, Evolution of asphalt binder microstructure due to tensile loading determined using AFM and image analysis techniques, International Journal of Pavement Engineering, 16(4) (2015) 337-349.

[46] S. Caro, E. Masad, A. Bhasin, D.N. Little, Moisture susceptibility of asphalt mixtures, Part 2: characterisation and modelling, International Journal of Pavement Engineering, 9(2) (2008) 99-114.

[47] Y. Lu, L. Wang, Nanoscale modelling of mechanical properties of asphalt–aggregate interface under tensile loading, International Journal of Pavement Engineering, 11(5) (2010) 393-401.

[48] Y. Lu, Atomistic characterization and modeling of the deformation and failure properties of asphalt-aggregate interface, Virginia Tech, 2010.

[49] W. Powell, J. Potter, H. Mayhew, M. Nunn, The structural design of bituminous

roads, 1984.

[50] J. Brunton, S. Brown, P. Pell, Development of the Analytical Design Method of Asphalt Pavements, Sixth International Conference on The Structural Design of Asphalt Pavements, pp. 13-17.

[51] A.A. Tayebali, J.A. Deacon, C.L. Monismith, DEVELOPMENT AND EVALUATION OF SURROGATE FATIGUE MODELS FOR SHRP A-003A ABRIDGED MIX DESIGN PROCEDURE (WITH DISCUSSION), Journal of the Association of Asphalt Paving Technologists, 64 (1995).

[52] N.R. Council, Fatigue response of asphalt-aggregate mixes, 1994.

[53] A. Claessen, J. Edwards, P. Sommer, P. Uge, Asphalt pavement design--the shell method, Volume I of proceedings of 4th International Conference on Structural Design of Asphalt Pavements,, 1977, pp. 22-26.

[54] B.-W. Tsai, J.T. Harvey, C.L. Monismith, WesTrack fatigue performance prediction using Miner's law, Transportation research record, 1809(1) (2002) 137-147.

[55] A. Caballero, C.M. Lopez, I. Carol, 3D meso-structural analysis of concrete specimens under uniaxial tension, Computer Methods in Applied Mechanics & Engineering, 195(52) (2006) 7182-7195.

[56] A. Gelman, J. Hill, Data analysis using regression and multilevel/hierarchical models, Cambridge university press2006.

[57] D.R. Cox, The regression analysis of binary sequences, Journal of the Royal Statistical Society: Series B, 20(2) (1958) 215-232.

[58] C. Polykretis, C. Chalkias, Comparison and evaluation of landslide susceptibility maps obtained from weight of evidence, logistic regression, and artificial neural network models, Natural Hazards: Journal of the International Society for the Prevention & Mitigation of Natural Hazards, 93(1) (2018) 249-274.

[59] B.T. Pham, D.T. Bui, I. Prakash, Landslide susceptibility assessment using bagging

ensemble based alternating decision trees, logistic regression and J48 decision trees methods: a comparative study, Geotechnical & Geological Engineering, 35(6) (2017) 2597-2611.

[60] M. Andrejiova, A. Grincova, D. Marasova, Failure analysis of rubber composites under dynamic impact loading by logistic regression, Engineering Failure Analysis, 84 (2018) 311-319.

[61] H. Lee, J.A. Chun, H.-H. Han, S. Kim, Prediction of frost occurrences using statistical modeling approaches, Advances in Meteorology, 2016 (2016).

[62] A.U. Haq, J.P. Li, M.H. Memon, S. Nazir, R. Sun, A hybrid intelligent system framework for the prediction of heart disease using machine learning algorithms, Mobile Information Systems, 2018 (2018).

[63] M. Chang, M. Maguire, Y. Sun, Stochastic modeling of bridge deterioration using classification tree and logistic regression, Journal of Infrastructure Systems, 25(1) (2019) 04018041.

[64] K. Shaaban, D. Muley, D. Elnashar, Evaluating the effect of seasonal variations on walking behaviour in a hot weather country using logistic regression, International Journal of Urban Sciences, 22(3) (2018) 382-391.

[65] Y. Ali, M. Irfan, A.S. Buller, H.A. Khan, H.M. Gul, A binary logistic model for predicting the tertiary stage of permanent deformation of conventional asphalt concrete mixtures, Construction & Building Materials, 227 (2019) 116608.

[66] D. Rys, J. Judycki, M. Pszczola, M. Jaczewski, L. Mejlun, Comparison of low-temperature cracks intensity on pavements with high modulus asphalt concrete and conventional asphalt concrete bases, Construction & Building Materials, 147 (2017) 478-487.

[67] Y. Wang, Ordinal logistic regression model for predicting AC overlay cracking, Journal of Performance of Constructed Facilities, 27(3) (2013) 346-353.

[68] R.A. Ketcham, W.D. Carlson, Acquisition, optimization and interpretation of X-

ray computed tomographic imagery: applications to the geosciences, Computers & Geosciences, 27(4) (2001) 381-400.

[69] N.A. Hassan, G. Airey, A. Collop, Microstructural characterisation of rubber modified asphalt mixtures, University of Nottingham United Kingdom, 2012.

[70] A.G. Michette, C.J. Buckley, X-ray Science and Technology, (1993).

[71] P.E. Stutzman, Cement Clinker Characterization by Scanning Electron Microscopy, Cement Concrete & Aggregates, 13(2) (1991) 6.

[72] S. Diamond, Interactive Digital Image Feature Analysis as Applied to Cement and Concrete Microstructural Investigations, Digital Image Processing: Techniques & Applications in Civil Engineering, 1993.

[73] M.E. Kutay, E. Arambula, N. Gibson, J. Youtcheff, Three-dimensional image processing methods to identify and characterise aggregates in compacted asphalt mixtures, International Journal of Pavement Engineering, 11(6) (2010) 511-528.

[74] Shashidhar, N., X-Ray Tomography of Asphalt Concrete, Journal of the Transportation Research Board, 1681 (1999) 186-192.

[75] E. Masad, B. Muhunthan, N. Shashidhar, Internal Structure Characterization of Asphalt Concrete Using Image Analysis, Journal of Computing in Civil Engineering, 13(2) (1999) 88-95.

[76] A.A. Alomari, L. Tashman, E. Masad, A. Cooley, T. Harman, Proposed Methodology for Predicting HMA Permeability, Asphalt Paving Technology: Association of Asphalt Paving Technologists-Proceedings of the Technical Sessions, 71(1) (2002) 30-58.

[77] H.M. Zelelew, A.T. Papagiannakis, Wavelet-based characterisation of aggregate segregation in asphalt concrete X-ray computed tomography images, International Journal of Pavement Engineering, 12(6) (2011) 553-559.

[78] Y.H. Duan, X.N. Zhang, L. Zhi, D.Y. Wang, A New Method to Characterize the

Stone-Stone Contact Degree of Asphalt Mixture Using X-ray Computed Tomography Images, International Journal of Pavement Research & Technology, 4(6) (2011) 356-364.

[79] C. Bhabatosh, Digital image processing and analysis, PHI Learning Pvt. Ltd.1977.

[80] H. Wang, C. Wang, Z. You, X. Yang, Z. Huang, Characterising the asphalt concrete fracture performance from X-ray CT Imaging and finite element modelling, International Journal of Pavement Engineering, 19(3) (2018) 307-318.

[81] C. Polykretis, C.J.N.H.J.o.t.I.S.f.t.P. Chalkias, M.o.N. Hazards, Comparison and evaluation of landslide susceptibility maps obtained from weight of evidence, logistic regression, and artificial neural network models, 93 (2018).

[82] M. Sonka, V. Hlavac, R. Boyle, Image processing, analysis, and machine vision, Cengage Learning2014.

[83] Q. Dai, M.H. Sadd, Z. You, A micromechanical finite element model for linear and damage-coupled viscoelastic behaviour of asphalt mixture, International Journal for Numerical & Analytical Methods in Geomechanics, 30(11) (2010).

[84] L. Uthus, M. Hopkins, I. Horvli, Discrete element modelling of the resilient behaviour of unbound granular aggregates, International Journal of Pavement Engineering, 9(6) (2008) 387-395.

[85] M. Khanal, R. Tomas, Application of DEM to evaluate and compare process parameters for a particle failure under different loading conditions, Granular Matter, 12(4) (2010) 411-416.

[86] J. Chen, B. Huang, F. Chen, X. Shu, Application of discrete element method to Superpave gyratory compaction, Road materials & pavement design, 13(3) (2012) 480-500.

[87] M.H. Sadd, Q. Dai, A comparison of micro-mechanical modeling of asphalt materials using finite elements and doublet mechanics, Mechanics of Materials, 37(6) (2005) 641-662.

[88] J.R. Williams, A.P. Pentland, SUPERQUADRICS AND MODAL DYNAMICS FOR DISCRETE ELEMENTS IN INTERACTIVE DESIGN, Engineering Computations, 9(2) (1992) 115-127.

[89] H.J. Tillemans, H.J. Herrmann, Simulating deformations of granular solids under shear, Physica A: Statistical Mechanics & its Applications, 217(3-4) (1995) 261-288.

[90] A.V. Potapov, C.S. Campbell, A fast model for the simulation of non-round particles, Granular Matter, 1(1) (1998) 9-14.

[91] G. Mustoe, M. Miyata, Material Flow Analyses of Noncircular-Shaped Granular Media Using Discrete Element Methods, Journal of Engineering Mechanics, 127(10) (2008) 1017-1026.

[92] L. Yu, Z. You, Simulation of Cyclic Loading Tests for Asphalt Mixtures Using User Defined Models within Discrete Element Method, Geotechnical Special Publication, (179) (2008).

[93] L. Pournin, M. Weber, M. Tsukahara, J.-A. Ferrez, M. Ramaioli, T.M. Liebling, Three-dimensional distinct element simulation of spherocylinder crystallization, Granular Matter, 7(2-3) (2005) 119-126.

[94] H. Abou-Chakra, J. Baxter, U. Tüzün, Three-dimensional particle shape descriptors for computer simulation of non-spherical particulate assemblies, Advanced Powder Technology, 15(1) (2004) 63-77.

[95] Y. Lee, C. Fang, Y.R. Tsou, L.S. Lu, C.T. Yang, A packing algorithm for three-dimensional convex particles, Granular Matter, 11(5) (2009) 307-315.

[96] X. Yang, Z. You, C. Jin, H. Wang, Aggregate representation for mesostructure of stone based materials using a sphere growth model based on realistic aggregate shapes, Materials and Structures, 49(6) (2016) 2493-2508.

[97] X. Yang, Q. Dai, Z. You, Z. Wang, Integrated experimental-numerical approach for estimating asphalt mixture induction healing level through discrete element modeling of a single-edge notched beam test, Journal of Materials in Civil Engineering,

27(9) (2015) 04014259.

[98] E.J. Garboczi, N.S. Martys, H.H. Saleh, R.A. Livingston, Acquiring, analyzing, and using complete three-dimensional aggregate shape information, Aggregates: Concrete, Bases, & Fines, 2001.

[99] J. E., Garboczi, Three-dimensional mathematical analysis of particle shape using X-ray tomography and spherical harmonics: Application to aggregates used in concrete, Cement & Concrete Research, (2002).

[100] Z. Qian, E.J. Garboczi, G. Ye, E. Schlangen, Anm: a geometrical model for the composite structure of mortar and concrete using real-shape particles, Materials and Structures, 49(1-2) (2016) 149-158.

[101] P. Romero, E. Masad, A. Members, RELATIONSHIP BETWEEN THE REPPRESENTATIVE VOLUME ELEMENT AND MECHANICAL PROPERTIES OF ASPHALT CONCRETE, Journal of Materials in Civil Engineering, 13(1) (2001) p.77-88.

[102] E. Masad, N. Somadevan, H.U. Bahia, S. Kose, Modeling and Experimental Measurements of Strain Distribution in Asphalt Mixes, Journal of Transportation Engineering, 127(6) (2001) 477-485.

[103] A. Papagiannakis, A. Abbas, E. Masad, Micromechanical Analysis of Viscoelastic Properties of Asphalt Concretes, Transportation Research: Record Journal of the Transportation Research Board, 1789 (2002) 113-120.

[104] Q. Dai, Prediction of Dynamic Modulus and Phase Angle of Stone-Based Composites Using a Micromechanical Finite-Element Approach, Journal of Materials in Civil Engineering, 22(6) (2010) 618-627.

[105] Z. You, W.G. Buttlar, Discrete Element Modeling to Predict the Modulus of Asphalt Concrete Mixtures, Journal of Materials in Civil Engineering, 16(2) (2004) 140-146.

[106] Z. You, W.G. Buttlar, Application of Discrete Element Modeling Techniques to

Predict the Complex Modulus of Asphalt-Aggregate Hollow Cylinders Subjected to Internal Pressure, Journal of the Transportation Research Board, 1929(1929) (2005) 218-226.

[107] Z. You, W. Buttlar, Micromechanical Modeling Approach to Predict Compressive Dynamic Moduli of Asphalt Mixtures Using the Distinct Element Method, Transportation Research Record Journal of the Transportation Research Board, 1970(1970) (2006) 73-83.

[108] L. Wang, Stress Concentration Factor of Poroelastic Material by FEM Simulation and X-ray Tomography Imaging.

[109] Z. Bing, L. Wang, M.T. Tumay, An Evaluation of the Stress Non-Uniformity Due to the Heterogeneity of AC in the Indirect Tensile Test, Geotechnical Special Publication, (146) (2005) 29-43.

[110] Dassault Systèmes Simulia Corp.

[111] Z. You, S. Adhikari, Q. Dai, Three-dimensional discrete element models for asphalt mixtures, Journal of engineering mechanics, 134(12) (2008) 1053-1063.

[112] Z. You, S. Adhikari, M.E. Kutay, Dynamic modulus simulation of the asphalt concrete using the X-ray computed tomography images, Materials & Structures, 42(5) (2009) 617-630.

[113] T. You, R. Al-Rub, E.A. Masad, D.N. Little, Three-Dimensional Microstructural Modeling of Asphalt Concrete by Use of X-Ray Computed Tomography, Transportation Research Board: Journal of the Transportation Research Board, 2373(1) (2013) 63-70.

[114] Avizo, Avizo User's Guide, FEI Visualization Sciences Group, 2009.

[115] Z. Bažant, J. Planas, Fracture and Size Effect in Concrete and Other Quasibrittle Materials, Civil and Environmental Engineering, (1997).

[116] G.I. Barenblatt, The formation of equilibrium cracks during brittle fracture.

General ideas and hypotheses. Axially-symmetric cracks, Journal of Applied Mathematics and Mechanics, 23(3) (1959) 622-636.

[117] G.I. Barenblatt, The Mechanical Theory of Equilibrium Cracks in Brittle Fracture, Advances in Applied Mechanics, 7 (1962) 55-129.

[118] D.S. Dugdale, Yielding of steel sheets containing slits, Journal of the Mechanics & Physics of Solids, 8(2) (1960) 100-104.

[119] K. Park, G.H. Paulino, Computational implementation of the PPR potential-based cohesive model in ABAQUS: Educational perspective, Engineering Fracture Mechanics, 93(Complete) (2012) 239-262.

[120] A. P., Klein, and, W. J., Foulk, and, P. E., Chen, and, A. S., Physics-based modeling of brittle fracture: cohesive formulations and the application of meshfree methods, Theoretical & Applied Fracture Mechanics, (2001).

[121] J. Roesler, G.H. Paulino, K. Park, C. Gaedicke, Concrete fracture prediction using bilinear softening, Journal of Computing in Civil Engineering, 29(4) (2007) 300-312.

[122] K. Park, Potential-based fracture mechanics using cohesive zone and virtual internal bond modeling, Dissertations & Theses - Gradworks, (2009).

[123] G.H. Paulino, S.H. Song, W.G. Buttlar, Cohesive zone modeling of fracture in asphalt concrete, the 5th International RILEM Conference–Cracking in Pavements: Mitigation, Risk Assessment, and Preservation,, 2004.

[124] Q.D. Yang, M.D. Thouless, Mixed-mode fracture analyses of plastically-deforming adhesive joints, International Journal of Fracture, 110(2) (2001) 175-187.

[125] M.J.v.d.B.a. b, P.J.G.S. A, M.G.D.G. A, An improved description of the exponential Xu and Needleman cohesive zone law for mixed-mode decohesion, Engineering Fracture Mechanics, 73(9) (2006) 1220-1234.

[126] L.A. Girifalco, V.G. Weizer, Application of Morse Potential Function to Cubic Metals, Physical Review, 114((3)) (1958) 687.

[127] Needleman, A., A Continuum Model for Void Nucleation by Inclusion Debonding, Journal of Applied Mechanics, 54(3) (1987) 525.

[128] A. Needleman, An analysis of tensile decohesion along an interface, Journal of the Mechanics & Physics of Solids, 38(3) (1990) 289-324.

[129] J.H. Rose, J. Ferrante, J.R. Smith, Universal Binding Energy Curves for Metals and Bimetallic Interfaces, Physical Review Letters, 47(9) (1981).

[130] V. Tvergaard, Effect of fibre debonding in a whisker-reinforced metal, Materials Science & Engineering A, 125(2) (1990) 203-213.

[131] V. Tvergaard, J.W. Hutchinson, The influence of plasticity on mixed mode interface toughness, Journal of the Mechanics & Physics of Solids, 41(6) (1993) 1119-1135.

[132] I. Scheider, W. Brocks, Simulation of cup–cone fracture using the cohesive model, Engineering Fracture Mechanics, 70(14) (2003) 1943-1961.

[133] K.D. Papoulia, C.H. Sam, S.A. Vavasis, Time continuity in cohesive finite element modeling, International Journal for Numerical Methods in Engineering, 58(5) (2010) 679-701.

[134] G.T. Camacho, M. Ortiz, Computational modelling of impact damage in brittle materials, International Journal of Solids & Structures, 33(20-22) (1996) 2899-2938.

[135] J.S. Baylor], Impact-induced delamination of composites: a 2D simulation, Composites Part B: Engineering, (1998).

[136] Horacio, D. ., Espinosa, and, Pablo, D. ., Zavattieri, A grain level model for the study of failure initiation and evolution in polycrystalline brittle materials. Part I: Theory and numerical implementation, Mechanics of Materials, (2003).

[137] K. Park, Concrete fracture mechanics and size effect using a specialized cohesive zone model, University of Illinois at Urbana-Champaign, 2005.

[138] S.H. Song, G.H. Paulino, W.G. Buttlar, Simulation of Crack Propagation in Asphalt Concrete Using an Intrinsic Cohesive Zone Model, Journal of Engineering Mechanics, 132(11) (2015) 1215-1223.

[139] M.L. Falk, A. Needleman, J.R. Rice, A critical evaluation of cohesive zone models of dynamic fracture, Springer US, 11(PR5) (2001) 43-50.

[140] K.D. Papoulia, S.A. Vavasis, P. Ganguly, Spatial convergence of crack nucleation using a cohesive finite-element model on a pinwheel-based mesh, International Journal for Numerical Methods in Engineering, 67(1) (2010) 1-16.

[141] Y.R. Kim, Cohesive zone model to predict fracture in bituminous materials and asphaltic pavements: state-of-the-art review, International Journal of Pavement Engineering (2011).

[142] Y.S. Jenq, J.D. Perng, Analysis of crack propagation in asphalt concrete using a cohesive crack model, Journal of the Transportation Research Board, 1317(1317) (1989) 90-99.

[143] Y.S. Jenq, C.J. Liaw, L. Pei, Analysis of crack resistance of asphalt concrete overlays. A fracture mechanics approach, Journal of the Transportation Research Board, 1388(1388) (1993) 160-166.

[144] C. Xu, T. Siegmund, K. Ramani, Rate-dependent crack growth in adhesives: I. Modeling approach, International Journal of Adhesion & Adhesives, 23(1) (2003) 15-22.

[145] S.H. Song, G.H. Paulino, W.G. Buttlar, Cohesive Zone Simulation of Mode I and Mixed-Mode Crack Propagation in Asphalt Concrete, (2005) 1-10.

[146] D.H. Allen, C.R. Searcy, A micromechanical model for a viscoelastic cohesive zone, International Journal of Fracture, 107(2) (2001) 159-176.

[147] Kim, Yong-rak, Damage-Induced Modeling of Asphalt Mixtures through Computational Micromechanics and Cohesive Zone Fracture Damage-Induced Modeling of Asphalt Mixtures through Computational Micromechanics and Cohesive

Zone Fracture, Journal of Materials in Civil Engineering, 17(5) (2005) 477-484.

[148] Y.R. Kim, D.H. Allen, D.N. Little, Computational Model to Predict Fatigue Damage Behavior of Asphalt Mixtures under Cyclic Loading, Transportation Research Record: Journal of the Transportation Research Board, 1970(1) (2006) 196-206.

[149] Y.R. Kim, D.H. Allen, D.N. Little, Computational Constitutive Model for Predicting Nonlinear Viscoelastic Damage and Fracture Failure of Asphalt Concrete Mixtures, International Journal of Geomechanics, 7(2) (2007) 102-110.

[150] Y.R. Kim, F. Aragão, D.H. Allen, D.N. Little, Damage modeling of bituminous mixtures considering mixture microstructure, viscoelasticity, and cohesive zone fracture, Canadian Journal of Civil Engineering, 37(8) (2010) 1125-1136.

[151] K.Z. Rami, S. Amelian, Y.R. Kim, T. You, D.N. Little, Modeling the 3D fracture-associated behavior of viscoelastic asphalt mixtures using 2D microstructures, Engineering Fracture Mechanics, 182 (2017).

[152] P. Liu, J. Hu, D. Wang, M. Oeser, S. Alber, W. Ressel, G.C. Falla, Modelling and evaluation of aggregate morphology on asphalt compression behavior, Construction & Building Materials, 133(Complete) (2017) 196-208.

[153] W. Trawiński, J. Tejchman, J. Bobiński, A three-dimensional meso-scale modelling of concrete fracture, based on cohesive elements and X-ray μCT images, Engineering Fracture Mechanics, 189 (2018).

[154] X. Yongsong, H.M. Hawthorne, Evaluating the Cohesive Strength of a Surface Material by Controlled Scratching, Tribology and Interface Engineering Series, Elsevier2006, pp. 186-209.

[155] R. Moraes, R. Velasquez, H.U. Bahia, Measuring the Effect of Moisture on Asphalt-Aggregate Bond with the Bitumen Bond Strength Test, Transportation Research Record Journal of the Transportation Research Board 2209(1) (2011) 70-81.

[156] M.A. Elseifi, L.N. Mohammad, H. Ying, S.C. Iii, Modeling and evaluation of the cracking resistance of asphalt mixtures using the semi-circular bending test at

intermediate temperatures, Road Materials & Pavement Design (2012).

[157] S.H. Song, G.H. Paulino, W.G. Buttlar, Simulation of Crack Propagation in Asphalt Concrete Using an Intrinsic Cohesive Zone Model, Journal of Engineering Mechanics 132(11) (2015) 1215-1223.

[158] L. Dan, Z. Chuanfeng, Q. Yong, B. Heng, L. Keyao, H. Junfei, Analysing the effects of the mesoscopic characteristics of mineral powder fillers on the cohesive strength of asphalt mortars at low temperatures, Construction & Building Materials 65 (2014) 330-337.

[159] A.K. Apeagyei, J.R. Grenfell, G.D. Airey, Moisture-induced strength degradation of aggregate–asphalt mastic bonds, Road Materials & Pavement Design, 15(sup1) (2014) 239-262.

[160] BSI, Bitumen and bituminous binders. Measurement of density and specific gravity. Capillary-stoppered pyknometer method, British Standards Istitution, 2007.

[161] BSI, Bitumen And Bituminous Binders - Determination Of Needle Penetration, 2015.

[162] BSI, Bitumen and bituminous binders - Determination of the softening point - Ring and Ball method, 2015.

[163] BSI, Bitumen and bituminous binders. Determination of dynamic viscosity of bituminous binder using a rotating spindle apparatus, BSI London, UK, 2018.

[164] C. EN, Bituminous Mixtures–Test Methods for Hot Mix Asphalt–Part 35–Laboratory Mixing, 2004.

[165] B. En, Specimen prepared by roller compactor, in bituminous mixtures-test methods for hot mix asphalt British Standard Instituation.

[166] ASTM, Standard Test Method for Determining the Complex Shear Modulus (G*) Of Bituminous Mixtures Using Dynamic Shear Rheometer, 2014.

[167] BSI, Bituminous mixtures. Test methods. Conditioning to address oxidative ageing, British Standards Publication, 2017.

[168] BSI, Bituminous mixtures - Test methods - Part 12: Determination of the water sensitivity of bituminous specimens, British Standards Institution, 2018.

[169] BSI, Bituminous mixtures - Test methods - Part 24: Resistance to fatigue, British Standards Institution, 2018.

[170] A. Cocurullo, G. Airey, A. Collop, C. Sangiorgi, Indirect tensile versus two-point bending fatigue testing, Proceedings of the institution of civil engineers-transport,, Thomas Telford Ltd, 2008, pp. 207-220.

[171] V.B. Nguyen, N. Thom, Using a beam wheel tracker fatigue test to evaluate fatigue performance of asphalt mixtures, Engenaria Civil/Civil Engineering (2020) 1-17.

[172] W.A. Kalender, X-ray computed tomography, Physics in Medicine & Biology, 51(13) (2006) R29.

[173] M.A. Miner, Cumulative damage in fatigue, (1945).

[174] P. Hopman, P. Kunst, A. Pronk, A renewed interpretation method for fatigue measurements-verification of Miner's rule, Proceedings of The 4th Eurobitume Symposium, Madrid, 1989, pp. 557-561.

[175] W.V. Dijk, H. Moreaud, A. Quedeville, P. Uge, The fatigue of bitumen and bituminous mixes, International Conference on the Structural Design of Asphalt Pavements, 1972.

[176] H.D. Benedetto, A. Soltani, P. Chaverot, Fatigue damage for bituminous mixtures: A pertinent approach, Asphalt Paving Technology: Association of Asphalt Paving Technologists-Proceedings of the Technical Sessions, 65 (1996) 142-158.

[177] Y.R. Kim, D.N. Little, R.L. Lytton, Fatigue and Healing Characterization of Asphalt Mixtures, Journal of Materials in Civil Engineering, 15(1) (2003) 75-83.

[178] H.-J. Lee, Uniaxial constitutive modeling of asphalt concrete using viscoelasticity and continuum damage theory, North Carolina State University1996.

[179] G.M. Rowe, M.G. Bouldin, Improved techniques to evaluate the fatigue resistance of asphaltic mixtures, 2nd Eurasphalt & Eurobitume Congress Barcelona,, 2000.

[180] G.M. Rowe, PERFORMANCE OF ASPHALT MIXTURES IN THE TRAPEZOIDAL FATIGUE TEST (WITH DISCUSSION), Journal of the Association of Asphalt Paving Technologists, 62 (1993).

[181] W.V. Dijk, W. Visser, The energy approach to fatigue for pavement design, (1977).

[182] Y.R. Kim, D.N. Little, R.L.J.J.o.M.i.C.E. Lytton, Fatigue and Healing Characterization of Asphalt Mixtures, 15(1) (2003) 75-83.

[183] K. Ghuzlan, S. Carpenter, Energy-Derived, Damage-Based Failure Criterion for Fatigue Testing, Transportation Research Record: Journal of the Transportation Research Board, 1723 (2000) 141-149.

[184] R.L. Lytton, CHARACTERIZING ASPHALT PAVEMENTS FOR PERFORMANCE, transportation research record: journal of the transportation research board, 1723(1) (2000) 5-16.

[185] A.C. Pronk, P.C. Hopman, Energy dissipation: the leading factor of fatigue, (1991).

[186] A. Pronk, Evaluation of the dissipated energy concept for the interpretation of fatigue measurements in the crack initiation phase, (1995).

[187] Shen, Shihui, Dissipated Energy Concepts for HMA Performance: Fatigue and Healing, dissertation abstracts international, (2006).

[188] S. Shen, X. Lu, Energy Based Laboratory Fatigue Failure Criteria for Asphalt Materials, Journal of testing & evaluation, 39(3) (2011) p.313-320.

[189] S. Menard, Applied logistic regression analysis, Sage2002.

[190] M. Liu, C. Udhe-Stone, C.T. Goudar, Progress curve analysis of qRT-PCR reactions using the logistic growth equation, Biotechnology Progress, 27(5) (2011) 1407-1414.

[191] R. Pastor-Barriuso, E. Guallar, J. Coresh, Transition models for change-point estimation in logistic regression, Statistics in Medicine, 22(7) (2003) 1141.

[192] A. Modarres, H. Ramyar, P. Ayar, Effect of cement kiln dust on the low-temperature durability and fatigue life of hot mix asphalt, Cold Regions Science & Technology 110(feb.) (2015) 59-66.

[193] C.L. Monismith, ANALYTICALLY BASED ASPHALT PAVEMENT DESIGN AND REHABILITATION: THEORY TO PRACTICE, 1962-1992, Transportation Research Record, (1992).

[194] K. Eriksen, MICROSCOPICAL ANALYSIS OF ASPHALT-AGGREGATE MIXTURES RELATED TO PAVEMENT PERFORMANCE, Danish Road Institute Note, (1993).

[195] Z.Q. Yue, W.B. Bekking, I. Morin, Application of digital image processing to quantitative study of asphalt concrete microstructure, Transportation Research Record, (1995).

[196] L. Tashman, E. Masad, B. Peterson, H. Saleh, Internal structure analysis of asphalt mixes to improve the simulation of superpave gyratory compaction to field conditions, Maine Law Review, 61(1) (2001) 490-498.

[197] E. Masad, V.K. Jandhyala, N. Dasgupta, N. Somadevan, N. Shashidhar, Characterization of Air Void Distribution in Asphalt Mixes using X-ray Computed Tomography, Journal of Materials in Civil Engineering, 14(2) (2002) 122-129.

[198] L. Wang, H.S. Paul, T. Harman, J. D'Angelo, Characterization of aggregates and asphalt concrete using X-ray computerized tomography a state of the art report, Asphalt Paving Technology: Association of Asphalt Paving Technologists-Proceedings of the

Technical Sessions, 73(1) (2004) 467-500.

[199] D. Braz, R.T. Lopes, L. Motta, Analysis of the percentage voids of test and field specimens using computerized tomography, Nuclear Instruments and Methods in Physics Research, 422(1) (1999) 942-948.

[200] L. Tashman, E. Masad, D. Little, R. Lytton, Damage Evolution in Triaxial Compression Tests of HMA at High Temperatures, Journal of the Association of Asphalt Paving Technologists, 73 (2004) p.53-87.

[201] R. Khan, Quantification of microstructural damage in asphalt, university of nottingham, 2010.

[202] H.M. Zelelew, A.T. Papagiannakis, A volumetrics thresholding algorithm for processing asphalt concrete X-ray CT images, International Journal of Pavement Engineering, 12(6) (2011) 543-551.

[203] A. Molenaar, M. Ven, M. Mohajeri, Experimental study into the fundamental understanding of blending between reclaimed asphalt binder and virgin bitumen using nanoindentation and nano-computed tomography, Road materials & pavement design, (2014).

[204] D. Castillo, S. Caro, M. Darabi, E. Masad, Studying the effect of microstructural properties on the mechanical degradation of asphalt mixtures, Construction & Building Materials, 93 (2015) 70-83.

[205] Nejad, F. Moghadas, Aliha, M. Rm, Fazaeli, H., Aghajani, A. S., Effect of temperature and air void on mixed mode fracture toughness of modified asphalt mixtures, Construction & Building Materials, (2015).

[206] H. Khosravi, S.M. Abtahi, B. Koosha, M. Manian, An analytical–empirical investigation of the bleeding mechanism of asphalt mixes, Construction & Building Materials, 45(aug.) (2013) 138-144.

[207] S. Kodippily, T.F. Henning, J.M. Ingham, G. Holleran, Computed tomography scanning for quantifying chipseal material volumetrics, Journal of Computing in Civil

Engineering, 28(3) (2014) 04014002.

[208] E. Coleri, J.T. Harvey, Y. Kai, J.M. Boone, Micromechanical investigation of open-graded asphalt friction courses' rutting mechanisms, Construction & Building Materials, 44(jul.) (2013) 25-34.

[209] E. Coleri, J.T. Harvey, Y. Kai, J.M. Boone, A micromechanical approach to investigate asphalt concrete rutting mechanisms, Construction & Building Materials, 30 (2012) 36-49.

[210] Y. Seo, Y.R. Kim, Using Acoustic Emission to monitor fatigue damage and healing in Asphalt Concrete, Ksce Journal of Civil Engineering, 12(4) (2008) 237-243.

[211] L. Tashman, E. Masad, D. Little, H. Zbib, A microstructure-based viscoplastic model for asphalt concrete, International Journal of Plasticity, 21(9) (2005) 1659-1685.

[212] I. Song, Damage analysis in asphalt concrete mixtures based on parameter relationships, Texas A&M University., Texas A&M University,, 2004.

[213] R. Khan, A.C. Collop, The Use of X-Ray Computed Tomography to Characterize Microdamage in Asphalt, Road Materials & Pavement Design, 11(sup1) (2010) 89-109.

[214] A. Yin, X. Yang, C. Zhang, G. Zeng, Z. Yang, Three-dimensional heterogeneous fracture simulation of asphalt mixture under uniaxial tension with cohesive crack model, Construction & Building Materials, 76(feb.1) (2015) 103-117.

[215] M. Miljkovic, M. Radenberg, Effect of compaction energy on physical and mechanical performance of bitumen emulsion mortar, Materials & Structures, 49(1-2) (2016) 193-205.

[216] P.S. Kandhal, F. Parker, Aggregate tests related to asphalt concrete performance in pavements, Transportation Research Board1998.

[217] J. Chen, M.K. Chang, K.Y. Lin, Influence of coarse aggregate shape on the strength of asphalt concrete mixtures, Highway Research Record, (2005).

[218] J.E. Stephens, K.C. Sinha, EFFECT OF AGGREGATE SHAPE ON BITUMINOUS MIX CHARACTER, (1978).

[219] C.L. Monismith, INFLUENCE OF SHAPE, SIZE, AND SURFACE TEXTURE ON THE STIFFNESS AND FATIGUE RESPONSE OF ASPHALT MIXTURES, Highway Research Board Special Report, (1970).

[220] Y. Li, S. Wu, Y. Dai, C. Li, W. Song, H. Li, C. Li, B. Shu, Transitions of component, physical, rheological and self-healing properties of petroleum bitumen from the loose bituminous mixture after UV irradiation, Fuel, 262 (2020) 116507.

[221] X.P. Xu, A. Needleman, Void nucleation by inclusion debonding in a crystal matrix, Modelling & Simulation in Materials Science & Engineering, 1(2) (1999) 111.

[222] S.H. Song, G.H. Paulino, W.G. Buttlar, A bilinear cohesive zone model tailored for fracture of asphalt concrete considering viscoelastic bulk material, Engineering Fracture Mechanics, 73(18) (2006) 2829-2848.

[223] X. Yang, Z. You, Z. Wang, Q. Dai, Review on heterogeneous model reconstruction of stone-based composites in numerical simulation, Construction & Building Materials, 117(aug.1) (2016) 229-243.

[224] P. Liu, D. Wang, F. Otto, J. Hu, M. Oeser, Application of semi-analytical finite element method to evaluate asphalt pavement bearing capacity, International Journal of Pavement Engineering, (2018) 1-10.

[225] J. Ferellec, G. Mcdowell, Modelling realistic shape and particle inertia in DEM, Géotechnique, 60(3) (2010) 227-232.

[226] Y. Sun, C. Du, C. Zhou, X. Zhu, J. Chen, Analysis of load-induced top-down cracking initiation in asphalt pavements using a two-dimensional microstructure-based multiscale finite element method, Engineering Fracture Mechanics, 216 (2019) 106497.

[227] J. Hu, Z. Qian, D. Wang, M. Oeser, Influence of aggregate particles on mastic and air-voids in asphalt concrete, Construction & Building Materials, 93(sep.15) (2015) 1-9.

[228] J. Hu, P. Liu, D. Wang, M. Oeser, Y.J.C. Tan, B. Materials, Investigation on fatigue damage of asphalt mixture with different air-voids using microstructural analysis, 125(OCT.30) (2016) 936-945.

[229] J. Goodrich, Asphalt and polymer modified asphalt properties related to the performance of asphalt concrete mixes (with discussion), In Association of Asphalt Paving Technologists Proc, 57 (1988).

[230] P. Rahulkumar, A. Jagota, S.J. Bennison, S. Saigal, Cohesive element modeling of viscoelastic fracture: application to peel testing of polymers, International Journal of Solids & Structures, 37(13) (2000) 1873-1897.

[231] M.L. Williams, R.F. Landel, J.D. Ferry, The Temperature Dependence of Relaxation Mechanism in Amorphous Polymers and Other Glass Forming Liquid, Journal of the American Chemical Society, 77(14) (1955).

[232] F. Renaud, J.L. Dion, G. Chevallier, I. Tawfiq, R. Lemaire, A new identification method of viscoelastic behavior: Application to the generalized Maxwell model, Mechanical Systems & Signal Processing, 25(3) (2011) 991-1010.

[233] D.S.S. Corporation, ABAQUS/Standard User's Manual, Version 6.14, Dassault Systemes Simulia Corporation Rhode Island, USA, 2014.

[234] J. Ma, Im2mesh (2D image to triangular meshes), MATLAB Central File Exchange, 2021.

[235] V.P. Nguyen, An open source program to generate zero-thickness cohesive interface elements, Advances in Engineering Software 74(AUG.) (2014) 27-39.

[236] D.W. Spring, G.H. Paulino, A growing library of three-dimensional cohesive elements for use in ABAQUS, Engineering Fracture Mechanics 126 (2014) 190-216.

[237] Z. Wu, X. Xu, Q. Liu, Y. Yang, A zero-thickness cohesive element-based numerical manifold method for rock mechanical behavior with micro-Voronoi grains, Engineering Analysis with Boundary Elements 96 (2018) 94-108.

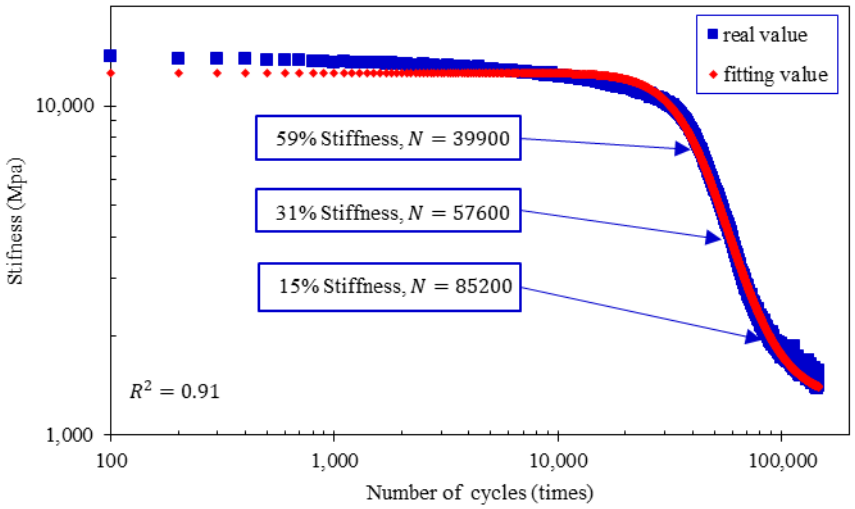
[238] X. Frank, F. Radja, S. Nezamabadi, J.Y. Delenne, Tensile strength of granular aggregates: Stress chains across particle phase versus stress concentration by pores, PHYSICAL REVIEW E, 102(2) (2020).

[239] H. Wang, C. Zhang, L. Yang, Z. You, Study on the rubber-modified asphalt mixtures' cracking propagation using the extended finite element method, Construction & Building Materials, 47(Complete) (2013) 223-230.

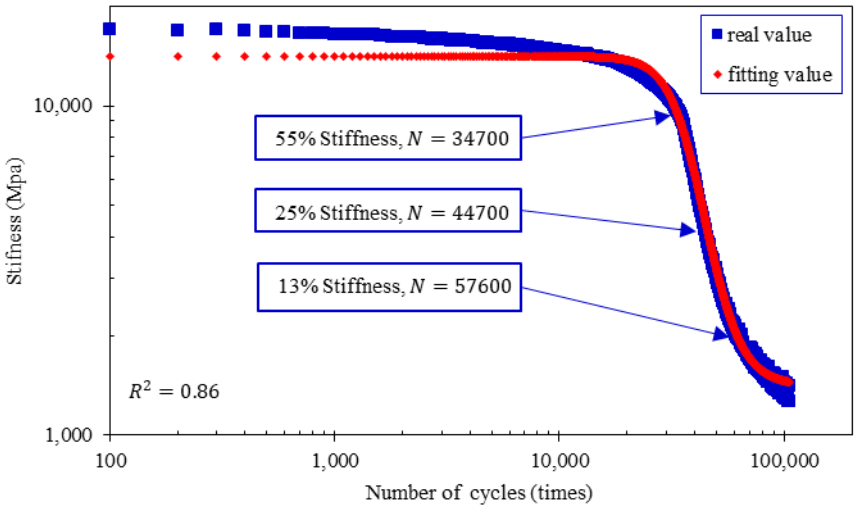
[240] I.J. Baek, I.L. Alqadi, Finite element method modeling of reflective cracking initiation and propagation : Investigation of the effect of steel reinforcement interlayer on retarding reflective cracking in hot-mix asphalt overlay, Transportation Research Record: Journal of the Transportation Research Board, 1949(1) (2006) 32-42.

Appendix A- SCTM Fitting Results under Different Temperatures, Strains, Conditions

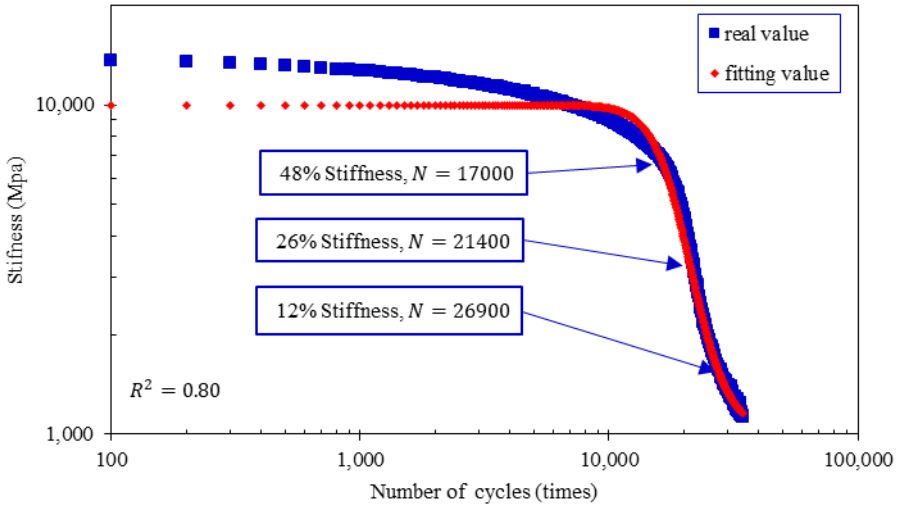
(a)



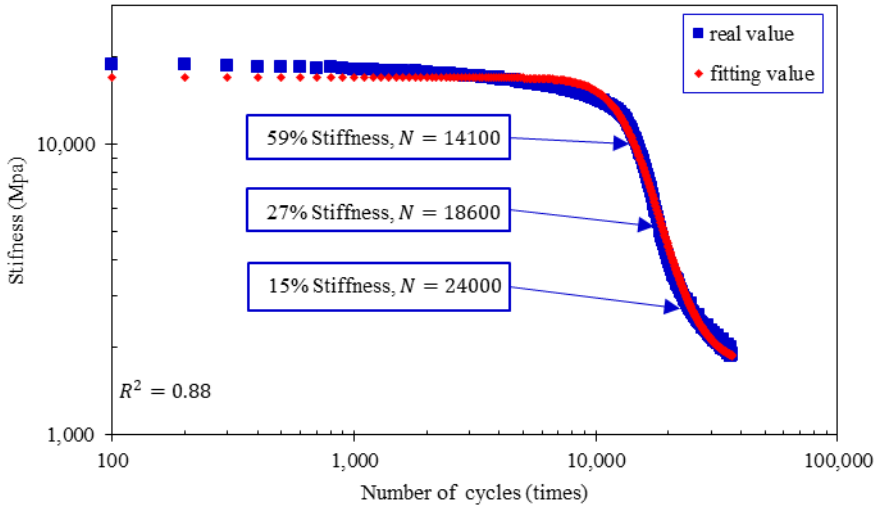
(b)



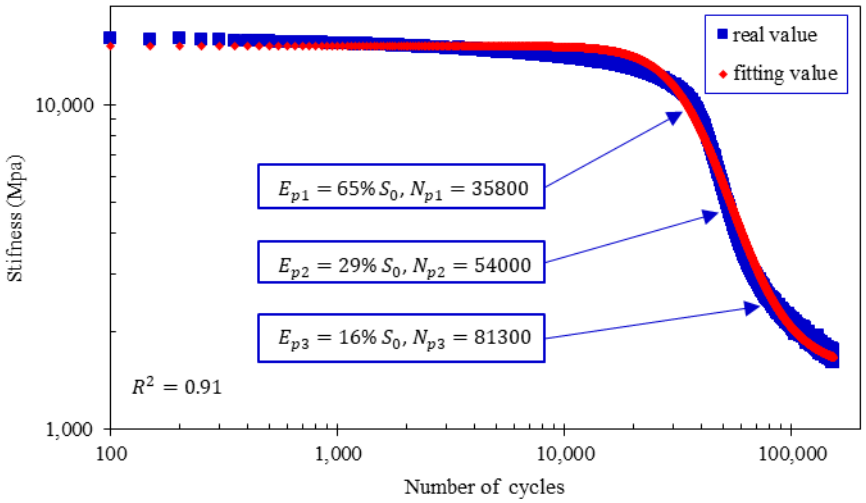
(c)


real value
fitting value
48% Stiffness, N = 17000
26% Stiffness, N = 21400
12% Stiffness, N = 26900
R^2 = 0.80
Stifness (Mpa)
10,000
1,000
100
1,000
10,000
100,000
Number of cycles (times)

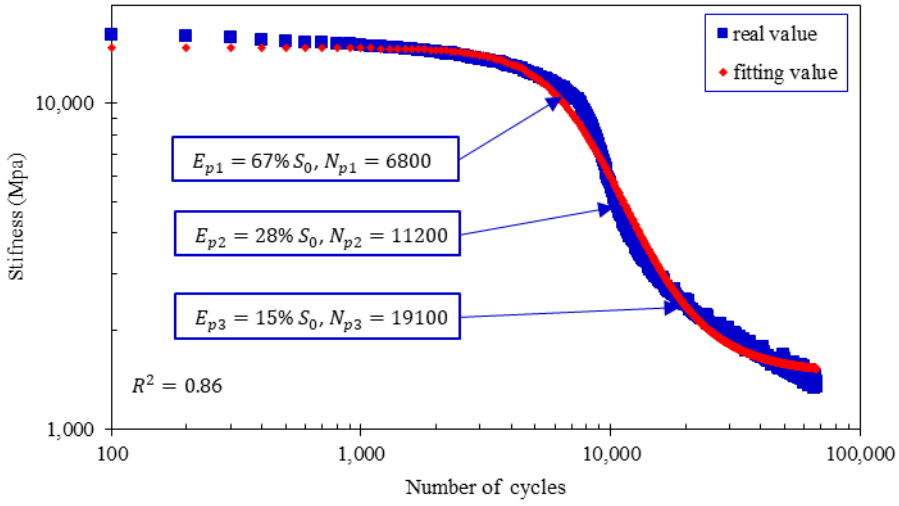
(d)


real value
fitting value
59% Stiffness, N = 14100
27% Stiffness, N = 18600
15% Stiffness, N = 24000
R^2 = 0.88
Stifness (Mpa)
10,000
1,000
100
1,000
10,000
100,000
Number of cycles (times)

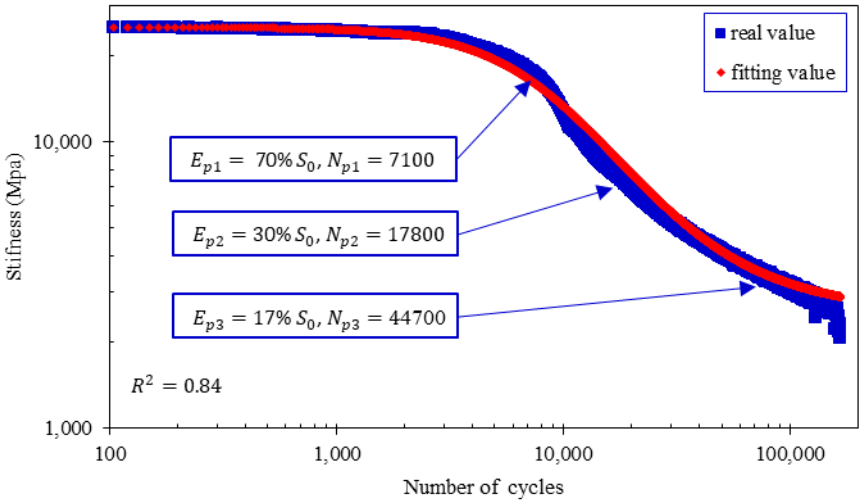
(e)


real value
fitting value
E_{p1} = 65% S_0, N_{p1} = 35800
E_{p2} = 29% S_0, N_{p2} = 54000
E_{p3} = 16% S_0, N_{p3} = 81300
R^2 = 0.91
Stifness (Mpa)
10,000
1,000
100
1,000
10,000
100,000
Number of cycles

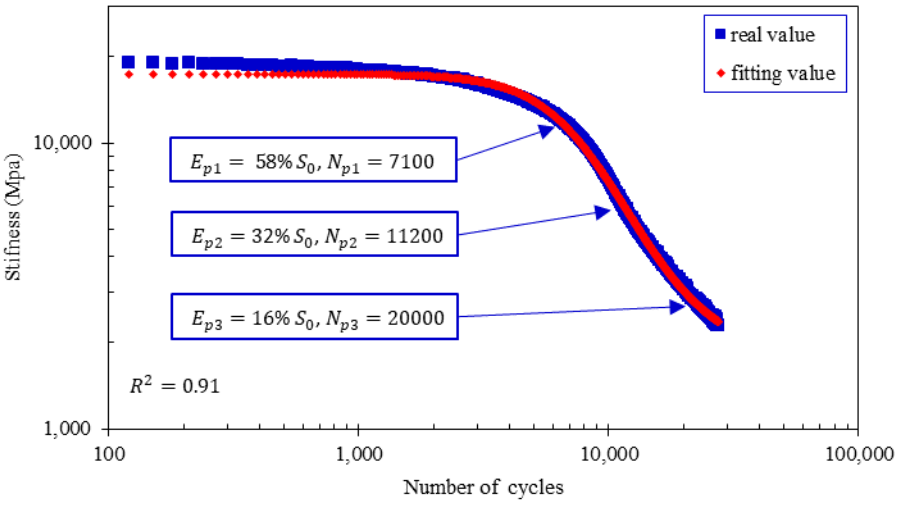
(f)


real value
fitting value
$E_{p1} = 67\% S_0, N_{p1} = 6800$
$E_{p2} = 28\% S_0, N_{p2} = 11200$
$E_{p3} = 15\% S_0, N_{p3} = 19100$
$R^2 = 0.86$
Stifness (Mpa)
Number of cycles
10,000
1,000
100
1,000
10,000
100,000

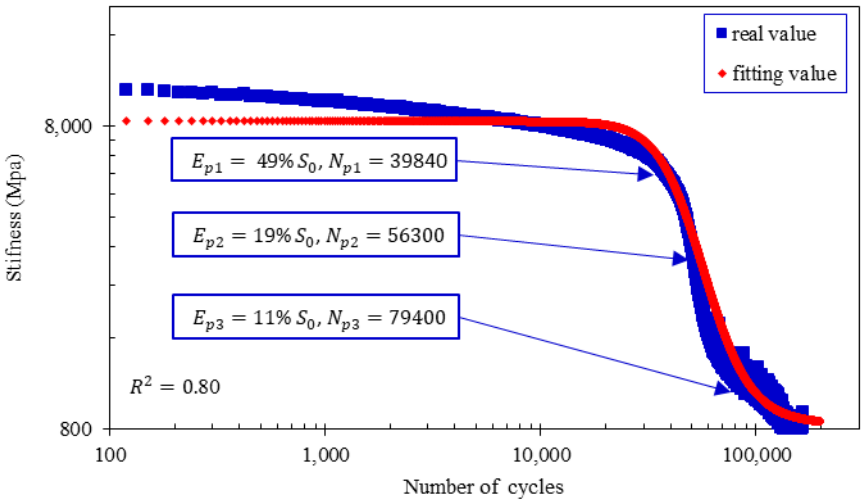
(g)


real value
fitting value
$E_{p1} = 70\% S_0, N_{p1} = 7100$
$E_{p2} = 30\% S_0, N_{p2} = 17800$
$E_{p3} = 17\% S_0, N_{p3} = 44700$
$R^2 = 0.84$
Stifness (Mpa)
Number of cycles
10,000
1,000
100
1,000
10,000
100,000

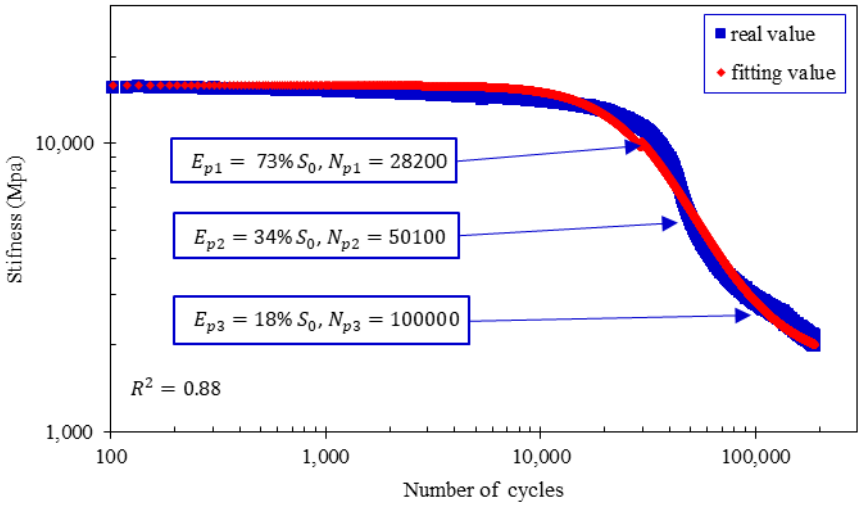
(h)


real value
fitting value
$E_{p1} = 58\% S_0, N_{p1} = 7100$
$E_{p2} = 32\% S_0, N_{p2} = 11200$
$E_{p3} = 16\% S_0, N_{p3} = 20000$
$R^2 = 0.91$
Stifness (Mpa)
Number of cycles
10,000
1,000
100
1,000
10,000
100,000

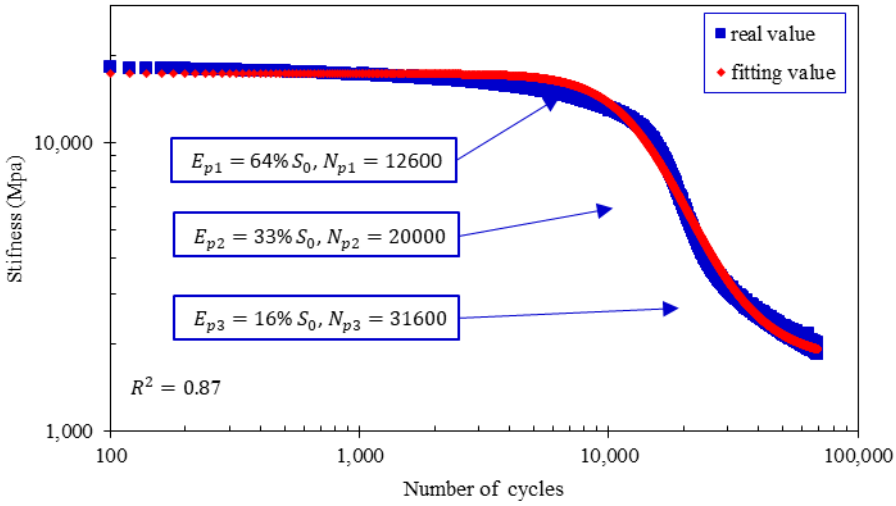
(i)


real value
fitting value
E_{p1} = 49% S_0, N_{p1} = 39840
E_{p2} = 19% S_0, N_{p2} = 56300
E_{p3} = 11% S_0, N_{p3} = 79400
R^2 = 0.80
8,000
800
100
1,000
10,000
100,000
Stifness (Mpa)
Number of cycles

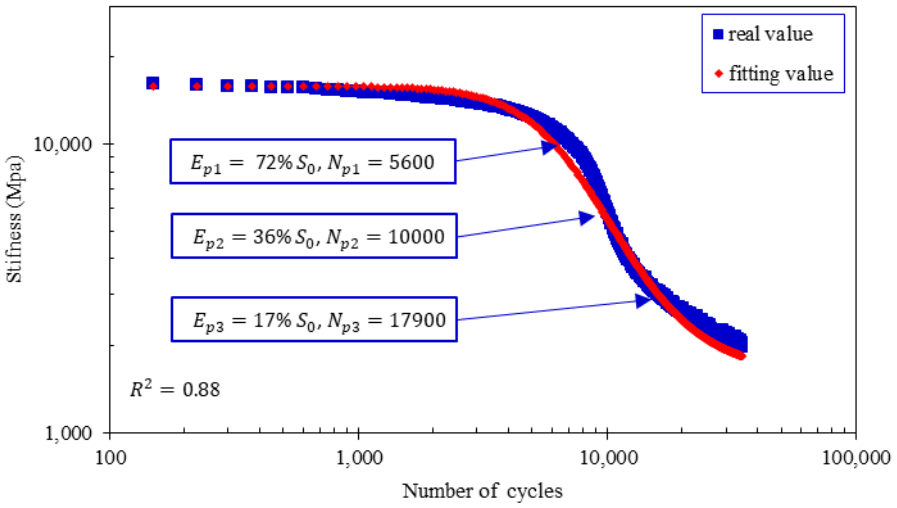
(j)


real value
fitting value
E_{p1} = 73% S_0, N_{p1} = 28200
E_{p2} = 34% S_0, N_{p2} = 50100
E_{p3} = 18% S_0, N_{p3} = 100000
R^2 = 0.88
10,000
1,000
100
1,000
10,000
100,000
Stifness (Mpa)
Number of cycles

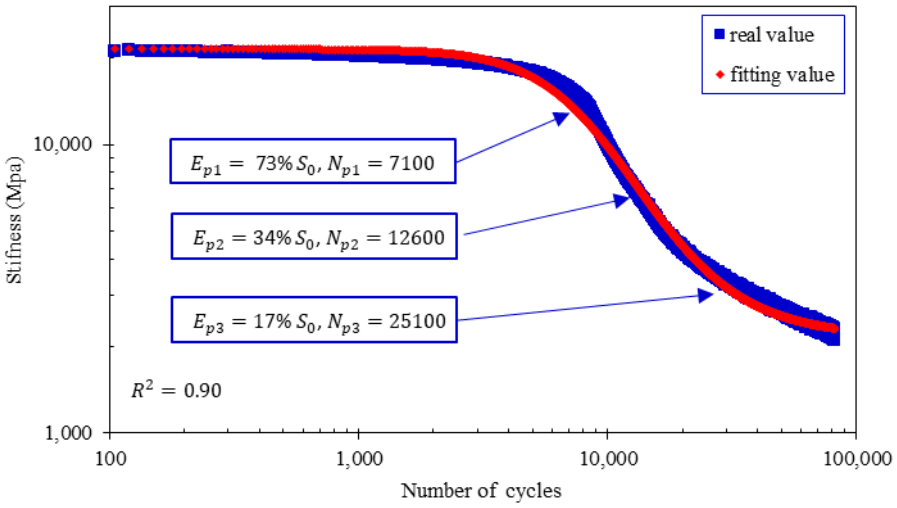
(k)


real value
fitting value
E_{p1} = 64% S_0, N_{p1} = 12600
E_{p2} = 33% S_0, N_{p2} = 20000
E_{p3} = 16% S_0, N_{p3} = 31600
R^2 = 0.87
10,000
1,000
100
1,000
10,000
100,000
Stifness (Mpa)
Number of cycles

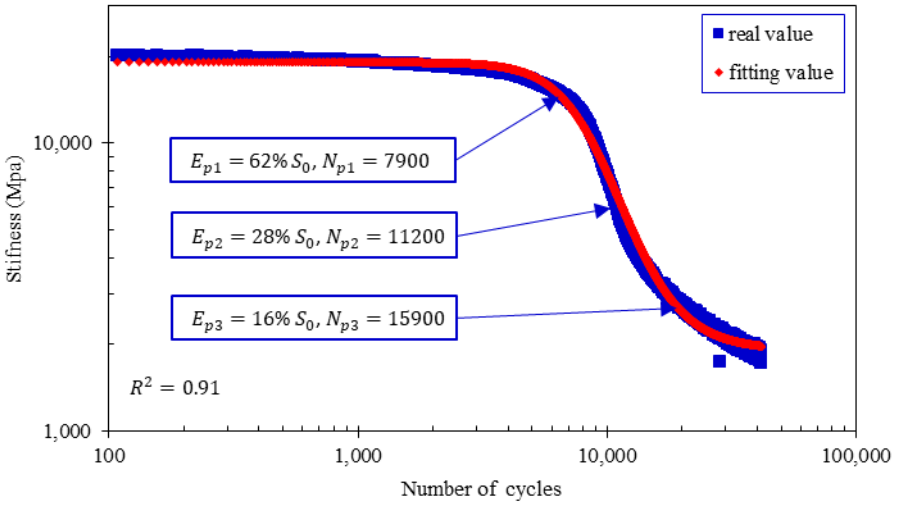
(l)


real value
fitting value
E_{p1} = 72% S_0, N_{p1} = 5600
E_{p2} = 36% S_0, N_{p2} = 10000
E_{p3} = 17% S_0, N_{p3} = 17900
R^2 = 0.88
Stifness (Mpa)
10,000
1,000
100
1,000
10,000
100,000
Number of cycles

(m)


real value
fitting value
E_{p1} = 73% S_0, N_{p1} = 7100
E_{p2} = 34% S_0, N_{p2} = 12600
E_{p3} = 17% S_0, N_{p3} = 25100
R^2 = 0.90
Stifness (Mpa)
10,000
1,000
100
1,000
10,000
100,000
Number of cycles

(n)


real value
fitting value
E_{p1} = 62% S_0, N_{p1} = 7900
E_{p2} = 28% S_0, N_{p2} = 11200
E_{p3} = 16% S_0, N_{p3} = 15900
R^2 = 0.91
Stifness (Mpa)
10,000
1,000
100
1,000
10,000
100,000
Number of cycles

(o)

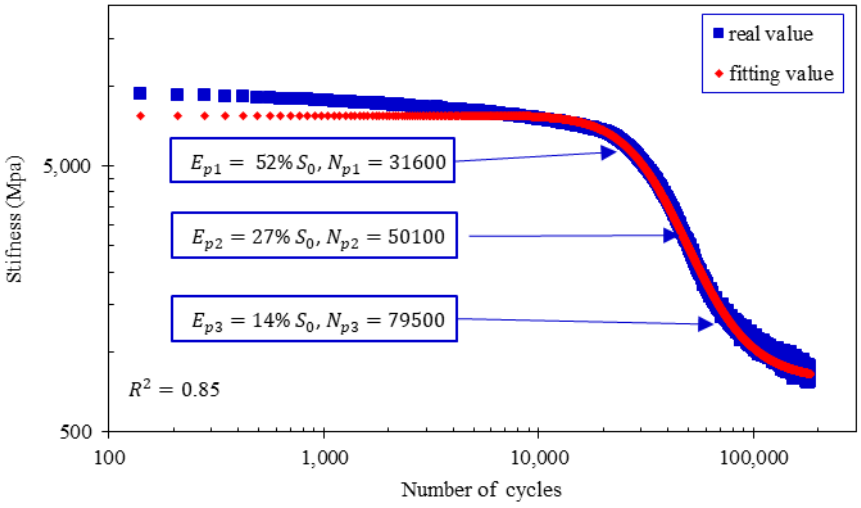
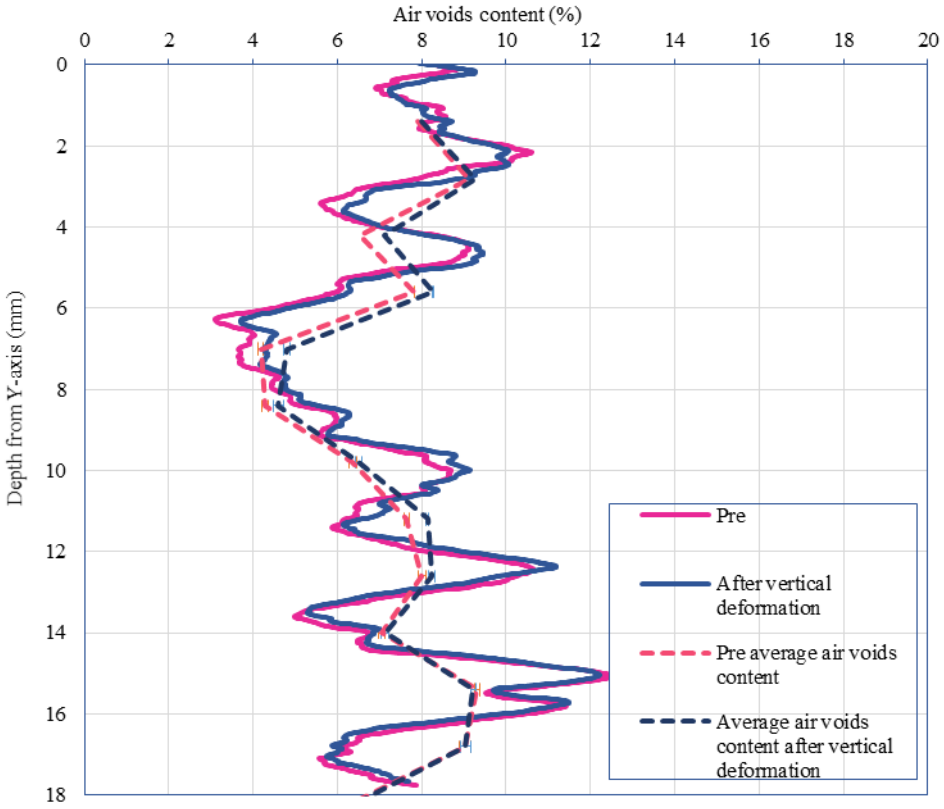


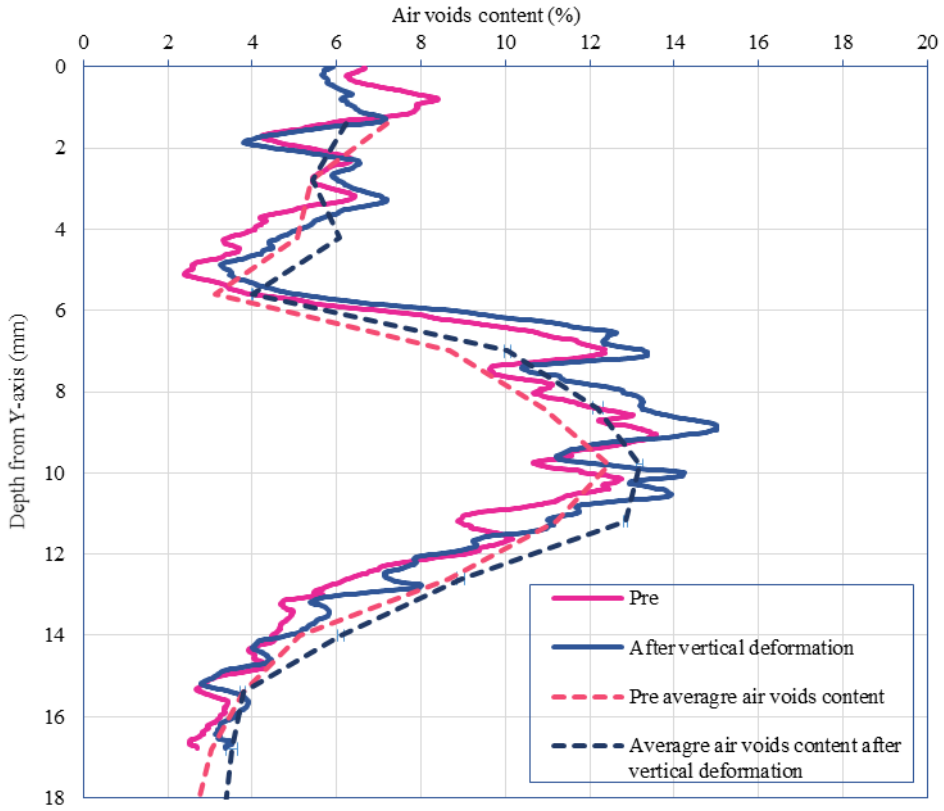
Figure: Fitting results under different temperatures, strains, conditions: (a) 10℃ and 150με; (b) 10℃and 200με; (c) 10℃ and 250με; (d) 5℃ and 200με; (e) 10℃ and 150με aged; (f) 10℃ and 250με aged; (g) 0℃ and 200με aged; (h) 5℃ and 200με aged; (i) 20℃ and 200με aged; (j) 10℃ and 150με aged+ moisture damaged; (k) 10℃ and 200με aged+ moisture damaged; (l) 10℃ and 250με aged+ moisture damaged; (m) 0℃ and 200μεaged+ moisture damaged; (n) 5℃ and 200μεaged+ moisture damaged and (o) 20℃ and 200μεaged+ moisture damaged.

Appendix B- Air Voids Distribution

(a)



(b)


Air voids content (%)
0
2
4
6
8
10
12
14
16
18
20
Depth from Y-axis (mm)
0
2
4
6
8
10
12
14
16
18
Pre
After vertical deformation
Pre averagre air voids content
Averagre air voids content after vertical deformation

(c)

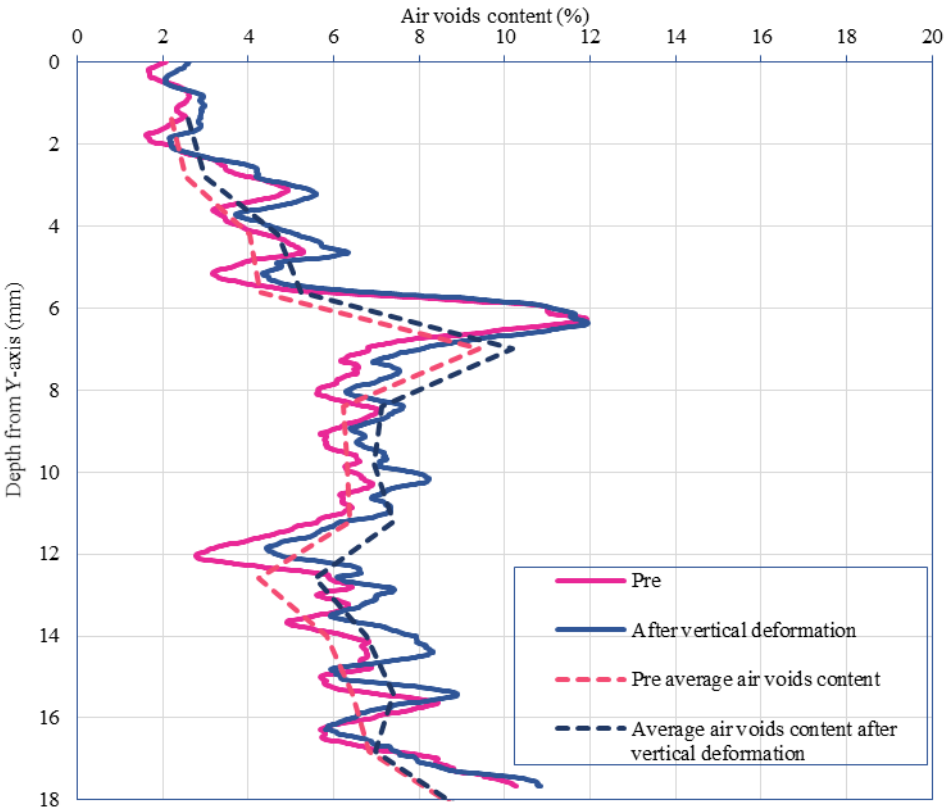
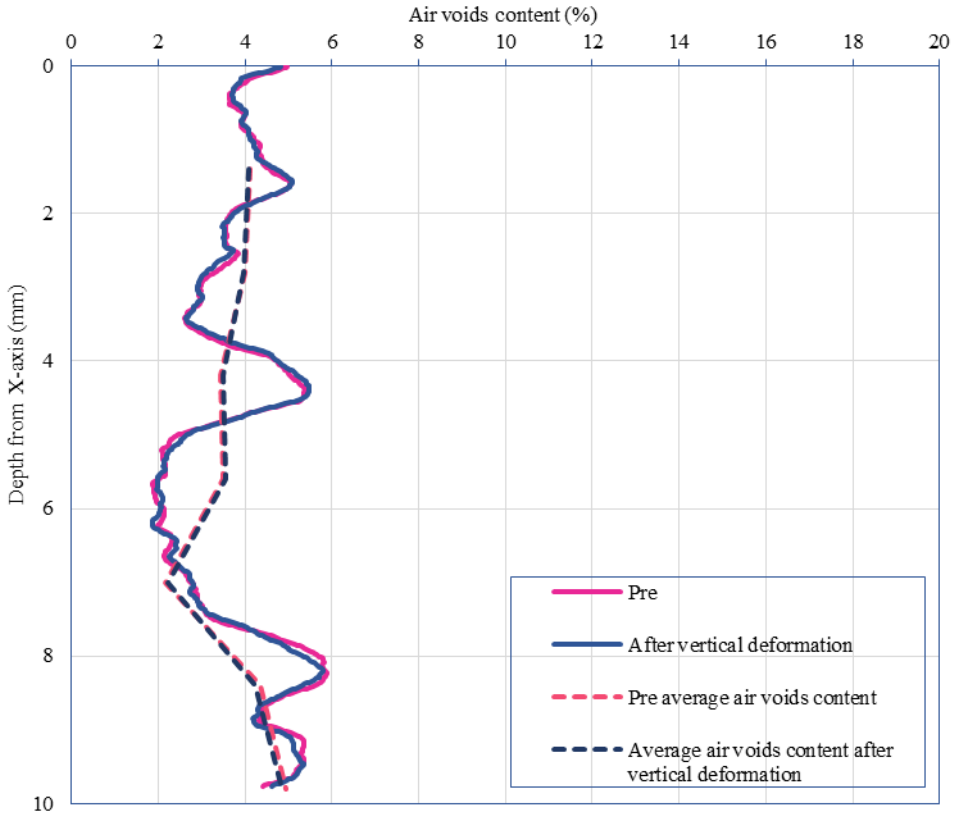
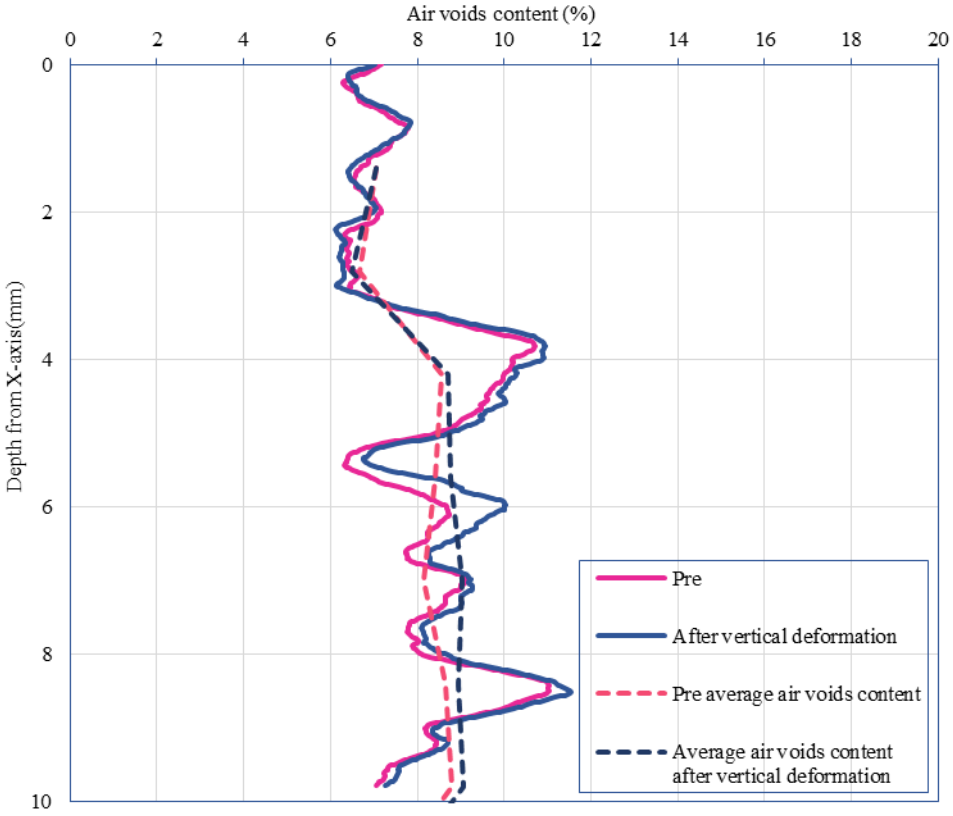

Air voids content (%)
0
2
4
6
8
10
12
14
16
18
20
Depth from Y-axis (mm)
0
2
4
6
8
10
12
14
16
18
Pre
After vertical deformation
Pre average air voids content
Average air voids content after vertical deformation

Figure: Air voids distribution in Y direction at (a) 0.6mm; (b) 0.8mm; (c) 1.1mm vertical deformation.

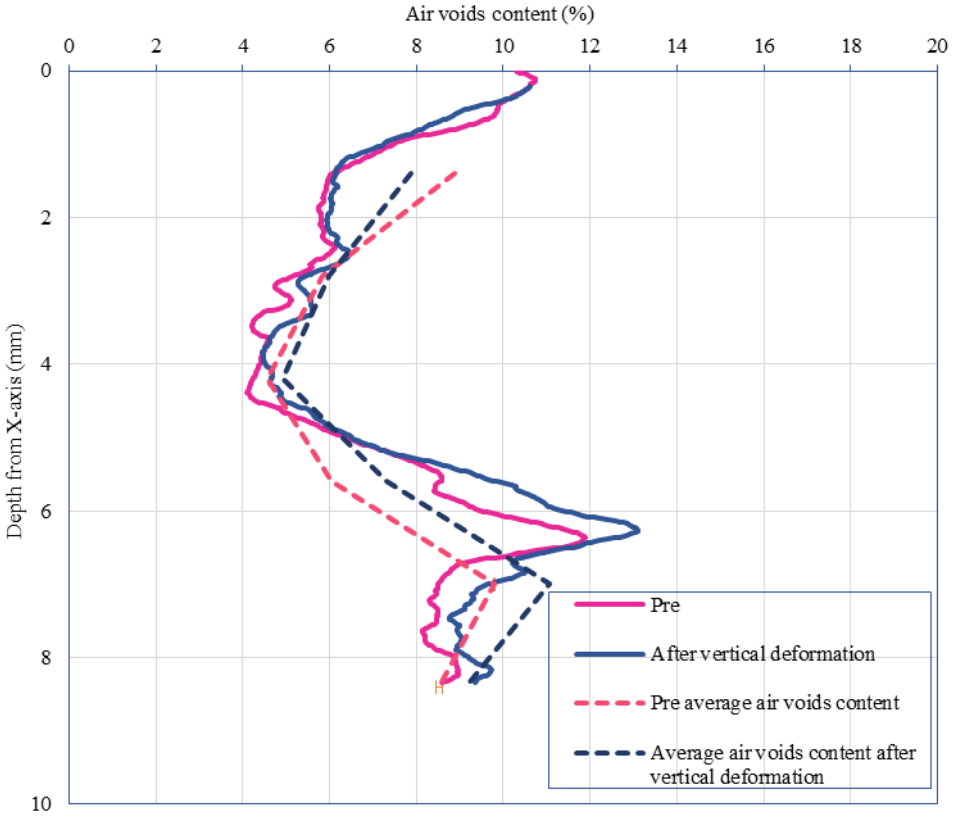
(a)



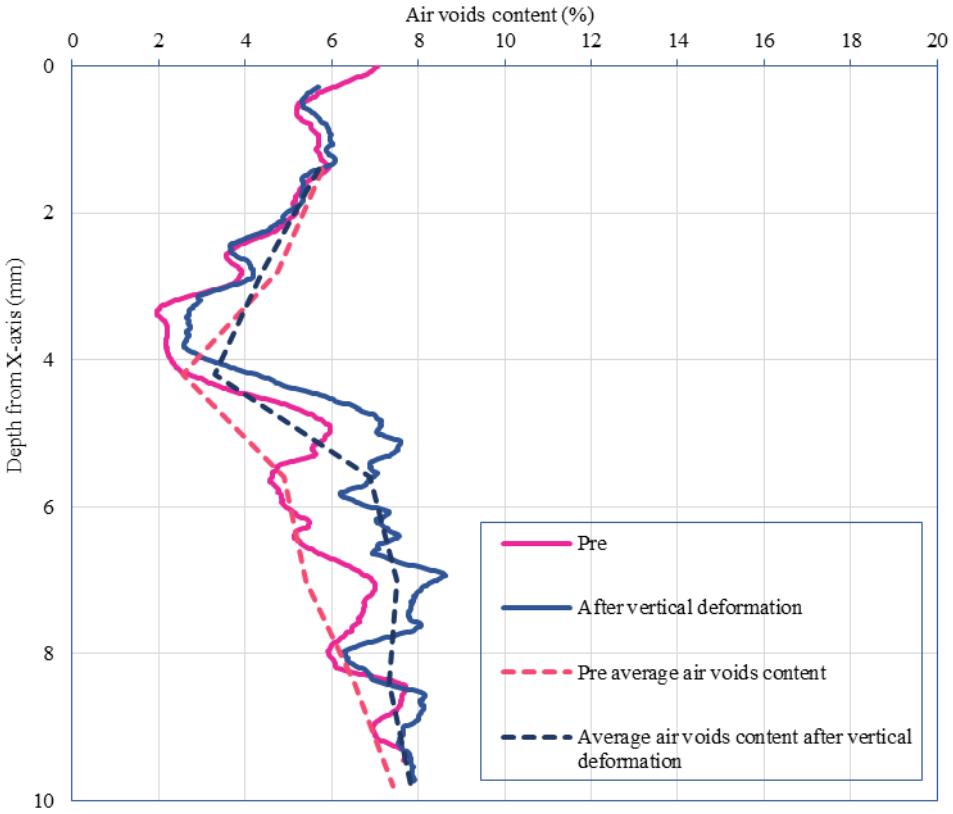
(b)


Air voids content (%)
0
2
4
6
8
10
12
14
16
18
20
Depth from X-axis(mm)
0
2
4
6
8
10
Pre
After vertical deformation
Pre average air voids content
Average air voids content after vertical deformation

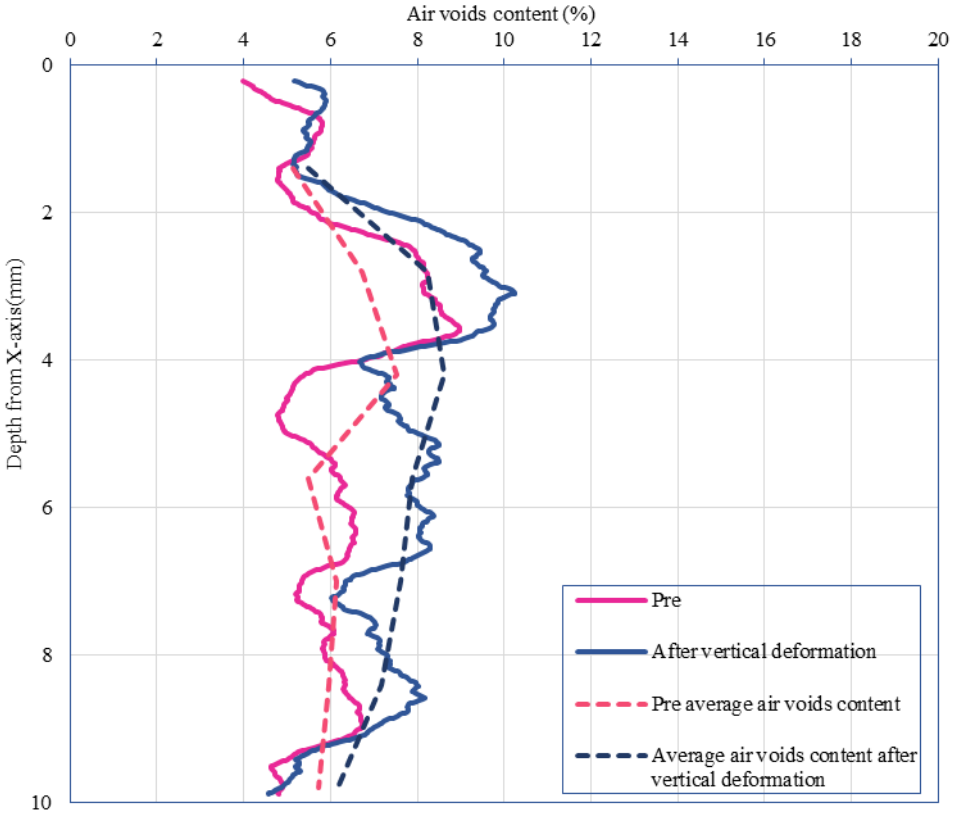
(c)


Air voids content (%)
0
2
4
6
8
10
12
14
16
18
20
Depth from X-axis (mm)
0
2
4
6
8
10
Pre
After vertical deformation
Pre average air voids content
Average air voids content after vertical deformation

(d)


Air voids content (%)
0
2
4
6
8
10
12
14
16
18
20
Depth from X-axis (mm)
0
2
4
6
8
10
Pre
After vertical deformation
Pre average air voids content
Average air voids content after vertical deformation

(e)


Air voids content (%)
0
2
4
6
8
10
12
14
16
18
20
Depth from X-axis(mm)
0
2
4
6
8
10
Pre
After vertical deformation
Pre average air voids content
Average air voids content after vertical deformation

(f)

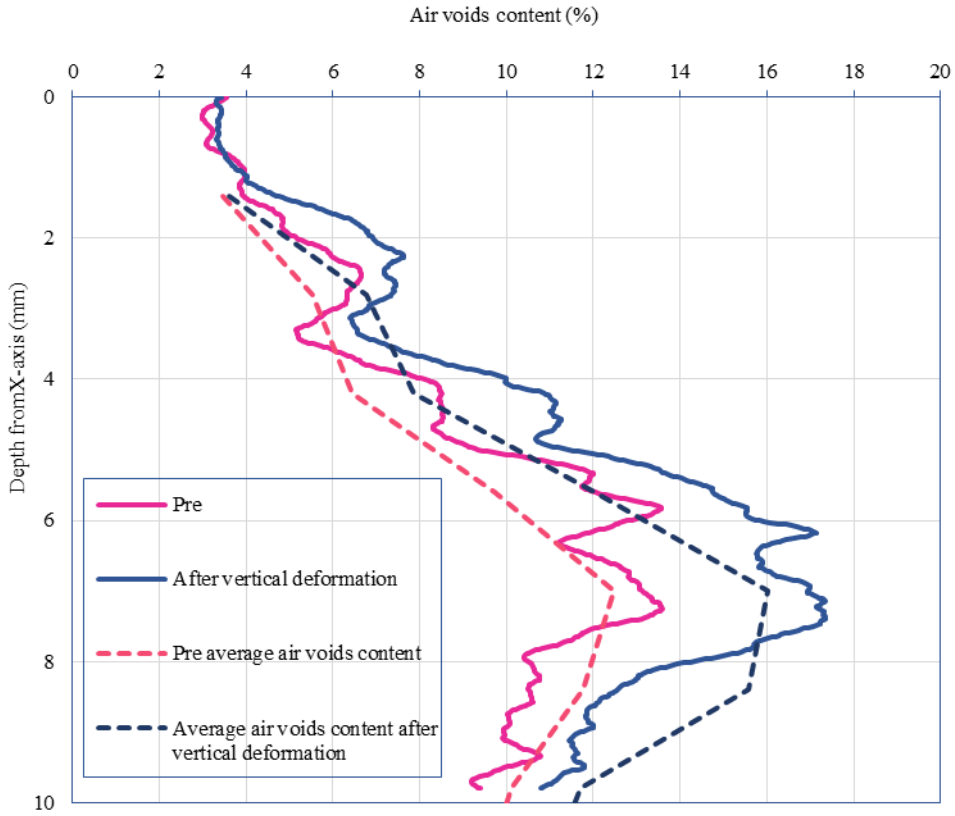
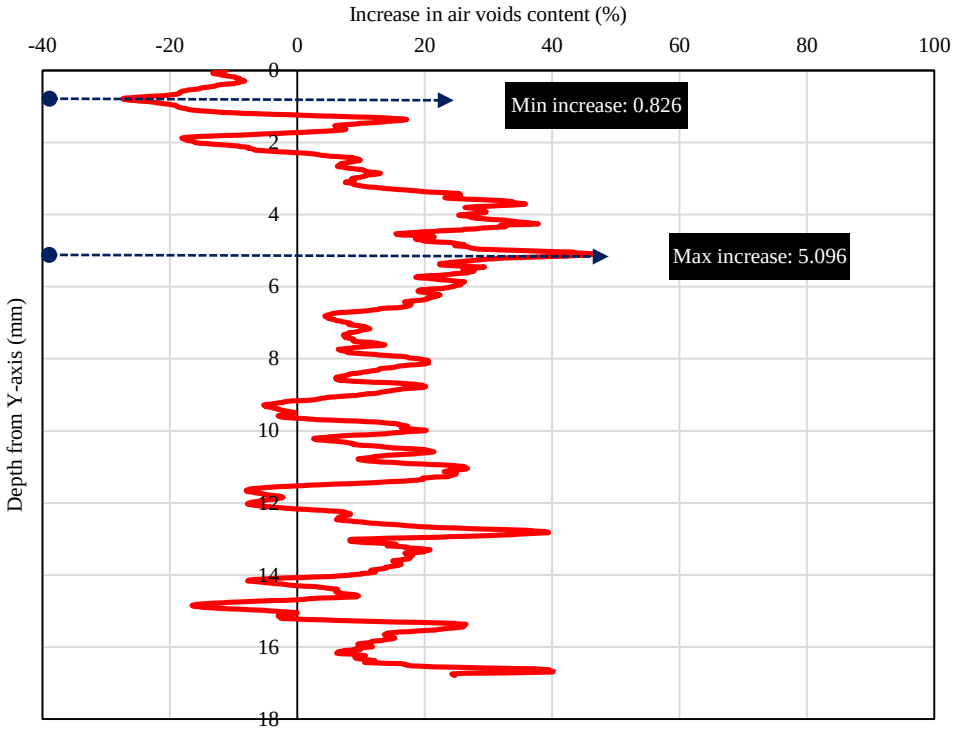


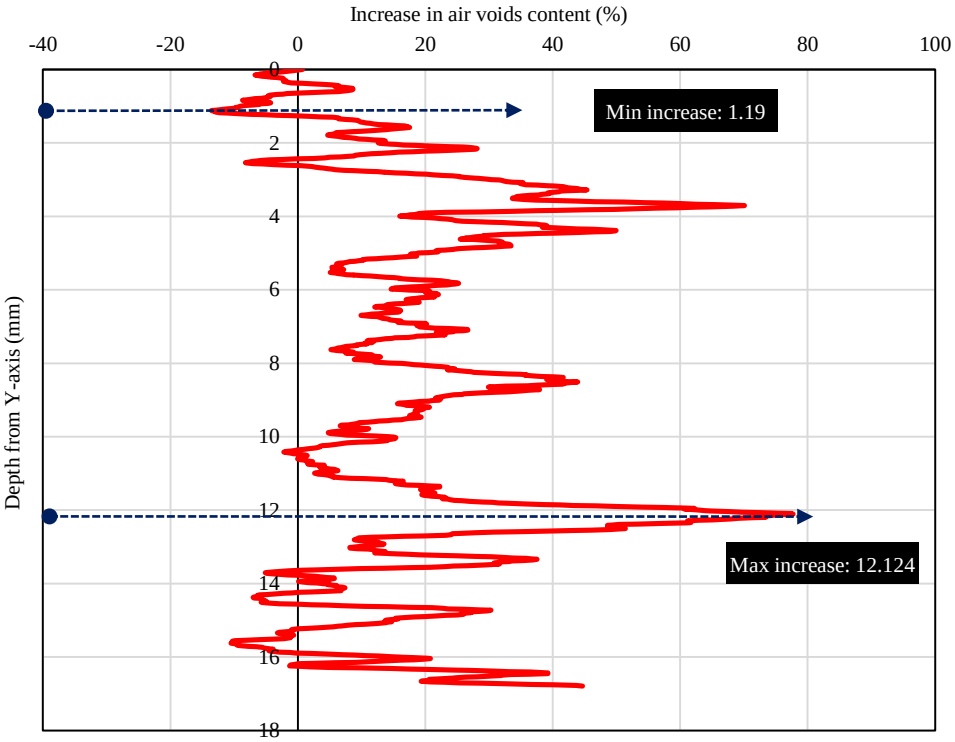
Figure: Air voids distribution in X direction at (a) 0.4mm; (b) 0.6mm; (c) 0.8mm; (d) 0.9mm; (e) 1.1mm (f) 1.4mm vertical deformation.

Appendix C- Increase in Air Voids Content

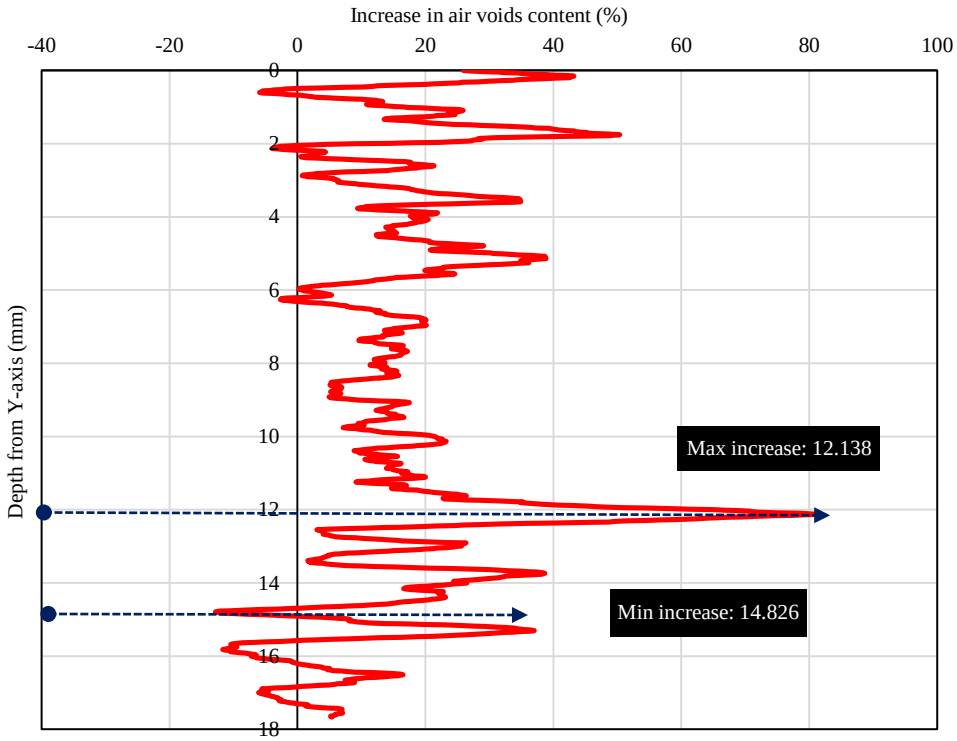
(a)



(b)



(c)



(d)

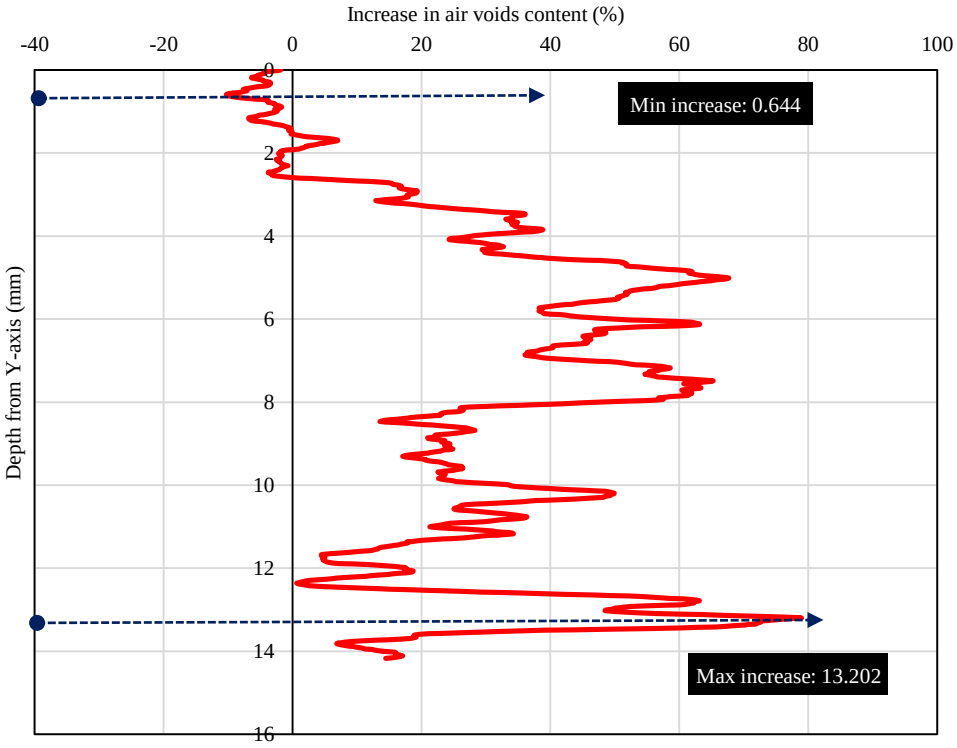
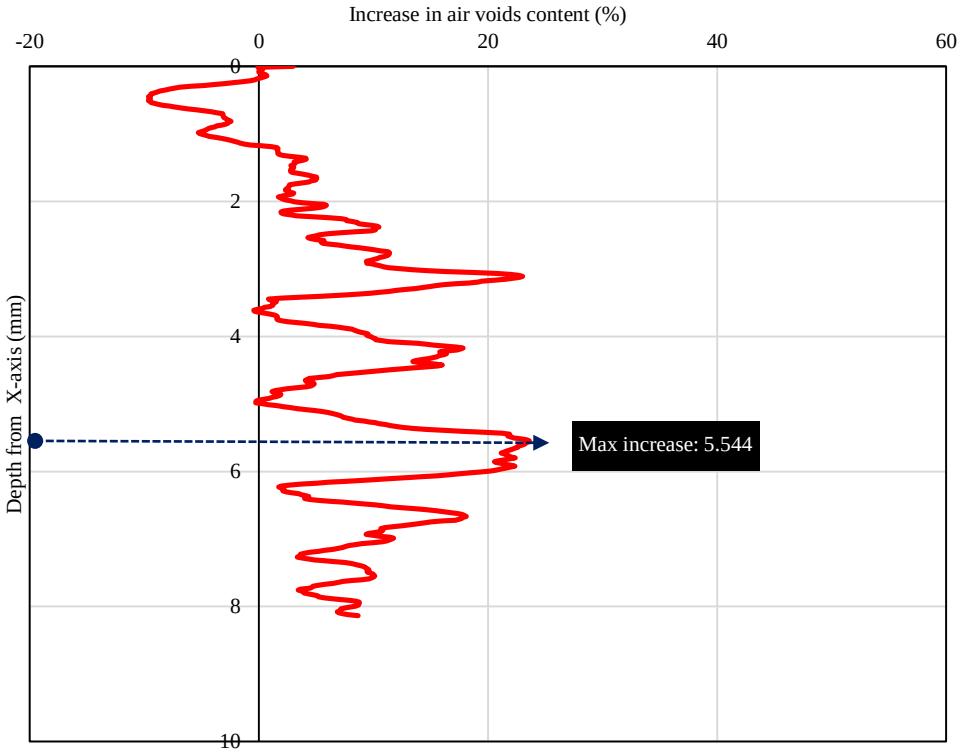
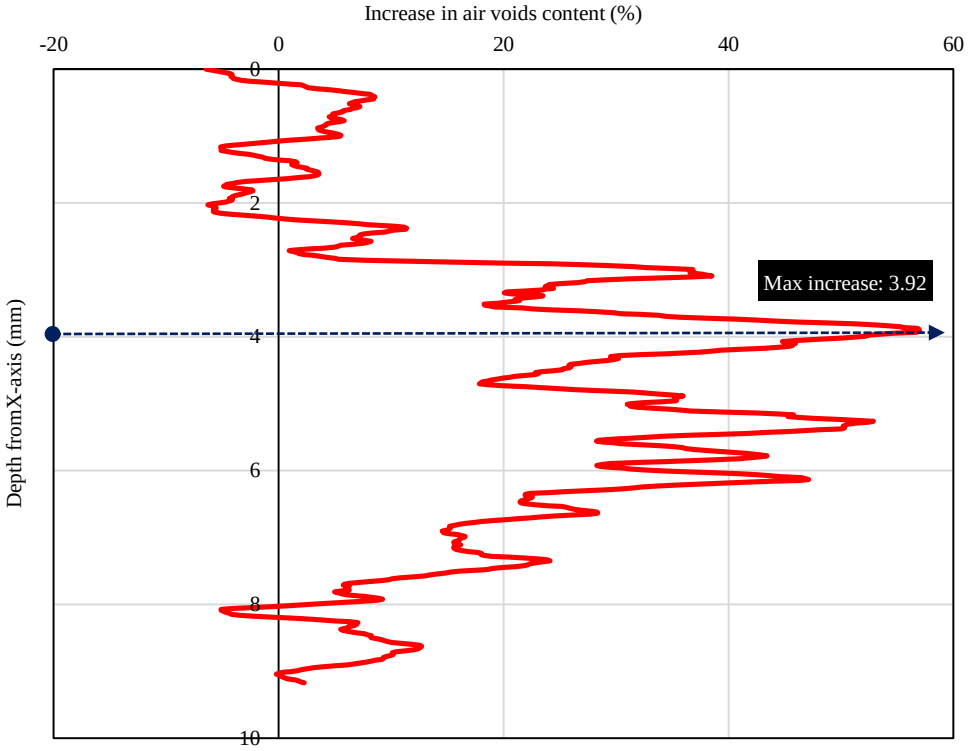


Figure: Increase in air voids content at (a) 0.8, (b) 0.9, (c) 1.1 and (d) 1.4mm vertical deformation in Y direction.

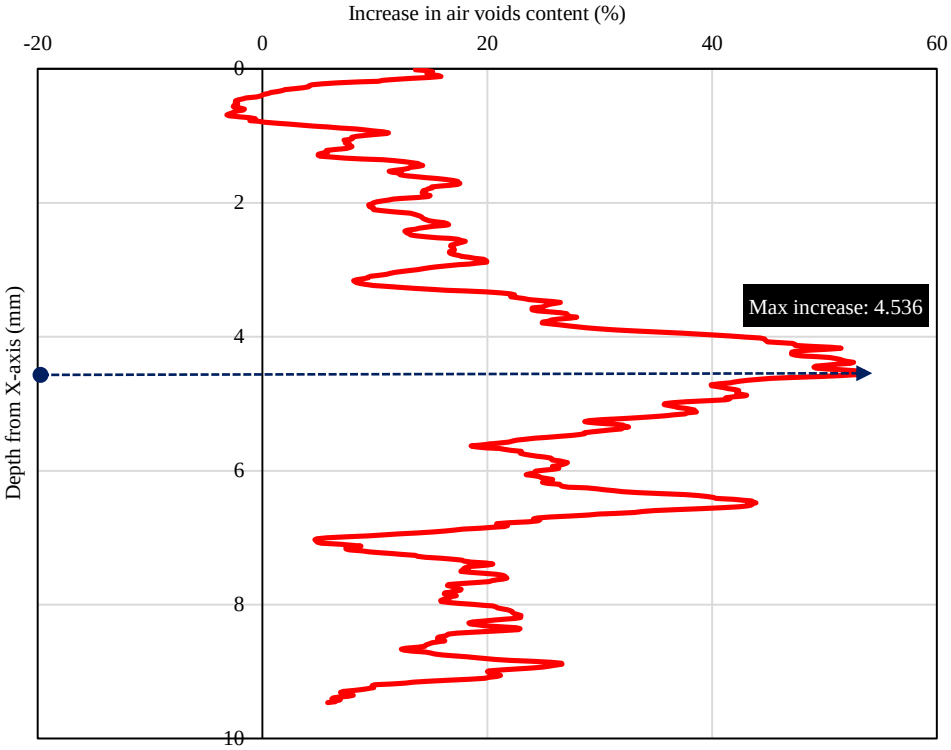
(a)


Increase in air voids content (%)
-20
0
20
40
60
0
2
4
6
8
10
Depth from X-axis (mm)
Max increase: 5.544

(b)


Increase in air voids content (%)
-20
0
20
40
60
0
2
4
6
8
10
Depth fromX-axis (mm)
Max increase: 3.92

(c)



(d)

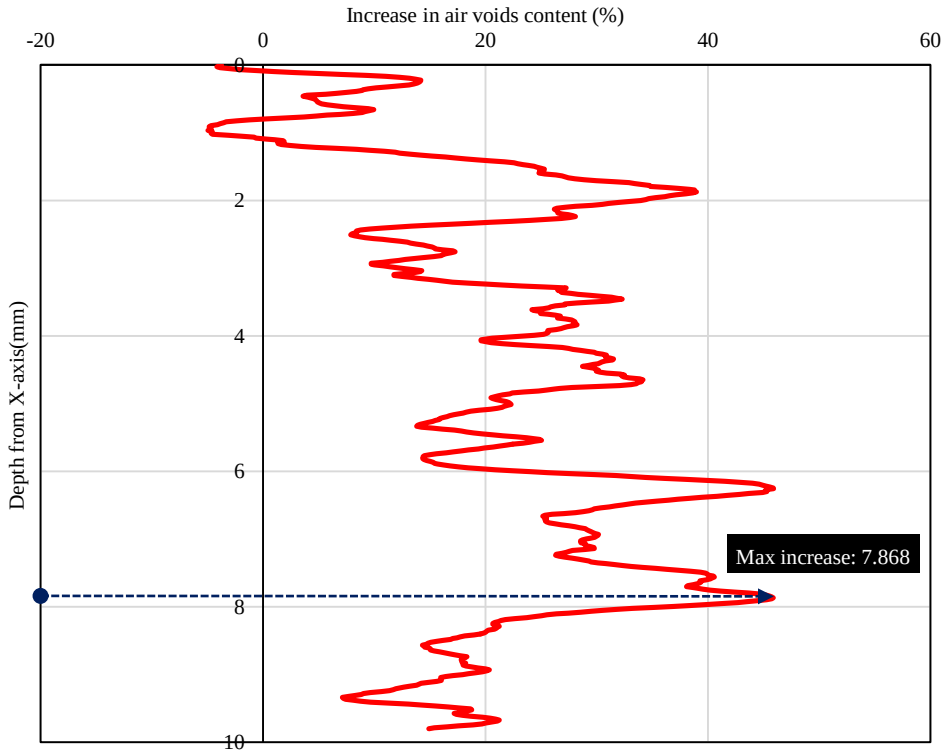


Figure: Increase in air voids content at (a) 0.8, (b) 0.9, (c) 1.1 and (d) 1.4mm vertical deformation in X direction.